

# Evaluating Cell-mimicking Giant Unilamellar Vesicles as Simplified Biological Models using Single Molecule Methods

---

**Pashiini Supramaniam**

Department of Chemistry

Imperial College London

A Thesis submitted for the  
Degree of Doctor of Philosophy

Date of Submission: September 2020

*In memory of Sarojah Chellappan.*

*To my mother, who fought her own battle everyday with such elegance and grace, to  
you, I dedicate this thesis.*

*All that I am, or hope to be, I owe it to you.*

# Declaration

---

I declare that this thesis entitled '*Evaluating Cell-mimicking Giant Unilamellar Vesicles as simplified Biological Models using Single Molecule Methods*' is the result of my own research except where otherwise noted, and with the following exceptions:

- The chip geometry of the PASH chip was developed with my doctoral supervisor, Dr Ali Salehi Reyhani. The validation of the platform assay was conducted by me.

Pashiini Supramaniam

August 2020

# Copyright Declaration

---

The copyright of this thesis rests with the author and is made available under a Creative Commons Attribution Non-Commercial No Derivatives licence. Researchers are free to copy, distribute or transmit the thesis on the condition that they attribute it, that they do not use it for commercial purposes and that they do not alter, transform, or build upon it. For any reuse or redistribution, researchers must make clear to others the licence terms of this work.

# Abstract

---

One of the main drivers within the field of bottom-up synthetic biology is to develop artificial chemical machines, perhaps even living systems, that have programmable functionality. Bottom-up methods take an engineering approach to biology, with multiple downstream applications. Such applications that require very specific quantities of product e.g., antibodies, drug, or vaccines, necessitate the design of vesicles with total and precise control of a vesicle's molecular machinery.

There exists a wide range of toolkits to produce and engineer artificial cells with an ever-increasing array of functionality and capability. However, little attention has been given to the quality control of vesicle production; so, to date, there is a paucity of techniques that are able to measure their molecular constituents precisely upon formation and with absolute quantification. The work outlined here presents the development of a microfluidic-based methodology that is able to characterise artificial cells at the single vesicle level with single molecule resolution.

High content fluorescence microscopy was used to assess the properties of Giant unilamellar vesicles (GUVs) and their statistics at the population level. Since this technique is semi-quantitative, the *relative* of concentration of protein across the GUV population was determined however the *absolute* concentration of protein within each GUV was not.

To overcome this, a lab-on-a-chip approach was taken to determine the precise number of biomolecules within each GUV and across the population of GUVs. The pulldown-

array single-molecule high-throughput (PASH) chip was developed and capable of determining the encapsulation efficiency of protein within GUVs produced by phase transfer of an inverted emulsion. Using this approach, it was possible to determine the variability of the encapsulation efficiency between GUVs across a population as well as between different populations while testing batch-to-batch variation. The encapsulation efficiency measured to be  $11.4 \pm 6.2\%$  across all tested parameters. This has consequences to the use of GUVs as precise biological models as well as for their development in a variety of biotherapeutic applications. To determine whether GUVs with specific concentrations of biomolecules could be produced by phase transfer, changes in the concentration of the seeding materials and reagents were investigated; while inefficiencies in encapsulation could be overcome, the variation in concentration could not.

The results presented in this thesis help to understand the limitation of the phase transfer technique applied to systems biology research. In biological systems, measuring changes in gene expression at the transcriptomic and proteomic level is important. When used to develop simplified models of protein expression, these results indicate that vesicles produced using phase transfer may only be confidently used to produce 10-fold changes in encapsulant protein. It is possible to distinguish different GUV populations with a precision down to a two-fold change in encapsulant protein but with significant population overlap. The understanding of the limitations of encapsulation efficiency provides insight into the potential relevance of such systems for a variety of therapeutic applications such as smart drug delivery.

# Acknowledgements

---

*“Because it broke me, it made me stronger”*

A chaotic journey that began in 2016, the PhD has seen a worldwide pandemic, England’s “it’s coming home” chants, endless cups of caffeinated beverages, several emotional breakdowns and an unhealthy amount of peanut butter, yet, here I am, a little bit alive and a whole lot stronger. Here is a toast to me, for soldiering ahead even with overheated lasers, malfunctioning computers, and green circle hauntings. Nevertheless, none of this would have been possible without the support and strength of those around me.

Firstly, I would like to express my heartfelt gratitude and appreciation to the two most amazing supervisors, Dr Ali Salehi-Reyhani and Professor Oscar Ces for not only giving me the opportunity to work on this project but also for the countless ways they’ve contributed to my growth both professionally and personally. I have always found our scientific discussions, ideas, and insights extremely helpful in providing me clarity with the project. When the days seemed dark with no end at sight, I am glad to have had the world’s best supervisors in my corner cheering me on. Words cannot describe how grateful I am for all the pep talk and banter. Both Ali and Oscar have been great champions in providing me with the freedom and independence of pursuing my own research ideas and interest outside the scope of the project, and for that I will always be thankful. A special thank you to the Single-Cell Proteomics group and the Membrane

Biophysics group for sharing instruments notably access to the level 4 wet lab facilities and the TIRF systems that were required for me to carry out my studies.

I would like to thank Stelios Chatzimichail, one half of the OG of the ASR group for the crash course in microfluidics and for being a walking scientific encyclopaedia. There never seems to be anything Ste does not know and that will never cease to amaze me. Beyond this, Ste has put up with me and all my bad puns, vegan lifestyle, and rants. I must also express my thanks to members of the SCP group both past and present in particular, Suhuur Osman, Zainab Ahmed, Shababa Selim, Ksenia Katsanovskaja, and Eve Chan. The fourth-floor office was our little haven amidst the noise outside. The good times of extended tea breaks, fruitful scientific discussion and JetPunk quizzes have enriched my PhD experience and made it one for the memories. I would also like to take this opportunity to thank the members of the ASR group at King's College London particularly Zibo Wang, crowned "King of Droplets", contributing to the work done in Chapter 4 and 5.

A special thank you goes out to my squad both in Malaysia and the UK for all the support. You ensured that I maintained a healthy work-life balance with an unhealthy amount of Saturday brunches, Sunday dimsums, cheeky midweek holidays and most importantly pastry supplies from Arapina. To my flatmates, Rose and Deven, I cannot begin to state how much easier you both made the thesis writing process. Despite a worldwide lockdown, our food challenges, state allowed walks and workout sessions helped me hold on to my sanity throughout. To Megat, Zunny, Yew Wing, and Acacia, thank you for allowing me to vent, to rant, and to do whatever it took to complete the PhD. A special mention to one Mr Harry Styles, for keeping me entertained with your

wonderful music throughout the entire PhD. It truly takes a community to complete a successful PhD.

Finally, it is my pleasure and honour to thank the three most important people in my life. To my parents and brother, your unconditional and unrelenting support and love throughout has made the journey a less exhausting one. Thank you for always pushing me, challenging me, and for always having faith in me even when I have not done so in myself. But mostly for always being there, even when I pretend like I do not need it, I always most definitely do.

# Publications

---

The work detailed in chapter 1 and 3 has contributed to the following publications:

1. **Supramaniam, P.**; Ces, O.; Salehi-Reyhani, A. Microfluidics for Artificial Life: Techniques for Bottom-Up Synthetic Biology. *Micromachines* 2019, 10, 299.
2. Chatzimichail, S., **Supramaniam, P.**, Ces, O. & Salehi-Reyhani, A. Counting proteins in single cells with addressable droplet microarrays. *J. Vis. Exp.* 2018, 1–12.

# Table of Content

---

<b>Declaration</b> .....	<b>3</b>
<b>Abstract</b> .....	<b>4</b>
<b>Acknowledgements</b> .....	<b>6</b>
<b>Publications</b> .....	<b>9</b>
<b>List of Abbreviations</b> .....	<b>13</b>
<b>List of figures</b> .....	<b>15</b>
<b>List of Tables</b> .....	<b>24</b>
<b>1. Introduction</b> .....	<b>25</b>
<b>1.1 Chapter Outline</b> .....	<b>25</b>
<b>1.2 Synthetic biology</b> .....	<b>26</b>
1.2.1 What is synthetic biology? .....	<b>26</b>
1.2.2 Bottom up and top down.....	<b>31</b>
<b>1.3 Artificial cells</b> .....	<b>34</b>
1.3.1 What are artificial cells? .....	<b>34</b>
1.3.2 Membrane bound artificial cells .....	<b>36</b>
<b>1.4 Microfluidics</b> .....	<b>48</b>
1.4.1 Advantages of microfluidics .....	<b>49</b>
1.4.2 Principles governing microfluidics .....	<b>51</b>
<b>1.5 Thesis overview and Aims</b> .....	<b>56</b>
<b>1.6 Thesis Outline</b> .....	<b>61</b>
<b>2. General Methods and Materials</b> .....	<b>62</b>
<b>2.1 Chapter Outline</b> .....	<b>62</b>
<b>2.2 Single Molecule Microarray Methodology</b> .....	<b>63</b>
<b>2.3 Optical Setup</b> .....	<b>63</b>
2.3.1 Optical Trapping .....	<b>67</b>
2.3.2 Optical Lysis .....	<b>69</b>
2.3.3 Total Internal Reflection Fluorescence Microscopy .....	<b>69</b>
2.3.4 Fluorescence Microscopy .....	<b>71</b>
<b>2.4 Formation of GUVs</b> .....	<b>74</b>
2.4.1 Types of lipid used.....	<b>74</b>
2.4.2 Preparation of lipid in oil .....	<b>74</b>
2.4.3 Inverted Emulsion Phase Transfer .....	<b>75</b>
<b>2.5 Single Molecule Counting and Data Analysis</b> .....	<b>77</b>

2.5.1	Non-Congested Image Processing .....	79
2.5.2	Congested Image Processing .....	84
<b>3.</b>	<b>Emulsion Phase Transfer to study size distribution of GUVs .....</b>	<b>86</b>
<b>3.1</b>	<b>Chapter Outline: .....</b>	<b>86</b>
<b>3.2</b>	<b>Introduction.....</b>	<b>87</b>
3.2.1	Liposomes .....	87
3.2.2	Conventional Techniques of Giant Unilamellar Vesicles fabrication.....	89
3.2.3	Wide Field Fluorescence Microscopy of Vesicles.....	95
<b>3.3</b>	<b>Experimental Methods .....</b>	<b>97</b>
3.3.1	Phase transfer of an Inverted Emulsion for vesicle production .....	97
3.3.2	Preparing vesicles for imaging.....	98
3.3.3	Wide Field Fluorescence Microscopy Imaging .....	99
<b>3.4</b>	<b>Results and Discussion.....</b>	<b>101</b>
3.4.1	Optimisation of Wide Field Imaging .....	101
3.4.2	Methodology and Optimisation of Data Analysis.....	106
3.4.3	Data Analysis Discussion.....	130
<b>3.5</b>	<b>Chapter Conclusions.....</b>	<b>154</b>
<b>4.</b>	<b>Absolute quantification of GUV using microfluidic technology .....</b>	<b>156</b>
<b>4.1</b>	<b>Chapter Outline .....</b>	<b>156</b>
4.1.1	Understanding Encapsulation Efficiency .....	157
<b>4.2</b>	<b>Introduction.....</b>	<b>162</b>
4.2.1	Single Cell Analysis.....	162
4.2.2	Microarray Platform.....	167
4.2.3	Single Cell Protein Pulldown Microarray Experiments.....	177
<b>4.3</b>	<b>Experimental Methods .....</b>	<b>182</b>
4.3.1	Fabrication of Pulldown Array Single-molecule High throughput (PASH) chip .....	182
4.3.2	Inverted Emulsion Phase Transfer for GUV Generation .....	189
4.3.3	Device Filling and GUV loading .....	190
4.3.4	Data collection and Analysis.....	191
4.3.5	Calibration Curve.....	194
<b>4.4</b>	<b>Results and Discussions .....</b>	<b>196</b>
4.4.1	Pulldown Array Single Molecule High-throughput (PASH) chip Development.....	196
4.4.2	Streptavidin AF488 and Biotinylated BSA Assay .....	202
4.4.3	Calibration Curve of Streptavidin AF488 and Biotinylated BSA Assay .....	204
4.4.4	Encapsulation efficiency .....	208
4.4.5	Application of GUVs .....	218
<b>4.5</b>	<b>Chapter conclusion .....</b>	<b>226</b>

<b>5. Conclusions and Future Work .....</b>	<b>228</b>
<b>5.1 Summary of Key Findings.....</b>	<b>228</b>
<b>5.2 Future Work.....</b>	<b>230</b>
5.2.1 On-chip Droplet Formation.....	230
5.2.2 Automation of Data Analysis.....	234
<b>5.3 Concluding Statements .....</b>	<b>235</b>
<b>References.....</b>	<b>237</b>

# List of Abbreviations

---

AF-488	Alexa Fluor-488
ATP	Adenosine triphosphate
BSA	Bovine Serum Albumin
$C_a$	Capillary number
CCD	Charge-coupled device
DIB	Droplet interface bilayer
DNA	Deoxyribonucleic acid
<i>E.coli</i>	<i>Escherichia coli</i>
FACS	Fluorescence activated cell sorting
GUV	Giant Unilamellar Vesicle
IF	Immunofluorescence
LOD	Limit of Detection
MAC chip	Microfluidic antibody capture chip
MC7	Human estragon receptor-positive breast cancer cell line
MLV	Multilamellar vesicle
NA	Numerical aperture
NSB	Non-specific binding
PASH Chip	Pulldown Array Single-molecule High throughput chip
PBS	Phosphate buffered saline
PBSA	Bovine serum albumin in phosphate buffered saline
PCR	Polymerase chain reaction
PDMS	Polydimethylsiloxane
$P_e$	Peclet number
PFS	Perfect Focus System
POPC	1-palmitoyl-2-oleoyl-sn-glycero-3-phosphocholine
PTIE	Phase transfer inverted emulsion
PURE	Protein Synthesis Using Recombinant Elements
$R_e$	Reynold's Number

RNA	Ribonucleic acid
SNR	Signal to noise
SUV	Small unilamellar vesicle
TIRF	Total internal reflection fluorescence
W/O	Water-in-oil
WGE	Wheat germ extract

# List of figures

---

<b>Figure 1.1</b> The progress of the field of synthetic biology branching out from classical and molecular biology. The coloured boxes within the timeline represent key scientific and technical milestones (black), key milestones within synthetic biology (orange) and milestones of synthetic biology (green) with therapeutic applications and metabolic engineering. The image is modified from the reference 5 and 6.....	28
<b>Figure 1.2:</b> The conceptualisation of the hierarchy within synthetic biology by drawing an analogy to computer engineering. <sup>7</sup> .....	30
<b>Figure 1.3:</b> The two contrasting approach used for the design and construction of artificial cells within the field of synthetic biology. Using a top-down approach, artificial cells are constructed by replacing and removing the genomes of living organisms, reducing its complexity, and retaining the minimum substance to sustain life. Whilst a bottom-up approach involves the building of artificial cells from scratch by the assembly of non-living components with living components to form a system that mimics closely a living cell. The image is reproduced from the indicated reference. <sup>8</sup> .....	31
<b>Figure 1.4:</b> A representation of an artificial cells containing some key cellular elements. The model features a membrane of defined composition and symmetry, a cell-free protein expression system by incorporating an in-vitro translation-transcription pathway, inclusion of non-biological components used for cellular recognition, insertion of transmembrane proteins for transport of molecules between the membrane based upon an external, stimulus response, and cellular communication between the model and a biological cell. The figure is reproduced from the specified reference. <sup>16</sup> .....	36
<b>Figure 1.5:</b> A schematic drawing depicting the different morphologies of a vesicle and the approximate sizes of unilamellar vesicles. SUV small unilamellar vesicles, MLV multilamellar vesicles, LUV large unilamellar vesicles, MVV Multivesicular vesicles, GUV giant unilamellar vesicles, GV giant vesicles. The figure is modified from Stano et al. (not to scale) <sup>35</sup> .....	38
<b>Figure 1.6:</b> A schematic of an artificial cell containing an encapsulated biological cell. The cell serves an organelle-like function, processing chemical elements by using a synthetic enzymatic cascade. Figure modified from the following reference. <sup>45</sup> .....	40
<b>Figure 1.7:</b> A schematic of the protometabolic formation of carbohydrate inside a lipid vesicle. The image on the right most shows the bioluminescence reaction of the bacteria in response to the presence of a carbohydrate complex. The image is adapted and modified from the following references. <sup>46</sup> ....	41
<b>Figure 1.8:</b> The proposed functioning of the synthetic mechanosensitive signalling pathway. The calcium ions are initially impermeable due to the presence of the bilayer. However, the addition of $\alpha$ -hemolysin to the outer membrane results in a calcium influx which activates the secretoryphospholipase A2 (sPLA <sub>2</sub> ). This results in the activation of the mechanosensitive channel of large conductance (MscL), releasing the encapsulated dye molecules into the artificial cell. The image above was reproduced from the following reference. <sup>49</sup> .....	42
<b>Figure 1.9:</b> The folding of the 3D printed water-in-oil droplets network capable of self-folding and transmitting electrical signals across a pathway. Image reproduced from referenced paper. <sup>50</sup> .....	43
<b>Figure 1.10:</b> The figure above shows a schematic description of the inverted emulsion phase transfer a) Water-in-oil emulsions are prepared by mixing the aqueous phase with the lipid-in-oil solution. A monolayer form spontaneously to stabilise the emulsions. b) A water-in-oil column is then prepared using a secondary aqueous phase and lipid-in-oil mixture. A monolayer self assembles at the interface. The emulsion is transferred to the column. The inset shows as the droplets pass through the interface either through gravity or mechanical manipulation, it picks up a secondary layer of lipid to form a bilayer. ....	47
<b>Figure 1.11:</b> A schematic of the different flow regimes. a) A schematic of laminar flow in a micron-sized channel. b) In the presence of two immiscible fluids that flow side by side, mixing between them only occur via diffusion. c) A schematic depiction of turbulent flow.....	51

<b>Figure 1.12:</b> Hydrodynamic fluid focusing that employs the laminarity of the fluid. The main flow stream is focused at the centre of the channel using the side streams. Due to laminar flow, the mixing that occurs between the two different flow path is governed solely by diffusion.....	53
<b>Figure 1.13:</b> The comparison between continuous flow and segmented flow: The schematic above represents the continuous flow (top) and segmented flow (bottom) in a microchannel. The use of segmented flow (droplet microfluidics) in devices have addressed the limitations brought upon by continuous flow and is explained and outlined in detail in the referenced publication. <sup>79</sup> .....	55
<b>Figure 2.1:</b> The experimental workflow of the different components that encompass the work carried out throughout the thesis.....	62
<b>Figure 2.2:</b> The setup of the optical imaging platform that was used during the experiments carried out in this thesis. Image reproduced from Salehi-Reyhani PhD Thesis 2011, Imperial College London...	64
<b>Figure 2.3:</b> Schematic of the PFS in use with an oil/water immersion objective. 770 LED= LED emitting at 770nm, L-CCD, FC= filter cube. Image reproduced from Salehi-Reyhani PhD Thesis 2011, Imperial College London. ....	65
<b>Figure 2.4:</b> The complete optical set up of 473 nm continuous wave TIRF laser (blue), a 1070nm continuous wave trapping laser (red) and 1064nm pulsed lysis laser (green). Image reproduced from Salehi-Reyhani PhD Thesis 2011, Imperial College London. ....	67
<b>Figure 2.5:</b> The working principle of an optical trap. The $F_{\text{scat}}$ causes a movement of the particle along the path of the incident beam whilst the $F_{\text{grad}}$ acts as an attractive force which pulls the particle back to the centre of the focal point. ....	68
<b>Figure 2.6:</b> Experimental images of the optical lysis process of an MCF-7 cell showing i) before the application of the optical pulse ii) during the process iii) after the pulse. The complete lysis of the cell is observed in image III. The bright white flash in image II is the result of electrons recombining with the plasma due to the laser-induced breakdown of a femtolitre volume of media. Figure adapted from footage from reference <sup>84</sup> .....	69
<b>Figure 2.7:</b> Comparative figure between a widefield epifluorescence microscopy (top) and TIRF microscopy (bottom). The evanescence wave formation at the critical angle causes the excitation of the fluorophore in the aqueous medium to occur at 100 nm from the surface. This reduces the background noise. Image retrieved from reference <sup>85</sup> .....	71
<b>Figure 2.8:</b> Epifluorescence inverted-microscope configuration. The optical paths of the excitation (blue line) and emission (green) through the objective lens are identical however shown separately here for visual clarity. 1: Light source typically a mercury arc lamp 2: Excitation Filter. 3: Dichroic beam splitter mirror that separates out the excitation light from the resultant emission signal. 4: Objective lens. 5: Sample 6: Emission filter 7: Signal detector, typically a CCD Camera that captures the fluorescent images. ....	72
<b>Figure 2.9:</b> An example of a fluorescence filter cube fitted into the carousel of the fluorescence microscope. Image reproduced from reference <sup>86</sup> .....	72
<b>Figure 2.10:</b> The figure above shows the chemical structure of POPC used in the generation of the giant unilamellar vesicles and water in oil droplets throughout the thesis. ....	74
<b>Figure 2.11:</b> The formation of GUVs using inverted emulsion phase transfer. a) The lipid-oil mixture is formed by dissolving the lipid film using mineral oil. b) The lipid oil mixture is pipetted into the solution containing the aqueous solution. c) This leads to the formation of an interfacial lipid monolayer. d) Water-in-oil emulsions are prepared by mixing the internal aqueous solution (AF-488 Streptavidin in 200 mM sucrose) with the lipid-in-oil solution. This was then pipetted into an Eppendorf tube containing the external aqueous phase (200 mM glucose). e) This mixture was then centrifuged to accelerate the movement the emulsion the interface during centrifugation. The presence of a density gradient results in the formation of Giant Unilamellar Vesicles.....	76
<b>Figure 2.12:</b> Exemplar images of simulated antibody spots. Each of the spot is generated using a pre-determined number of single molecules randomly located inside a circular area, mimicking a microarray spot. The number of single molecules per spot increases from left to right. A transition from non-	

congested ( $10^2$ - $10^3$ ) to semi congested ( $10^4$ ) to a fully congested region ( $10^5$ - $10^6$ ) can be visually noted. The red arrow denotes a single molecule. The figure is extracted from reference.<sup>88</sup> ..... 78

**Figure 2.13:** The workflow of processing non-congested images ..... 79

**Figure 2.14:** The stages of the non-congested single molecule counting algorithm. a) The original image b) An exemplar image of the laser profile constructed by passing through background image a gaussian blur filter. c) The flattened image produced by dividing image (a) with (b). d) After applying a threshold of 3 standard deviations of the background, the SM mask produced consists of the remaining particles that are counted as single molecules depending on its circularity and cluster size. The effects of field flattening, gaussian blurring and background subtraction across a single molecule image can be observed via the line profile of the corresponding images. The line profile, a diagonal line drawn across the image from top left corner to bottom right corner corresponds to the pixel intensity of the image. .... 80

**Figure 2.15:** An exemplar image of the Baseline Noise Offset. The profile of the flattened and background subtracted image is obtained using a line profile drawn from the top left corner to top right corner. The inset image shows a rather noisy profile, with fluctuations of the pixel intensity close to but not zero. This fluctuation can be categorised as the baseline noise offset. .... 82

**Figure 2.16:** The workflow of processing congested images using the congested algorithm..... 85

**Figure 3.1:** The figure above shows the 3D model of the POPC lipid that was used as the lipid component of the GUV throughout this thesis. a) The phospholipid molecule is divided into the polar headgroup region (hydrophilic) consisting of a phosphate group and a glycerol backbone in this case and the non-polar (hydrophobic) region consisting of the carbon chain. b) The figure shows a simplified vesicle consisting of a bilayer, with an aqueous core and hydrophobic bilayer membrane. A single bilayer membrane is typically ~5nm thick. The lipid molecules are oriented such that the “water hating” tail group faces inwards and the “water-loving” head group faces the exterior aqueous medium. .... 87

**Figure 3.2:** A schematic of natural swelling method used to produce GUVs. a) The lipid is dissolved in an organic solvent b) The evaporation of the solvent and self- assembly of lipid molecules into several stacks of bilayer. c) The addition of buffer hydrates the dried lipid film. d) The swelling of the stack of bilayer lipid films form vesicles..... 90

**Figure 3.3:** The illustration above shows the stacked lipid bilayers deposited above the polymer surface. This allows for an increased flow of the buffer solution that helps in the formation of GUVs..... 91

**Figure 3.4:** The illustration above shows the formation of vesicles using electroformtion method. Figure reproduced from the stated reference.<sup>117</sup> ..... 92

**Figure 3.5:** The figure above is an illustration of the inverted phase emulsion transfer. a) The water-in-oil droplets b) The interface formed between the two phases in which the droplets pass through and picks up the outer layer of the bilayer. c) The vesicle that is formed is of a unilamellar bilayer. .... 93

**Figure 3.6:** An exemplar image of a water-in-oil droplet imaged at the interface using phase contrast microscopy and fluorescence microscopy. Figure reproduced from the following reference <sup>123</sup> ..... 94

**Figure 3.7:** The figure above shows the 8 well chamber that was used for the wide field imaging. The 200mM glucose solution and GUV solutions were filled at a 1:2 ratio to the top of the chamber. Achieving a flat interface and no concave meniscus helped to avoid inhomogeneous backgrounds due to the scattering of fluorescence excitation light. The surface functionalisation that is used is a thin layer of BSA on the surface to prevent the adsorption of GUVs. Illustration not to scale. .... 99

**Figure 3.8:** GUVs encapsulated with streptavidin Alexa Fluor 488 (green) were resuspended in collection buffer systems containing the denoted percentage (w/v) of BSA in 20 0mM glucose in PBS. The concentration range of the BSA tested here is between 0.6 mM to 0.075Mm. The GUVs were incubated at room temperature for 30 minutes prior to imaging. The images here show the extend of the GUV rupture to the corresponding solutions. Minimal rupture was observed with 0% BSA. .... 103

**Figure 3.9:** Intensity line profile of a GUV in two scenarios. a. A representation of an ideal line profile of a GUV with well-defined edges and no noise. The sharp rise to maxima and drop to minima is indicative of the fluorescent signal within the GUV. b. A representation of a typical line profile of a GUV. The gradual increase and decrease of the intensity measurement represent the decrease of the

fluorescence across the GUV due to the difference in the projected volume of the GUVs as a result of the imaging..... 108

**Figure 3.10:** a) The relationship between the area measured in the bright field channel and FITC channel respectively for all individually isolated GUV. The estimation of the edges from the ground truth using the bright field images and FITC image for both large and small sized GUVs show minimal deviation from the ground truth. b) The relationship between the GUV area in the bright field and the FITC for smaller area GUVs between 0-250  $\mu\text{m}^2$ . The measurements were carried out on GUVs (n=82), encapsulated with AF 488..... 109

**Figure 3.11:** a) The relationship between the area difference measured in bright field and FITC against that measured in bright field. The variation between of GUVs at the lower end is higher. As the volume is a function calculated using information obtained from the area measured, the error associated with the overestimation or underestimation of the area is multiplicative. b. The percentage difference of the volume difference calculated in bright field and FITC against the volume of bright field GUVs for the same set of data. The measurements were carried out on GUVs n=82, encapsulated with AF 488... 110

**Figure 3.12** Exemplar images of GUVs used to measure the area of the GUVs a) GUVs of a larger area and volume have a more distinct edge appearance in both the bright field and fluorescence channel b) Smaller volume GUVs have a less distinct edge appearance thus making the approximation of the edges more difficult. .... 112

**Figure 3.13:** Exemplar image of GUV acquired using a) phase contrast microscopy b) Bright Field Microscopy. The image of the GUV obtained from phase contrast is has significantly more defined edges in comparison to the bright field.(Scale bar: 50  $\mu\text{m}$ ) Image modified from indicated reference. <sup>140</sup> ..... 113

**Figure 3.14:** The figure above shows the three varying possible appearances of the GUV when formed using emulsion based phase transfer. a) A “clean” GUV with minimal lipid junk and debris on the external lipid envelope of the vesicles. This makes determining the edges clearer. b) The GUV that is produced contains a slightly higher lipid junk in the outer lipid envelope. However, it is shown that this does not affect the fluorescence intensity as the region of interest lies within the internal compartment in where the encapsulated fluorescence material is concentrated. c) The GUV produced here has an extremely messy out lipid layer, with two distinct rings forming the external layer and internal layer is observed. In order to identify the edges, the area is measured from the internal edges as shown in the FITC image. .... 114

**Figure 3.15:** Exemplar of GUVs excluded from the manual segmentation method. a) The GUVs were imaged between the borders of two tiles that were stitched together. b) GUVs that are visibly clumped together in which the perimeter of the GUVs are hard to be distinguished were also excluded. c) The GUVs that are in close proximity to the larger clumped objects would be more affected by the halo effect (red circles) compared to those that have a cleaner background (white circles)..... 115

**Figure 3.16:** The method used for estimating the background within each data set. Random circles approximately the size of the GUVs are superimposed onto the data set to obtain the background intensity. The circles are superimposed within regions away from the bright halo of the GUVs. .... 116

**Figure 3.17: The effect of background subtraction on the data.** The effect of the background subtraction on to the data. The GUVs with a lower volume are more affected by the background subtraction in comparison to that of a higher volume. This is because, at a lower volume, the fluorescence intensity is of a lower value overall, thus the contribution from the background may appear larger than that at a higher volume. (n= 762)..... 118

**Figure 3.18:** The figure above shows an exemplar GUV and the line profile of its fluorescence intensity. .... 121

**Figure 3.19:** The comparisons of manual segmentation and the three different thresholding method. Here, it shows that the using Huang thresholding method may lead to an overestimation as indicated by the area beyond the perimeter of the GUV. For both Max Entropy and Otsu, an underestimation in the size of the GUV is noted. In some instances, artefacts that could have been a result of imaging is picked up by the thresholding method. .... 122

**Figure 3.20:** Level of thresholding that on two different scenarios. a) In an ideal scenario, where the signal to noise ratio is  $\gg 1$  and the angle is  $90^\circ$ , the apparent size measurements are irrespective of the intensity thresholding. b) In the case of a high signal to ratio with angle approaching  $90^\circ$ , the level of thresholding has an effect on the apparent size measurements. .... 123

**Figure 3.21:** Intensity line profile used to demonstrate the effects of thresholding on two different scenarios of GUVs found in the dataset. a) High signal o noise ratio where the signal intensity of the GUV is significantly higher than the noise level. The thresholding has an effect on the apparent size measurement and is denoted by  $\Delta d$ . b) Low signal to noise ratio in which the signal intensity is close to the noise level thus making it more sensitive to the thresholding. The difference in the apparent size measurement due to the thresholding level is denoted by  $\Delta d'$ . As expected, the less intense GUV is more sensitive to the thresholding, hence, it may have a larger error in size measurements as a result. .... 124

**Figure 3.22:** The illustration above exemplifies the effect of overestimating and underestimating the area of the GUV in relation to the intensity measurement. The image is a representation of a possibility of the data that would be obtained from the image analysis methods. The green circle and line correspond to a “perfect estimation” of the thresholding which would capture majority of the intensity information. a) The overestimation of the data set represented by the blue circle and line shows the fluorescence intensity and radius information obtained would not correspond with the ‘ideal estimation’. However, as fluorescence information of the true value would have been captured, the additional information would most likely be due to the background which can be corrected for. Overestimation therefore affects the size information more severely. b) The underestimation of the GUV would likely lead to a loss in both the fluorescence intensity information and size information as represented by the red dotted line and circle. .... 126

**Figure 3.23:** The figure above shows the analysis modules in the pipeline used in Cell Profiler. The pipeline was optimised to be used for large images such as the ones used in this thesis. .... 127

**Figure 3.24:** An illustration of the graphical representation of the information obtained from the data analysis. The equation represents the relationship between the volume and intensity. The change in the position of a particular data point along the graph due to the errors can be presented as a unit vector. The four different scenarios indicate the contribution of the error on the data set. .... 131

**Figure 3.25:** The effect of the errors in both the volume and intensity measurements on the GUVs with a low signal to noise ratio. a) An equal error contribution of the errors has an equal impact on the area and intensity measurement, therefore stretching the data along the true distribution. b) In the case of where the underestimation of the volume leads to a higher contribution of error by the volume causes the gradient of the line to flatten as it tilts upwards. c) The overestimation of the volume of the GUVs in which the contribution of error in the volume is more significant leads to a downward tilt, shifting the gradient closer to 1. .... 132

**Figure 3.26:** Graph of volume measured using different data analysis method against the calculated volume from the ground truth. The perceived ground truth here is obtained from measuring the area of the vesicles from the bright field images. (n= 82) The inset shows a close up on the data points analysed using manual segmentation techniques and Otsu thresholding method. Both these techniques seem to be in close agreement with the ground truth. Upon statistical analysis of the data, it was found that the mean of the data obtained from manual segmentation had a 4% difference with the mean of the ground truth, whilst when using Otsu, there was a 17% difference. The standard deviation of the data obtained using Otsu, indicated that the data was more spread out that both manual segmentation and the ground truth. .... 134

**Figure 3.27:** Graphs of the intensity against volume of each of the method. The resultant graphs were compared against the ground truth and the manual segmented data. .... 138

**Figure 3.28:** The comparison of the fluorescence intensity measurement obtained from the different data analysis method (n=82). Cell Profiler is shown to be closest to the ground truth followed by Otsu and Manual Segmentation. This indicates that any possible deviation from the ground truth is could be primarily due to the error in size estimation. .... 138

**Figure 3.29:** Graph of Volume vs Intensity of 1, 10 and 100 $\mu$ M calcein. The automated Fiji Filters under segment a significant portion of the data leading to the extension of the data points on the lower end of the data. The intensity measurement however is preserved with the Y-intercept within the same order of magnitude. Cell Profiler on the other hand over segments the GUVs leading to an extension of the data points on the higher end. The over estimation of the GUV area leads to the overestimation of the GUV intensity of at the higher end. .... 141

**Figure 3.30:** Exemplar illustration on how the data can be analysed and interpreted using the automated data analysis methods. a) In the case of an even segmentation, in which the perimeter of the GUVs is clearly defined, maximum area and intensity information is retained. b) The appearance of the GUV in which i) The GUVs are symmetrical with an uneven distribution of the intensity. The incorrect segmentation of the vesicles leads to a tilt in the gradient of the graph. The contribution of the error in the size measurement would be more significant in comparison to the error in the intensity measurement. ii) The GUVs are asymmetrical with an uneven distribution of the intensity. The incorrect segmentation in this case would lead to a tilt in the gradient, with a larger contribution from the vesicle on the left in comparison..... 143

**Figure 3.31** The average intensity and volume comparison of 10  $\mu$ M Calcein data. The average values here show that using Cell Profiler when compared to the ground truth, the average volume of the data is almost 15 times higher, however, the difference between the average intensity is only about 1.6 times higher. With the automated Fiji Filters, the difference between the average intensity value and the difference between the average volume values are with 20-30% of the ground truth values (Manual Segmentation n=438, Huang n=471, Max Entropy n=202 , Otsu n=252, and Cell Profiler n=796) .. 145

**Figure 3.32:** Graph of volume vs Intensity of 1 $\mu$ M Calcein using comparing CellProfiler and Manual Segmentation. ai) The mask produced by Cell Profiler showing the over segmenting of clumped GUVs adding to phantom small volume vesicles. ii) The corresponding fluorescence section of the segmented area. b(i) The mask produced by Cell Profiler showing the under segmenting of a clumped GUVs in which the cluster of GUVs is considered as one giant vesicles, adding to the phantom large volume vesicles. ii) The corresponding fluorescence image of the imaged section. .... 146

**Figure 3.33:** Assessment of GUVs with logarithmically increasing concentrations of Calcein a) Manual segmentation of individual GUVs to measure the diameter, in which the volume is calculated and total fluorescence. The gradient of each of the lines indicate a positive correlation between the GUV volume and encapsulation efficiency with a constant concentration. .... 147

**Figure 3.34:** Assessment of GUVs encapsulated with  $10^6$  molecules  $\text{pL}^{-1}$  using the different data analysis methods. The automated Fiji Filters under segment a significant portion of the data leading to the extension of the data points on the lower end of the data. The intensity measurement however is conserved with the Y-intercept within error. Cell Profiler on the other hand over segments the GUVs leading to an extension of the data points on the higher end. The over estimation of the GUV area leads to the overestimation of the GUV intensity of at the higher end. .... 148

**Figure 3.35:** Concentration range of Streptavidin using 3 varying concentrations. The increase between each line should be of a factor of 10, however, this was not the case. The slight difference between these values shows the sensitivity of the data analysis method. .... 149

**Figure 3.36:** Assessment of the sensitivity of manual segmentation of  $10^6$  molecules  $\text{pL}^{-1}$ . The graph shows that vesicles of a lower signal to noise ratio is more sensitive to minor adjustments and changes in the parameters of the manual segmentation method as expected. .... 150

**Figure 3.37:** Assessment of the batch to batch variation of the different populations of GUV with the same starting seed solution. .... 151

**Figure 3.38:** The variation in the concentration across a range of volume in a) 10 $\mu$ m calcein b)  $10^6$  molecules  $\text{pL}^{-1}$  ..... 152

**Figure 4.1:** Averaging results from bulk measurement can lead to misleading results. a) Averaging values from two distinct population distribution often leads to the misrepresentation of the true expression level of both populations. b) Taking an ensemble average measurement has the tendency to

mask measurements from rare subpopulations leading to the loss of information about heterogeneity. ....	163
<b>Figure 4.2:</b> Schematic illustration of the central dogma within a single cell. Understanding the level of proteins provide a complete picture of cellular function. Figure adapted from reference <sup>163</sup> .....	165
<b>Figure 4.3:</b> The three categories of protein microarrays. a) Analytical protein microarray mostly represented by the use of antibodies as detector molecules on the surface of the substrate The targeted proteins in this class can be detected using direct labelling or a sandwich based assay format b) Functional protein microarrays involve the immobilisation of protein molecules as detectors and have broad applications in studying protein based interactions .c) Reverse-phase microarray is a contrast of the first two types of microarray where cell the lysate samples are immobilised on the surface of the substrate and can be detected using direct labelling. Image modified from the reference <sup>173</sup> .....	169
<b>Figure 4.4:</b> A schematic illustration showing an antibody sandwich complex that is often found in protein microarrays. ....	170
<b>Figure 4.5:</b> Microfluidic devices used in single-cell proteomic analysis. a) A schematic of the microfluidic antibody capture (MAC) chip developed by Reyhani et al. Image reproduced from reference <sup>58</sup> b) An illustration of the SCBC platform developed by the Heath group. The fluorescent readout obtained from the device, in which each strip corresponds to an analyte in a panel of 10 proteins. Image adapted from reference <sup>182</sup> .....	176
<b>Figure 4.6:</b> A schematic depicting the general workflow of the single GUV protein pulldown microarray experiment using the Pulldown Array Single molecule High-throughput (PASH) chip. Image modified from the following reference <sup>177</sup> .....	177
<b>Figure 4.7:</b> Time-resolved image series showing the process involved in the lysis of a cell using optical lysis. Plasma formation (a) Shock wave propagation (b-c) Expansion of cavitation bubble (d-i) and the subsequent collapse (i-k). Image is reproduced from reference <sup>187</sup> .....	181
<b>Figure 4.8:</b> The schematic of the Pulldown Array Single-molecule High-throughput (PASH) chip. Each of the device consists of a main channel that is connected to 100 individual analysis chambers. The length of the main channel is 36 mm, with a height of 35µm. The volume of each of the chamber is approximately 2.93 nL. ....	183
<b>Figure 4.9:</b> Major steps involved in the photolithography of producing silicon wafer for the fabrication of microfluidic devices. a) The design of the channels is drawn up in a CAD program which is then used to produce the photomask. b) An epoxy photoresist, SU-8 is spin coated onto a silicon wafer. c) The photomask is applied on top of the coated wafer and is exposed to UV rays. d) The exposure to UV rays causes SU-8 to form crosslinks and solidify. This allows the design to be etched onto the surface of the wafer. The design presented here is an example and does not reflect the design of the microfluidic chip design used in this thesis. ....	183
<b>Figure 4.10:</b> The figure above describes the chemical reaction scheme of the silanisation process that takes place in the last step of photolithography. ....	185
<b>Figure 4.11:</b> An exemplar image of a printed and aligned microarrayed spot within the analysis chamber of the PASH chip imaged under bright field with 4X magnification. The inset image shows the arrayed protein spot viewed under a 60× objective. ....	188
<b>Figure 4.12:</b> The custom made alignment jig used to align the microarrayed slide to the analysis chambers of the chip. The translation screws allow for fine adjustments of the PDMS piece relative to the position of the glass slide. Image reproduced from Magness.A PhD thesis 2017, Imperial College London. ....	189
<b>Figure 4.13:</b> a) i) The microfluidic pump syringe system setup used to introduce the GUVs into the assembled PASH chip ii) The complete set-up of the pump attached to the outlet on the chip. The pump is mounted on the microscope stage as above. b) The loading of the GUVs into the main channel followed by the use of optical tweezers to individually isolate the vesicles into the chambers. The red square is used as a reference point at which the laser is focused at. c) An example of the process of optically lysing the GUV to release the contents into the chamber. The labelled lipid material is	

compromised and the intraGUVular material is dispersed within the analysis chamber, free to be assayed. .... 191

**Figure 4.14:** The different type of images acquired over the duration of a single GUV pulldown experiment. a) An image of the printed antibody spot on the surface of the substrate acquired prior to the filling of the chip. b) The background images readout i) Spot background image obtained after the chip has been filled with the blocking solution of 200mM glucose and 4% BSA. ii) Spot background image obtained after the optical trapping of the GUVs and prior to optical lysis. The resultant SM count in from this set of images are used to determine the contribution of diffusion background. c) An example of t a 60×FITC fluorescence image of individually isolated GUVs in the chambers of the chip. These images are used to obtain the size information and the fluorescence information of the GUV. d(i-iv) The TIRF readout of a time course single molecule data viewed using under 488 nm illumination.. 193

**Figure 4.15:** GUVs encapsulated with streptavidin Alexa Fluor 488 (green) were resuspended in collection buffer systems containing 200mM glucose in PBS. The concentration of lipid used within the lipid oil solution varied between 2 to 0.13 mg ml<sup>-1</sup>. The GUVs were incubated at room temperature for 30 minutes prior to imaging. The images here indicate the reduced yield of the GUVs as the concentration of lipid in mineral oil is reduced. .... 197

**Figure 4.16:** The lipid in oil mixture from using different concentration of the lipid. a) The pellet at the bottom of the Eppendorf shows the successful generation of GUVs using 2mg mL<sup>-1</sup> lipid. b) The lipid in oil solution was unable to be used as to form GUVs as it crashed out due to the oversaturation of the lipid molecules in the oil. .... 198

**Figure 4.17:** The comparison of the diffusion background single molecule counts between the control analysis chambers in the device. Chambers that are not filled with a GUV are used as the control. The background SM count of the experiment is 526 ± 191 molecules. The bottom row of the device exhibits a significantly smaller change in SM count from the background in comparison to the chambers on the top row. .... 200

**Figure 4.18:** Calibration curve produced for the AF488 Streptavidin determined for the PASH chip using the analysis chambers (2.93nL). The level of non-specific binding using a BSA functionalised coverslip is 25 ± 1.85 molecules. The dynamic range of the system lie between 10<sup>5</sup> – 10<sup>7</sup> at the linear part of the calibration curve. The conversion of single molecule count to the number of streptavidin molecules per vesicles is done by solving the number of streptavidin molecules present per chamber (x) based on the detected TIRF signal (y). (n=25)..... 207

**Figure 4.19:** Exemplar images of GUVs due to the difference in the efficiency of encapsulating molecules within the GUVs produced using emulsion based phase transfer a) An example of a vesicle that is extremely concentrated in a cluster surrounded by other vesicles with a lower concentration. The vesicles surrounding this bright vesicle are all approximately the same size. b) The presence of ‘ghost vesicles’ where the vesicle coalesces to an adjacent vesicle that is significantly brighter than itself. This ghost vesicle is often only visible due to the attached vesicle. .... 209

**Figure 4.20:** a) The plot of the volume of GUV against the number of protein molecules in GUV b)The encapsulation efficiency of the vesicles produced using emulsion based phase transfer spans between two orders of magnitude varying from 2.4- 41 %. The orthogonal variation as a function to the volume is significantly apparent. The mean of the encapsulation efficiency was calculated at 11.4% represented by the dashed line. The coloured regions on the graph indicate the confidence level. The purple region represents a 68% confidence interval (± 1 standard deviation away from mean). The green region and yellow region represent a 95% (2 standard deviation away from mean) and 99% (3 standard deviation away from mean) confidence interval respectively. .... 212

**Figure 4.21:** The calibrated SM count of the single vesicle pulldown experiments obtained using chemical and optical lysis.(n=125) The close correlation between the two data sets indicate that the method of lysis is not a contributing factor to the low EE values..... 215

**Figure 4.22 :** The box plot showing the distribution of the encapsulation efficiency as a function of the different batches of the vesicles produced. The horizontal line at the bottom indicates the lowest value of the EE for each of the batch. The red line in the centre of the box is the median EE. The lower

edge and upper edge of the boxes represent the lower and upper quartile respectively. The top horizontal line indicates the 98<sup>th</sup> percentile of the populations. Batch 2 and batch 4 have an outlier each on the upper side of data. ( Total n=125, Batch 1:8 Batch 2:19 Batch 3:29 Batch 4:14 Batch 5:14 Batch 6:14 Batch 7:20 Batch 8:7) ..... 217

**Figure 4.23:** The plot of the measured number of molecules per GUV against volume of both the single molecule pulldown data (red) and the calibrated microscopy data (blue). The microscopy data is calibrated by a factor obtained from the ratio of the two constants of the respective distributions. (Calibrated microscopy n=1780 single molecule n= 125) ..... 220

**Figure 4.24:** a) The plot of the calibrated molecules per GUV against the volume of the concentration series b) The distribution of the concentration series as a function of the concentration per GUV. The histogram shows the close agreement between the nominal and measured concentration series, further increasing confidence in the methodology that was developed. .... 222

**Figure 5.1:** The figure above shows the design of the droplet generation chip. a) The device consists of a header with 4 inlets for the reagents, 2 outlets, a flow focusing junction (inset) and the serpentine channel. b) The geometries and the size of the channels of the device. Reproduced from reference <sup>199</sup> ..... 231

**Figure 5.2:** Comparison of size distribution of initial emulsion and resultant vesicle. a) W/O droplets produced before the transfer (N = 133 (1 M), 143 (100 mM)) b) Vesicle resulting from the transfer of the droplets. (N = 159 (1 M), 67 (100 mM)) Two varying concentration of the glucose solution was used in this experiment by Hamada et al. to show the dependence of the system on sugar molecules in the aqueous buffer solution. The histogram here is reproduced from the reference <sup>200</sup> ..... 233

**Figure 5.3:** The image of the droplets obtained using the droplet generation chip. The droplets were imaged using wide field microscopy. This methodology shows a narrow distribution of the droplet. These data were acquired together with another doctoral student, Zibo Wang. .... 234

# List of Tables

---

<b>Table 1.1:</b> An overview of the methods that have been employed to produce Giant Unilamellar vesicles (GUVs). The table is reproduced from Supramaniam et al. <sup>56</sup> .....	44
<b>Table 2.1:</b> The table shows specifications of the filter set corresponding to the fluorophores that were used in the thesis. The fluorophores that were used through in the thesis are AF-488 tagged streptavidin and calcein with an absorption and emission maximum of 496 nm and 519 nm respectively. ....	73
<b>Table 3.1:</b> Parameters of the automated data analysis technique. ....	133
<b>Table 3.2:</b> Calculated mean, variance and standard deviation values of the volumes that were measured using information obtained from each of the data analysis method. ....	135

# **1. Introduction**

## **1.1 Chapter Outline**

The overall aim of this thesis is to describe the progress that has been made in developing a microfluidic platform used to understand the encapsulation efficiency of Giant Unilamellar Vesicles (GUVs), generally used as biological models in understanding biochemical processes that occur at a cellular level. This introductory chapter aims to provide a general background of the themes covered within this thesis. A brief review of the current literature concerning these topics is presented in this introduction to put into context the underlying concepts that govern the key findings of this thesis.

- **Synthetic Biology**

A literature review of synthetic biology is presented to provide the reader with overarching view of the development in the field in the context of artificial cells. Additionally, the different approaches used to build artificial models are also discussed.

- **Artificial Cells**

The development of cell-like constructs known as artificial cells to be used as simplified mimics of biological models is discussed. The conventional methods used to produce these cell-mimicking vesicles is covered with an in-depth analysis.

- **Microfluidics**

The concepts that underpin the formation of vesicles using this technology is discussed. Additionally, the advantages of employing microfluidics as part of the technological platform is discussed.

## **1.2 Synthetic biology**

### **1.2.1 What is synthetic biology?**

Synthetic biology is a multidisciplinary field that ties together different disciplines which include genetic design and engineering, biology, nanotechnology, physics and chemistry. In practice, it has been viewed as a field that manipulates the structure and function of DNA in order to create new biological systems in accordance to engineering principles. An engineering perspective will enable the building of biological systems in a more rational and systematic way. This approach can be applied to varying level of complexities that exists in nature ranging from basic building units (design and synthesis of novel genes and proteins) to their interaction with one another (regulation mechanisms, signal sensing, or enzymatic reactions) to novel multi-component modules to genetically engineered cells. <sup>1</sup>

In the simplest of terms, the aim of synthetic biology is to make engineering of biological systems simpler and more predictable. Another aim of the field is to standardise the accumulated knowledge of these systems to allow its utility in the synthetic biology design process. On a practical level, the direct application of engineering concepts to biology may seem difficult; however, conceptually, there are several commonalities. In fact, the use of engineering design principles of modularity, standardisation and characterisation together with existing biological knowledge and

available biotechnological breakthroughs, has massively changed the current concepts on how to manipulate biological systems. The growth of this field has only been further fuelled by a series of breakthroughs in genomic research and genetic engineering. This provided a pathway both essential for the construction and assembly of biomolecular parts.<sup>2</sup> Conventional genetic engineering approaches to solve complex issues usually involve the tweaking of one or several genes. However, synthetic biology offers a contrasting approach using novel and engineering driven perspective that often focuses on the changes to existing cellular architectures or the building of systems from the ground up. Despite synthetic biology being often connected to its origins in genetic engineering, the substantial amount of growth in scope, expectation and output it has undergone, synthetic biology has emerged as a much wider field of its own. The use of engineering principles in designing biological systems has made synthetic biology different from the other subfields of biology. A strong emphasis on modularisation allows for the individual components to be designed, tested, and characterised individually. These components can later be added together to emulate the complex functioning nature of a living cell.

The scope of research carried out in synthetic biology can be broken down in to four major points. Design of artificial systems, construction of system with biological and/or non-biological elements, testing developed system for functionality and finally the analysis to determine the closeness to which the built system has mimicked the function and structure of a natural system.

Therefore, owing to the multidisciplinary nature of the field, pinpointing an exact definition of synthetic biology has proven to be a challenge. However, at its core, the

field centres upon designing, constructing and characterising improvements or novel biological systems. Viewed as a disruptive technology at the heart of the so-called Bioeconomy<sup>3</sup>, synthetic biology has demonstrated significant potential in manufacturing commercially viable solutions to global problems within the pharmaceuticals, biofuels, chemicals, and biomaterials industry.<sup>4</sup> Over the past few years, the field has gained a significant amount of traction despite being a relatively new research field. The timeline below (**Figure 1.1**) charts the technological lifetime and growth of the field.

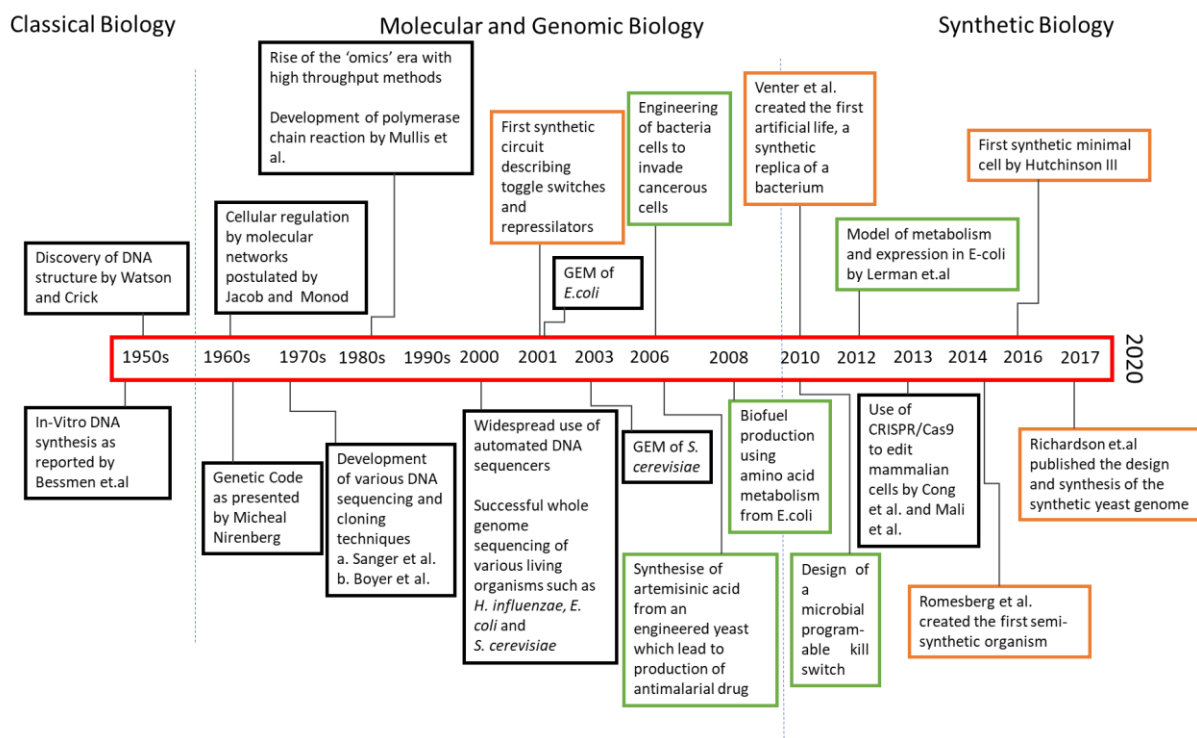


**Figure 1.1** The progress of the field of synthetic biology branching out from classical and molecular biology. The coloured boxes within the timeline represent key scientific and technical milestones (black), key milestones within synthetic biology (orange) and milestones of synthetic biology (green) with therapeutic applications and metabolic engineering. The image is modified from the reference 5 and 6.

The early starting point of the field was in the creation of simple gene regulatory circuits that were able to carry out specific functions. With the objective of creating a “toolbox” of genetic parts that can be readily combined and accessed to form more complex systems, the parts were categorised accordingly based on their complexity. One useful analogy to conceptualise the method of synthetic biology is using the computer engineering hierarchy. <sup>7</sup> **(Figure 1.2).**

Within this hierarchy, each part can be assembled into a more complex system that carries out a certain task. The lower tier usually consists of elements such as DNA, RNA, proteins, and metabolites and is analogous to the physical layers of transistors, capacitors and resistors. The subsequent layer comprises of a collection of various elements to form devices. These devices carry out biochemical reactions that enable the regulation of the information and manipulation of different physical processes such as a riboswitch regulation expression of gene. This is akin to engineered logic gates that carry out specific computations in a computer. The module layer utilises a diverse collection of biological devices to form complex pathways that can function like integrated circuits. The connection of these modules to one another and their integration within host cells allow for the extension and modification of cellular behaviour. Though these engineered cells can perform task of varying complexity independently, more sophisticated and coordinated tasks can be possible within populations of communicating cells much like a large network of computers.<sup>7</sup>

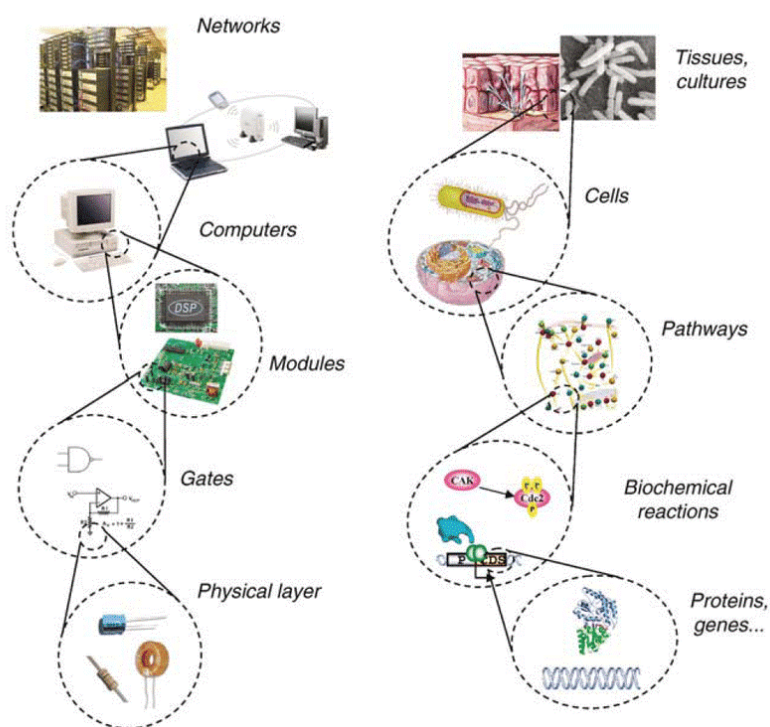


**Figure 1.2:** *The conceptualisation of the hierarchy within synthetic biology by drawing an analogy to computer engineering.*<sup>7</sup>

Despite the progress that has been made within this field, one of the biggest challenges that still exist within the field is the incomplete knowledge of how life works, the true complexity of cells and their interactions. The basic toolkit within synthetic biology still lies within biomolecules such as DNA, RNA, and proteins. An assembly of artificial systems with the inclusion of these molecules are often complex and requires a large amount of genetic reprogramming, genetic screening as well as DNA and protein synthesis. Another big critique of this field lies with the nature of living cells. Cells are constrained in volume with high concentrations of macromolecule and small molecule that diffuse freely within a complex three-dimensional matrix. Its ability to self-assemble and its consequent stochastic behaviour often pose a challenge to synthetic biologist. Thus, the lack of understanding coupled with the complexity of each systems make it a challenge to mimic the true nature of biological systems. However, synthetic

biology is still closely tied to living cells. Therefore, from a standpoint of synthetic biology, it is desirable to overcome these challenges using a set of standardised engineering solution.

### 1.2.2 Bottom up and top down

The capability to develop artificial living systems with programmable functionality is one of the main aims of synthetic biology. But due to the diverse nature of synthetic biology; the approach taken towards reaching this goal can be broadly divided into two main complementary themes; top-down and bottom-up approaches.

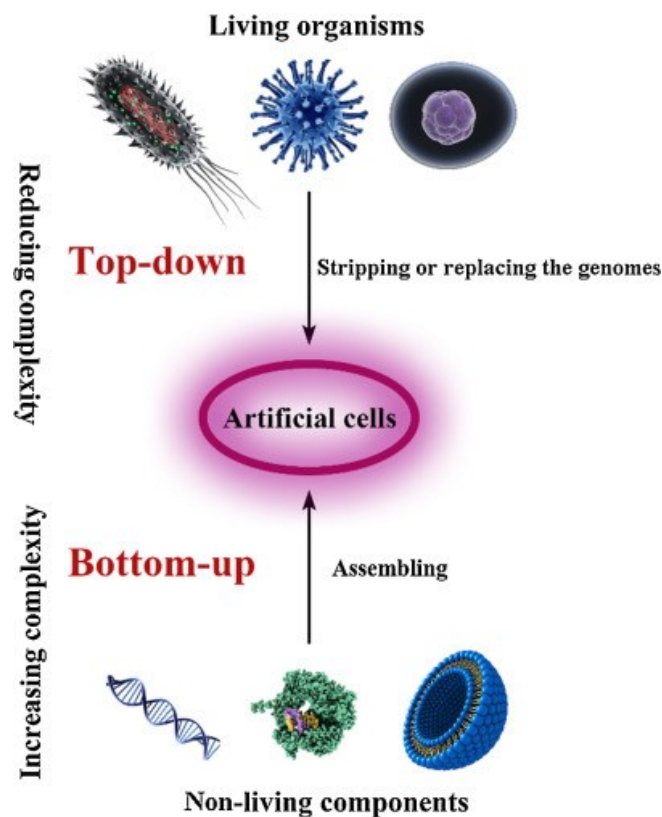


**Figure 1.3:** The two contrasting approach used for the design and construction of artificial cells within the field of synthetic biology. Using a top-down approach, artificial cells are constructed by replacing and removing the genomes of living organisms, reducing its complexity, and retaining the minimum substance to sustain life. Whilst a bottom-up approach involves the building of artificial cells from scratch by the assembly of non-living components with living components to form a system that mimics closely a living cell. The image is reproduced from the indicated reference. <sup>8</sup>

With the aim of creating synthetic life, the top-down methodology is exploited by rationally reducing the cells natural genomes of the cells to a minimal set of genes that allows for the cell to sustain life under defined condition. The top-down approach begins from a simple living organism in which the genome is stripped down to the lowest number of genes and may be replaced with a synthetic genome.<sup>9</sup> The top-down approach results in synthetic cells usually derived from reprogramming or altering the existing cellular genome to yield a desired functionality. The resultant synthetic cell is usually still a living cell and is closely related to its biological ancestor. This approach brings together various biological elements such as promoters and genes to form a functional system. This may involve the designing of a specific metabolic or signalling pathway within a cell. The use of a living host cell or a chassis allows for the use of the existing metabolites, co-factors, transcription pathways.<sup>10</sup> One of the most notable achievements in top-down biology has been the production of a viable and synthetic bacteria using only genome data as a blueprint as shown by Venter et al.<sup>9 11</sup> . As most efforts within the field of synthetic biology have mainly focused on the top-down approach, resulting in a higher number of scientific papers in comparison to bottom-up synthetic biology. This is because to the tools and technologies required are more established and this approach is seen to be a less complex process in contrast to a bottom-up approach. Despite the advantages present in developing artificial cells using a top-down approach, one of the let-downs of this approach is the inherent complexity of the top-down modified cell that may hinder their use as cell models. For instance, the introduction of new synthetic pathways may lead to potential crosstalk, thus masking

any true understanding of cellular systems.<sup>10</sup> The problems posed by the complexity of natural organisms can be overcome by using a bottom-up approach.

The bottom-up approach involves the creation of artificial life *de-novo*. Complementary to the top-down approach, bottom-up techniques of constructing artificial systems use chemical building blocks or non-biotic components. The complexity and functionality to mimic living cells can be achieved by the addition of these components step-by-step. This approach provides the ability to design and construct complex biological systems from ground up whilst simultaneously providing a deeper understanding of the complex cellular phenomena that takes place. A major goal of bottom-up synthetic biology is to be able to develop cell models that could closely mimic the fundamental structural and functional principles of real cells.<sup>12</sup> The cell-like structures formed using bottom-up techniques are sometimes referred to as artificial cells or protocells. The ability to reconstitute these processes from an isolated and well-characterised component, allows for the emergence of more complex cell-like behaviour such as spatial patterning and membrane remodelling that were quantified in a more appropriate manner. The process of developing new biological systems typically resembles an iterative design-build-test-learn cycle, like in conventional engineering.<sup>13</sup> However, it is important to note that a significant amount of progress has been made in bottom-up synthetic biology. A major contributing factor to this success is the constant advancement in technologies like microfluidics, cell-free expression, and membrane science. An inherent advantage of using this method is the fact that researchers are not restricted by the starting point of a biological cell. The systems developed are often novel unlike those seen in nature. In addition, the complexity of the resulting structure can be controlled as the structures are

developed from the ground-up. The artificial cells can be designed specifically for carrying out a handful number of functions. This may prove useful to those interested in understanding the origins of life.

## **1.3 Artificial cells**

### **1.3.1 What are artificial cells?**

One of the most interesting application of cell-free systems lie in the construction of minimal cells using a bottom-up approach. The understanding of cell-free systems provides a solid foundation for the design of minimal synthetic cells from individual components.<sup>14</sup>

Artificial cells are traditionally defined as cell-like compartment that have the capability to encapsulate bioactive materials within a membrane to carry out a designated function. A concept first introduced in 1957 by Dr Thomas Ming Swi Chang<sup>15</sup>, these constructs were built in order to address the inherent disadvantages of working with live biological cells. The term artificial cells as it is widely known as is a terminology applied to systems which merge both synthetic and natural chemical components to closely mimic cellular functions.<sup>8</sup> Other terms that these constructs are referred to as include protocells, minimal cells, and semi-synthetic cells. These structures may contain basic biological building blocks that assemble into polymers such as proteins and nucleic acid, various cellular machinery such as lipids, enzymes, membrane channels and structural proteins as well as synthetic elements such as nanoparticles, and electronic interfaces which can interact with one other in functional ways to constitute pathways and circuits.<sup>16</sup>

The properties of an ideal minimal cell would comprise of i) the inclusion of an information carrying polymer that could be synthesised directly within a membrane bound volume ii) transport of molecules within membrane boundaries of the cell and different compartments to support basic biosynthetic reactions iii) a catalytic reaction linked to the replication process to allow for variation of the resulting species to occur iv) well-regulated cellular division and growth like capabilities v) self-assembly of the artificial membrane through either accumulation of material or conversion of precursor molecules.<sup>17</sup> Though we are far away from constructing a system that fully meets all the properties, synthetic biologists have come a long way. Artificial cells have been envisioned to be the basis of a new generation of biomimetics structures that can be capable of carrying out basic functions of self-repair, of communicating with other cells, and of responding to external or internal stimuli, akin to a biological cell.<sup>16</sup> The ability to encapsulate various types of biologically active material either individually or in combination has allowed artificial cells to be used in various applications such as therapeutics, targeted drug delivery, biosensing and programmable microreactors.<sup>18-20</sup> Artificial cells could also be utilised as a biomimetic model of biological cells, hence allowing biological systems to be investigated in more controlled and simple manner alongside understanding the origin of life.<sup>21</sup> A key attraction of using artificial cells as models of biological cells lie within its inherent simplicity. These models are simple enough to experimentally derive an understanding of the various underlying mechanisms of cellular biology and at the same time approximate aspects that may only appear in more complex systems.<sup>22</sup> Artificial cells can be generated using a variety of approaches that include bulk self-assembly and emulsion-based approaches. However,

research into the development of these structures has taken a new trajectory in recent years due to the emergence of enabling technologies such as microfluidics. These methods will be discussed in more detail in section 1.4 .

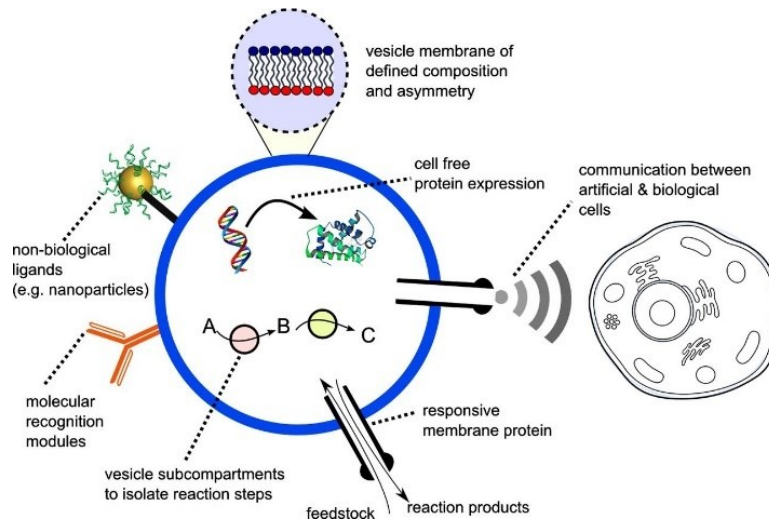


**Figure 1.4:** A representation of an artificial cells containing some key cellular elements. The model features a membrane of defined composition and symmetry, a cell-free protein expression system by incorporating an in-vitro translation-transcription pathway, inclusion of non-biological components used for cellular recognition, insertion of transmembrane proteins for transport of molecules between the membrane based upon an external, stimulus response, and cellular communication between the model and a biological cell. The figure is reproduced from the specified reference.<sup>16</sup>

### 1.3.2 Membrane bound artificial cells

Historically, the simplest component that can be mimicked in order to construct an idealised artificial cell would be the biological membrane. Biological membranes provide a physical boundary that separates the internal and external environment. They play a key role in mediating signal transduction and transport of molecules into and out of a cell. The major constituents of a membrane are generally phospholipids and membrane proteins. The phospholipids form a bilayer membrane structure to create a hydrophobic barrier that allow the movement of soluble or ionic substance through. The composition of the membrane therefore plays an extremely important role in the structure of both biological and artificial cells. Thus, efforts have been focused closely

on developing cell mimetic structures that closely resemble the lipid bilayer. The barriers that define the internal and the external barriers can be built based upon polymers,<sup>23</sup> coacervates,<sup>24,25</sup> water droplets,<sup>26</sup> pickering emulsions<sup>27</sup> and proteinosomes.<sup>28</sup> However, one of the most attractive classes of model systems are those built using lipid membranes a barrier. This simply comes down to its biocompatibility and the close resemblance to a biological membrane.

Common model membrane systems include black lipid membranes in which bilayers are formed across a hydrophobic aperture and a solid substrate supported bilayer which consist of a continuous bilayer sitting on a solid support surface. Other widely used model membranes include droplet interface bilayers (DIBs), and vesicles. Various aspects of these model membranes can be adjusted for systematic study of their effects of biological processes including lipid composition,<sup>29</sup> membrane asymmetry,<sup>30</sup> degree of compartmentalisation,<sup>31</sup> and their intrinsic mechanical properties.<sup>32</sup> However, the most commonly used chassis as artificial cells models are lipid vesicles, featured heavily throughout the thesis and will be outlined below. For an in-depth review of the alternative model systems, refer to Chan et al.<sup>33</sup>

### **1.3.2.1 Lipid Vesicles**

Since their discovery by Alec Bangham in the 1960s, liposomes were a perfect candidate to be used as models for cellular membranes.<sup>34</sup> Lipid vesicles or liposomes are fully enclosed spherical lipid bilayer shells with an internal and external aqueous phase. Depending on the preparation method, different types of bilayer structures can be obtained, and categorised accordingly to size and lamellarity as shown in **Figure 1.5**. The simplest morphology of these vesicle structure is that of a unilamellar vesicle. The

structure here is enclosed by a single bilayer. Depending on the size of the vesicles, it can be further categorised into small unilamellar vesicles (SUVs) (diameter  $d < 50\text{nm}$ ), large unilamellar vesicles (LUVs) ( $100 < d < 200\text{nm}$ ) or giant unilamellar vesicles (GUVs) ( $d > 1\mu\text{m}$ ). Vesicles with a few or several concentric lamellae are categorised as oligo- and multi-lamellar vesicles (MLV) whilst vesicles containing vesicles in a non-concentric way are known as multivesicular vesicles. (MLV)

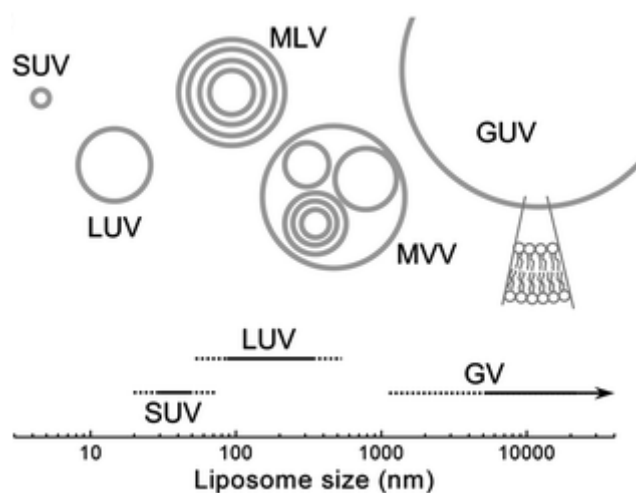


**Figure 1.5:** A schematic drawing depicting the different morphologies of a vesicle and the approximate sizes of unilamellar vesicles. SUV small unilamellar vesicles, MLV multilamellar vesicles, LUV large unilamellar vesicles, MVV Multivesicular vesicles, GUV giant unilamellar vesicles, GV giant vesicles. The figure is modified from Stano et al. (not to scale)<sup>35</sup>

Vesicles have the advantage of being stable with a range of different lipid compositions and can be easily formed. The small aqueous volumes contained within the vesicles make them useful as biological assays that involve the activities of pore forming proteins, in which dyes that are encapsulated within them can be released to be measured. This makes vesicles a platform of choice for a wide range of drug-membrane or protein-membrane interaction studies.<sup>36,37</sup> The close resemblance of the lipid vesicle

to a biological membrane also makes them a suitable candidate for targeted drug delivery carriers as they could easily insert themselves within the membrane of the cell. The vesicles can also be used to deliver drugs of varying lipophilicities with hydrophobic drugs being carried in the bilayer itself and hydrophilic drugs being carried in the internal aqueous environment.<sup>38</sup>

Vesicles are often the starting point for other model membrane structures including supported lipid bilayers and DIBs. There are plenty of methods to form liposomes and these are often relatively easy. One of the most common methods is the thin-film hydration or the Bangham method<sup>39</sup> which involves the dispersion of the lipid film through an aqueous solution to obtain MLVs. These vesicles could be extruded and sonicated to downsize the vesicles to form small unilamellar vesicles (SUVs).<sup>40</sup>

However, in comparison to its counterparts, the use of GUVs as lipid vesicles are considered the gold standard. This is mainly due to its comparable size with a biological cell mainly a eukaryotic cell. The large size of this vesicles makes it easier to be observed under an optical microscope and for single vesicles to be detected.

Some notable and impressive biological features introduced into a vesicle structure to closely mimic a biological cell to date include:

*Protein Expression:* Early work in this area involved the encapsulation of ribosomal subunits and enzymes to allow for the synthesis of protein.<sup>41</sup> Building on from this, protein synthesis was still investigated to a great extent in order to help develop artificial cell construct. Example of works include the encapsulation of biological toolkit required for transcription and translational process that synthesises fluorescent protein.<sup>42</sup> The

incorporation of membrane protein pores allowed for the continuous synthesis of proteins due to the uptake of the required starting material from the environment.<sup>43</sup>

*Nucleic acid Synthesis:* The encapsulation of reverse transcription PCR reaction mixture within a vesicle for the use of RNA detection. The results obtained was further proof that lipid vesicles could be used as biomimetic reactors capable of performing PCR reactions, with applications as an analytical or diagnostic tool with additional functionality.<sup>44</sup>

*Compartmentalisation:* The development of compartmentalising reactions in vesicles within vesicles mimics organelles in cells. Recent work has shown the ability to encapsulate living cells within lipid vesicles allowing the artificial cell to leverage on the cellular biochemistry. The encapsulated cells serve as living modules inside the synthetic cells akin to organelles.<sup>45</sup>

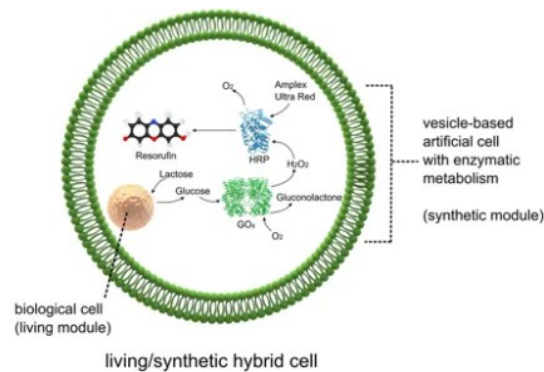


**Figure 1.6:** A schematic of an artificial cell containing an encapsulated biological cell. The cell serves an organelle-like function, processing chemical elements by using a synthetic enzymatic cascade. Figure modified from the following reference.<sup>45</sup>

*Vesicle-cell communication:* A lipid bound protometabolism was encapsulated within a vesicle. This system synthesises complex carbohydrates which have the capability to

engage the natural quorum sensing mechanism of a bacteria and stimulate a bioluminescent response.<sup>46</sup>

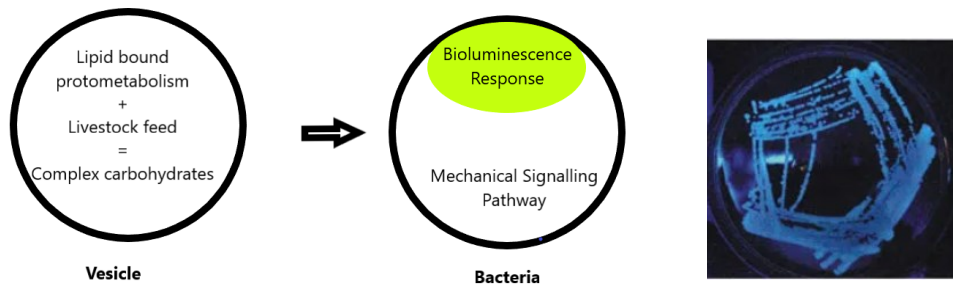


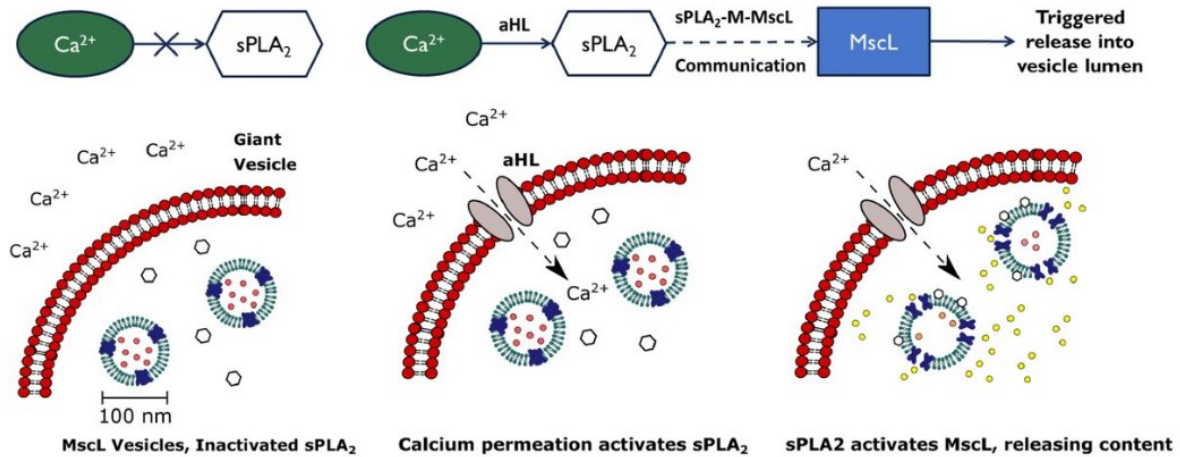
**Figure 1.7:** A schematic of the protometabolic formation of carbohydrate inside a lipid vesicle. The image on the right most shows the bioluminescence reaction of the bacteria in response to the presence of a carbohydrate complex. The image is adapted and modified from the following references.<sup>46</sup>

*Cytoskeletal elements:* An artificial DNA cytoskeleton was formed underneath the membrane of the lipid membrane using electrostatic interaction. This majorly improved the mechanical stability, and tolerance of the liposome towards osmotic shock.<sup>47</sup>

*Artificial photosynthetic cell:* The encapsulation of cell-free protein synthesis systems together with small proteoliposomes consisting of purified ATP synthase and bacteriorhodopsin in a vesicle allow for the synthesis of protein using energy produced by light. The produced ATP is used as a substrate for the transcription and translation, driving the synthesis of constituent proteins of ATP synthase and bacteriorhodopsin, essential components of the proteoliposome. This system has paved way for the construction of energetically independent artificial cells.<sup>48</sup>

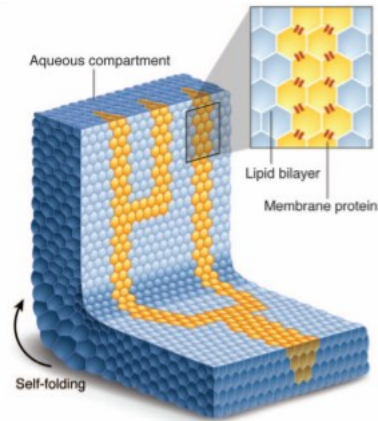
*Cellular Response and Signalling:* This was done by building artificial pathway with biochemical parts using a plug-and-play approach. The artificial cells developed were able to sense calcium ions and responded by fluorescing. This breakthrough is an

important development as it could be utilised in the field of biomedicine for targeted drug delivery.<sup>49</sup>



**Figure 1.8:** The proposed functioning of the synthetic mechanosensitive signalling pathway. The calcium ions are initially impermeable due to the presence of the bilayer. However, the addition of  $\alpha$ -hemolysin to the outer membrane results in a calcium influx which activates the secretory phospholipase A2 (sPLA<sub>2</sub>). This results in the activation of the mechanosensitive channel of large conductance (MscL), releasing the encapsulated dye molecules into the artificial cell. The image above was reproduced from the following reference.<sup>49</sup>

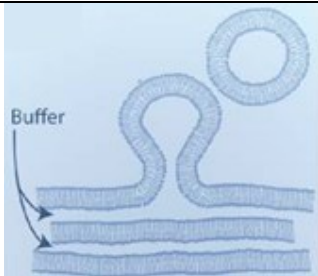
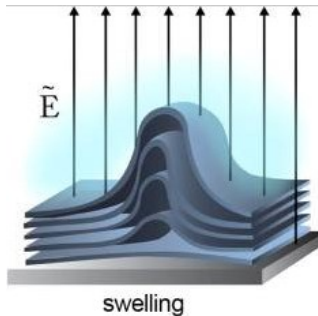
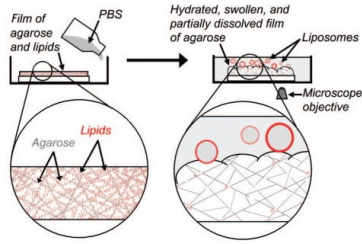
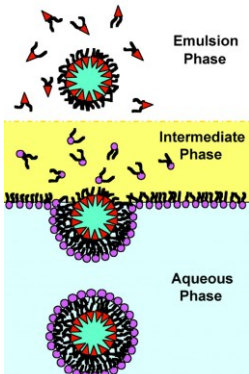
*Tissue-like mimetics:* Initial work demonstrated 3D printing thousands of water-in-oil droplets to create a complex 3D-patterned functional soft structures which are made up of hundreds of aqueous compartments. The droplet networks demonstrated the ability to be folded into various geometric designs, controlled by gradient osmolarity alongside a selective conducting pathway by the addition of membrane proteins. These structures could be developed to be used for medical applications.<sup>50</sup> Following on from this, 3D synthetic tissues made up on hundreds of these synthetic cells were created. Combining the tissue mimic alongside light- activated protein expression of  $\alpha$ -hemolysin in a subset of synthetic cells, a conductive pathway which functionally mimics neuronal transmission was achieved.<sup>51</sup>

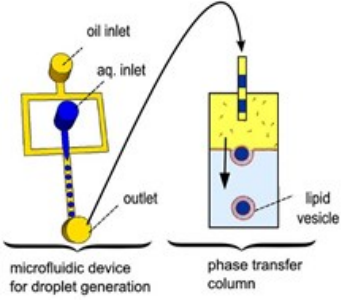
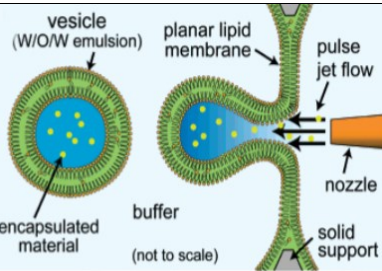
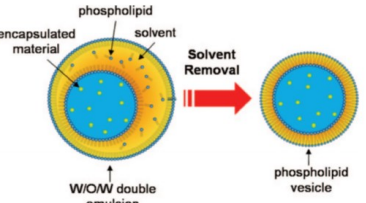


**Figure 1.9:** The folding of the 3D printed water-in-oil droplets network capable of self-folding and transmitting electrical signals across a pathway. Image reproduced from referenced paper.<sup>50</sup>

These structures could be produced using several methods including gentle hydration,<sup>52</sup> electroformation,<sup>53</sup> gel- assisted swelling,<sup>54</sup> emulsion-based approaches<sup>55</sup> and microfluidic based techniques. A general overview of each of the technique is outlined in the table below. However, only reverse emulsion phase transfer technique is relevant to this thesis and will be discussed in further detail.

**Table 1.1:** An overview of the methods that have been employed to produce Giant Unilamellar vesicles (GUVs). The table is reproduced from Supramaniam et al. <sup>56</sup>

Method	Method Description	Schematic	Limitations
Natural hydration	The vesicles are produced by resuspending pre-hydrated stacked layers of lipid bilayer in an aqueous buffer		Long and slow process with formation of low-quality vesicles.
Electroformation	Vesicles are formed by the spontaneous swelling of a lipid bilayer deposited on an indium tin oxide electrode alongside the introduction of an externally applied electric field.		Use of electric fields could oxidise lipids and damage encapsulant materials Low homogenous vesicle production in physiological buffer
Gel-assisted Swelling	Layers of lipid bilayers are deposited on to a porous layer of polymer. The vesicles are then produced by resuspending these layers by an enhanced flow of buffers.		The vesicles produced could be contaminated with the polymer of choice (agarose) within the lipid bilayer which affects the properties of the vesicle. There were also difficulties in detaching the vesicles from the surface of the polymer.
Emulsion based approach	A water-in-oil (W/O) droplet with the first monolayer is generated and passed through an interface where it picks up a second lipid layer to form a unilamellar vesicle.		The vesicles that are generated using this method are heterogenous in size and the encapsulation efficiency has not been properly quantified.

<p>Droplet-emulsion using microfluidics</p>	<p>A two-step process in which the first step involves the formation of the W/O droplet using a microfluidic device and the second step involves the passing of the resultant droplet through an interface to form vesicles.</p>		<p>Specialised equipment and infrastructure required alongside significant expertise to carry out fabrication of device.</p>
<p>Microfluidic Jetting</p>	<p>Preformed planar lipid bilayers are pulsed with an inkjet nozzle/piezo-actuated syringe to form the resulting vesicles.</p>		<p>Vesicles generated contain large quantities of residual oil and solvents within the bilayer in addition to the complicated and specialised set-up.</p>
<p>Microfluidic double-emulsion templates</p>	<p>W/O/W droplets are formed with an organic phase in the middle which is evaporated to obtain a lipid bilayer.</p>		<p>The use of volatile organic solvents limits the use of most of the vesicles produced for biological applications.</p>

### 1.3.2.2 Emulsion based phase transfer

The past decade has seen the development of emulsion-based approaches to form GUVs. It was developed in order to overcome some of the limitations faced by methods that preceded it as highlighted in the table above. With this method, the GUVs are formed by the self-assembly of two independent lipid monolayers. This process is called the inverted emulsion phase transfer, and is modified from the method developed by Pautot et al.<sup>55</sup> The first step in this method is the preparation of a stable inverted emulsion. The aqueous solution that is to be emulsified is mixed with the oil mixture that contains the surfactants, or in this case the lipids. As the water droplets are formed,

the lipid molecules adsorb at the interface of the aqueous solution and oil mixture to form a monolayer. This stabilises the emulsion and helps reduce coalescence of the drops for a period. The monolayer that is formed makes up the inner leaflet of bilayer of the final vesicle. A water-oil column is prepared using an aqueous phase and an oil phase with the lipid dissolved in. The emulsion is then gently transferred into this oil column. As the w/o droplets descend past the interface formed, it picks up a second layer of lipid. The second layer acts as the outer leaflet of the bilayer forming a unilamellar vesicle. The droplets can be driven past the using gravitational methods. The water droplets are loaded with dense internal solution such as glucose or sucrose solutions to ensure they sink through the column. This is due to the difference in the density between the internal solution and the external solution. This process could be further enhanced using centrifugation.<sup>57</sup> The vesicles that are produced using this method is more monodisperse and unilamellar in comparison. It could also be used to produce asymmetrical membranes as demonstrated by Elani et al.<sup>30</sup> Other advantages using phase transfer method is the ability to amend the droplets formed onto a microfluidic format due to the starting point of water-in-oil droplets.

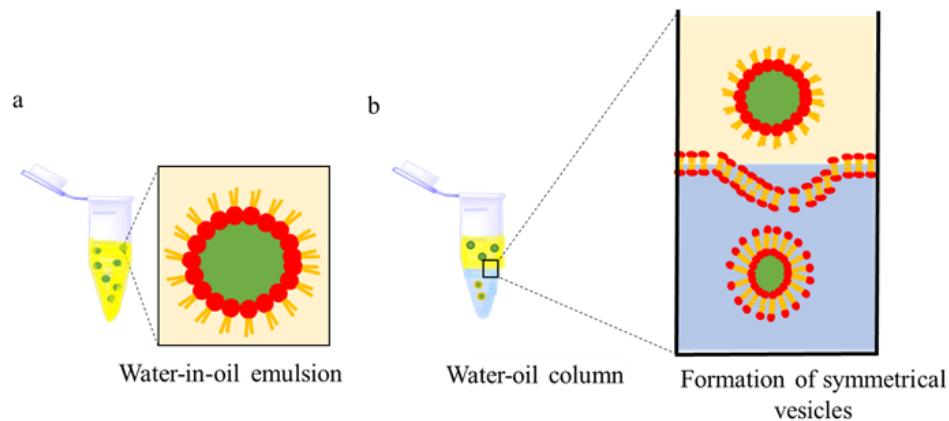


**Figure 1.10:** The figure above shows a schematic description of the inverted emulsion phase transfer a) Water-in-oil emulsions are prepared by mixing the aqueous phase with the lipid-in-oil solution. A monolayer form spontaneously to stabilise the emulsions. b) A water-in-oil column is then prepared using a secondary aqueous phase and lipid-in-oil mixture. A monolayer self assembles at the interface. The emulsion is transferred to the column. The inset shows as the droplets pass through the interface either through gravity or mechanical manipulation, it picks up a secondary layer of lipid to form a bilayer.

Though the resulting GUVs formed are more controlled in lamellarity, the distribution of the size is still relatively large. During the entire process, the encapsulated material remains distinct from the hosting buffer, therefore making high encapsulation efficiency possible. The encapsulation efficiency is assumed to be a 100%, however, very little work has been done to fully account for this. The assumption of a good encapsulation efficiency has prompted a heavy use of phase transfer to produce vesicle based artificial cells. The encapsulation of large, charged biomolecules is significantly harder using the alternatives method. Hence, the true understanding of the encapsulation efficiency of the molecules and methods to tighten the size distribution of the resulting vesicles are studied and attempted in this thesis.

One of the major aims within synthetic biology is to create an artificial cell model with a set of specified function, the features on the resulting membrane that is formed alongside the encapsulated materials within should also be controlled. The five major variables that should be considered whilst constructing artificial cells are the size

distribution and absolute size of the vesicle, the lateral organisation and biomolecular content of the membrane, spatial organisation of the encapsulated membrane, and biomolecular content of sub-compartmentalisation. Precise control over the formation of these structures is required for the range of their application. Therefore, the use of microfluidic technologies is employed owing to its high throughput, on demand generation and its fine control over the vesicle parameters.<sup>16</sup> Methods such as electroformation are not ideal in the encapsulation of biomolecules, an important prerequisite in the generation of artificial cells. Therefore, there has been an increased effort in the development of GUV formation with a focus on microfluidic technology.

#### **1.4 Microfluidics**

The emergence of microfluidics was dubbed a game changer in scientific research and industry. A relatively new field that has only garnered a considerable amount of success in the recent years, its application has been remarkably explored in many disciplines. Microfluidics fundamentally describes the manipulation of fluids at a micrometre scale, typically within micron sized channels either in planar chips or devices. Initially developed for the microchip industry, the field has grown into its own with the use of the technology in a plethora of applications. Initially, most of the microfluidic analysis devices were simply miniaturised versions of a macroscale system, however, now more devices are taking advantage of the microscale properties unique to microfluidics. These devices range from powerful analytical tools to analyse biological molecules<sup>58</sup> to the miniaturisation of molecular reactions<sup>59</sup> and platforms for cell growth.<sup>60</sup> The ultimate goal of microfluidics system however lies in the desire to develop lab-on-chip devices, where laboratory functions are integrated on a portable and sometimes disposable

devices. In line with this objective, one of the most exciting applications of the technology in biosynthesis that has drawn an increased attention lies within its use in fabricating artificial cells.<sup>26</sup> For a more detailed overview of microfluidic and microdroplet technologies and their application, the reader is referred to one of the many thorough reviews that have been published.<sup>61–64</sup>

### **1.4.1 Advantages of microfluidics**

Microfluidics allows for the miniaturisation of a variety of biological processes which is attractive for several reasons. The microchannels and compartments that have been carved out within a microfluidic device whether in polydimethylsiloxane (PDMS), plastic or glass-made can be tuned to carry out specific functions and reactions. The ability to do this on a micron scale allows for a higher degree of control especially for physical processes. Moreover, this calls for the use of small sample sizes, particularly beneficial when dealing with expensive reagents or low-abundance samples like rare cells or circulating tumour cells. The small size of the device also ensures strong interactions between the cells, the fluid flow, and the channels hence improving efficiency and sensitivity. At the same time, the use of these devices also pave way for the implementation of new protocols such as single cell analysis or on-chip cell culture, procedures that were not possible on a macroscale level.<sup>65</sup> The systems also have small instrumental footprint, is of low cost, portable and have increasingly become disposable. This is one of the leading reasons that more point-of-care diagnostic tools have turned to incorporating microfluidics as part of their technology.<sup>66</sup> The miniaturisation of reaction volumes to a micron scale allows for parallelisation of analytical processes. Therefore, microfluidic systems provide high throughput solutions

in the generation and analysis of reactions especially in regards to droplet-based systems.<sup>67</sup>

Droplet based microfluidics is a platform in which the droplets are presented as picolitre “test-tubes” for a range of studies, specifically in chemical synthesis. These compartments referred to as microreactors can host a range of various synthetic reactions. In comparison to bulk methods, the use of microfluidic systems is more beneficial in terms of a higher reaction efficiency, faster analysis and reaction time frames, better thermal homogeneity and on-demand synthesis triggered by a range of stimuli. Additionally, the increased compartmentalisation of analytes and biomolecules also allows for single cell or single molecule detection and analysis.<sup>68</sup> As the volumetric flow rate of individual fluids in the system can be precisely defined, this ensures a higher degree of control to be achieved. This is particularly important as it allows for a high throughput production of monodisperse water-in-oil droplets. This is a particularly appealing property to have especially when developing platforms to construct model membranes with highly controlled properties. The micron scale features in microfluidic devices are comparable to those of cellular systems, hence making these platforms a desirable candidate to be used to study cellular processes that occur within this scale, namely in the vascular system.<sup>69</sup> This feature has allowed for the use of microfluidic in developing technologies such as organ-on-a-chip and the fabrication of compartments like living cells on a chip. The various technological benefits including miniaturisation, continuous processing and reproducibility have presented an unprecedented opportunity for microfluidics to be used as a novel platform in the construction of artificial cell models using a bottom-up approach.

## 1.4.2 Principles governing microfluidics

### 1.4.2.1 Reynolds and Peclet Number

As the size of the channel in which the liquid flows decrease, local effects such as surface tension, laminar vs. turbulent flow, Reynolds number and surface chemistry start to play a larger role in the physics and chemistry of the reactions that is under investigation. The control and understanding of fluid dynamics and the chemical composition has allowed the use of microfluidic devices in producing emulsions, which are droplets of two immiscible fluids that are mixed. Generally, one fluid is dispersed in the form of tiny droplets within the other fluid. However, to fully understand fluids at a microscale, and the formation of microdroplets within these devices, it is paramount to have an overview of the underlying principles of fluid mechanics.

The behaviour of fluids at the size regimes associated with a microfluidic device differs from those on a macroscale. The fluid motions in micrometre sized channels are dominated by laminar flow, in which two streams flowing side by side flow in parallel to one another with mixing between them only occurring via diffusion. However, in the latter, turbulent flow dominates, where flow is characterised by chaotic mixing as shown in **figure 1.12**.

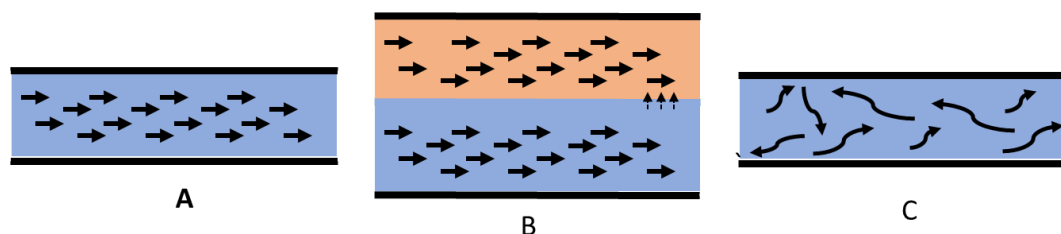


**Figure 1.11:** A schematic of the different flow regimes. a) A schematic of laminar flow in a micron-sized channel. b) In the presence of two immiscible fluids that flow side by side, mixing between them only occur via diffusion. c) A schematic depiction of turbulent flow.

The flow regime of a system is dependent on the dimensionless number, Reynolds number,  $Re$ . Reynolds number represents the ratio between the inertial and viscous forces and is defined as

$$Re = \frac{\rho u D_H}{\mu} \quad \text{Eq. 1.1}$$

Where  $\rho$  is the fluid density,  $u$  is the flow velocity,  $D_H$  is the characteristics dimension of the system and  $\mu$  is the dynamic viscosity. At high  $Re$  values, for instance by an increase in the flow rate of the fluid, the flow transitions to turbulent flow at specific ranges of  $Re$  numbers ( $Re > 4000$ ). At this flow regime, the inertial forces dominate. In regions where the  $Re$  number is low ( $Re < 1$ ), flow is dominated by the viscous stresses and pressure gradients, and inertial forces are negligible, leading to laminar flow. The flow of the fluid in this regime allows for the motion of the streams and particles within the fluid to be more predictable and controllable. The low Reynolds number may lead to interesting occurrences, for example, when two fluids are flowed in a channel side by side, they do not mix in the traditional sense, as mixing only occurs through diffusion.<sup>70</sup> The use of laminar flow in microfluidic systems have been well exploited for various applications. For instance, this characteristic has been used to produce stable gradients of small molecules, proteins and growth factors.<sup>71,72</sup> The gradients are typically perpendicular to the flow of the fluid and can be produced both on surfaces and in solution with a temporal and spatial stability.<sup>73</sup> Hydrodynamic focusing is also another example in which these principles are exploited. The constituents of the central stream are flowed laminarily through a channel and can be focused laterally by using the side streams. This relies on the lack of mixing modes between the flows besides

diffusion. Similarly, multi-phase flows concerning two immiscible fluids can be employed with a higher degree of control by the exploiting the interaction of physical parameters such as interfacial tension, shear stress and the channel dimensions.

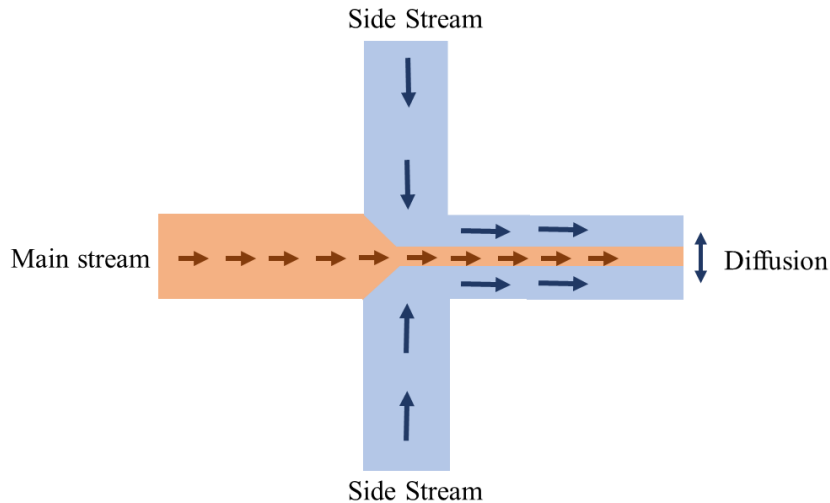


**Figure 1.12:** Hydrodynamic fluid focusing that employs the laminarity of the fluid. The main flow stream is focused at the centre of the channel using the side streams. Due to laminar flow, the mixing that occurs between the two different flow path is governed solely by diffusion.

As laminar flow naturally arises with low Reynolds number in microfluidics, mixing that only occurs by diffusion results in long mixing times. Thus, the dimensionless Peclet number (Pe) is used to indicate the ratio between diffusive and convective transport and is defined as shown in **Equation 1.2**.

$$P_e = \frac{v \cdot L}{D} \quad \text{Eq. 1.2}$$

Where  $v$  is the flow velocity,  $L$  is the length or width of the channel and  $D$  is the diffusivity of a substance ( $\text{m}^2\text{s}^{-1}$ ). This number could also be represented as ratio of diffusive to convective times scales. The interaction between these two forces could be exploited in a microfluidic device, called a T-sensor.<sup>74</sup> These are a class of analytical devices that benefit from having low Pe values, where quick mixing is not desired. Besides being used in many competitive immunoassays, these sensors can be used for

various other applications such as understanding reaction kinetics.<sup>75</sup> The relationship between convection and diffusion can be utilized for sorting and filtering applications.<sup>70</sup> Hence, low Reynolds number and Peclet number characterises laminar flow regimes where diffusion dominates in the mixing of two different fluids.

#### ***1.4.2.2 Continuous flow vs segmented flow***

The operation of microfluidic systems can broadly be divided into two categories, continuous and segmented flow. Continuous flow describes the flow of single phase through a region in a microchannel device. Continuous flow operations are well suited for the use of centrifugal fluidics and large-scale integration applications. The drawbacks of a continuous flow system lie in its issues related to Taylor dispersion, the interaction of fluids with the channel walls, potential cross contamination, and long channel lengths. This limits the effectiveness of using these systems as a tool in a variety of situations.<sup>76</sup> The use of additional methods to manipulate fluids are essential in order to truly realise the full potential of system miniaturisation, thus to this end segmented flow (or droplet-based) microfluidics have become increasingly popular.

Segmented flows are typically formed by the creating discrete microdroplets carried by an immiscible continuous phase along a microchannel. The formation of these discrete and isolated droplets with volumes on the pico- to nanolitre overcomes the limitations posed by continuous flow systems. The adoption of segmented flow means the key problems associated with dispersion and dilution of reaction mixtures are also eliminated.<sup>77</sup> The formation of the droplets is a spontaneous process and is normally a result of the shear force and interfacial tension at the liquid-liquid interface. The formation of droplets can be achieved at rates up to several kHz, whilst maintain a high

degree of control over the size and composition, making droplet-based systems an attractive platform for high throughput screening assays with high levels of reproducibility.<sup>78</sup> The application of these platforms within the field of biophysics and biotechnology namely in constructing artificial cell models have been extensively explored and will be highlighted herein.

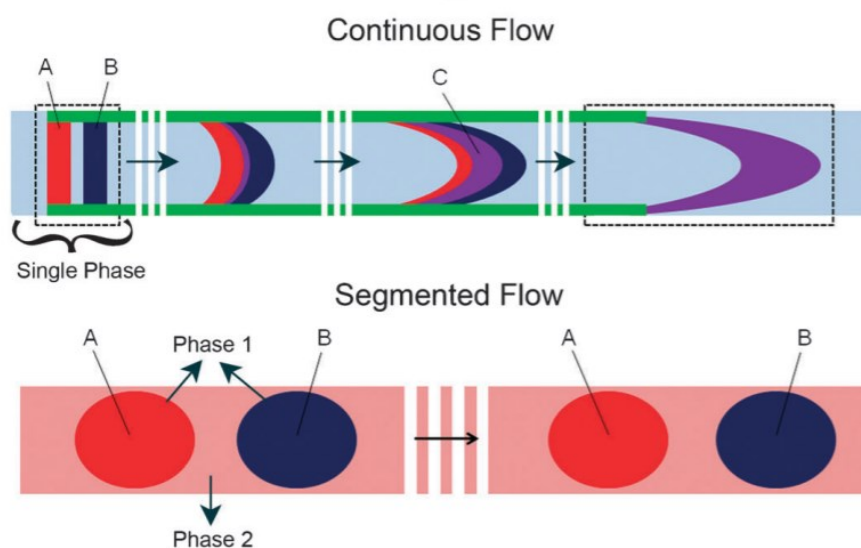


**Figure 1.13:** The comparison between continuous flow and segmented flow: The schematic above represents the continuous flow (top) and segmented flow (bottom) in a microchannel. The use of segmented flow (droplet microfluidics) in devices have addressed the limitations brought upon by continuous flow and is explained and outlined in detail in the referenced publication.<sup>79</sup>

## 1.5 Thesis overview and Aims

Artificial cells have been used as simplified biological models to understand the complexity of the human cell and the varying processes that are encompassed within it. Typical artificial cells should not only ideally have similar structures but also essential properties of living cells. One of the ultimate targets of constructing artificial cells is to be able to create a cell that can be considered “alive” with the ability to self-maintain, self-reproduce, evolve, and die. This is obviously an extremely challenging task because even the simplest known organisms can be very complex. Thus, the simplified goal has been to construct a model that possesses three of the main features that allows it to perform the essential functions of life. These three elements are the inclusion of information-carrying molecules, cell membranes and metabolism systems. Information carrying molecules such as DNA and RNA define the nature and function of the cells. The ability to include these molecules alongside different components of the transcription and translation mechanisms has allowed for the development of cell-free protein expression systems. The majority of these processes requires a source of chemical energy to carry on and sustain itself. In living cells, metabolic processes catalysed by a set of enzymes drive these reactions with the help of an energy source supplied in the form of ATP. Supplied from the external environment of the cell, energy molecules would have to pass through the membrane. Therefore, an important element of building an artificial cell would be to ensure the permeability of the membrane. The membrane of a living cell is often complex and is hard to accurately mimic, however, when building a biological model, it is expected to possess features that closely resemble it. This is one of the reasons why liposomes have been considered the gold

standard of the building blocks for artificial cells when using a bottom-up approach. A bottom-up approach allows for the construction of these models from scratch using either synthetic or natural components. The application of engineering principles within the remit of synthetic biology has allowed for the development of these artificial models. The models that are generated should have precisely defined parameters that will allow this to become a realistic and achievable goal. Recent advances in the field of synthetic biology have allowed for the ability to encapsulate and synthesise macro biomolecules within lipid vesicles. Not only has this provided researchers with a better understanding of the different complex cellular processes within a cell but also allowed the development of systems that more closely mimic a living cell. These advancements have also allowed researchers to build synthetic bioreactors by encapsulating several vesicles within each other, like organelles within a cell.

Bottom-up synthetic biology which employs simple engineering principles is used to build artificial cells from scratch. So, how can we summarise the different cellular processes?

Understanding parameters such as class of molecules, the exact number of each type of molecules alongside their interaction is essential. Analytical chemistry has produced several techniques that allows for the assessment of these parameters. For instance, the types of molecules and their interactions can be measured using mass spectrometry and NMR. ELISA based assay techniques have been used to measure the protein-protein interaction in a cell. However, what is difficult to measure is the exact number of molecules of a specific species, a glaring limitation that should be addressed especially if these models are to be used for therapeutic applications.

Hence, the principal aim of this thesis is to develop a microfluidic based platform to understand the encapsulation efficiency of lipid vesicles in a more quantitative approach using single-molecule imaging techniques. Lipid vesicles or GUVs have often been used as a standard building block for artificial cells when using a bottom-up approach. The central focus of the thesis looks at the quantitative analysis of the encapsulation efficiency of the current methodology used to generate GUVs. This is a vital objective as prior work carried out in this field mainly focused on semi-quantitative methods using fluorescence analysis. However, these methods to date are not capable of generating and reporting absolute quantification of molecules within the vesicles, therefore, they are unable to measure the encapsulation efficiencies. Encapsulation efficiency is an important matrix when assessing the synthesis of GUVs for applications where the absolute amount of the substance in the GUV is required. The potential of these models as drug delivery cargos for therapeutic applications also depend on its ability to encapsulate and retain an exact concentration of drugs. Therefore, it is crucial that a method which allows absolute quantification of the encapsulation efficiency be developed to help improve the precise engineering of these structures.

Determining the exact number of molecules is difficult due to the paucity of techniques capable of doing so. Previous work carried out by the group led to the development of a single molecule microfluidic techniques that can be used to assess the abundance of protein within single biological cells. This method has been validated by measuring the protein abundance of a varying range with populations of different cancer cell lines.<sup>80</sup>

The use of single molecule measurement techniques allows us to successfully quantify the absolute encapsulation efficiencies of the GUVs that were produced using inverted

emulsion phase transfer, a facile method to produce GUVs in high yield. The resultant encapsulation efficiency using the techniques in this project was determined to be between 2.4%- 42% with an average encapsulation efficiency of 11.4%. By taking into account the variation of the encapsulation efficiency that were obtained, the encapsulation efficiency could be compensated for by increasing the volume of the starting material encapsulated within these vesicles. This would also allow these models to be applied as standards when investigating a specific cellular process instead of using living cells. However, this compensation may not be the most practical solution as the materials could be rare or expensive. Another factor that should be taken into consideration is the wide size variation of the GUVs produced using emulsion phase transfer.

One approach that could be taken to tighten the distribution is to filter the resultant vesicles. This could include the use of physical methods such as sieves or in line filters that would separate out vesicles according to size. However, a more competent method would be to employ methods that would provide total control over the size of the vesicles from the point of production. This can be done by using microfluidic technologies to tightly control the distribution of the vesicles. By tightening the volumes of the GUVs, the concentration of the GUVs would be restricted, hence allowing for an improved encapsulation efficiency. An improved encapsulation efficiency would allow for the optimising of producing vesicles with well-defined cell mimics. In order to achieve this, an approach that can be taken is to develop a hybrid method of producing the water-in-oil droplets on a microfluidic device and using phase transfer to produce the vesicle. This would offer the ability to narrow down the distribution of the water-

in-oil droplets. By using droplets with a controlled size, the resultant vesicles that are produced should have a fixed volume and encapsulation efficiency. This would subsequently be studied by employing single molecule measuring techniques to a microfluidic device that can manipulate, lyse, and analyse the content of single vesicles.

## **1.6 Thesis Outline**

This thesis is organised into five chapters and is structured as below.

Chapter 2 provides details of the general techniques and methods employed within the thesis.

Chapter 3 evaluates the results of fluorescence microscopy to study the distribution in size and encapsulated protein concentration in vesicles produced using phase transfer, including details on the assessment and development of data analysis methods of the acquired data.

Chapter 4 showcases the development of the Pulldown Array Single-molecule High throughput (PASH) chip platform used to measure the absolute number of biomolecules encapsulated with the GUVs. The PASH chip is a microfluidic based device used to manipulate, lyse and analyse the protein content of single lipid vesicles, which enabled the encapsulation efficiency to be determined.

In Chapter 5, the work is concluded and discusses future work.

## 2. General Methods and Materials

### 2.1 Chapter Outline

The chapter details the general methods and materials used throughout the thesis. The first part of the chapter is a brief description of the different imaging platforms used throughout the thesis followed by the general preparation of giant unilamellar vesicles (GUVs). Methods and materials specific to certain chapters will be detailed in said chapter.

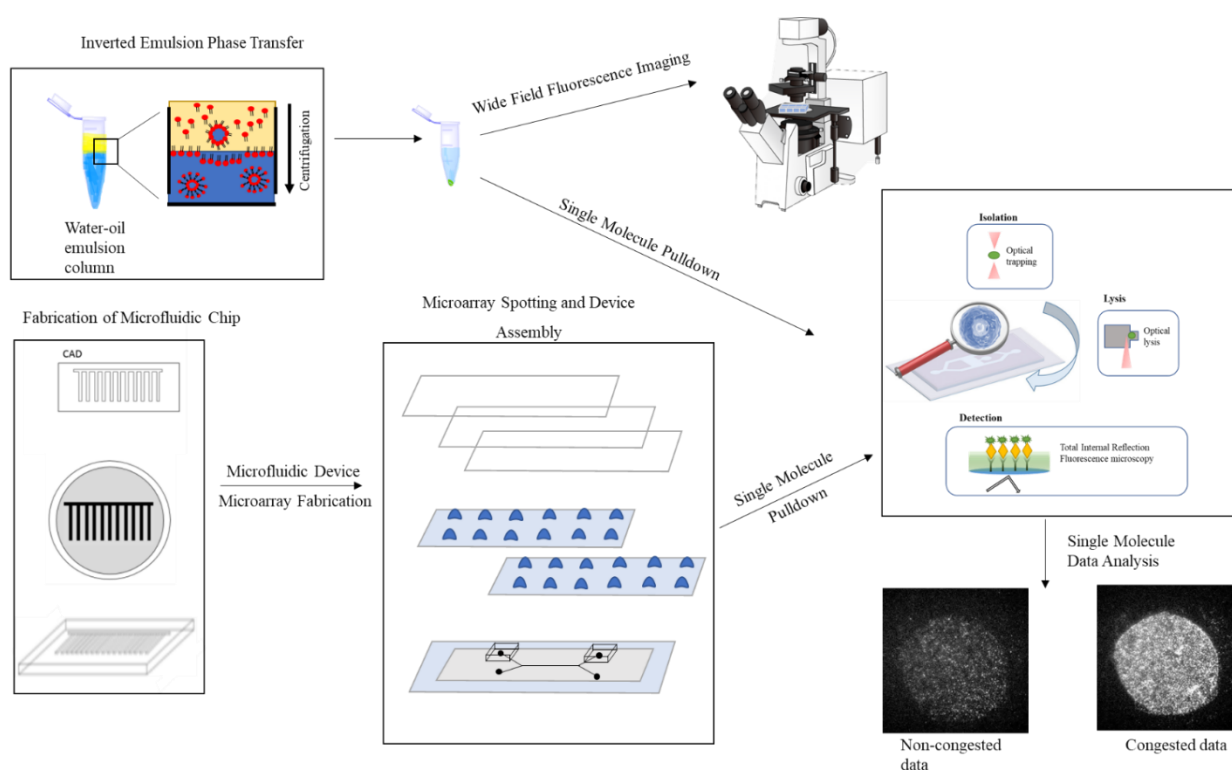


**Figure 2.1:** The experimental workflow of the different components that encompass the work carried out throughout the thesis.

## 2.2 Single Molecule Microarray Methodology

The assembly of the PASH Chip involves the bonding of a microfluidic chip and a printed protein microarray. The microfluidic device is fabricated using soft lithographic technique to produce the SU-8 wafers which are subsequently used as a mould to produce the microfluidic chips. The protein microarrays are produced using microcontact printing on a functionalised surface of the coverslip. These coverslips are then aligned to the analysis chambers of the microfluidic chip to produce an assembled PASH chip. Upon full assembly, the device can be used either for single cell experiments or single GUV experiments. In both cases, the cells/GUVs are individually isolated using optical tweezers and then subsequently lysed. Biomolecules released from lysed GUVs are captured by immobilised capture agents that form each microarray spot. Optical evanescent wave microscopy ensures only bound molecules are detected and single molecule image analysis is then used to extract data from the acquired images. A detailed description of each of the steps can be found in Chapter 4.

## 2.3 Optical Setup

The imaging platform for the experiments was carried out on a fully motorised Nikon Eclipse Ti-E inverted microscope. **(Figure 2.2)**

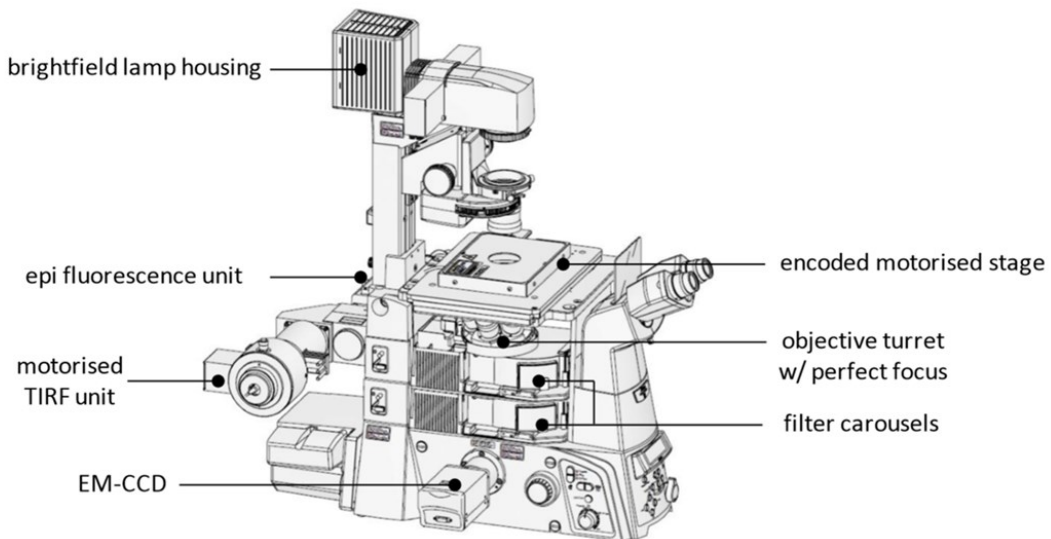


**Figure 2.2:** The setup of the optical imaging platform that was used during the experiments carried out in this thesis. Image reproduced from Salehi-Reyhani PhD Thesis 2011, Imperial College London.

The microscope used is capable of performing wide-field fluorescence imaging and total internal reflection (TIRF) microscopy. The objective turret within the microscope is populated with achromat  $10 \times 0.25$  NA dry, plan fluor  $20 \times 0.5$  NA dry, plan fluor  $40 \times 0.9$  NA dry and apo TIRF  $60 \times 1.49$  NA oil immersion Nikon objectives. The objective turrets can be translated in the Z-plane to control the focal plane. The motorised TIRF unit fitted within the system allows the laser incident angle and power to be controlled by software. This is particularly useful especially when performing experiments that require multiple wavelengths. The ability to carry out time lapse imaging can be adversely affected by focal drift, which is the inability of a microscope to maintain its focus on a selected focal plane over an extended period. This problem is exacerbated when using high magnification and numerical aperture oil immersion objectives. The system used here incorporated a focus tracking and compensation system (Perfect Focus System (PFS); Nikon). With the PFS, stable time lapse imaging can be achieved over a multitude of points across several square centimetre area of the

microfluidic device or imaging plates. The PFS accomplishes this by using a near infrared light (770 nm) generated by an auxiliary optical system that is introduced into the optical route of the microscope via a dichromatic mirror. The beam is focused onto the interface between the upper surface of the coverslip and specimen when using oil immersion objectives. As the PFS is engaged, a portion of the beam is projected on to the reference plane to ensure the interface is in focus. **(Figure 2.3)** The system then continually feeds positional data back to the circuitry controlling the focus mechanism to ensure that the focus is maintained independent of the positioning of the specimen. Non-static single molecule imaging of multiple fields of view over a large area and over time would not be possible without a focus tracking system.

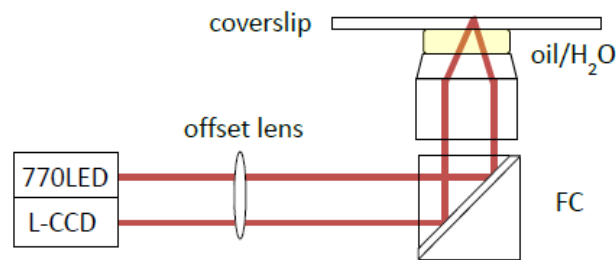


**Figure 2.3:** Schematic of the PFS in use with an oil/water immersion objective. 770 LED= LED emitting at 770nm, L-CCD, FC= filter cube. Image reproduced from Salehi-Reyhani PhD Thesis 2011, Imperial College London.

The microscope is supported by two sets of filter carousels, each containing 6 dichroic filter cube positions. The upper carousel contains standard Nikon filter sets such as DAPI, FITC and TRITC filters in addition to a TIRF illumination dichroic (z488RDC; Chroma, USA). Two carousels are left empty as one is required for bright field imaging and the other for external light sources reflected from the lower carousel. The lower carousel contains a filter set used for optically coupling external infra-red lasers, used for optical trapping and optical lysis. The filter set contains a single-edge dichroic

(LPD01-532R-25; Laser 2000, UK) and long pass filter (LP03-532RS-25; Laser 2000, UK).

The optical set up is used for cell/vesicle manipulation, lysis, and subsequent analysis. The principals of these are explained in-depth in the following sections. The optical set up used for the optical trap is formed using a single beam produced by 0.1-0.5 W ytterbium fibre laser (YLM-5; IPG Photonics, UK) at 1070 nm. The vesicles/cell is strongly confined using these optical powers, allowing them to be manipulated into isolated analysis chambers from a main flow channel. The distance over which objects are moved exceeds the field of view ( $136.5 \mu\text{m} \times 136.5 \mu\text{m}$ ) so the optical trap remains centred in the object plane and the motorised stage is translated accordingly to move objects.

Lysis of cells or GUVs to disrupt the lipid-membrane and liberate encapsulated biomolecules for analysis can be achieved in a multitude of ways, typically using chemical detergents. Lysis was achieved here by optical methods. Optical lysis is achieved by the delivery of a single high energy infra-red pulse of light. A neodymium-doped yttrium aluminium garnet laser (Nd: YAG) delivered pulses at 6 ns at a wavelength of 1064 nm. The maximum energy of the pulses at the back aperture of the objective was 14  $\mu\text{J}$ , with a pulse width of 4-6 ns.

Imaging of the microarrayed spots to monitor binding of biomolecules is achieved by total internal fluorescence (TIRF) microscopy. The laser system used for TIRF imaging is either a single coloured 473 nm continuous wave laser or a four colour Stradus VersaLase (Vortan) system operating at 405 nm, 488 nm, 532 nm, and 647 nm. For the purposes of experiments carried out in this thesis, the TIRF measurements were only

carried out using 488 nm laser with a laser power of approximately 3mW. The subsequent images were taken using an Andor iXON DU-897E electron-multiplying CCD camera. The resolution of the TIRF images was  $512 \times 512$  pixel, the electron multiplier gain (EM-Gain) of 10 and exposure time of 900 ms. The software used by the microscope for acquiring images is NIS-Elements (Nikon).

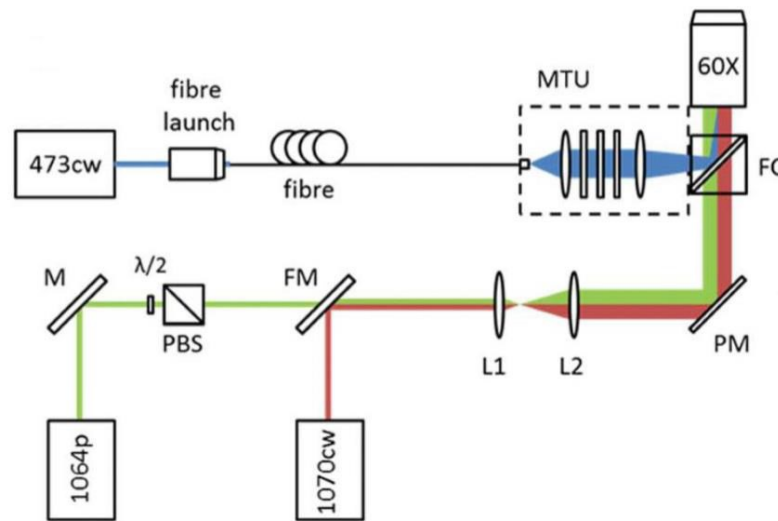


**Figure 2.4:** The complete optical set up of 473 nm continuous wave TIRF laser (blue), a 1070nm continuous wave trapping laser (red) and 1064nm pulsed lysis laser (green). Image reproduced from Salehi-Reyhani PhD Thesis 2011, Imperial College London.

### 2.3.1 Optical Trapping

The development of single beam gradient force optical trap or “optical tweezers” was pioneered by Arthur Ashkin in the early 1970s.<sup>81</sup> The ability of this system to apply picoNewton level forces to micron sized particles while simultaneously measuring displacement with nanometre level precision has made it a valuable tool in the field of biology and physics.<sup>82</sup>

In a typical set up of an optical tweezer, the incoming light source usually originates from a tightly focused laser beam through an objective lens with a high numerical aperture. As the laser holds, or *traps*, a dielectric particle, in this case either a vesicle or cell in place, confinement is achieved. The force that is experienced by the particle has two components. The first, a scattering force,  $F_{\text{scat}}$ , associated with the scattering of photons as it hits the surface of the particle and the second, a gradient force,  $F_{\text{grad}}$ , which arises due to the intensity profile of the laser beam. The  $F_{\text{scat}}$  results in a net momentum transfer between the photon and the object. This causes the object to move along the direction of the beam. The  $F_{\text{grad}}$ , acts as an attractive force which then pulls the particle towards the centre of the focal point, hence effectively trapping the particle. A sharper focus of the incident light source provides a steeper gradient hence ensuring a more stable trap. As the optical trap holds the sample in position, the movement of the motorised stage allows for the manipulation and translation of the sample's position within the microfluidic device. This is akin to navigating a house by moving the rooms around you.

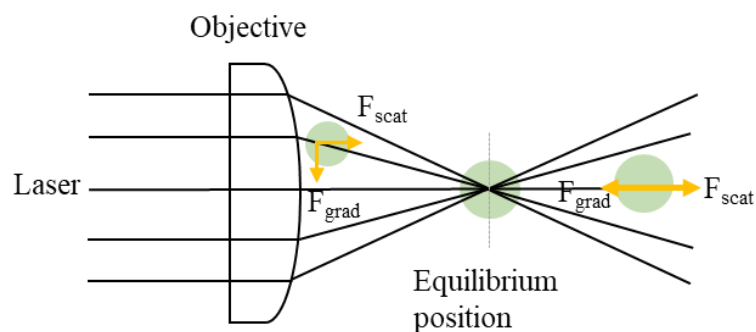


**Figure 2.5:** *The working principle of an optical trap. The  $F_{\text{scat}}$  causes a movement of the particle along the path of the incident beam whilst the  $F_{\text{grad}}$  acts as an attractive force which pulls the particle back to the centre of the focal point.*

### 2.3.2 Optical Lysis

The use of laser pulses to rapidly carry out lysis of individual cells is a relatively recent development.<sup>83</sup> The system works by focusing a laser beam through an objective lens with a high numerical aperture. By focusing the laser source on to a small spot, this results in localised plasma formation. This is followed by the formation of a shock wave and the generation of a cavitation bubble that can expand and contract within microseconds. The expansion of the cavitation bubble inflicts a differential shear stress on to the membrane of the cell/vesicles hence causing it to rupture and subsequently release the contents of the cell/vesicle. The speed of this technique makes it an ideal tool for the study of highly dynamic processes in cells.

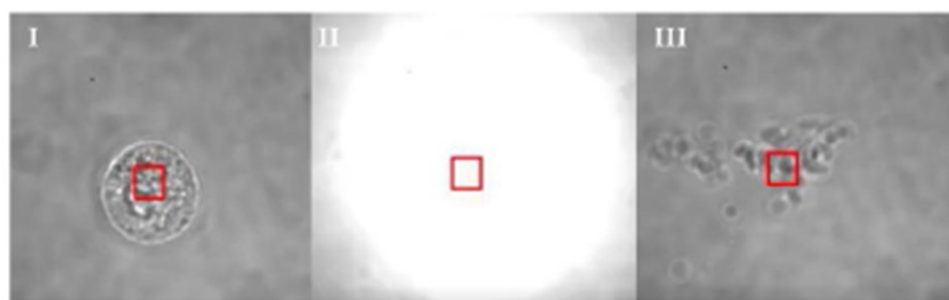


**Figure 2.6:** Experimental images of the optical lysis process of an MCF-7 cell showing i) before the application of the optical pulse ii) during the process iii) after the pulse. The complete lysis of the cell is observed in image III. The bright white flash in image II is the result of electrons recombining with the plasma due to the laser-induced breakdown of a femtolitre volume of media. Figure adapted from footage from reference<sup>84</sup>

### 2.3.3 Total Internal Reflection Fluorescence Microscopy

Total Internal Reflection Fluorescence (TIRF) Microscopy is an imaging technique that exploits the unique property of an induced evanescent wave generated within a region adjacent to the interface between two different media with differing refractive indices. As light passes through a medium of differing refractive index at an angle (incidence angle), the light undergoes refraction in the new medium and partial reflection into the

existing medium. As the incidence angle increases, the refractive angle increases to a point where the incidence angle will equate to the critical angle. At this point, the refraction is parallel to the interface. Beyond the value of the critical angle, the light is completely reflected in to the first medium. This generates a highly restricted electromagnetic field that is adjacent to the interface. This field is known as the evanescence wave and operates at a similar frequency to the incident ray. The evanescence wave decays exponentially away from the boundary of the interface, hence, only extending up to around 100 nm into the specimen in the z- direction. This is exploited to excite only the fluorophores that are bound to the capture agents microarrayed on the surface of the coverslip. Since fluorescent molecules unbound in the bulk are not excited this helps to avoid the need for a wash step to be included for the measurement thus simplifying the workflow. The use of this technique avoids the excitation of fluorophores in the bulk space and helps improve the signal to noise ratio compared to widefield epifluorescence measurements.

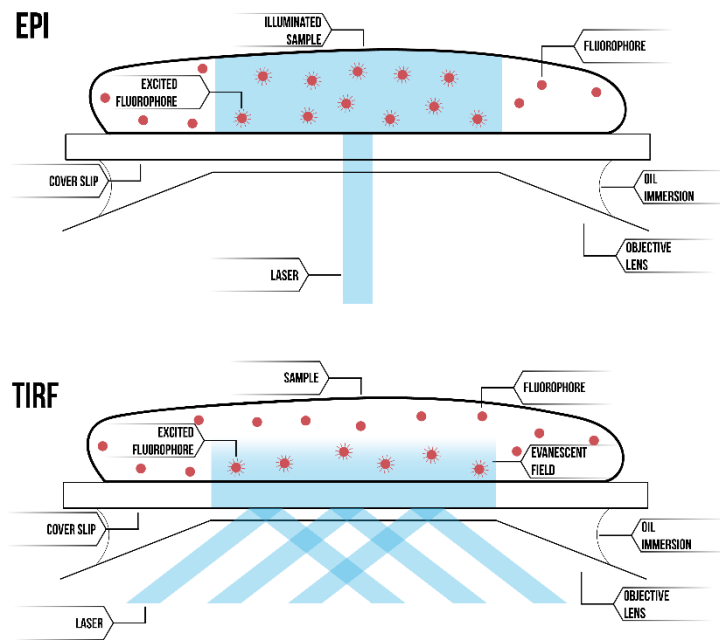


**Figure 2.7:** Comparative figure between a widefield epifluorescence microscopy (top) and TIRF microscopy (bottom). The evanescence wave formation at the critical angle causes the excitation of the fluorophore in the aqueous medium to occur at 100 nm from the surface. This reduces the background noise. Image retrieved from reference <sup>85</sup>

### 2.3.4 Fluorescence Microscopy

Wide-field fluorescence microscopy was heavily employed for majority of the work carried out in this thesis. The fluorescence imaging was carried out on a Nikon Eclipse Ti-E inverted microscope (**Figure 2.2**). The configuration of the inverted epifluorescence microscope used in the thesis is illustrated in **Figure 2.8**. The illumination of the sample from below allows the objective lens to be used as an illumination condenser and fluorescent light collector.

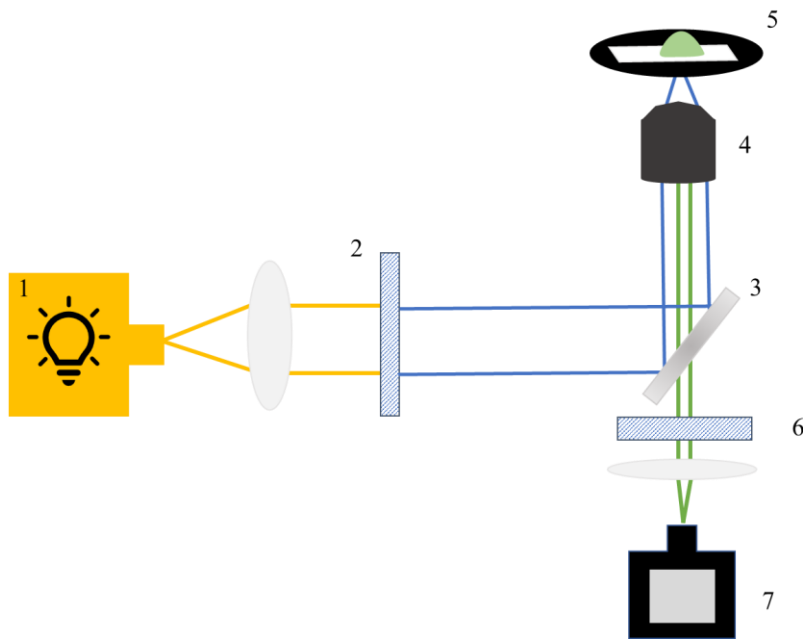


**Figure 2.8:** Epifluorescence inverted-microscope configuration. The optical paths of the excitation (blue line) and emission (green) through the objective lens are identical however shown separately here for visual clarity. 1: Light source typically a mercury arc lamp 2: Excitation Filter. 3: Dichroic beam splitter mirror that separates out the excitation light from the resultant emission signal. 4: Objective lens. 5: Sample 6: Emission filter 7: Signal detector, typically a CCD Camera that captures the fluorescent images.

The microscope used for these measurements is fitted with specific filter cubes (**Figure 2.9**).

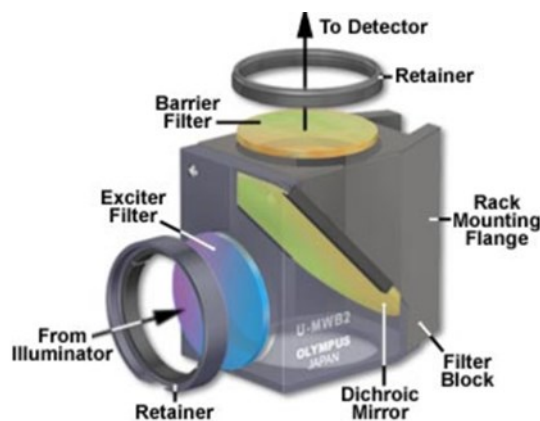


**Figure 2.9:** An example of a fluorescence filter cube fitted into the carousel of the fluorescence microscope. Image reproduced from reference <sup>86</sup>

Emission light from the light source (mercury arc lamp) passes through the excitation filter, which passes specific bands of light matched to the excitation profile of the fluorophore to be excited. The light is then reflected by a dichromatic mirror. These mirrors are specialised interference filters that reflect light of shorter wavelengths and allow beams of longer wavelengths to pass through. The transmitted light excites fluorophores in the sample. As the fluorophore is in an excited state, it eventually emits light at a lower energy (higher wavelength). The emitted light then passes through the dichromatic mirror to an emission filter. The emission filter filters out the illumination light from the weaker emitted fluorescence. The resulting emission is then gathered at the detector and can be observed via the eyepiece or camera. The intensity of the excitation light can also be controlled using neutral density (ND) filters. The microscope that was used is capable of housing 6 different filter cubes in each of its 2 filter carousels. The excitation and emission of the fluorophore determines the filter set that was used for imaging (**Table 2.1**).

**Table 2.1:** The table shows specifications of the filter set corresponding to the fluorophores that were used in the thesis. The fluorophores that were used through in the thesis are AF-488 tagged streptavidin and calcein with an absorption and emission maximum of 496 nm and 519 nm respectively.

Filter Name	Excitation Range (nm)	Emission Range (nm)	Dichroic Central Wavelength (nm)	Fluorophore
FITC	467 – 498	513 – 556	506	Alex-Fluor 488 Calcein

## 2.4 Formation of GUVs

### 2.4.1 Types of lipid used

The lipid used for the generation of the vesicles is shown in the **figure 2.10** outlining the chemical structure of the lipid. POPC (1-palmitoyl-2-oleoyl-sn-glycero-3-phosphocholine) is generally considered a model lipid due to its close resemblance to the mammalian phospholipid composition.

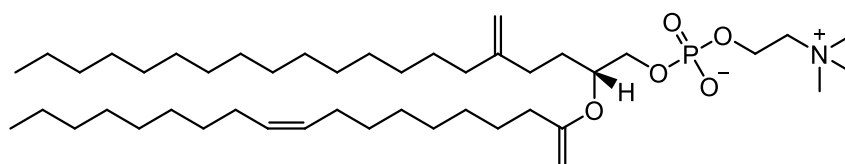


**Figure 2.10:** The figure above shows the chemical structure of POPC used in the generation of the giant unilamellar vesicles and water in oil droplets throughout the thesis.

### 2.4.2 Preparation of lipid in oil

In order to prepare a lipid-in-oil mixture, the lipid was first prepared as a film. The lipid powder was weighed in a glass vial before being dissolved in a minimal amount of chloroform. The chloroform was evaporated off using a gentle stream of nitrogen. This forms a thin layer of lipid along the walls of the glass vial. To ensure that no residual solvent is trapped within the layers of the lipid, the glass vial was placed under vacuum in a lyophiliser overnight. Mineral oil was then added to the film and the sample was mixed. The concentration range of the lipid-in-oil solution that was tested were of 0.13, 0.5, 1 and 2 mg mL<sup>-1</sup>. The optimum concentration of the solution was found to be 2 mg mL<sup>-1</sup> and was used in the remaining experiments.

### 2.4.3 Inverted Emulsion Phase Transfer

The GUVs formed throughout using phase transfer of an inverted emulsion, a method adapted and modified from previous work reported in literature.<sup>55</sup> It is a facile technique without the need for highly specialised equipment. The technique also provides and better control over the symmetry of membrane when compared to the other techniques of vesicle formation. Additionally, it can also be extended to the formation of asymmetrical vesicles with differing lipid compositions on the inner and outer lipid membrane.

Prior to beginning the steps of the inverted emulsion phase transfer, three different solutions are prepared beforehand. The internal solution of the seed solution containing streptavidin protein, that is fluorescently labelled with Alexa Fluor-488 in 200 mM sucrose is prepared. This is done by mixing 60  $\mu\text{L}$  of the stock solution of the protein ( $2.21 \text{ mg mL}^{-1}$ ,  $36.8 \mu\text{M}$ ) with 10  $\mu\text{L}$  of sucrose solution ( $0.47 \text{ g mL}^{-1}$   $1.37 \text{ M}$ ). Upon preparation of the lipid-in-oil solution as described above, 250  $\mu\text{L}$  of the lipid-in-oil solution is mixed with 25  $\mu\text{L}$  of the internal seed solution to form water-in-oil (W/O) emulsion droplet. This mixture is pipetted up and down vigorously and vortexed to ensure it is thoroughly mixed. The droplets are stabilised by the presence of the lipid within the solution. In a separate Eppendorf tube, 150  $\mu\text{L}$  of glucose solution ( $0.036 \text{ g mL}^{-1}$ ,  $0.2 \text{ M}$ ) was prepared. The W/O emulsion droplets was then pipetted into the Eppendorf tube. This formed two distinct phases within the tube: one layer containing the oil phase sitting above the aqueous phase. The remaining lipid molecules in the oil phase forms a monolayer at the interface between these two phases. The polar headgroups, which are hydrophilic face the aqueous phase whilst the non-polar tail

groups protrude into the upper oil phase containing the excess lipid. These tubes were then centrifuged for 30 min at 9000 rpm. The force of the centrifuge aids the movement of the droplets through the interface where it picks up a second layer of lipid to form a unilamellar vesicle. The resulting vesicles then sediment at the bottom of the centrifuge tube. The remaining oil layer is gently removed, and the aqueous phase is resuspended in 150  $\mu$ L of the glucose solution prepared. This is then centrifuged for 7 minutes at 6000 rpm with the supernatant removed. This process is repeated three times in order to help reduce the fluorescent background that could be caused by non-encapsulated fluorescent molecules from ruptured vesicles. The resulting GUVs solution is resuspended in a buffer solution when ready to be flowed through the PASH chip. The buffer system used in the experiment is 200 mM glucose in PBS. The process summarised in **Figure 2.11**.

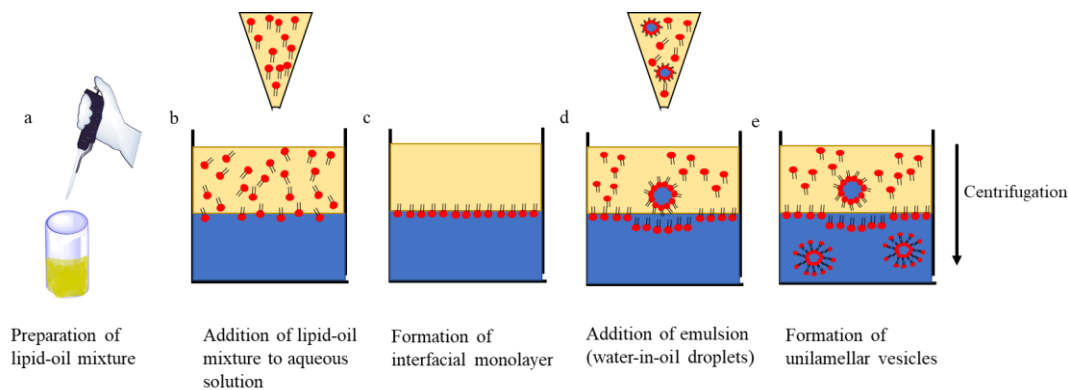


**Figure 2.11:** The formation of GUVs using inverted emulsion phase transfer. a) The lipid-oil mixture is formed by dissolving the lipid film using mineral oil. b) The lipid oil mixture is pipetted into the solution containing the aqueous solution. c) This leads to the formation of an interfacial lipid monolayer. d) Water-in-oil emulsions are prepared by mixing the internal aqueous solution (AF-488 Streptavidin in 200 mM sucrose) with the lipid-in-oil solution. This was then pipetted into an Eppendorf tube containing the external aqueous phase (200 mM glucose). e) This mixture was then centrifuged to accelerate the movement the emulsion the interface during centrifugation. The presence of a density gradient results in the formation of Giant Unilamellar Vesicles.

## 2.5 Single Molecule Counting and Data Analysis

The raw data that is collected consists of a stack of  $512 \times 512$  pixel 16-bit multi-frame images. The images recorded post optical lysis can be categorised based on the density of the fluorescent molecule recorded in each frame. The different subsets in which the images can be categorised into are:

- a) Non-Congested Images
- b) Congested Images
- c) Semi-congested Images

The description of each of this category is based closely on the spatial proximity of the single molecules to one another. In order to resolve the single molecules and obtain the number of single molecules, a peak fitting algorithm is used in which each single molecule is fitted to an isotropic 2D gaussian peak. This technique of identifying single molecule peaks and fitting them with 2D gaussian peak is commonly used in fluorescent microscopy.<sup>87</sup>

Images are considered to be 'non-congested' when the density of single molecules is sufficiently low where all single molecules are sparse and can be individually spatially resolved. For 'non-congested' images, the detection accuracy of the counting algorithm tends to be close to 100%.<sup>88</sup> However, as the density of the signal increases as a result of a higher concentration of captured molecules, the detection accuracy decreases as the overlap between the peaks increases. Images are considered to be 'semi-congested'. As the concentration of the target biomolecule in the analysis volume increase, the density of fluorophores is such that single molecules completely overlap, and none can be resolved; the images are then 'congested'. The use of the same algorithm as the non-

congested image would be inappropriate and leads to the number of molecules being severely undercounted. Therefore, to count the number of single molecules in congested images the total spot intensity is divided by the average intensity of single molecules. When using this method to estimate the single molecule count, the accuracy of the counting algorithm is  $\sim 100\%$ .<sup>88</sup> It is important to note here that the images obtained in the experiments carried out in this thesis generally fall either in the non-congested or the congested regime.

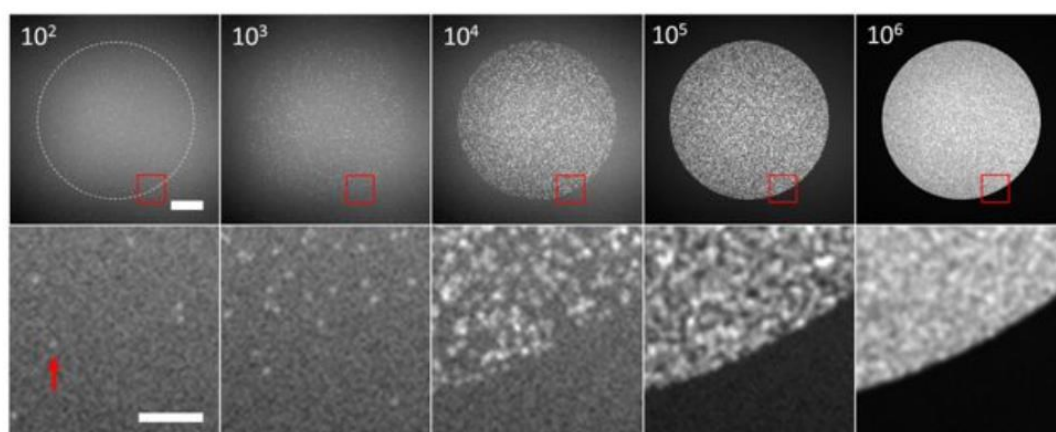


**Figure 2.12:** Exemplar images of simulated antibody spots. Each of the spot is generated using a pre-determined number of single molecules randomly located inside a circular area, mimicking a microarray spot. The number of single molecules per spot increases from left to right. A transition from non-congested ( $10^2$ - $10^3$ ) to semi congested ( $10^4$ ) to a fully congested region ( $10^5$ - $10^6$ ) can be visually noted. The red arrow denotes a single molecule. The figure is extracted from reference.<sup>88</sup>

All image processing procedures were carried out in Fiji/ImageJ.<sup>89</sup> The peak fitting algorithm was applied by using the GDSC Single Molecule Light microscopy (SMLM) plugin by Alex Herbert.<sup>90</sup> The format of the output data includes a table of the molecular localisation listed by the image frame number. This made the extraction of the data for the number of single molecules per frame straightforward. The Peak Fit SMLM plugin was benchmarked against other algorithms and was found to be one of the better performing algorithms for this data.<sup>91</sup>

### 2.5.1 Non-Congested Image Processing

The use of the algorithm for the processing of non-congested images is performed routinely for most of the work carried out in this thesis. A workflow of how the analysis is performed is outlined in **Figure 2.13**. Though the concentration of the proteins encapsulated into GUVs is such that spots typically become semi-congested or congested, the background binding signal for the capture spots is non-congested on the order of 10 to a few 100 single molecules per frame. This is a particularly important step as it used to estimate the average single-molecule intensity of the fluorophore.

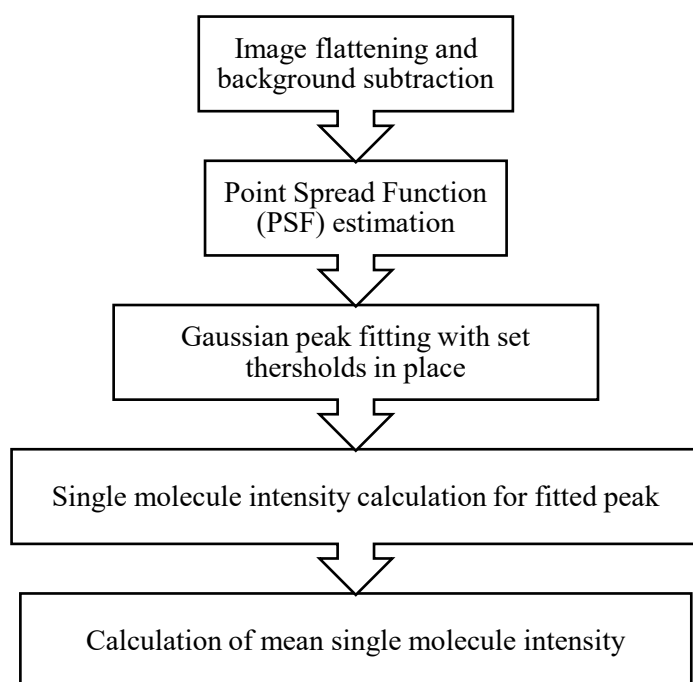


**Figure 2.13:** *The workflow of processing non-congested images*

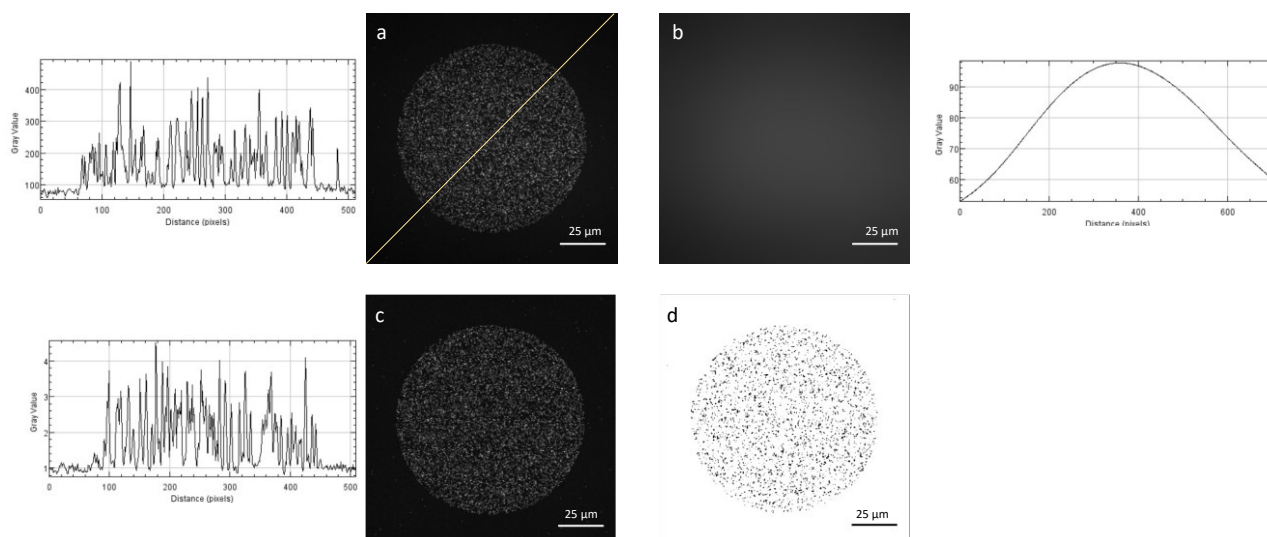


**Figure 2.14: The stages of the non-congested single molecule counting algorithm.** a) The original image b) An exemplar image of the laser profile constructed by passing through background image a gaussian blur filter. c) The flattened image produced by dividing image (a) with (b). d) After applying a threshold of 3 standard deviations of the background, the SM mask produced consists of the remaining particles that are counted as single molecules depending on its circularity and cluster size. The effects of field flattening, gaussian blurring and background subtraction across a single molecule image can be observed via the line profile of the corresponding images. The line profile, a diagonal line drawn across the image from top left corner to bottom right corner corresponds to the pixel intensity of the image.

The raw images are field flattened, background subtracted and baseline noise offset (BNO) compensated before peak identification and single molecule identification. The function of flattening an image is to remove the inconsistencies that arise from the uneven illumination from the excitation laser. As a result of the gaussian intensity profile of the illuminating TIRF laser, the excitation of a similar fluorophore at the edge of the image may be underestimated to one appearing at the centre. Thus, the image is normalised to ensure that they appear to have the same apparent brightness. This is achieved by dividing the raw images with a set of blank images (background images) from the same set of experiments. If background images are not available, a sufficiently sparse image may be used to flatten itself once a Gaussian blur is applied to the ‘dividing’ image. In general, the blank images often have very sparse single molecule and are in random positions. Hence, the probability of finding single molecules in the same position in successive frames is relatively low. A gaussian blur ( $r=50$  pixels) is

then applied to these background images before being divided with the raw image. The next parameter that is introduced is the baseline noise offset (BNO). This factor is introduced to describe the information within the intensity of the pixels that is still present in an already flattened and subtracted background image. As seen in **figure 2.15**, when the intensity line profile is measured across the image, the intensity randomly fluctuates with a mean value close to but not zero. This level is designated as the baseline noise level. The BNO is subtracted from each frame and ensures that the intensity contribution from dark pixels in the image averages to zero. To measure the BNO, the algorithm samples the edge pixels of a frame in order to avoid inadvertently sampling single molecules that are more likely to be found in the centre of the frame since this is where the capture spot is located.

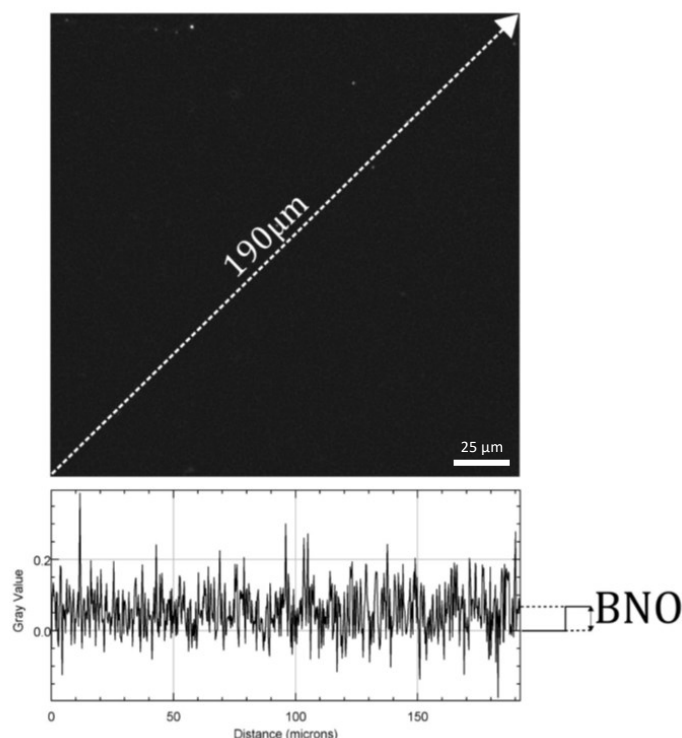


**Figure 2.15:** An exemplar image of the Baseline Noise Offset. The profile of the flattened and background subtracted image is obtained using a line profile drawn from the top left corner to top right corner. The inset image shows a rather noisy profile, with fluctuations of the pixel intensity close to but not zero. This fluctuation can be categorised as the baseline noise offset.

Once the BNO has been compensated, the total image intensity is the sum of the contributions from all single molecules in the frame. The resulting images that are generated can then be thresholded in order to produce images from which peak counting can be performed. In order to carry out the 2D gaussian peak fitting, the algorithms are implemented using the GDSC plugin by Alex Herbert. Point spread function (PSF) estimation allows for a reference point of a true single molecule to be determined prior to the single molecule identification and localisation on the acquired data. Single molecules are defined as a diffraction-limited point source, in which the diffraction pattern or the point spread function is set by Airy function.<sup>92</sup> So, the signal shape distribution of fluorescent objects on the raw images that do not correspond to this pre-estimated reference point are rejected.

The point spread function estimator first determines the average gaussian shape parameters of a sample by randomly selecting N peaks (N= 1000 by default) from all images in a dataset. Using least squares, each of the peaks are individually tested against the average single molecule shape parameters in order to be counted, or discounted, as a single molecule depending on the intensity and size. Therefore, the total number of single molecules is enumerated. The number of single molecules that have been identified in each individual image/frame and their associated properties (location, size, intensity) are then exported for further analysis. It is also important to note that each pixel does not correspond to a single molecule. It is such that the optical resolution of the system results in the fluorescent labelled streptavidin spanning several pixels. However, the PSF feature, part of the image analysis workflow allows for the properties of intensity and size of a defined number of candidate single molecules to be measured. Since we obtain this data using limiting concentrations of analyte, the statistics are such that we detect single molecules in isolation.

In summary the original images obtained from the TIRF microscopy are field flattened, filtered and then thresholded to produce images from which peak counting can be performed. These methods are computationally fast and allow datasets to be processed in a timely and efficient manner. For example, a full dataset comprising 200 fields each comprising, typically, 10 frames each can be fully processed in a few minutes using modest hardware.

### 2.5.2 Congested Image Processing

The number of a specific molecules expressed in biological cells or encapsulated in a GUV can span many orders of magnitude – 100s to  $10^8$  per cell or GUV. Using the image analysis techniques employed here, it is possible to distinguish single molecules up to  $\sim 3000$  molecules per  $100\ \mu\text{m}$  diameter spot. Concentrations of biomolecules in a cell/GUV, and subsequently the assay chamber, can result in a number of capture molecules that exceed this threshold and puts the antibody spot within the ‘congested regime’. A simplified of the workflow for congested image processing is outlined below **(Figure 2.16)**.

Like the non-congested counting algorithm, congested images also require to be flattened, background subtracted, and baseline noise offset compensated. In the latter part of this workflow, the average single molecule intensity calculated from a set of background images allows for the total single molecule count to be estimated. However, it is crucial that the mean of the single molecule fluorescence intensity in both the congested and non-congested data relate exactly to one another. Using the peak fitting algorithm, each of the single molecule from the congested image is fitted to an isotropic 2D gaussian profile to determine the total integrated single molecule intensity. This is then divided by the average single molecule intensity that has been determined using the background images of a non-congested image in order to obtain the number of single molecules.

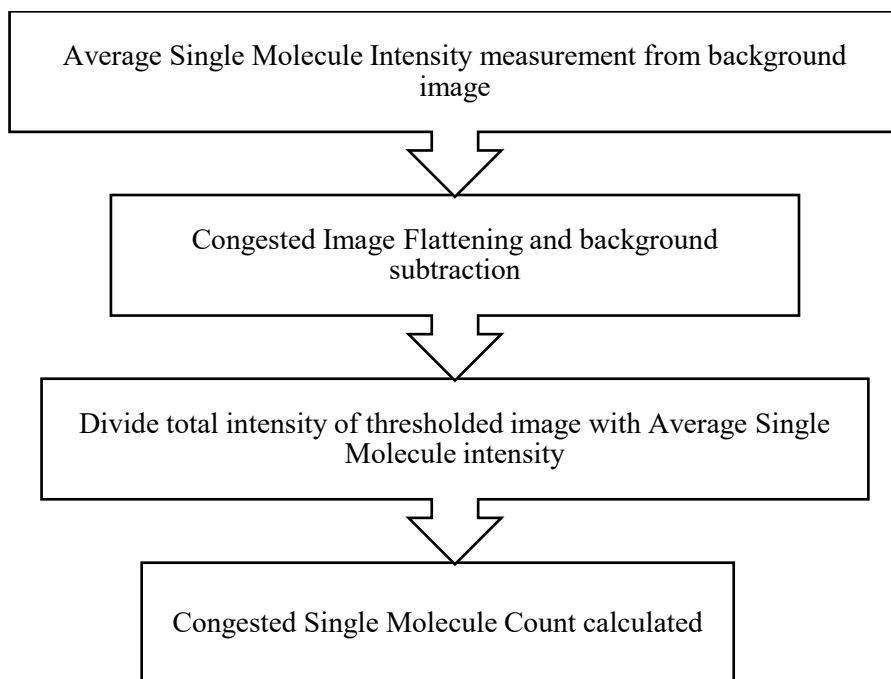


**Figure 2.16:** *The workflow of processing congested images using the congested algorithm*

### **3. Emulsion Phase Transfer to study size distribution of GUVs**

#### **3.1 Chapter Outline:**

This chapter describes the work carried out to measure the distribution of descriptive parameters of GUVs at the population level synthesised using emulsion-based phase transfer.

- **Wide Field Fluorescence Microscopy**

Wide field fluorescence imaging helped characterise and understand the size and fluorescence distribution of the GUVs that were produced using this technique.

Wide-field fluorescence imaging technique was optimised for the imaging of fluorescently labelled GUVs.

- **Optimisation of Data Analysis Method**

Manual Segmentation, Automated Fiji Filters and Cell Profiler data analysis tools were employed on wide field fluorescence images to develop and validate an image analysis method.

- **Characterisation of size and fluorescence intensity distribution of GUVs**

Two types of fluorescence molecules, calcein and streptavidin tagged with an Alexa-Fluor 488, were encapsulated within GUVs and imaged under optimised conditions and analysed to understand the distribution of the vesicles

## 3.2 Introduction

### 3.2.1 Liposomes

Much of the work carried out within this thesis involves the formation and study of vesicles, specifically GUVs. Lipid vesicles also known as liposomes are fully enclosed aqueous compartment containing a bilayer originating from the self-assembly of lipids in aqueous solution. They are often used as models to investigate the biophysical nature of membranes owing to the close resemblance to a biological cell.

One of the main constituents of membrane structures are phospholipid molecules. These molecules are amphipathic containing two components with different solubilities: 1) the hydrophilic polar head group, and 2) the hydrophobic non-polar tail region (**Figure 3.1**).

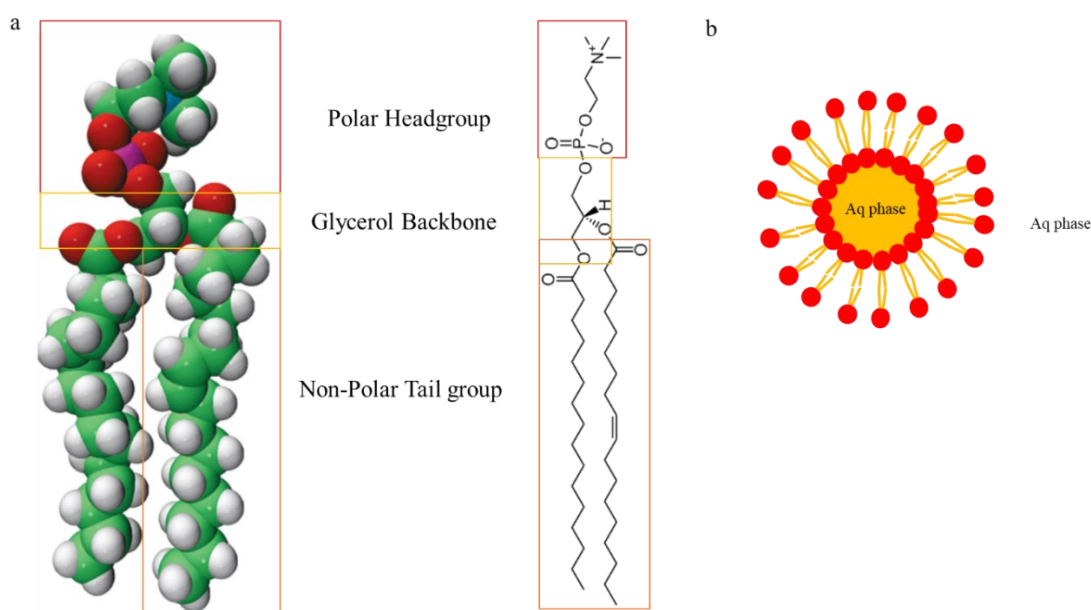


**Figure 3.1:** The figure above shows the 3D model of the POPC lipid that was used as the lipid component of the GUV throughout this thesis. a) The phospholipid molecule is divided into the polar headgroup region (hydrophilic) consisting of a phosphate group and a glycerol backbone in this case and the non-polar (hydrophobic) region consisting of the carbon chain. b) The figure shows a simplified vesicle consisting of a bilayer, with an aqueous core and hydrophobic bilayer membrane. A single bilayer membrane is typically ~5nm thick. The lipid molecules are oriented such that the “water hating” tail group faces inwards and the “water-loving” head group faces the exterior aqueous medium.

Lipid vesicles can be also be further classified according to their size and lamellarity. The ability to control the lamellarity and size of these lipid structures means they can be designed to perform specific functions. For instance, Giant Unilamellar Vesicles (GUVs), can be constructed to possess a bilayer with analogous thickness (~ 4 nm) and diameter (10-100 $\mu$ m) to that of a biological cell. Given their microscopic size, they are easily observed using light microscopy. Stable GUVs may be produced with a specific lipid composition in the bilayer and encapsulant/internal solution. This allows GUVs to be produced as a mimetic cell model but also used to study a variety of protein reconstitution experiments<sup>93-95</sup> and membrane leakage assays.<sup>96</sup> GUVs have been reported to be loaded with a variety of biomolecules such as DNA<sup>97</sup>, RNA<sup>44</sup>, and enzymes<sup>98-100</sup>. The ability to encapsulate purified cell lysates within the internal environment of the vesicles allow for these vesicles to be used as models to carry out in-vitro cell transcription and translation.<sup>101,102</sup> In recent years, there has been a growing interest in using GUVs as artificial cell models that could construct its own cytoskeleton<sup>103</sup>, synthesize proteins<sup>42</sup> and membrane proteins<sup>104</sup>, undergo cellular division.<sup>105</sup> Vesicles have also been investigated for use as vehicles for targeted drug delivery.<sup>38,106,107</sup> For example, hydrophilic drug molecules have been successfully encapsulated within liposomal drug delivery platforms.<sup>108</sup> Therefore, owing to this close resemblance and versatility in its application, GUVs have been considered the gold standard in the development of bottom-up cell mimetic models.

### **3.2.2 Conventional Techniques of Giant Unilamellar Vesicles fabrication**

Over the last 30 years, a variety of methods to produce vesicles have been developed. These methods include extrusion through a porous membrane, electroformation, freeze drying, hydration or swelling, double emulsions and budding.

#### ***3.2.2.1 Natural Swelling***

One of the earliest techniques reported is the natural swelling of lipid films as reported by Reeves and Dowben in 1969.<sup>52</sup> This method is also known as spontaneous swelling, or lipid film gentle hydration method. Using pre-hydrated layers of stacked lipid bilayers due to the combination of osmotic pressure, electrostatic interactions and hydrophobic effect, giant thin-walled vesicles were gently swelled over an extended period, typically days.<sup>109</sup> This method is the preferred method to produce vesicles incorporating charged lipids.<sup>110</sup>

However, despite its apparent simplicity and mild vesicle formation conditions, the method is difficult in practice and resultant vesicles are produced in low yields with a high tendency to form to multilamellar vesicles and lipid debris. The quality of the GUVs produced also exhibit ‘bad’ membrane quality with internal tubules and small vesicles attached. The unintended heterogeneity of vesicles produced from the same lipid films has also shown to be a concern.<sup>111</sup>

Therefore, the formation of vesicles using this technique is heavily dependent upon the hydration conditions as well the amount and uniformity of the deposited bilayer, which in themselves is difficult to control. The timescale typically within hours to produce GUVs using this method also puts this method at a disadvantage.<sup>112</sup>

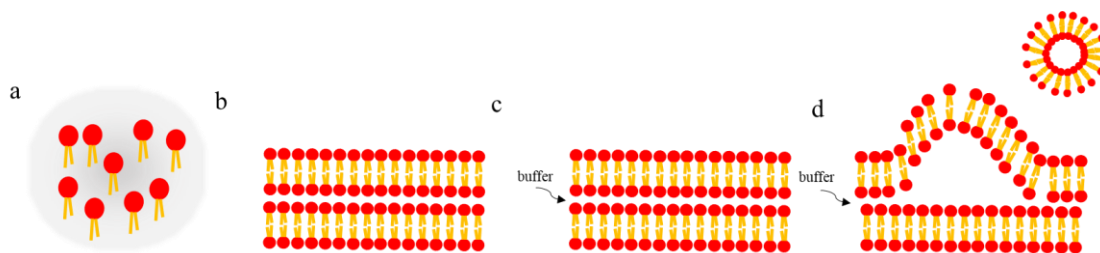


**Figure 3.2:** A schematic of natural swelling method used to produce GUVs. a) The lipid is dissolved in an organic solvent b) The evaporation of the solvent and self-assembly of lipid molecules into several stacks of bilayer. c) The addition of buffer hydrates the dried lipid film. d) The swelling of the stack of bilayer lipid films form vesicles.

In 2009, Horger et al. developed an agarose-assisted swelling technique to form GUVs.<sup>54</sup> The deposition of the lipid on a porous polymer layer enhanced the buffer flow from below and increased the number of unilamellar vesicles formed over a wide range of lipid composition in varying buffer solutions. Though the resultant vesicles did not show any visible defects as before, the lipids that were deposited penetrated the agarose layer. This therefore cause the vesicles that were formed to contain high amounts of agarose encapsulated within it. The presence of agarose not only affected fluorescence measurements (high background signal), but also altered the mechanical properties of the vesicles and increased the permeability of the membrane.<sup>113</sup>

Polyvinyl alcohol (PVA) was investigated as an alternative supporting polymer film by Weinberger et al.<sup>114</sup> The use of PVA prevented the deposition of the residual polymer within the vesicles as the method before. This method also allowed for the formation of vesicles under varying buffer conditions using a wide range of lipid composition. They also demonstrated the use of this method to successfully encapsulate actin molecules within the vesicles with no damage to the biomolecules as vesicle formation can be carried out at low temperatures. However, a drawback of this approach was the observed difficulty in gently detaching the vesicles that have been formed, while rigorous

detachment could rupture the vesicles or lead to increased defects within the membrane. To completely prevent polymers from dissolving into the membrane during vesicle formation, crosslinked hydrogel can also be used to regulate GUV size. This can be achieved by adjusting the size of the pores to control the intensity of the hydrogel.<sup>115</sup>

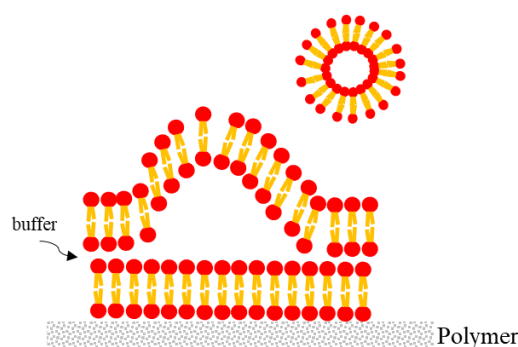


**Figure 3.3:** The illustration above shows the stacked lipid bilayers deposited above the polymer surface. This allows for an increased flow of the buffer solution that helps in the formation of GUVs.

### 3.2.2.2 Electroformation

Electroformation was first introduced by applying an electric field in the layer of lipid films deposited on to electrodes.<sup>53</sup> Lipid films from a chloroform stock solution are deposited and dried on Indium Tin Oxide (ITO) coated glass electrodes. Upon rehydration with an aqueous solution, an AC electric field is applied to the electrodes for about 1-2 hours typically resulting in high yields of GUVs. The vesicles are thought to be formed due to the combined effects electrostatic interaction, redistribution of bilayer counter ions, membrane surface, line tension charges and electro-osmotic effects.<sup>116</sup> Electroformation is a more widely used method in comparison to natural swelling due to its higher efficiency and reproducibility of the morphology and lamellarity.<sup>109</sup> This methodology also allows for the preparation of GUVs composing of negatively charged lipids. The GUVs that are formed using this method are generally

polydisperse in size (10-100  $\mu\text{m}$ ) and have reasonably high variability in the composition of the membrane.

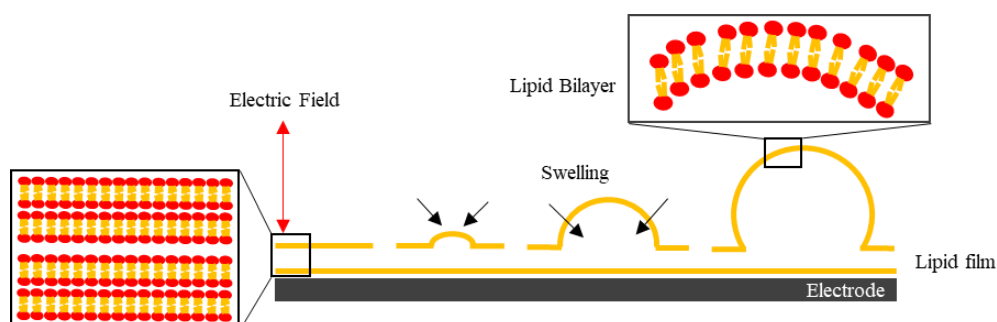


**Figure 3.4:** The illustration above shows the formation of vesicles using electroformation method. Figure reproduced from the stated reference.<sup>117</sup>

However, a large drawback of this method lies in its limitation of forming GUVs at low salt concentrations and its inefficiency of encapsulating large, charged molecules. This is because the encapsulation of large charged molecules requires the movement of compounds through the external layer of the lipid film. Depending on the molecular size and charge, such inner leaflet movement is extremely slow and not possible for macromolecules such as proteins and DNA.<sup>118</sup> The possibility of oxidising the lipids and causing damage to the encapsulant material due to the presence of an electric field is also a concern.<sup>119,120</sup> However, this is addressed through the use of platinum electrodes. This approach has been widely utilised as a potential method for GUV formation for the encapsulation of biomaterials that are directly microinjected in to the vesicles.<sup>121</sup>

### 3.2.2.3 Emulsion based phase transfer

The water-in-oil (w/o) emulsion transfer method involves the use of a stable w/o emulsion using an oil and bilayer forming lipid as the starting system for the preparation of giant vesicles. The reverse phase emulsion transfer method first introduced by Pautot

et al.<sup>55</sup> has been shown to successfully produce GUVs that possess a higher degree of unilamellarity and more monodisperse in comparison to swelling and electroformation. Elani et al.<sup>30</sup> demonstrated the use of this method to form vesicles with asymmetrical membranes, that have been useful studying the membrane behaviour and compartmentalisation, aspects that are important in developing artificial cell models. Dogma in the field has led to believe that the encapsulation efficiency is 100%, however, to date little work has been done to fully quantify and understand the efficiency of this technique.

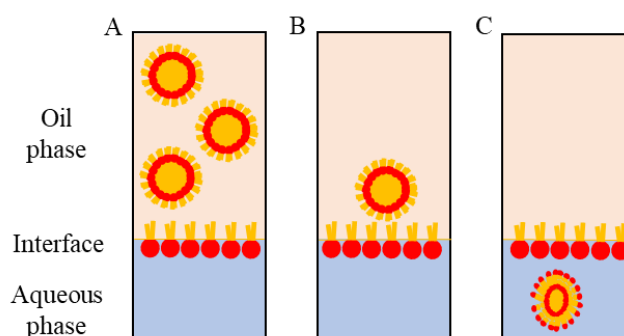


**Figure 3.5:** The figure above is an illustration of the inverted phase emulsion transfer. a) The water-in-oil droplets b) The interface formed between the two phases in which the droplets pass through and picks up the outer layer of the bilayer. c) The vesicle that is formed is of a unilamellar bilayer.

The emulsion that is produced is supported below by an aqueous solution to form a two-phase system. The oil phase - using dodecane,<sup>55</sup> mineral oil<sup>45</sup> or squalene<sup>122</sup> - contains a bilayer-forming lipid; for the GUVs produced in this work POPC is used. This two-phase system is incubated prior to the addition of the w/o emulsion. The formation of the interfacial region between the two phases becomes saturated with the lipid and forms a monolayer. Upon addition of the w/o emulsion, the droplets move towards the interface into the lower aqueous phase solution due to an density difference. Allowing the droplets to sediment through gravity is usually a long and slow process, therefore,

the process is assisted using centrifugation. As the droplets pass through the interface, it picks up the secondary leaflet to form a bilayer, making it a unilamellar vesicle. The w/o droplet migration can be further promoted by preparing the aqueous solution using sucrose and an equiosmotic glucose solution in the lower aqueous phase. The difference in the relative density between the sucrose and glucose solutions help the GUVs that have been formed to sediment in the aqueous solution. The movement of the droplets through the interface has been observed using fluorescence microscopy.<sup>123</sup>

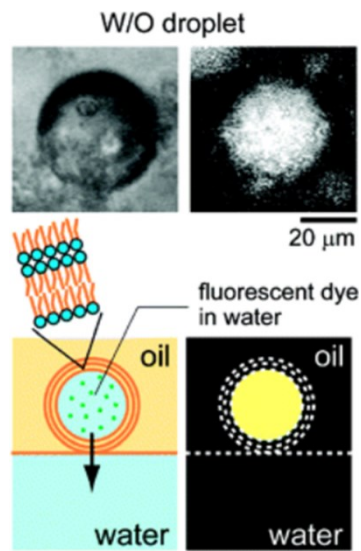


**Figure 3.6:** An exemplar image of a water-in-oil droplet imaged at the interface using phase contrast microscopy and fluorescence microscopy. Figure reproduced from the following reference <sup>123</sup>

### **3.2.3 Wide Field Fluorescence Microscopy of Vesicles**

Fluorescence microscopy has been an essential tool in the field of biology as it is able to identify cell and microscopic cellular components with a high degree of specificity amidst the non-fluorescing material. The development of fluorophores both synthetic and natural with known excitation and emission intensity profiles has also led to the widespread use in the biosciences. It comes in various forms and configurations, each with its own set of advantages depending on the desired application.

Wide field fluorescence microscopy is the simplest mode of fluorescence imaging technique in which the entire sample is illuminated using a specific wavelength, allowing for the fluorophores within the sample to be excited. The emitted light is visualised and captured using a camera. The use of this technique in general enables the identification and visualisation of various cells, cell components and defined proteins. The underlying key principle of this imaging technique relies on the use of fluorescent molecules or fluorophores to either label defined cellular structures or encapsulated within structures. Fluorophores are molecules that absorb light at specific wavelength (excitation wavelength) and emit it at a higher wavelength (emission wavelength). The absorbed energy excites the electrons from their ground states to a higher energy level, the excited state. Upon return to their ground state, a fluorescent photon is emitted.

Wide field microscopy exposes the whole specimen to light in contrast to confocal microscopy. Thus, signal from all focal planes is detected which leads to lower contrast in thick samples. Thus, this imaging method is most effective for samples that are thin with a low autofluorescence background. In the case of the GUVs, a thin monolayer of

the vesicles is required for the imaging as it minimises the interference of the out of plane background light.

The use of epifluorescence microscope allows the GUVs to be observed at frame rates up to a 100 Hz or temporarily fast behaviour with submicron resolution. This enables the features of GUVs to be observed and helps in understanding its formation. The use of fluorophores is necessary for observation either as free dyes or conjugated to biomolecules of interest. Molecular probes and dyes can potentially interfere with the membrane structure; however, recent studies have shown that the use of these dyes in small concentration (<1 mol %) has a minimal impact on the physical property of the membrane.<sup>124</sup> A critical step in the use of this microscopy is the type of fluorescent probe that is used. This is because some dyes are able to induce large changes in the host membrane causing experimental artifacts, which may result in the misinterpretation of the data. Another critical consideration when capturing fluorescence images is photobleaching, leading to a loss of fluorescence intensity. Therefore, the choice of fluorescent dye and probes are important considerations as well as the sensitivity of the instrument itself. Here, we used bright fluorophore with high quantum yield as well as a sensitive electron multiplying EM-CCD camera. These allow us to maintain high signal to noise ratios for short exposure times.

### 3.3 Experimental Methods

#### 3.3.1 Phase transfer of an Inverted Emulsion for vesicle production

The method to produce GUVs using phase transfer of an inverted emulsion (PTIE) used here is adapted and optimised from Pautot et al.<sup>55</sup> In order to produce GUVs using PTIE, a water-in-oil emulsion was first prepared. The first step in this is the preparation of the lipid-in-oil solution. POPC (Avanti Polar Lipids, United States) lipid film is prepared by weighing approximately 3 mg of the lipid powder dissolved in 250  $\mu\text{L}$  of chloroform. The chloroform is evaporated off using a gentle stream of nitrogen until it forms a thin layer of lipid along the walls of the glass vial. This approximately takes around 5 minutes. The lipid film is then left to dry further under vacuum in a lyophiliser overnight in order to remove any residual organic solvent. The dried lipid film is then reconstituted in 1.5 mL of light mineral oil (Sigma, UK) to obtain a lipid-in-oil solution with a final lipid concentration of  $2\text{mg mL}^{-1}$ .

Three different solutions are prepared prior to beginning the steps of PTIE. The internal aqueous phase of the seed solution containing either Alexa Fluor 488 (AF-488) tagged streptavidin protein purchased from Startech Scientific Limited ( $10^9$  molecules  $\text{nL}^{-1}$ ) or calcein ( $10\ \mu\text{M}$ ) in 200 mM sucrose is prepared. 250  $\mu\text{L}$  of the lipid in oil solution is then mixed with 25  $\mu\text{L}$  of the internal seed solution to form the water-in-oil (W/O) emulsion droplet. This mixture was thoroughly pipetted up and down, and vortexed in order to ensure it is mixed properly. In a separate Eppendorf tube, 150  $\mu\text{L}$  of 200 mM glucose solution was dispensed. The W/O emulsion droplets are carefully pipetted along the sides of the Eppendorf tubes to form a gentle layer above the glucose solution. This tube is then centrifuged for 30 minutes at 9000 rpm in order to drive emulsion droplets

through the interface formed by the two distinct phases. Upon completion, the vesicles are now sedimented at the bottom of the Eppendorf tube. The remaining oil layer is gently removed by pipette, and the pellet and remaining aqueous phase is resuspended using another 150  $\mu\text{L}$  of the glucose solution. This is then centrifuged once again for 7 minutes at 6000 rpm with the supernatant being removed at the end. This process is repeated around 3-4 times depending on the size of the pellet. This step is carried out to remove the fluorescent background from non-encapsulated molecules from ruptured vesicles. The resulting GUVs are then resuspended in 200 mM glucose solution before being transferred to the imaging well.

### **3.3.2 Preparing vesicles for imaging**

The imaging wells used for the wide field images were the 8 well Nunc Lab-Tex II chambered cover glass (ThermoFisher Scientific). Prior to imaging, the surfaces of four of the central wells were functionalised using 4% BSA in 200 mM glucose in order to prevent the absorption of the GUVs. 500  $\mu\text{L}$  of this solution was pipetted into the wells and left in the fridge overnight or for at least 4 hours. Prior to imaging, the wells are washed out using 500  $\mu\text{L}$  of PBS. A final solution of the 100  $\mu\text{L}$  of the external glucose solution is added to the well before the addition of GUVs. The GUVs are diluted into the well at a ratio of 1:2.

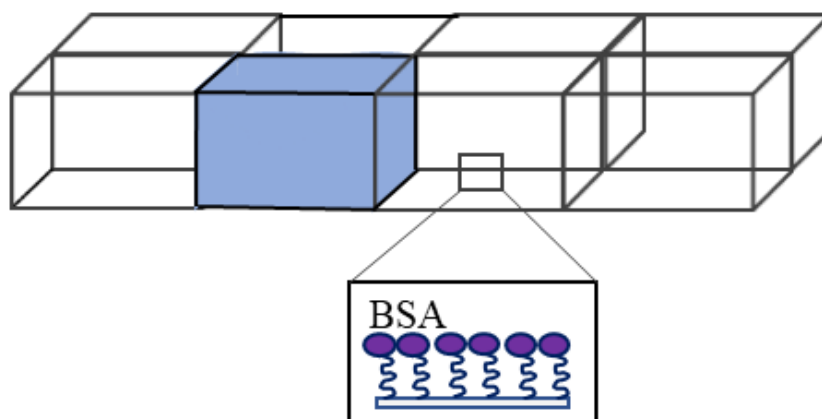


**Figure 3.7:** The figure above shows the 8 well chamber that was used for the wide field imaging. The 200mM glucose solution and GUV solutions were filled at a 1:2 ratio to the top of the chamber. Achieving a flat interface and no concave meniscus helped to avoid inhomogeneous backgrounds due to the scattering of fluorescence excitation light. The surface functionalisation that is used is a thin layer of BSA on the surface to prevent the adsorption of GUVs. Illustration not to scale.

### 3.3.3 Wide Field Fluorescence Microscopy Imaging

#### 3.3.3.1 Fluorescence Image Acquisition

The chambers filled with the respective solutions is then secured on the stage of the microscope. Widefield fluorescence microscopy was performed on an inverted microscope (Nikon Ti-E, Nikon, Japan) using a mercury lamp (Nikon, Japan) with the standard FITC filter set (Nikon, Japan). The images were acquired using an electron multiplied CCD camera (IXON DU-897E Andor Technologies, Ireland). The EM-CCD setting were as follows; 200 ms acquisition time, electron multiplier gains 10 with the readout mode set to 1 MHz at 16-bit. Tile scans of  $20 \times 20$  fields of view ( $2.66 \text{ mm} \times 2.66 \text{ mm}$ ) were acquired using a  $60\times$  1.49 NA oil immersion objective for the fluorescence channel subsequent to a brightfield acquisition using a halogen lamp. The use of an EM-CCD camera allows a wider range of concentrations to be probed with an improved sensitivity due to the camera's wide range of linearity and its high signal to noise ratio. The focal plane of the system was maintained using a Nikon Perfect Focus System (Nikon, Japan) and a motorised stage. The microscope platform was controlled

using NIS Elements software (Nikon, Japan) that allowed for the automated acquisition of the large field images.

## **3.4 Results and Discussion**

### **3.4.1 Optimisation of Wide Field Imaging**

This section describes the development and optimisation of the imaging protocols for the GUVs that were produced using the aforementioned method. The optimisation of the imaging parameters was crucial as it maintained the yield of GUV produced therefore providing a more accurate representation of the distribution.

#### **3.4.1.1 Buffer System**

The buffer in which the GUVs are suspended was optimised to ensure the long-term stability of GUVs during imaging. It also plays an important role in balancing the osmolarity of the overall system thus minimising or abrogating the rupture of the GUVs over short timescales of several hours to a day. The internal solution of the GUV consisted of 200 mM sucrose whilst the external solution contained 200 mM glucose. The denser GUVs would settle and remain on the coverslip surface for imaging. This sugar gradient is also crucial in ensuring the movement of the water-in-oil droplets through the interface during phase transfer. Glucose and sucrose have been extensively used in the preparation of vesicles in order to maintain the iso-osmotic conditions across the membrane.

BSA is a type of globular protein with an isoelectric point value of 4.7<sup>125</sup> At a neutral pH, the molecule is negatively charged. The varying charge density within the three domains of BSA influences the adsorption of BSA on to charged surfaces. It is an example of a non-covalent protein blocking agent.<sup>126</sup> This protein belongs to a soft protein class, which has the ability to easily change their structure and confirmation.

BSA is a commonly used blocking agent that is able to effectively improve the sensitivity of a particular assay by reducing the non-specific background interference whilst simultaneously improving the signal-to-noise ratio. BSA is mainly used as it is readily available and cost effective. In systems that employ a single molecule imaging technique, the use of a blocking agent is important as it reduces non-specific binding that could potentially be interpreted as false positive signals leading to the deviation from the true SM count. However, another aspect to be considered is the interaction that may occur between the hydrophobic region of the protein and the lipid bilayer. This interaction may potentially lead to the disruption in the integrity of the vesicle membrane.

Therefore, we first tested the integrity of the GUVs resuspended in 4% BSA (w/v) in the 200 mM glucose in PBS. GUVs were incubated in the test solution for 30 min. It was observed that the addition of the BSA into the solution lead to the near complete rupture of GUVs (**Figure 3.11**). Decreasing concentrations of BSA were tested. It was observed that the degree to which GUVs ruptured decreased as the concentration of BSA was decreased. No rupture was observed when using 200 mM glucose in PBS as the buffer. Therefore, GUVs were resuspended in this solution upon formation and for storage over short timescales.

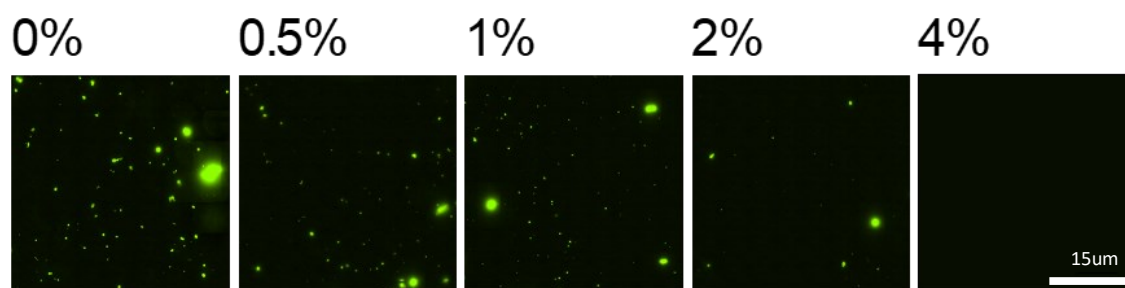


**Figure 3.8:** GUVs encapsulated with streptavidin Alexa Fluor 488 (green) were resuspended in collection buffer systems containing the denoted percentage (w/v) of BSA in 20 mM glucose in PBS. The concentration range of the BSA tested here is between 0.6 mM to 0.075M. The GUVs were incubated at room temperature for 30 minutes prior to imaging. The images here show the extend of the GUV rupture to the corresponding solutions. Minimal rupture was observed with 0% BSA.

It is suspected BSA adsorb onto the surface of the bilayer, especially at high bulk protein concentrations, and destabilises the membrane leading to rupture. Ruggeri et al.<sup>127</sup> demonstrated that for vesicles composed of neutrally charged lipids, similar to the GUVs produced here, the addition of BSA at concentrations up to 1mM (c.f. 4% BSA is equivalent to 601.5 M) showed minimal leakage. The mechanism that was proposed by this group suggested that the leakage in the presence of these proteins may occur due to the change in the membrane curvature as the protein adsorbs onto the membrane with no penetration into the lipid bilayer. Within the same field of view, a larger number of GUVs were imaged at reduced concentrations of BSA in the collection buffer. This supports the observation of a lower leakages in the GUVs which lead to the rupture of the vesicle. Though uncertain of exact mechanism, it could be surmised that the presence of BSA to a certain extent contributes to the rupture or leakage of the vesicles. Thus, moving forward, the collection buffer only consisted of 200mM of glucose, and this was to maintain the iso-osmolarity between the internal and external environment of the GUVs.

### 3.4.1.2 Surface Functionalisation

Another important parameter that had to be taken into consideration prior to imaging was the surface functionalisation of the imaging wells. In the absence of any surface functionalisation, the GUVs that were produced tended to aggregate over time and clumped together when dispensed into imaging wells. The interaction between the surface and lipid vesicles have been manipulated to form planar supported lipid bilayers and have been used to investigate the properties and functions of biological membranes.<sup>128–130</sup> However, for our purposes, the adsorption of the lipid vesicles onto the non-functionalised surface may form clusters of GUVs leading to the oversaturation of the CCD camera. Additionally, the adsorption of the vesicles on to the surface destabilises the vesicles as they deform into a hemispherical shape, leading to its rupture. Prior to adsorption, the vesicles were of spherical shape, as expected, due to the approximately equal internal and external osmotic pressure. The deformation of the GUVs upon adsorption is believed to be initiated by the formation of a rupture pore specifically near the rim of the glass-bilayer interface and was studied extensively by Hamai et al.<sup>131</sup>

Therefore, to avoid this, a thin film of BSA was used to passivate the imaging surface. On a charged surface, the adsorption of BSA is driven by the electrostatic attraction between the oppositely charged functional groups along the polypeptide chain of the BSA molecules and the negatively screened glass surface. Typically, the adsorption is restricted to a monolayer, formed at concentrations lower than 0.15 mM (10mg mL<sup>-1</sup>) with an incubation of 2 hours.<sup>132</sup> However, at higher surface concentrations of BSA, it is postulated that 2D aggregates are formed due to the unfolding of the tertiary structures

and reduction of the random coil in favour of the  $\beta$ -helical sheets.<sup>133</sup> In the presence of phosphate buffer, BSA molecules adsorb in a more compact and stable conformation. This is due to the high binding efficiency of the phosphate to the BSA alongside the screening of unfavourable structural electrostatic repulsions.<sup>134</sup> It has been observed that the protein molecule undergoes denaturation and some form of structural change in order to maximise favourable interactions between the surface and solvent. The amount of BSA deposited on the surface is dependent on the surface material as well. Reports have shown significant variations in the suitability of BSA as a blocking reagent with concentration ranges between 0.075 – 75  $\mu\text{M}$  (0.005 – 50  $\text{mg mL}^{-1}$ ) and incubation periods of 10 minutes to 2 hours.<sup>132</sup> Despite this variation, most studies have shown that BSA is a good blocking agent.<sup>135–137</sup> Studies in literature has shown that BSA is used as a universal blocking reagent, however a detailed understanding and optimisation of the condition is highly dependent upon the type of assay and surface. For example, Swerdya-Krawiec et al.<sup>138</sup> suggested that the adsorption of BSA on a hydrophilic surface has been shown to be a two-step process before complete passivation is achieved whilst it is a one step process on hydrophobic surfaces. Reimhult et al.<sup>136</sup> on the other hand observed higher blocking efficiency of BSA on two different surfaces using the same concentration of BSA. Meilczarski et al.<sup>132</sup> showed that the formation of a phosphate-BSA surface complex correlated with efficient blocking of non-specific interaction by the BSA layer. Therefore, in order to maximise the adsorption of BSA on the surface, the BSA was dissolved in PBS instead of distilled water with a maximum concentration of 4% (w/v) or 0.75  $\text{mM}$  (40  $\text{mg mL}^{-1}$ ). All glass surfaces were passivated for fluorescence microscopy of GUVs.

### **3.4.2 Methodology and Optimisation of Data Analysis**

All fluorescence data was acquired using wide field fluorescence microscopy and analysed using three different methods which will be discussed in detail below. Briefly, the first methodology employed is manual segmentation of the images in which a user-obtained outlines of the GUVs was used to segment images. The second method is an automated method using 3 different global thresholding techniques. The third technique that was tested out employed the use of CellProfiler<sup>139</sup> with an inhouse pipeline written specifically for the purpose of analysing these large widefield images. The methods were tested in their ability to obtain accurate information, specifically GUV total fluorescence intensity and area of the GUVs, used to estimate volume and concentration. Manual segmentation served as the ground truth dataset to which the unsupervised image analysis methods were compared.

#### **3.4.2.1 Manual Segmentation**

The first method is a manual analysis method in which the perimeter of an object is manually defined, to obtain per object information. Each GUV is identified within a large-field image acquired by a  $20 \times 20$  field tile scan. The perimeter of a GUV was defined at the boundary between the fluorescent encapsulated material and the surrounding dark background.

The first step in developing this method was to determine the accuracy in finding the edges of a GUV using fluorescence imaging. This can be achieved using manual segmentation instead of automated image processing methods due to the difficulty in defining the boundaries of the GUVs using brightfield images. The low change in the transmission between the internal and external solution makes it difficult to determine

the boundaries of the GUV which may lead to an inaccurate estimation of the true perimeter of the vesicle. In order to understand the accuracy of the perimeter approximation, the area measured in 60× bright field was compared to that at 60× FITC. In theory, the area measured at both bright field and FITC should be equal. However, in practice there was a discrepancy between these measurements. For bright GUVs, the signal-to-noise/background ratio is high, so the edges of the GUVs appear well-defined; however, a fluorescence halo, an artefact of imaging, was present. For dimmer GUVs, the edges were harder to define accurately due to the low contrast between the GUV and background. An intensity line profile for individual GUVs was obtained (**Figure 3.9**). In a perfect case, i.e., in the absence of any noise or artefacts of imaging, the line profile of the GUV would be well-defined with an instantaneous rise and drop at the edges, as illustrated in **figure 3.9(a)**. The increase in the intensity in the line profile would be a result of the fluorescence signal within the GUV. In this scenario, determining both the size of the GUV and the total fluorescence intensity would be trivial. A typical intensity line profile of these vesicles follows a gradual increase or decrease near the edges of the vesicle, as seen in **figure 3.9(b)**. The gradual change in intensity on either side is due to a difference in the thickness of the GUV. The GUV projected onto a 2D surface has a difference in the volume that is captured during imaging. The edges of the resultant image have a lesser volume projected on it, therefore, capturing a lower intensity of the fluorescence. In the centre however, the full diameter of the sphere is projected, therefore, leading to a higher intensity measurement. The halo ring effect surrounding the GUVs is mainly due to an effect of scattered light. The inclusion of

the fluorescence intensity due to the halo can lead to an overestimation in the area of the GUV.

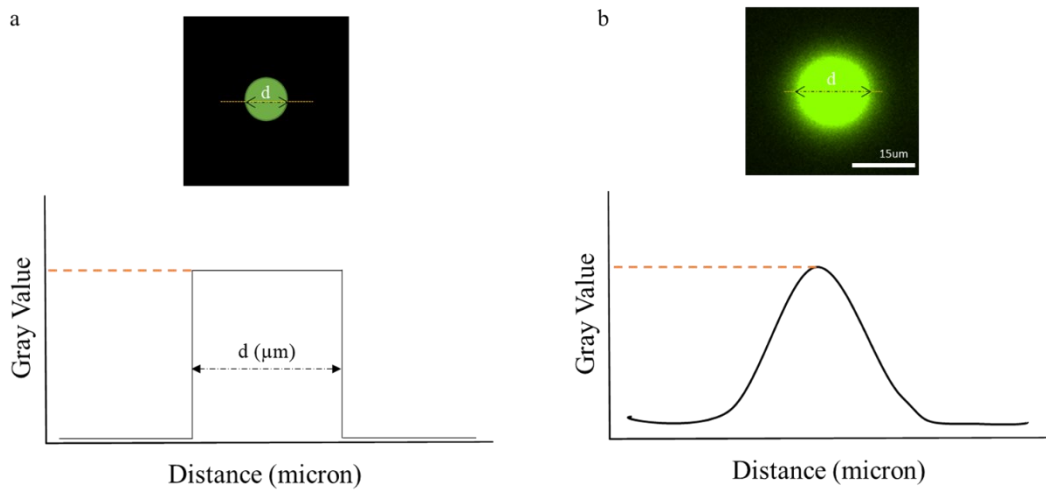


**Figure 3.9:** Intensity line profile of a GUV in two scenarios. a. A representation of an ideal line profile of a GUV with well-defined edges and no noise. The sharp rise to maxima and drop to minima is indicative of the fluorescent signal within the GUV. b. A representation of a typical line profile of a GUV. The gradual increase and decrease of the intensity measurement represent the decrease of the fluorescence across the GUV due to the difference in the projected volume of the GUVs as a result of the imaging.

Using a combination of both bright field images and fluorescent images of the same vesicle, we would be able to determine the true size of the GUVs.

GUVs were isolated into microfluidic analysis chambers such that a single GUV was visible per field of view and its location known. The area of each GUV was measured by independently tracing the perimeter in both the bright field images and the FITC image. The measurements obtained were then plotted against one another. The area measurements obtained from bright field images were compared with those from FITC images and is presented in the **Figure 3.10**.

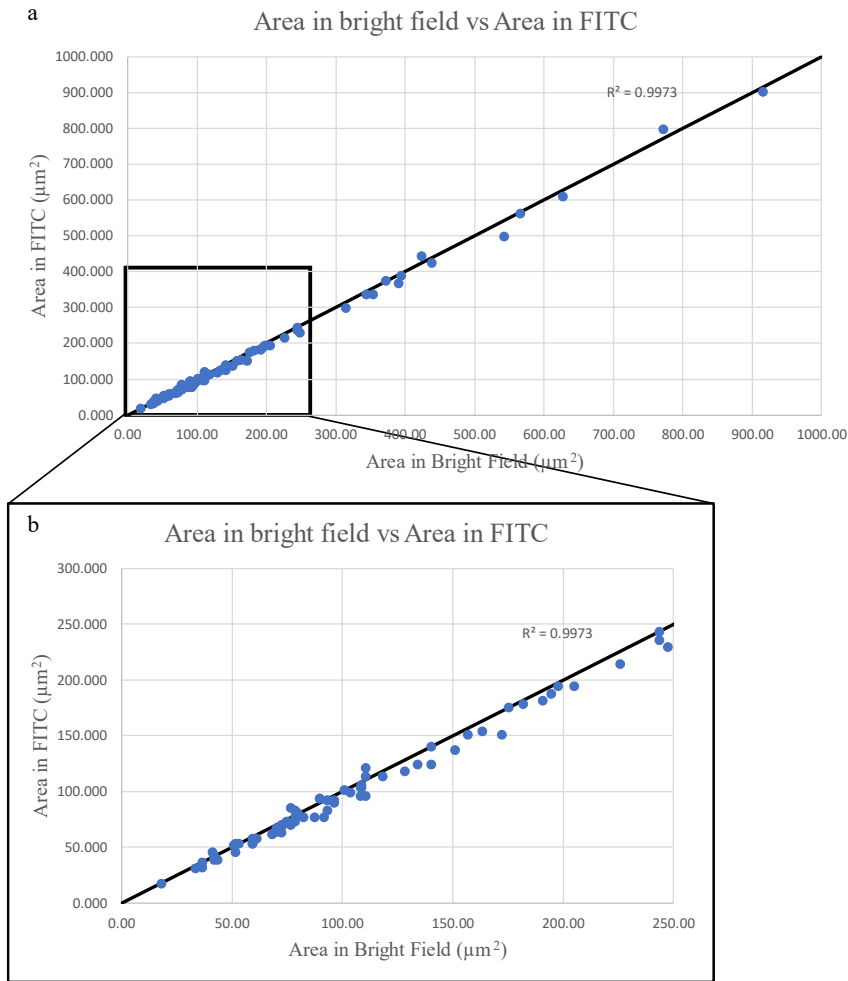


**Figure 3.10:** a) The relationship between the area measured in the bright field channel and FITC channel respectively for all individually isolated GUV. The estimation of the edges from the ground truth using the bright field images and FITC image for both large and small sized GUVs show minimal deviation from the ground truth. b) The relationship between the GUV area in the bright field and the FITC for smaller area GUVs between 0-250  $\mu\text{m}^2$ . The measurements were carried out on GUVs ( $n=82$ ), encapsulated with AF 488.

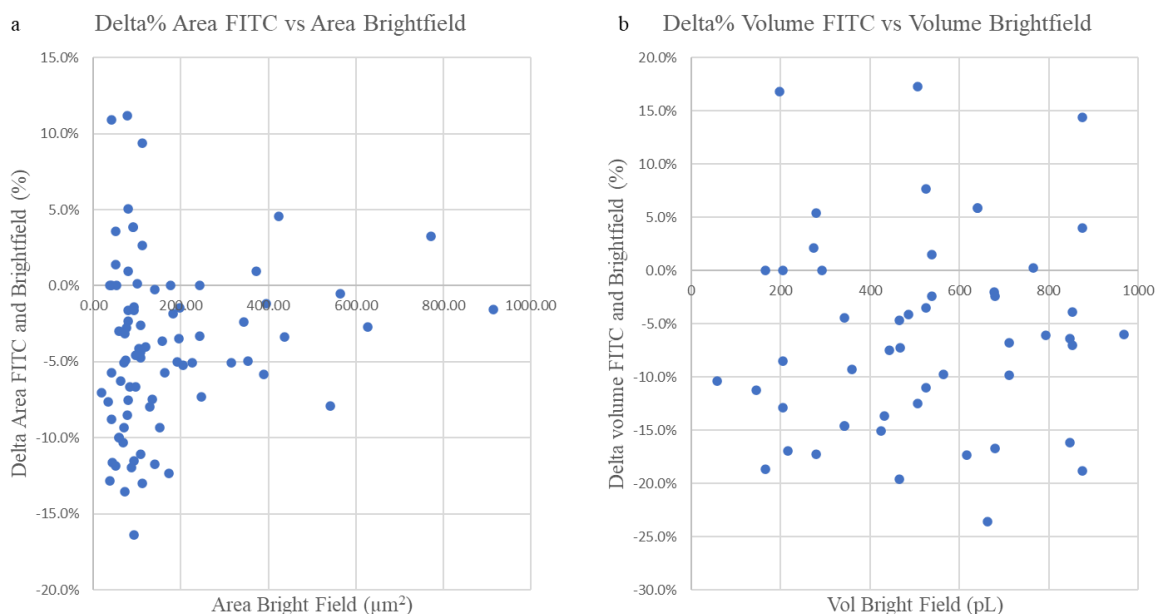
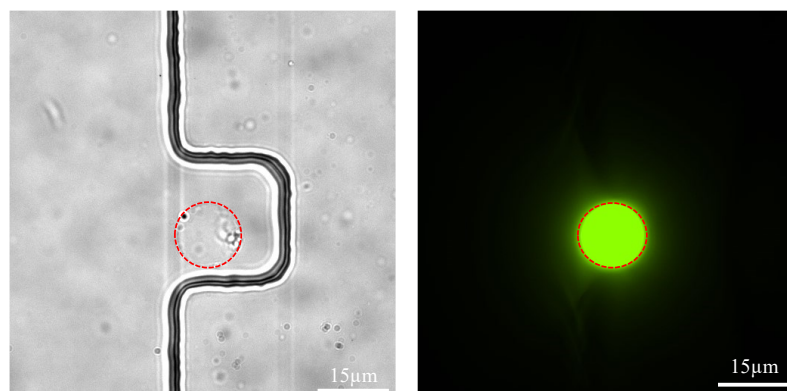


**Figure 3.11:** a) The relationship between the area difference measured in bright field and FITC against that measured in bright field. The variation between of GUVs at the lower end is higher. As the volume is a function calculated using information obtained from the area measured, the error associated with the overestimation or underestimation of the area is multiplicative. b. The percentage difference of the volume difference calculated in bright field and FITC against the volume of bright field GUVs for the same set of data. The measurements were carried out on GUVs  $n=82$ , encapsulated with AF 488.

Larger GUVs are easier to identify than smaller ones, both in brightfield and in fluorescence imaging, (**Figure 3.12 (a)**). Fluorescence images, where objects are distinguished against a dark low signal background, are easier to process but objects are surrounded by a ‘glow’ (out of focus light, scatter) that can lead to difficulty in precisely defining the limit of the GUV. Determining this limit is more straightforward in brightfield but much more challenging to process using automated image analysis. It was necessary, then, to determine the accuracy of the approach to segment GUVs in fluorescence and compare their shape parameters, i.e., area from which diameter and volume are calculated, to that obtained in brightfield. When determining the *ground truth* of the area and the intensity measurement, approximating the shape using the FITC measurement is sufficient as the comparison between bright field and FITC is  $\pm 5\%$  from the expected value. In the case of the GUVs measured at lower end, it becomes

increasingly difficult to distinguish the edges of the GUV on both bright field images and fluorescence images. The approximation of the area using bright field images alone may lead to an underestimation of the GUV area leading to under sampling the intensity measurement. However, the comparison between the bright field and FITC measurements was still within error with a variation of  $\pm 15\%$ . The overall variation in the difference of the calculated volume between the bright field and fluorescence measurements is 8%. Though it is still not a near perfect approximation, the deviation is small enough to continue using fluorescence measurements as means to determine the edges of the GUV. One way to overcome this could be by manipulating the difference of the refractive index of the internal and external solution. This, however, may not be the ideal solution as it may disrupt the iso-osmolarity of the solution which is crucial in maintaining the integrity of the vesicles. Moving forward, the fluorescent images were used to determine the area of the GUV with several caveats in place described in detail below.

a)



b)

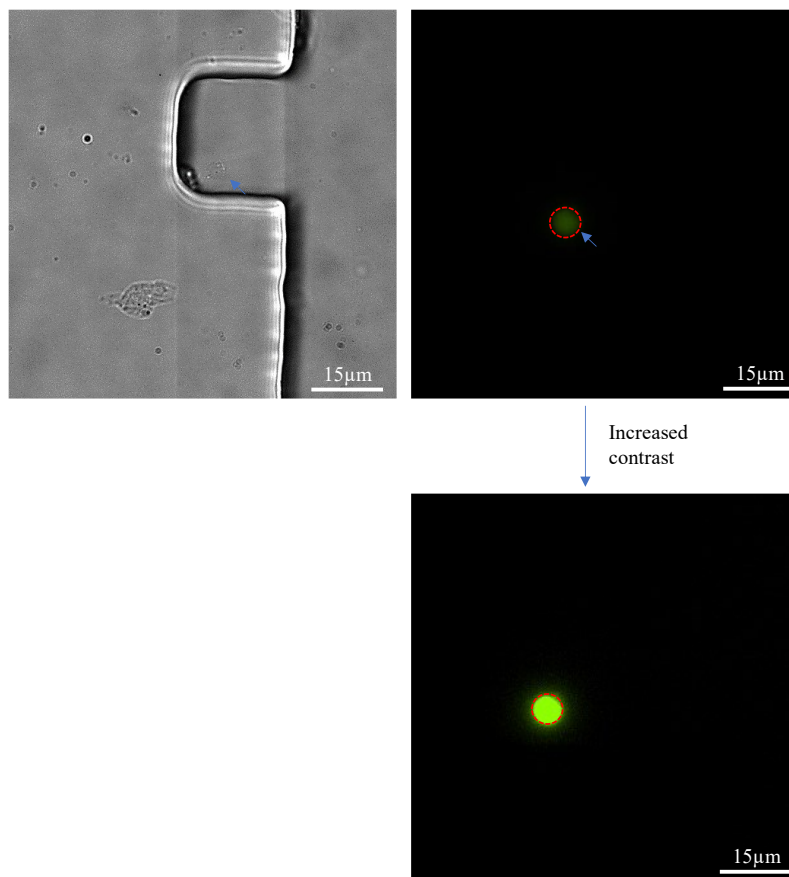


**Figure 3.12** Exemplar images of GUVs used to measure the area of the GUVs a) GUVs of a larger area and volume have a more distinct edge appearance in both the bright field and fluorescence channel b) Smaller volume GUVs have a less distinct edge appearance thus making the approximation of the edges more difficult.

An improvement to this methodology would be the use of phase contrast microscopy in place of bright field imaging. Phase contrast microscopy measures the difference of the refractive index between across the sample. For GUVs, the relative difference of the refractive index between the internal and external solution would help provide contrast. The images obtained would have made it easier to determine the edges of the GUVs therefore reducing the error associated with approximating the edges of the GUV.

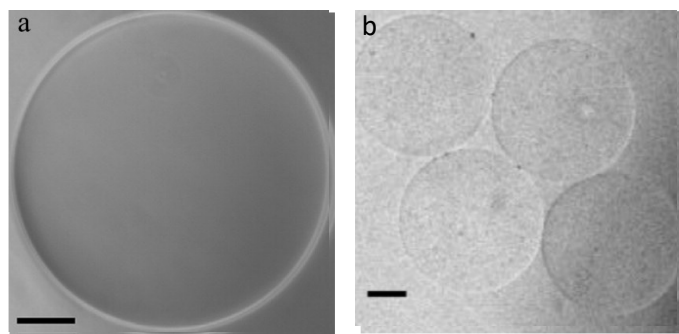


**Figure 3.13:** Exemplar image of GUV acquired using a) phase contrast microscopy b) Bright Field Microscopy. The image of the GUV obtained from phase contrast is has significantly more defined edges in comparison to the bright field. (Scale bar: 50  $\mu\text{m}$ ) Image modified from indicated reference.<sup>140</sup>

The appearance of GUVs produced using emulsion-based phase transfer could be described as follows. A proportion of GUVs are ‘clean’ with little to no lipid debris surrounding the external lipid layer as illustrated in **figure 3.14(a)**. Both the bright field image and FITC image show a distinct outline of the GUV edges, which made it easy for the GUV to be measured. A proportion of GUVs are produced with lipidacious material attached; the edges of GUVs are less visible when lipid debris occludes edges, see **figure 3.14(b)**. The bright field image here shows the additional lipid debris which can hinder image analysis. Some GUVs are produced where the external lipid bilayer is completely contaminated with lipid debris, making it a very ‘messy’ GUV in appearance. The lipidacious material or debris is not observed in fluorescence indications the absence of fluorescent encapsulant within or adsorbed in/on these features.

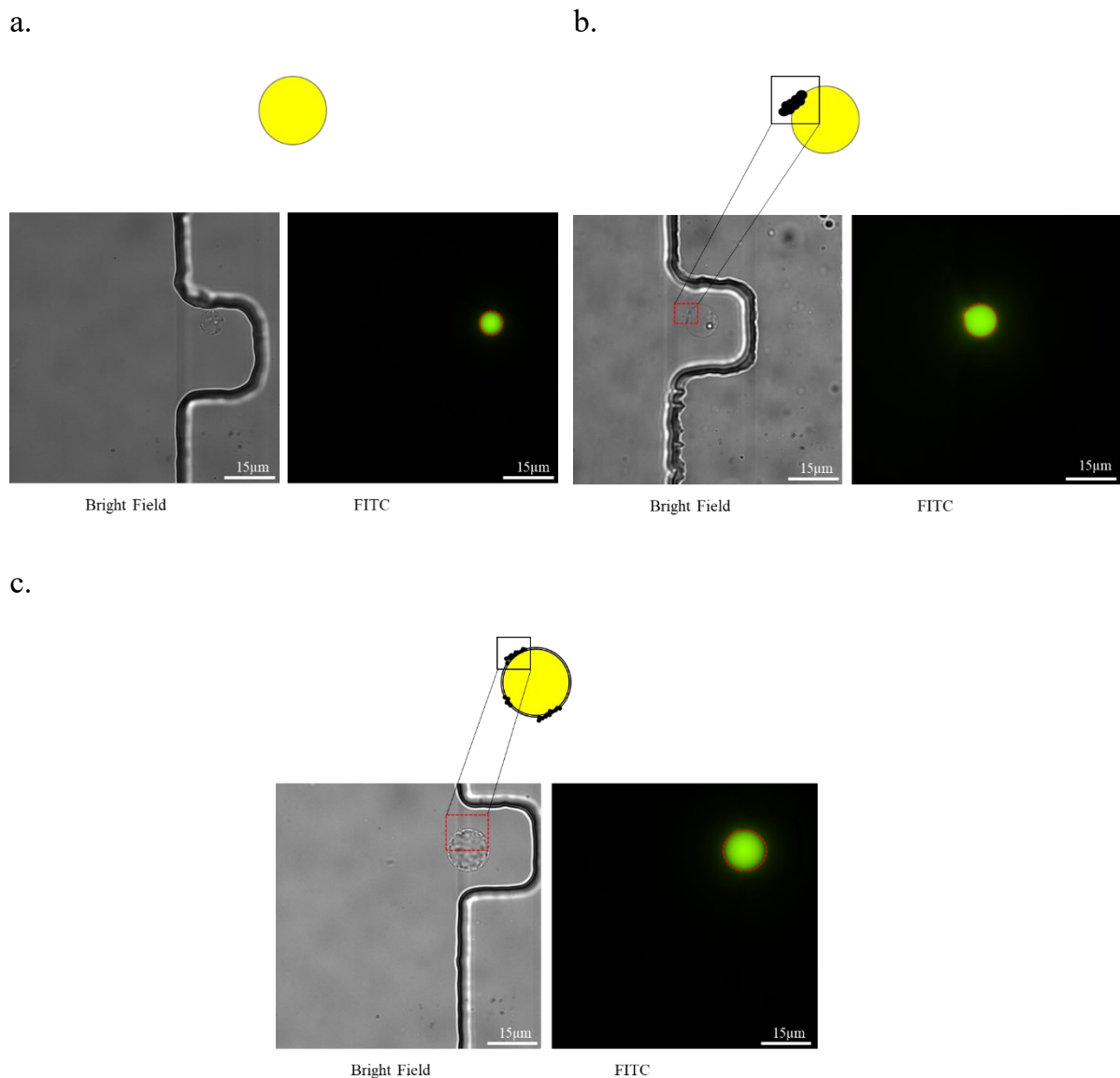


**Figure 3.14:** The figure above shows the three varying possible appearances of the GUV when formed using emulsion based phase transfer. a) A “clean” GUV with minimal lipid junk and debris on the external lipid envelope of the vesicles. This makes determining the edges clearer. b) The GUV that is produced contains a slightly higher lipid junk in the outer lipid envelope. However, it is shown that this does not affect the fluorescence intensity as the region of interest lies within the internal compartment in where the encapsulated fluorescence material is concentrated. c) The GUV produced here has an extremely messy out lipid layer, with two distinct rings forming the external layer and internal layer is observed. In order to identify the edges, the area is measured from the internal edges as shown in the FITC image.

When plating GUVs for imaging, some would clump into groups of GUVs in proximity, making edge detection more challenging and necessitating object recognition to distinguish connected GUVs. The GUVs in which the perimeters were indistinguishable from one another were not measured to avoid discrepancies in the data (**Figure 3.18a**).

GUVs that were imaged straddling the edges of images (**Figure 3.18b**) were also not included. GUVs that were stacked upon one another would contribute fluorescence signal to GUVs in focus and the blooming effect of their signal meant that GUVs within close proximity to large clusters of GUVs would also be disregarded.

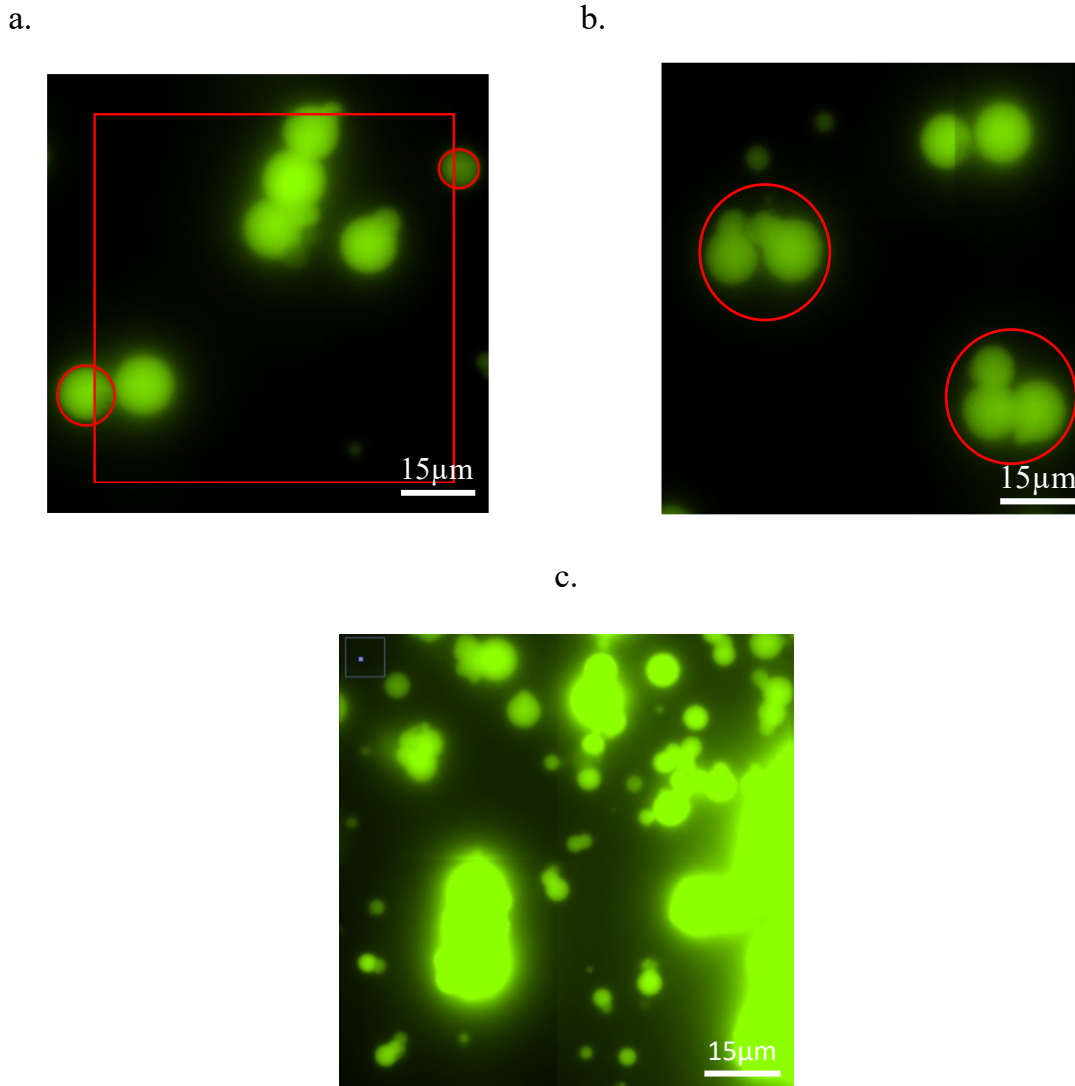


**Figure 3.15:** Exemplar of GUVs excluded from the manual segmentation method. a) The GUVs were imaged between the borders of two tiles that were stitched together. b) GUVs that are visibly clumped together in which the perimeter of the GUVs are hard to be distinguished were also excluded. c) The GUVs that are in close proximity to the larger clumped objects would be more affected by the halo effect (red circles) compared to those that have a cleaner background (white circles).

Although manual segmentation is time intensive, it is used to establish the ground truth of the data. It was used as a reference to validate and gauge the performance of the methods of automated image analysis presented in section 3.3.2.2.

Another important aspect that needs to be considered when analysing the data obtained from the images is the contribution of the background signal towards the total integrated intensity. The background was estimated across fields by superimposing regions of interest approximating the average size GUVs, as illustrated in **figure 3.16**.

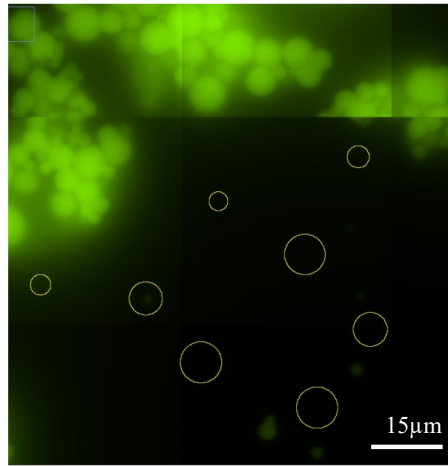


**Figure 3.16:** The method used for estimating the background within each data set. Random circles approximately the size of the GUVs are superimposed onto the data set to obtain the background intensity. The circles are superimposed within regions away from the bright halo of the GUVs.

The background fluorescence intensity for each of the data point is calculated using the **equation 3.1**:

$$I_{BKD}^{GUV} = \frac{N_{Pixel}^{GUV}}{(A \times ((P_x \cdot P_y)^2))} \quad Eq. 3.1$$

where,  $N_{pixel}^{GUV}$  represents the Raw Integrated Intensity measured using Fiji,  $A$  is the area of the GUV, and  $P_x$  and  $P_y$  represents the value of a micron unit per pixel, 0.266667 microns/pixel. This value is dependent on the combination of optics of the microscope,

and, here, is dictated primarily by which objective is used; all imaging was carried out using a 60× objective lens unless stated otherwise.

To calculate the Average background intensity,  $I_{\mu}^{BKD}$ ,

$$I_{\mu}^{BKD} = \frac{\Sigma I_{BKD}^{GUV}}{n} \quad \text{Eq. 3.2}$$

where  $\Sigma I_{BKD}^{GUV}$  is the total sum of the background fluorescence intensity and  $n$  is the total number of background sample.

The average background fluorescence intensity value is used to calculate the portion of a GUVs signal is contributed by background. Of course, this value is dependent upon the size of the GUV, the area for each of the GUV should be taken into consideration. Therefore, using the formula below, the background intensity is calculated for each of the GUV identified in the data set.

$$I_{BKD}^{GUV}(Data) = \frac{Area}{((P_x \cdot P_y)^2)} \times I_{\mu}^{BKD} \quad \text{Eq. 3.3}$$

The background intensity is then subtracted from the Raw Integrated Intensity before being corrected for the use of ND filters during measurements.

$$Corrected\ Raw\ IntDen = (Raw\ IntDen - I_{BKD}^{GUV}(Data)) \times ND\ filter\ value \quad \text{Eq. 3.4}$$

It is crucial to take in to account the contribution of the background fluorescence in analysing the data as it clearly influences the fluorescence intensity to a certain extent.

For instance, as seen in **Figure 3.17** which represents the fluorescence intensity against the volume of GUVs for a concentration of 100 μM of calcein, the non-corrected data shows a higher fluorescence value in comparison to the corrected data. Therefore, without considering background corrections, it is possible to overestimate the

fluorescence intensity of the resultant GUVs. Of course, it is important to consider uneven illumination and variations within and across fields that can lead to the need for more sophisticated methods of background correction. The variation in background across a  $20 \times 20$  (x mm  $\times$  x mm) was typically  $<10\%$ , measured as the relative standard deviation to the average background signal value. The area of the GUV is used to calculate the contribution of the background intensity and these errors will become compounded.

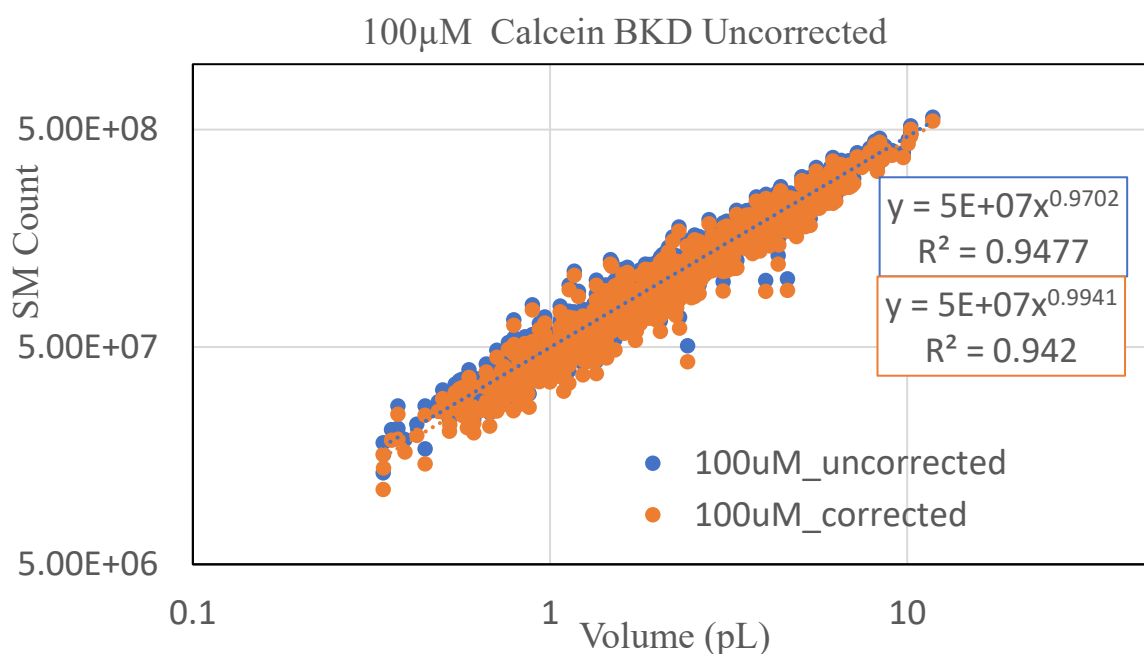


**Figure 3.17: The effect of background subtraction on the data.** The effect of the background subtraction on to the data. The GUVs with a lower volume are more affected by the background subtraction in comparison to that of a higher volume. This is because, at a lower volume, the fluorescence intensity is of a lower value overall, thus the contribution from the background may appear larger than that at a higher volume. ( $n=762$ )

### 3.4.2.2 Automated Fiji Analysis

Manual segmentation by trained users is generally relied upon as the most accurate approach to data analysis. However, it is time consuming and represents a major bottleneck in data analysis. Automated methods of image analysis were investigated, and their performance was determined by comparison with the results of manual segmentation, taken as the ground truth. Image J software (Fiji)<sup>89</sup> was used to obtain the fluorescence intensity and area of the GUVs. The image of interest was loaded in the programme before being thresholded and processed. Image thresholding binarises the 16-bit image using global thresholding methods. Global thresholding consists of setting the intensity threshold based on the histogram of the input image intensity. Typically, when signal to noise ratio (SNR) is sufficiently high, the intensity histogram should reveal two distinct peaks that correspond to the background (low intensity distribution) or objects of interest (higher intensity distribution), respectively. By setting the thresholding value, any pixels that have a value above the threshold are considered foreground pixels and, conversely, values below this level are considered background pixels. Three different methods that automatically calculate the threshold were tested. Apart from the thresholding value, the analyse particle feature in Image J also allows for the circularity and the diameter range to be predetermined. The circularity was set between 0.8-1.0 in which 1.0 indicates a perfect circle. The value of the circularity of the object in the image is calculated using the formula as shown in **Equation 3.5**. The size range of the objects to be identified was set between  $4 \mu\text{m}^2 - 66 \mu\text{m}^2$ .

$$\text{circularity} = 4\pi \left( \frac{\pi r^2}{(2\pi r)^2} \right) \quad \text{Eq.3.5}$$

The three different types of global thresholding methods were tested out were;

a) Huang's Thresholding

This thresholding method implements Huang's fuzzy thresholding using Shannon's entropy function.<sup>141</sup> The measure of fuzziness here represents the difference between the original image and its binary version. At a given threshold level, the fuzzy membership function is defined by the absolute difference between the pixel gray level and the average gray level of the region (foreground or background) in which it belongs to. The larger the difference, the smaller the membership value. The optimal threshold value would be when the fuzziness is minimised. This thresholding method works well with bilevel images, however, still fails for congested images as the clusters are still identified as one.

b) Otsu thresholding

This method is based on discriminant analysis. Otsu's thresholding method<sup>142</sup> involves iterating through possible threshold values and calculating the within class variance for the pixel levels on each side of the threshold, either in the foreground or the background. The purpose of this is to find the threshold value in which the sum of the foreground and background spreads is at a minimum. This method works well with images that have a bi-modal histogram. This is when an image has two distinct regions. In the presence of a high SNR ratio, it would be easier to distinguish the two regions. However, in the case of a congested images, the signal to noise ratio would be lower. The larger overlap between the background and foreground information would make it harder to find a threshold value, thus, increasing the error associated with this.

c) Maximum Entropy thresholding

This method is relatively similar to the Otsu thresholding technique however it follows the Kapur, Sahoo and Wong method.<sup>143</sup> Unlike the Otsu method which maximises the inter-class variance, the thresholding is done by maximising the entropy of the histogram of the image. In this context, entropy is a measure of the uncertainty of an event taking place. This value can be calculated in a straightforward manner from the histogram data.

The different threshold methods have a significant impact on the end results. The implementation of an overly harsh thresholding method could lead to the erosion the fluorescence intensity information mainly from the edge of the GUV. This could lead to an underestimation of the true size of the GUV, which then leads to undercounting both the volume and the area. When a line profile is drawn across a GUV, it is observed that the change in the signal is a gradual drop rather than a sharp increase and drop in the intensity as displayed in **figure 3.18**.

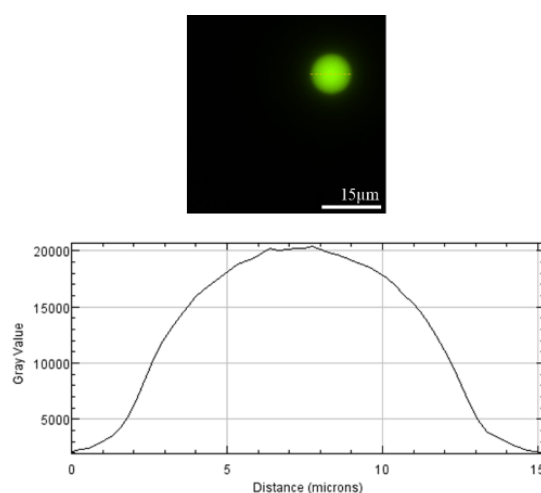


**Figure 3.18:** The figure above shows an exemplar GUV and the line profile of its fluorescence intensity.

The effect of the thresholding on to the wide field images were investigated using a cropped section of a wide field image. The three different thresholding methods were performed on each of the section and the resultant look up table (LUT) masks was overlaid on the original image. By performing this simple analysis, the harshness of each thresholding methods can be directly compared to the original image.

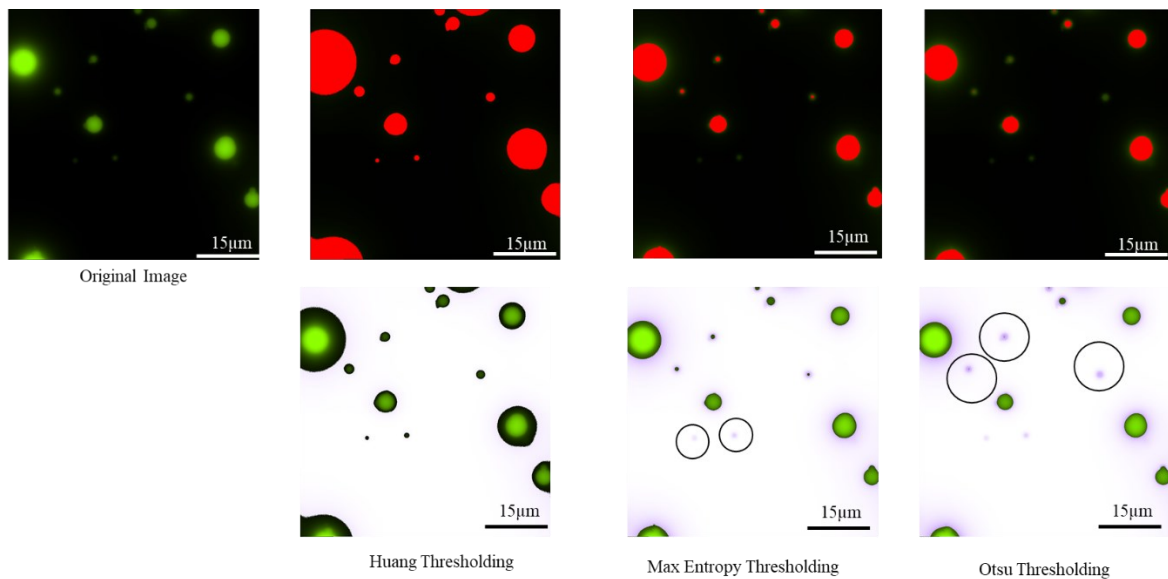


**Figure 3.19:** The comparisons of manual segmentation and the three different thresholding method. Here, it shows that the using Huang thresholding method may lead to an overestimation as indicated by the area beyond the perimeter of the GUV. For both Max Entropy and Otsu, an underestimation in the size of the GUV is noted. In some instances, artefacts that could have been a result of imaging is picked up by the thresholding method.

The use of Huang thresholding is observed to have overestimated the actual size of the GUV. When the LUT mask and the original image was overlaid on one another, the masks extend beyond the edges of the GUV, represented by the additional black area. The overestimation of the GUV area leads to the overestimation of the GUV volume as the volume is calculated with information obtained from the area of the GUV. In terms of the intensity measurement, this can lead to the overestimation of the fluorescence intensity as the background intensity is also taken into the measurement. However, this effect could be negated by background subtraction. With the use of Max Entropy

thresholding and Otsu thresholding, it is observed that the thresholding is significantly harsher. The overlaying of the masks and the original image show that it underestimates the size of the GUV. Both the intensity and size information are lost from the edges of the GUV. The purple ring surrounding the GUVs as seen in the image above shows the portions of each GUVs that do not overlay with the LUT mask. The exclusion of these areas leads to an underestimation of the GUV area, in turn the GUV volumes. It is also observed that from the two types of thresholding, GUVs that are smaller are excluded from the measurement all together. The type of thresholding selected has a relatively large effect on both the volume and intensity measurement.

Understanding how the type of thresholding can affect the quality of the information obtained from the data set can be presented using a line intensity profile of the GUV. For instance, taking an ideal case (**Figure 3.20 (a)**) into account, the thresholding method applied has no effect on the apparent size of GUV (**Figure 3.20 (b)**), however, in the case of the actual line profile that appears to be more of a bell curve, the level of thresholding effects the apparent size information.

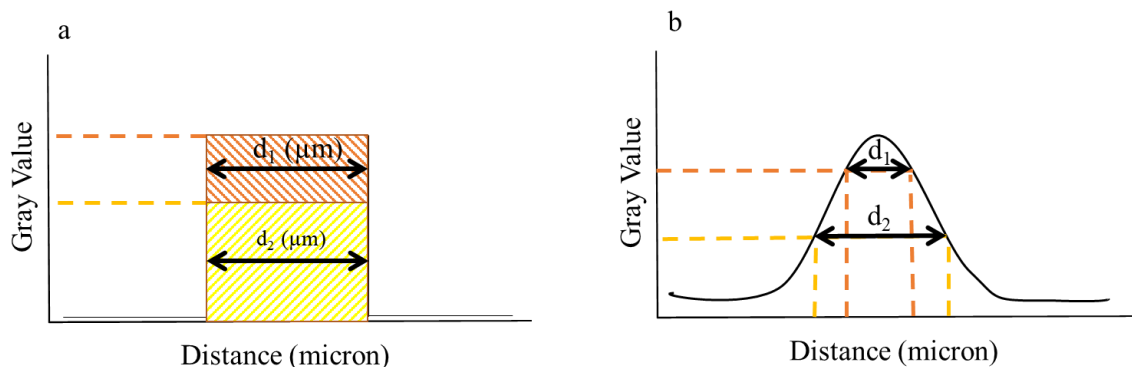


**Figure 3.20:** Level of thresholding that on two different scenarios. a) In an ideal scenario, where the signal to noise ratio is  $\gg 1$  and the angle is  $90^\circ$ , the apparent size measurements are irrespective of the intensity thresholding. b) In the case of a high signal to ratio with angle approaching  $90^\circ$ , the level of thresholding has an effect on the apparent size measurements.

However, the harshness of the thresholding levels affects vesicles of a low signal to noise ratio more than that of a higher signal to noise ratio. The angle of the curve,  $\theta$ , is an indication of the intensity of the signal. For vesicles with a high signal to noise ratio, the angle of the curve approaches  $90^\circ$  whilst for those with a lower signal to noise ratio, the angle approaches  $0^\circ$ . The illustration of the figure below shows the different cases and the effect of how different thresholding methods can affect the size information retained or lost. In both cases, the noise level is assumed to stay relatively same, as the variance of the background would be similar. The sensitivity on the non-ideal case is higher, therefore the thresholding would affect the data of the low signal to noise ratio more than the higher signal to noise ratio. The error of the low SNR ratio with respect to the size of the vesicle would be significantly higher in comparison. It is also important to note here that the GUVs of a higher signal to noise ratio is less sensitive thus is affected less by the harshness of the thresholding method. Therefore, it is crucial that the right thresholding method is selected to limit the loss of information especially in GUVs that are smaller.

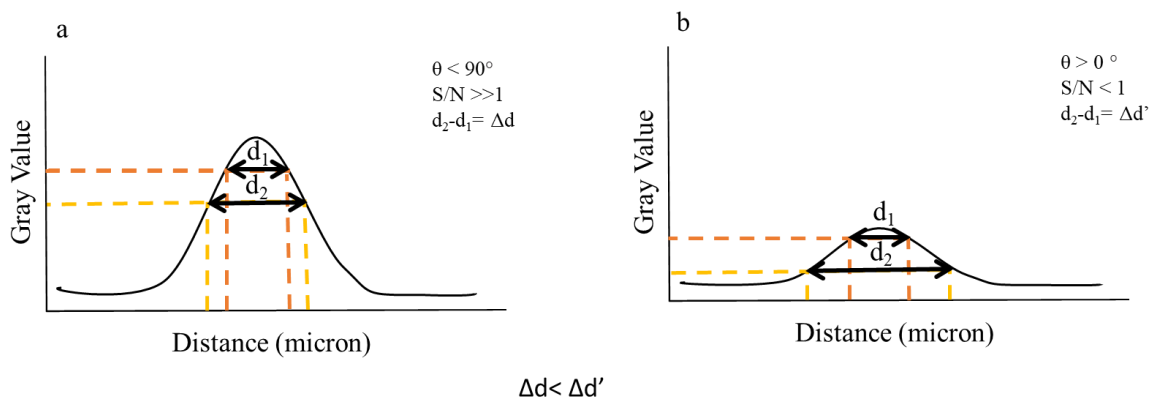


**Figure 3.21:** Intensity line profile used to demonstrate the effects of thresholding on two different scenarios of GUVs found in the dataset. a) High signal to noise ratio where the signal intensity of the GUV is significantly higher than the noise level. The thresholding has an effect on the apparent size measurement and is denoted by  $\Delta d$ . b) Low signal to noise ratio in which the signal intensity is close to the noise level thus making it more sensitive to the thresholding. The difference in the apparent size

*measurement due to the thresholding level is denoted by  $\Delta d'$ . As expected, the less intense GUV is more sensitive to the thresholding, hence, it may have a larger error in size measurements as a result.*

To fully comprehend how this affects the overall data analysis, we looked into how the underestimation or overestimation of the area, and as a result the volume of the GUV can have an impact on the dataset downstream. The error in the estimation of the area has a multiplicative effect on the volume is calculated as a function of the radius. To fully understand the effect of miscalculating the volume, a line profile of the GUV intensity is used to rationalise this as seen in **Figure 3.22**. The green circle illustrates the case in which a “perfect thresholding” method is employed. This would ensure the area and subsequently the volume is calculated correctly with minimal error. This would ensure majority of the fluorescence information to be captured. The red circle represents the case in which the area is underestimated due to harsh thresholding conditions. This leads to a much higher loss of real intensity measurement specifically at the edges of the GUV which will not be measured. With the overestimation of the volume on the other hand as illustrated by the blue circle, the additional intensity measurement that is considered will be lower. This is because the additional intensity measurement that can be partially accounted for by the background subtraction that is carried out during data analysis. This, therefore, leads to a significantly less increase in the intensity information upon overestimation of the volume in comparison to the previous case. However, both overestimating and underestimating the volume still play a role in the flattening of the gradient in the intensity vs volume graph of a wide field measurement. The deviation from the gradient is more pronounced at the lower volume and intensity. It is, therefore, crucial to select the most suitable thresholding method to avoid any loss of information that would affect the analysis down the line.

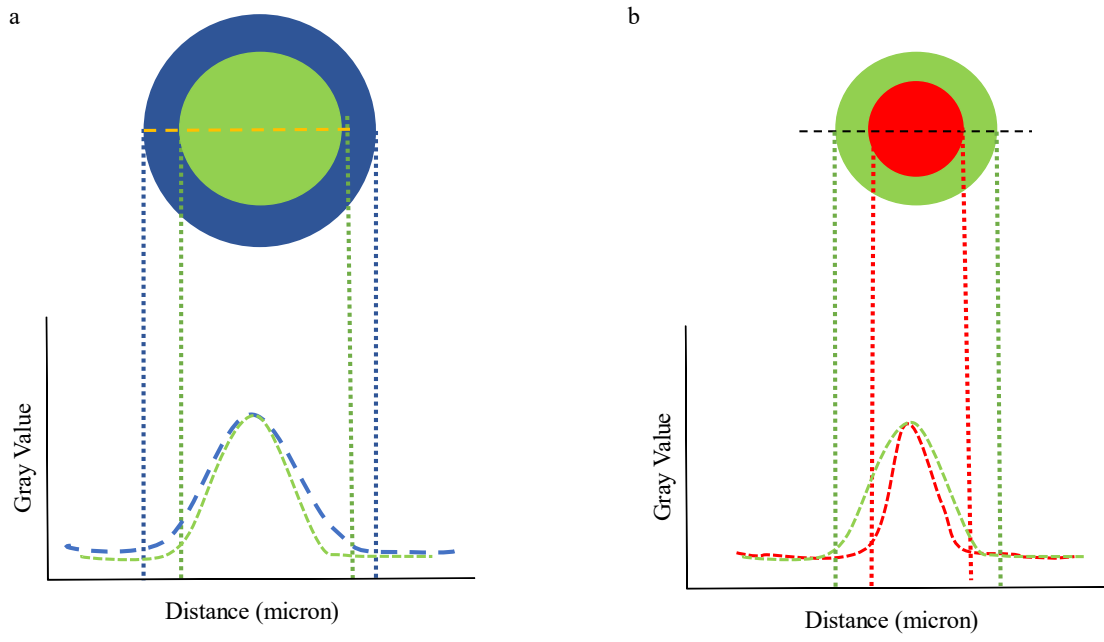


**Figure 3.22:** The illustration above exemplifies the effect of overestimating and underestimating the area of the GUV in relation to the intensity measurement. The image is a representation of a possibility of the data that would be obtained from the image analysis methods. The green circle and line correspond to a “perfect estimation” of the thresholding which would capture majority of the intensity information. a) The overestimation of the data set represented by the blue circle and line shows the fluorescence intensity and radius information obtained would not correspond with the ‘ideal estimation’. However, as fluorescence information of the true value would have been captured, the additional information would most likely be due to the background which can be corrected for. Overestimation therefore affects the size information more severely. b) The underestimation of the GUV would likely lead to a loss in both the fluorescence intensity information and size information as represented by the red dotted line and circle

### 3.4.2.3 Cell Profiler

Cell profiler is an open software tool that is normally used for cell imaging analysis, however, can also be applied for the purposes of this thesis. The first step requires the development of a cell profiler pipeline, which is a series of image processing modules in sequence. For the case of the images in this thesis, the analysis modules are outlined in **figure 3.23**. The settings for each analysis module can be tweaked accordingly for depending on the purpose of the measurement. Cell Profiler can also be run on a cropped test mode, which allows for only a section of the image to be analysed initially. For instance, the images that are fed for the full measurements are that of a  $20 \times 20$  tile scan. However, the inclusion of a crop analysis module, allows the image to be cropped down to a  $4 \times 4$  tile scan which is less time consuming especially when testing out various parameters to optimise the analysis method. This feature can be selected as and when needed.

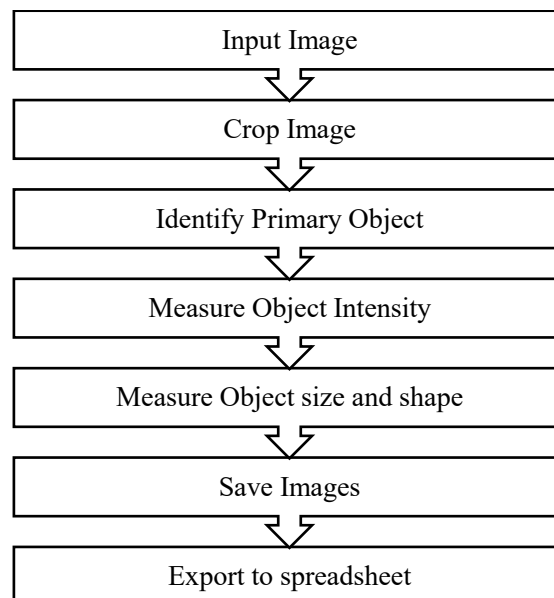


**Figure 3.23:** The figure above shows the analysis modules in the pipeline used in Cell Profiler. The pipeline was optimised to be used for large images such as the ones used in this thesis.

The first analysis module involves the identification of the primary objects within the image set. The module settings here allow for the diameter range (in pixel units) as well as the circularity of the object to be predetermined. This helps in the identification of the GUVs within a certain range to be detected. This function is particularly useful as it helps to distinguish the GUVs that are severely clumped together from individual GUVs. The clumped GUVs may not be considered; therefore, it does not affect the data analysis in understanding the relationship between the volume and fluorescence intensity.

The next analysis module is the intensity measurement. This module measures several intensity features across an entire image. The units of intensity within microscope images are typically described as intensity units or arbitrary intensity units. This is because the microscopes have not been calibrated to an absolute scale. The intensity units reported here are the integrated intensity units, which is a sum of all the pixel values whereas the mean intensity value is the mean of the pixel intensity within the image. A built-in function within the programme scales each pixel between 0-1 by the maximum possible intensity for the pixel in the image. Using the formula below, the maximum possible intensity of the pixel value can be calculated.

$$\textit{Maximum Intensity} = 2^{bpp} \qquad \textit{Eq. 3.6}$$

$$\textit{Maximum Intensity} = 2^{16}$$

$$\textit{Maximum Intensity} = 65536$$

where bpp denotes the bits per pixel value.

The images that are captured in this thesis are 16-bit images, hence the maximum possible intensity is 65536. To re-scale the intensity measurements, the corrected integrated density that is calculated is multiplied by this value. In theory, these values should correspond to a similar order of magnitude with the data obtained from the ground truth. The next analysis module measures the features of the GUVs, in this case, the area of the GUV is measured, and is used for further analysis. After inputting the settings in each of the analysis modules, the images are processed automatically, and the data is exported to a spreadsheet. The two main information that is used in the further analysis are the area of the identified GUVs and the raw integrated intensity.

It is important to note here that the measurement pipeline used in cell profiler has been largely optimised for large images such as the ones obtained throughout this thesis. However, it is there is a possibility of obtaining false positives using this analysis method. A possible source for false positives includes the inclusion of unseparated GUVs that still fall within the thresholding range in terms of size. This would not only affect the volume but also the fluorescence intensity.

### 3.4.3 Data Analysis Discussion

Wide field imaging was carried out as an initial step to understand the true distribution of sizes obtained from producing GUVs using Emulsion based phase transfer. Upon optimising the three different methodology of data analysis, the individual methods were tested out on a concentration series of both calcein and streptavidin. The key information obtained on each of the individual data sets are mainly the volume, calculated as a function of the area and the fluorescence intensity. The fluorescence intensity can be a quantitative measure of the number of molecules encapsulated within each GUVs that have been identified. The data set is presented as a volume (pL) against the fluorescence intensity graph.

As noted earlier, GUVs of a lower signal to noise ratio or smaller volume are more susceptible to both the thresholding and underestimation of the apparent size. It is important to understand the effect this has on the data analysis. **Figure 3.24** is an exemplar plot of the volume vs intensity measurement of the data analysis.

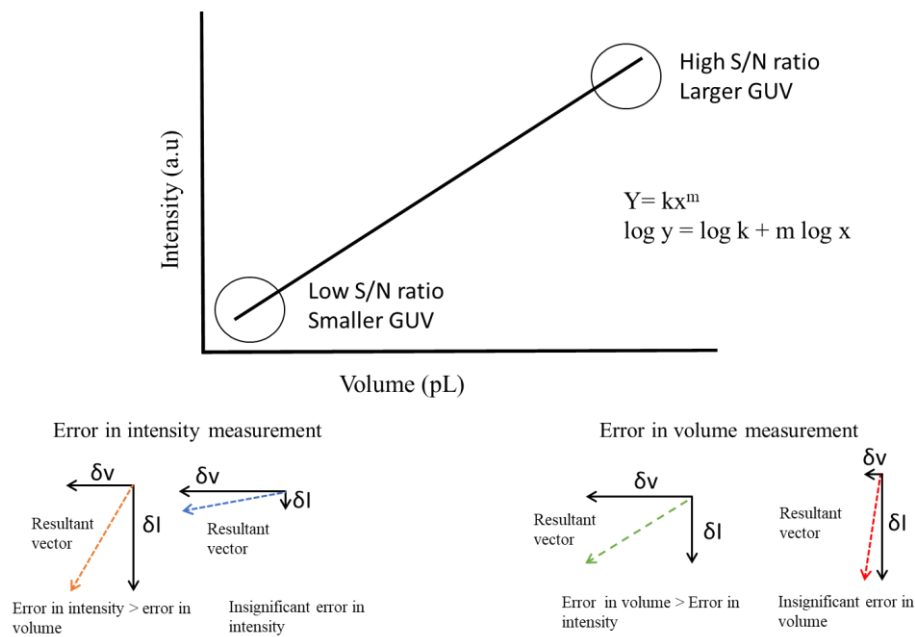


**Figure 3.24:** An illustration of the graphical representation of the information obtained from the data analysis. The equation represents the relationship between the volume and intensity. The change in the position of a particular data point along the graph due to the errors can be presented as a unit vector. The four different scenarios indicate the contribution of the error on the data set.

At the higher end, the measurements are less prone to errors, therefore minimising the change or tilt in the gradient of the line. However, at the lower end, the line can either tilt upwards or downwards depending on which parameter is affected by the error in segmentation. The change in both the volume and intensity can be presented as a unit vector. The tilt of the graph away from the ground truth would be of the movement along the resultant vector. Using this, several scenarios are outlined below to illustrate the effect it has on the tilt of the line.

In the case where the signal to noise ratio is low, the underestimation of both the area and intensity may lead to a more significant shift in the graph. For instance, in the case where there is an equal contribution of each of the error, the relative impact on the area and intensity measurement is equal. Therefore, the gradient of the line remains the same as the distribution is stretched along the line as illustrated in **figure 3.25(a)**. In the case

where a significant error is affects the volume measurement with insignificant error on the intensity measurement, the line tilt upwards, hence flattening the gradient. (**Figure 3.25(b)**). An overestimation in the volume of the GUV under these circumstances could lead to a significantly higher error in the volume comparatively to the error on the intensity measurement. This causes a downward tilt on the line, deviating away from the possible truth with the gradient becoming increasingly steeper as illustrated in **figure 3.25(c)**

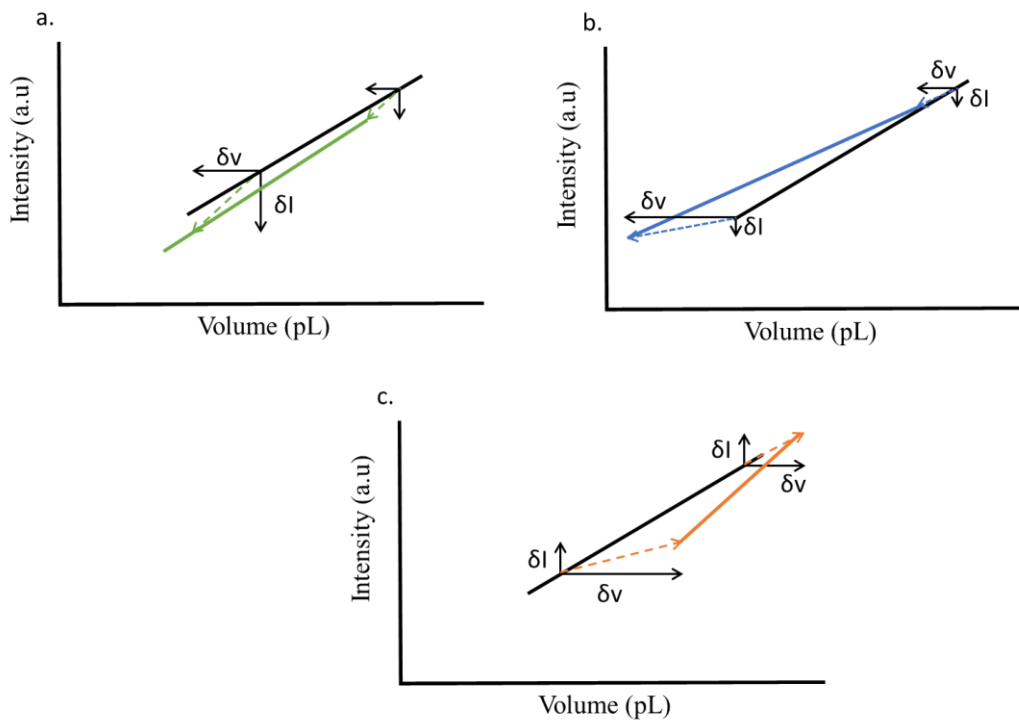


**Figure 3.25:** The effect of the errors in both the volume and intensity measurements on the GUVs with a low signal to noise ratio. a) An equal error contribution of the errors has an equal impact on the area and intensity measurement, therefore stretching the data along the true distribution. b) In the case of where the underestimation of the volume leads to a higher contribution of error by the volume causes the gradient of the line to flatten as it tilts upwards. c) The overestimation of the volume of the GUVs in which the contribution of error in the volume is more significant leads to a downward tilt, shifting the gradient closer to 1.

Prior to performing the data analysis on the wide field images, the three different methods were tested out using individually isolated GUVs, mimicking an ideal environment in which the vesicles would be well separated from one another. In this

case, the ground truth is built using information from both the bright field and fluorescence images. Manual segmentation was performed on only the fluorescence images of the individual GUV images. The parameters for the automated Fiji Filters and Cell Profiler are outlined in the table below.

**Table 3.1:** Parameters of the automated data analysis technique.

	<b>Automated Filter</b>	<b>Fiji</b>	<b>Cell Profiler</b>
<b>Area (pixel units)</b>	15-750	<b>Diameter (pixel units)</b>	15-250
<b>Circularity</b>	0.8- 1.0	<b>Circularity</b>	1.0

A graph of the volume (pL) against the fluorescence intensity was plotted for each of the measurement methods (**Figure 3.26**). It was shown that both the manual segmentation and Otsu thresholding method was in close agreement with the ground truth. Cell profiler, a commonly used image analysis tool is shown to severely overestimate the volumes of the GUV as with Huang and Max Entropy. A statistical analysis calculating the mean, variance and standard deviation of the different methods was performed to look at the degree of variation from the ground truth. With reference to **table 3.2**, Otsu and manual segmentation had the closest mean of 2.0942 pL (4.38% difference) and 2.3518 pL (17.22% difference) respectively to the ground truth. The standard deviation of the data obtained using manual segmentation showed that the spread of the dataset was similar to the ground truth with a difference of 12%. However, with Otsu, the data is a little more spread out in comparison with a standard deviation

of 4.3760 pL as opposed to 3.3188 pL of the ground truth. From the statistical analysis performed, it was clear that using the Huang thresholding method leads to a large deviation away from the ground truth. Both the mean and the standard deviation deviates significantly away from the ground truth. The difference of the mean is almost 10 times whilst the spread of the data as observed from the standard deviation is also around 8 times larger.

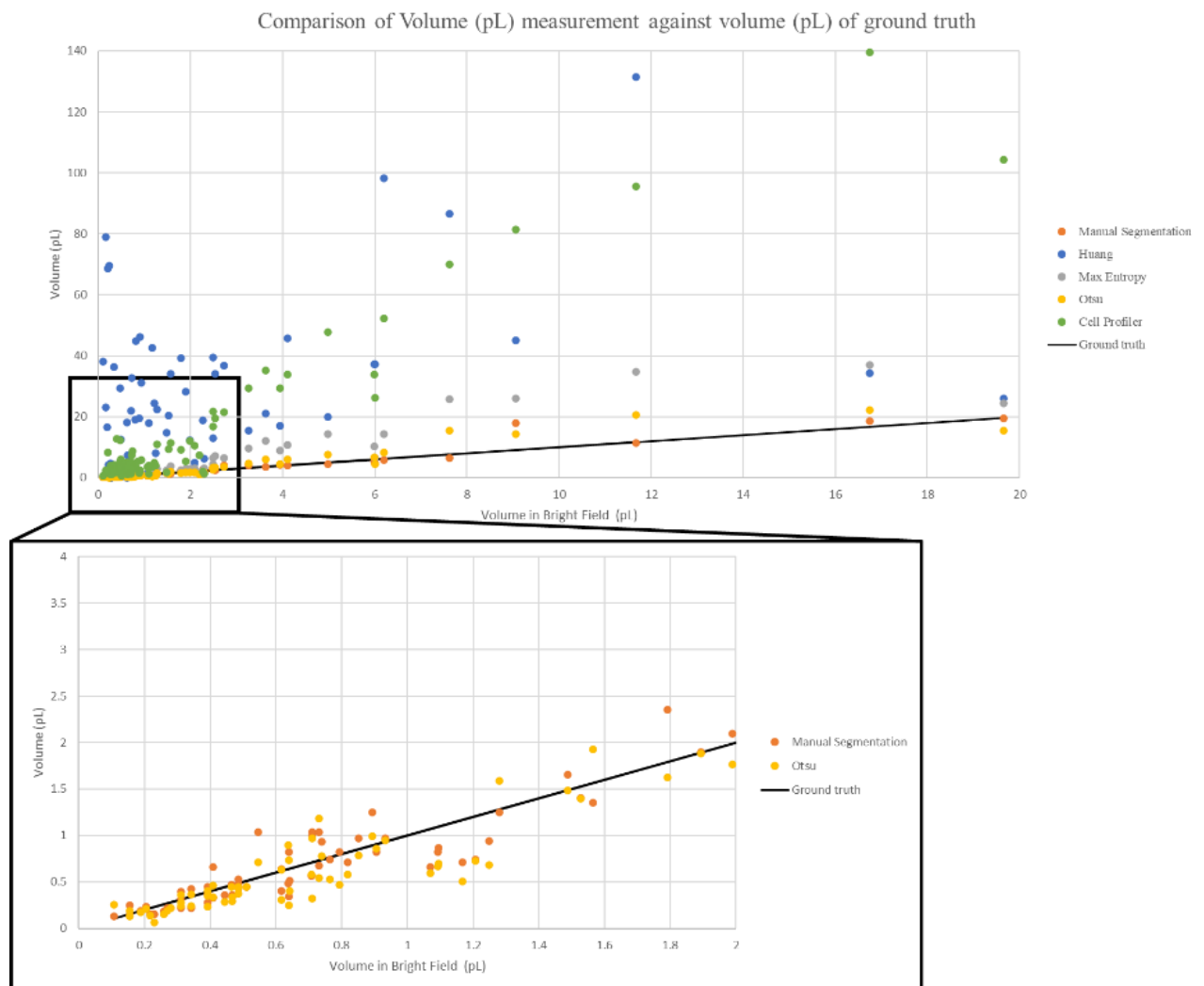


**Figure 3.26:** Graph of volume measured using different data analysis method against the calculated volume from the ground truth. The perceived ground truth here is obtained from measuring the area of the vesicles from the bright field images. ( $n = 82$ ) The inset shows a close up on the data points analysed using manual segmentation techniques and Otsu thresholding method. Both these techniques seem to

be in close agreement with the ground truth. Upon statistical analysis of the data, it was found that the mean of the data obtained from manual segmentation had a 4% difference with the mean of the ground truth, whilst when using Otsu, there was a 17% difference. The standard deviation of the data obtained using Otsu, indicated that the data was more spread out than both manual segmentation and the ground truth.

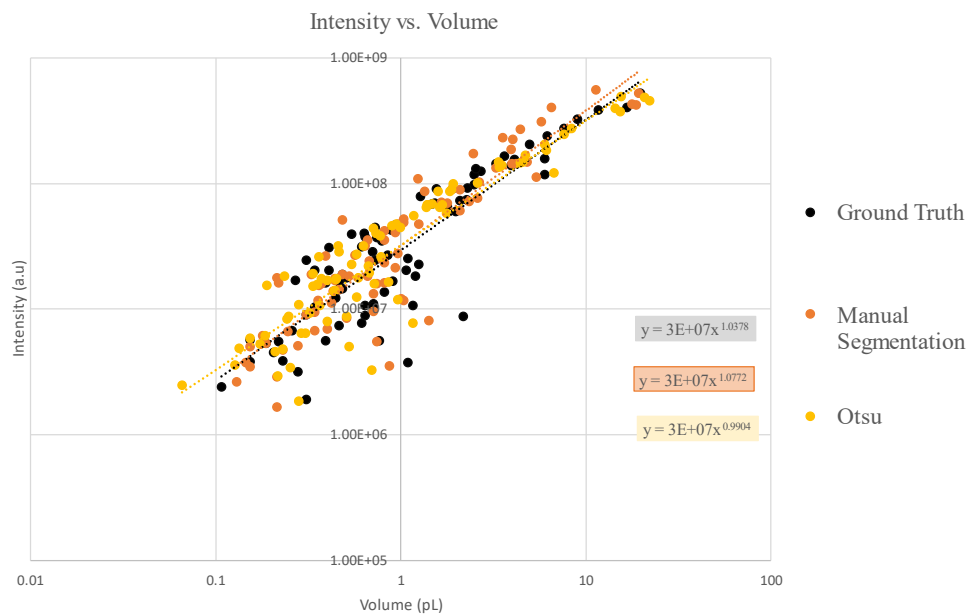
**Table 3.2:** Calculated mean, variance and standard deviation values of the volumes that were measured using information obtained from each of the data analysis method.

Method	Mean	Variance	Std deviation
Ground truth	2.0063	11.0147	3.3188
Manual Seg	2.0942	13.8468	3.7211
Otsu	2.3518	19.1490	4.3760
Max Entropy	4.0753	54.8372	7.4052
Cell Profiler	13.8275	613.7206	24.7734
Huang	20.7614	615.2403	24.8040

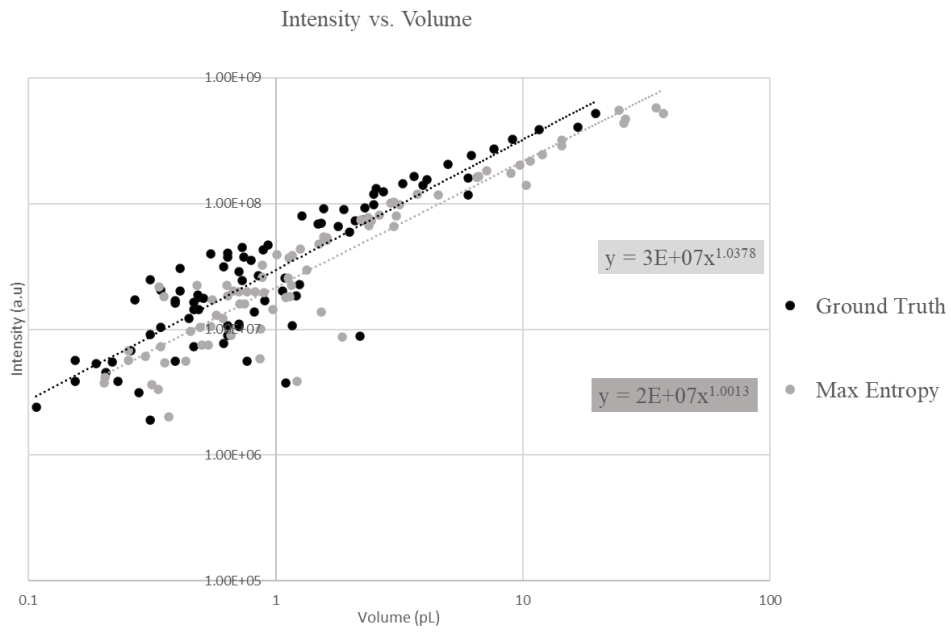
Using the volume and intensity information obtained using the different methods, a graph of these variables was plotted against one another as seen in **Figure 3.27**. Each of the individual methods perform relatively well for the GUVs on the larger end with the exception of the Huang thresholding. In the case, of Otsu and Manual Segmentation, the graphs closely overlap with one another, indicating that these methods may possibly be the most accurate in understanding the overall distribution of the GUVs. However, this data is representative of an ideal scenario in which the GUVs are well separated. Huang thresholding on the other hand severely overestimates the volume and in turn the intensity measurements of the GUV. At the higher end, however, the overestimation

of the volume contributes at a higher extent to the deviation away from the ground truth. The tilt at the lower end is a result of possible underestimation of some GUVs. This leads to an undercounting in the fluorescence intensity, hence shifting the line of best fit upwards. However, as the majority of the sample is severely overestimated, the combined effect of these both cases cause the flattening of the gradient instead of the gradient becoming steeper. The use of CellProfiler on the data set leads to the overestimation of the volume as well. Once again, the overestimation of the volume plays a more significant role in the deviation away from the ground truth.

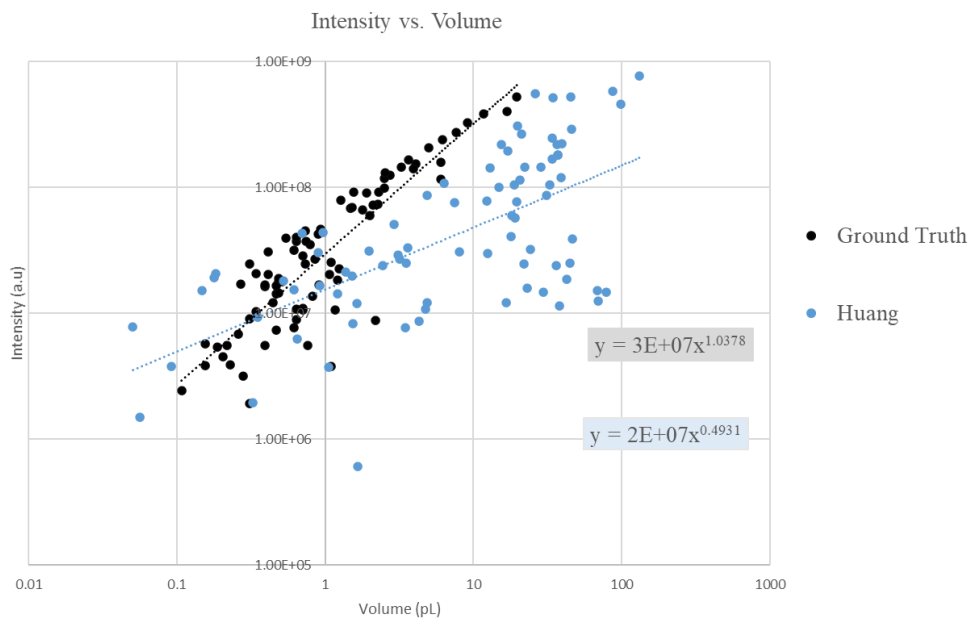
a



b



c



d

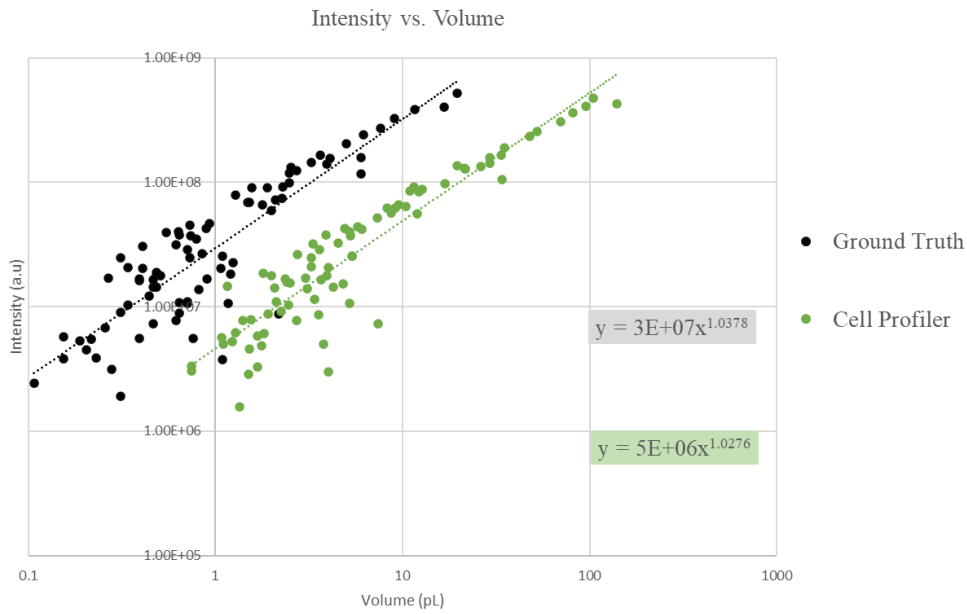


**Figure 3.27:** Graphs of the intensity against volume of each of the method. The resultant graphs were compared against the ground truth and the manual segmented data.

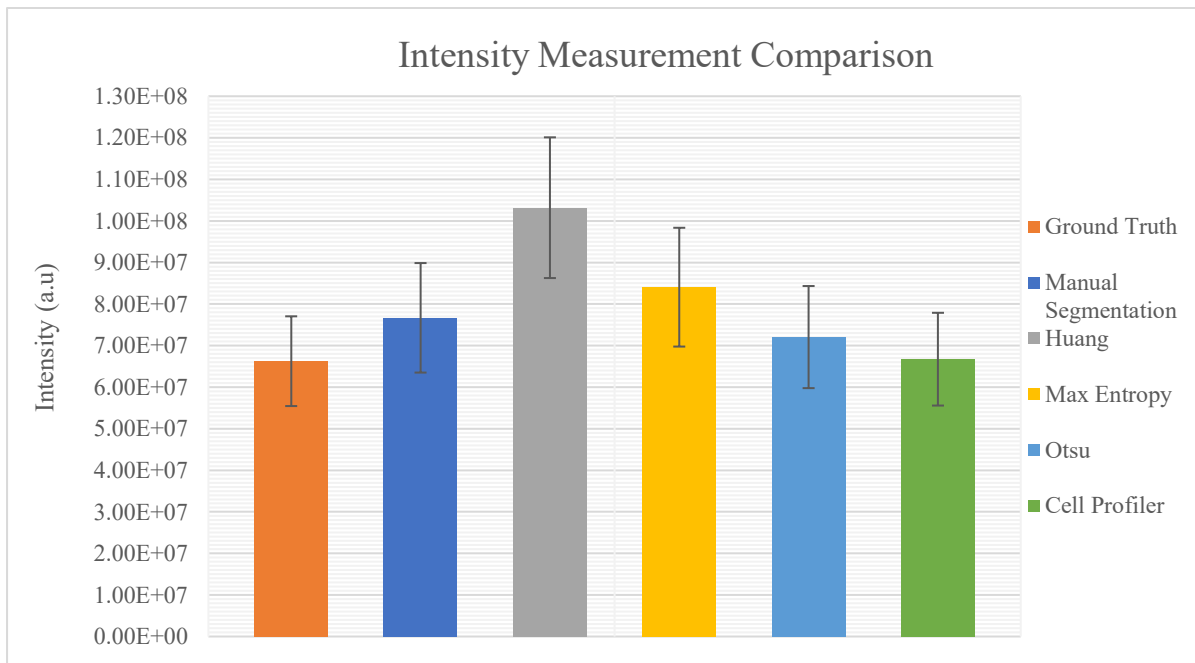


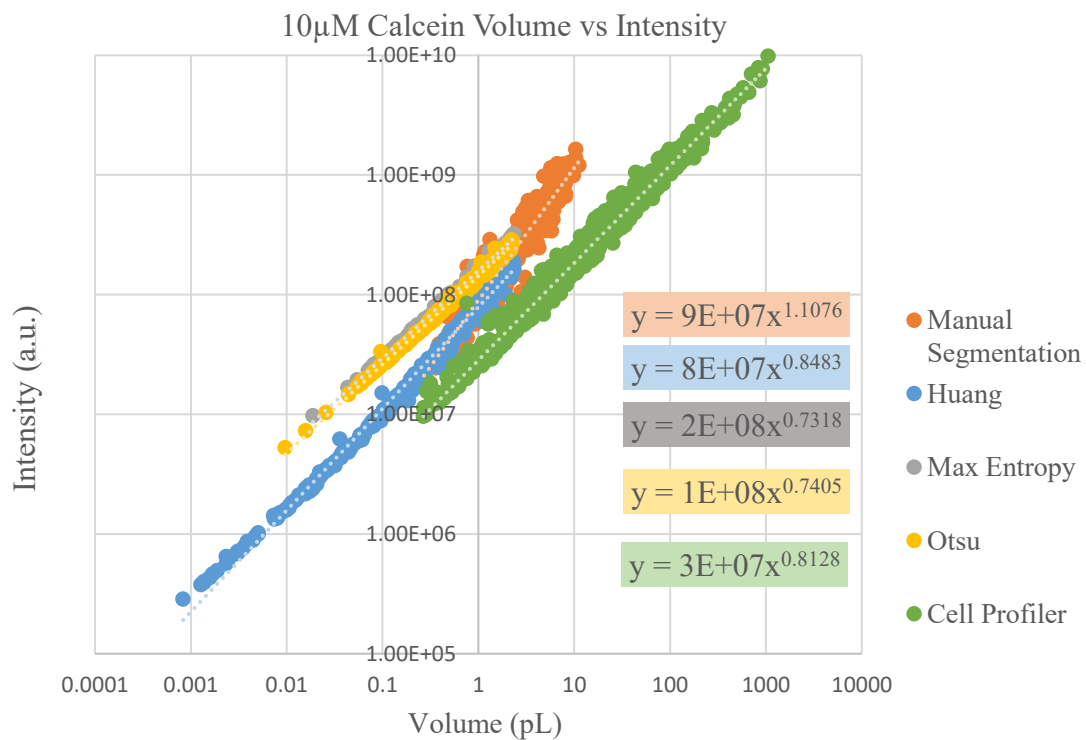
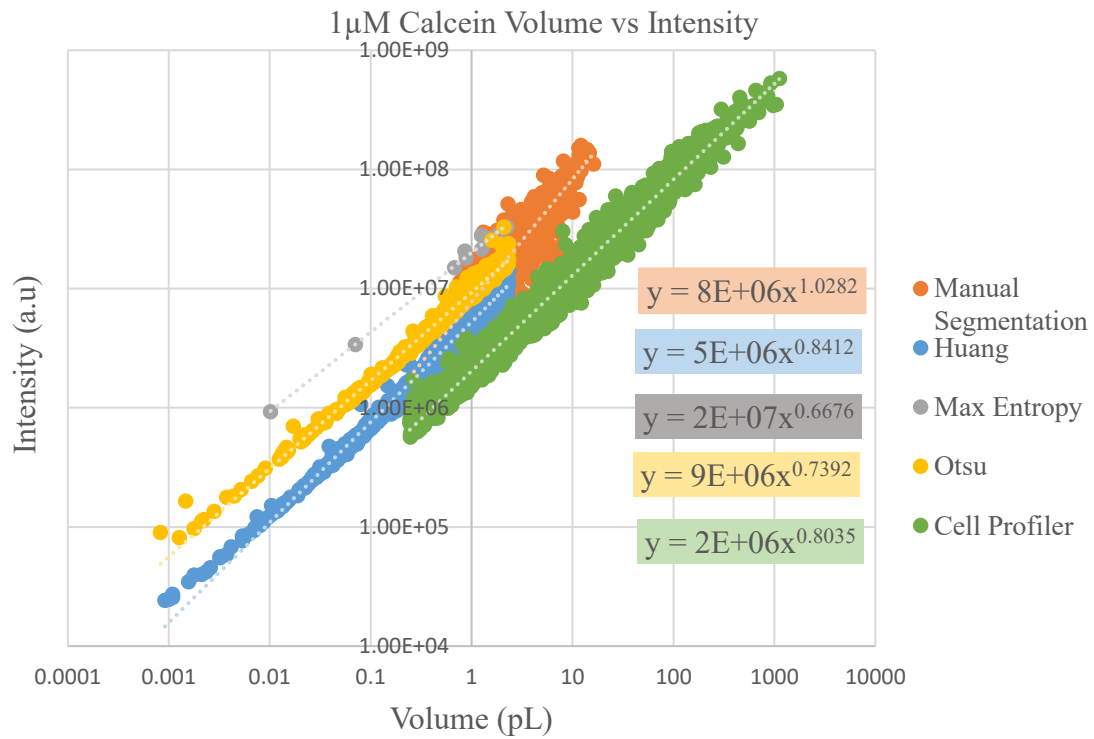
**Figure 3.28:** The comparison of the fluorescence intensity measurement obtained from the different data analysis method (n=82). Cell Profiler is shown to be closest to the ground truth followed by Otsu and Manual Segmentation. This indicates that any possible deviation from the ground truth is could be primarily due to the error in size estimation.

The comparison of the intensity measurement for each of the analysis methods show that Cell Profiler is effective in discriminating between the signal in the foreground and background. The deviation away from the ground truth could either be a result of the overestimation of the area or a calibration issue.

#### **3.4.3.1 Calcein**

From the individual GUV data set, it was shown that the manual segmentation method and Otsu thresholding method were in close agreement with the ground truth. To further investigate this, wide field data sets were analysed using all 5 different methods. GUVs

were produced with a logarithmically varying concentration of calcein encapsulated within it. The concentration range of calcein used were 1, 10 and 100 $\mu$ M.



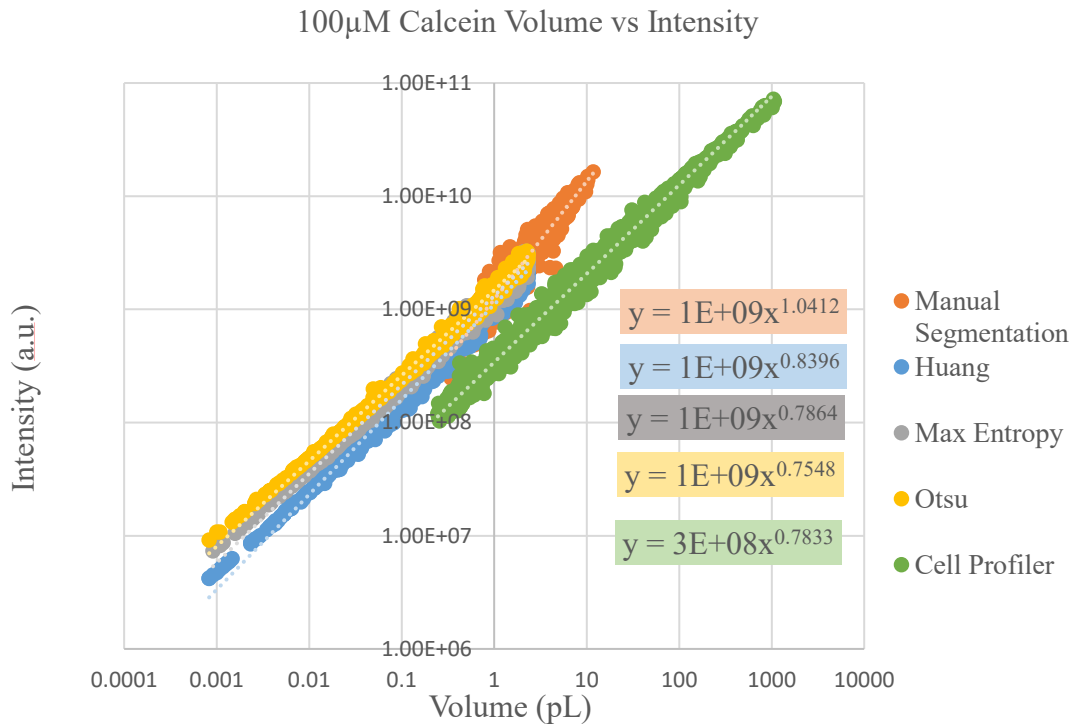


**Figure 3.29:** Graph of Volume vs Intensity of 1, 10 and 100 $\mu$ M calcein. The automated Fiji Filters under segment a significant portion of the data leading to the extension of the data points on the lower end of the data. The intensity measurement however is preserved with the Y-intercept within the same order of magnitude. Cell Profiler on the other hand over segments the GUVs leading to an extension of the data points on the higher end. The over estimation of the GUV area leads to the overestimation of the GUV intensity of at the higher end.

The graph in **figure 3.29** shows the results of the distribution of all three concentrations. At face value, the results here seem to indicate the different thresholding methods have minimal deviation away from the ground truth. However, upon closer inspection, it is observed that though the y-intercept of the different thresholding are in close agreement, there is a significant amount of deviation away from the ground truth in terms of the tilt of the gradient. Using the automated Fiji Filters, though Otsu performed relatively well in the well isolated GUVs, this does not seem to be the case with wide field images. Though the measurements partially overlap with the ground truth, at the lower end however, both Huang and Otsu detect objects almost two orders of magnitude smaller. This could possibly be where this method fails in discriminating seemingly small objects that may only be an artifact in the image rather than an actual vesicle. This

additional stretch at the backend of the graph contributes to the tilt in the gradient away from the ground truth.

The tilt in the gradient of the graph is most likely due to the mis-segmenting of the GUVs. For example, clumped GUVs that have well defined edges can be analysed using either manual segmentation or the automated data analysis methods. The techniques would be able to evenly segment the GUVs whilst retaining both the size and intensity information. However, in the presence of GUVs with less defined edges, the uneven segmentation of the GUVs has a significant effect on the volume against intensity graph especially when using automated data analysis methods. In the first case, **(Figure 3.30b(i))**, the overestimation of the area (i.e. the volume) of the GUV on the left side would lead to a much larger deviation of the volume from the ground truth compared to the intensity measurements. As the vesicle has a higher intensity measurement to begin with, the additional intensity information may seem less significant compared to the additional area information that is measured. Therefore, the tilt in this case would predominantly be due to an error in the size. The underestimation of the area of the GUV with the lower intensity also leads to a deviation in the volume that is more significant in comparison. The combined effect leads to a tilt in the gradient on the graph.

In the second case, **(Figure 3.30b(ii))**, the underestimation of the area (i.e the volume) of the GUV on the left side would lead to a large deviation in both the volume and intensity measurement from the ground truth . The loss of both the intensity information and area information in this case would be more significant due to its asymmetry. The overestimation of the area of the GUV with the lower intensity however leads to a

deviation in the volume and intensity that is much more significant in comparison. The combined effect leads to a tilt in the gradient on the graph.

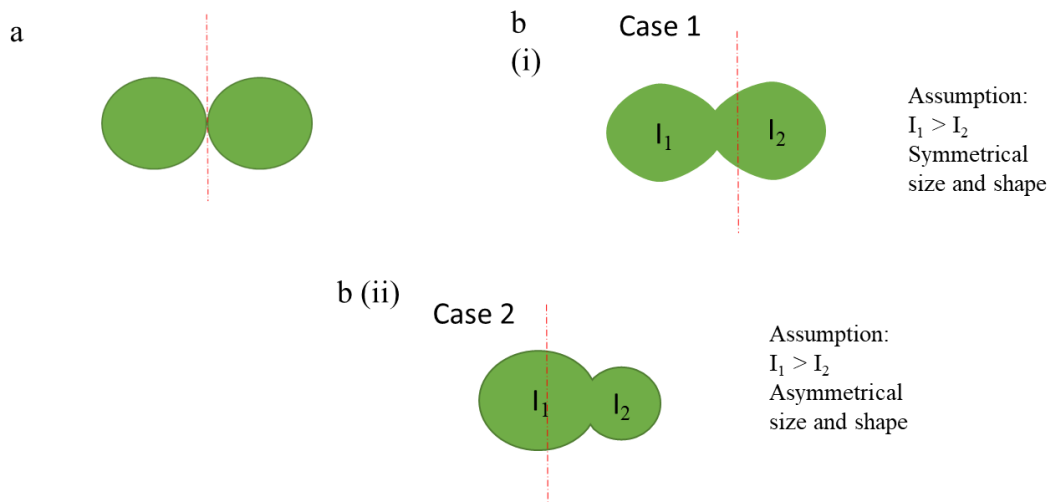


**Figure 3.30:** Exemplar illustration on how the data can be analysed and interpreted using the automated data analysis methods. a) In the case of an even segmentation, in which the perimeter of the GUVs is clearly defined, maximum area and intensity information is retained. b) The appearance of the GUV in which i) The GUVs are symmetrical with an uneven distribution of the intensity. The incorrect segmentation of the vesicles leads to a tilt in the gradient of the graph. The contribution of the error in the size measurement would be more significant in comparison to the error in the intensity measurement. ii) The GUVs are asymmetrical with an uneven distribution of the intensity. The incorrect segmentation in this case would lead to a tilt in the gradient, with a larger contribution from the vesicle on the left in comparison.

The comparison of the average values of the intensity and volume between the ground truth and the different data analysis method show that the deviation of the data from the ground truth using Cell Profiler is largely contributed by the error in the volume. Whilst using the different automated Fiji filters, the difference between the two difference is within the same range. This could be an indication that the deviation of the data using

these methods is due to a combined contribution from both the volume and intensity measurements.

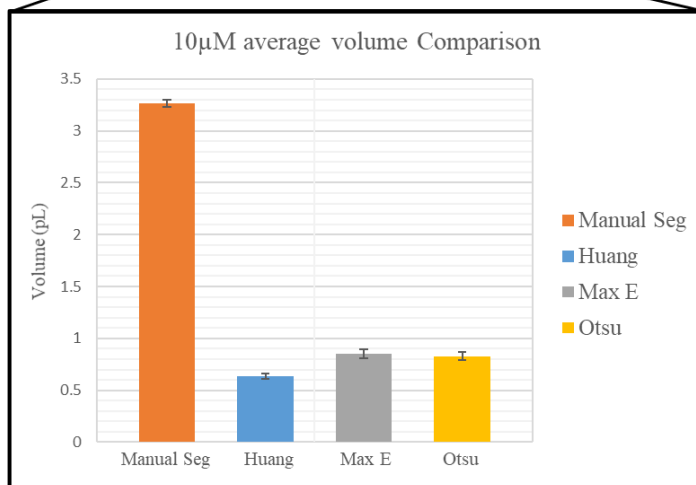
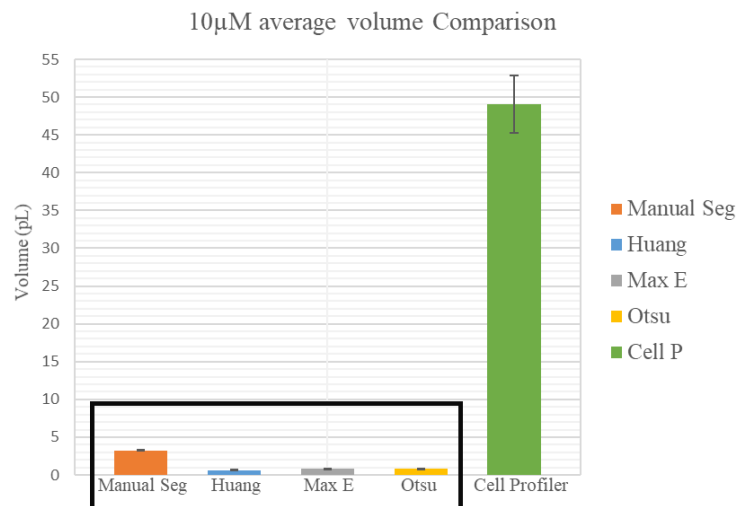
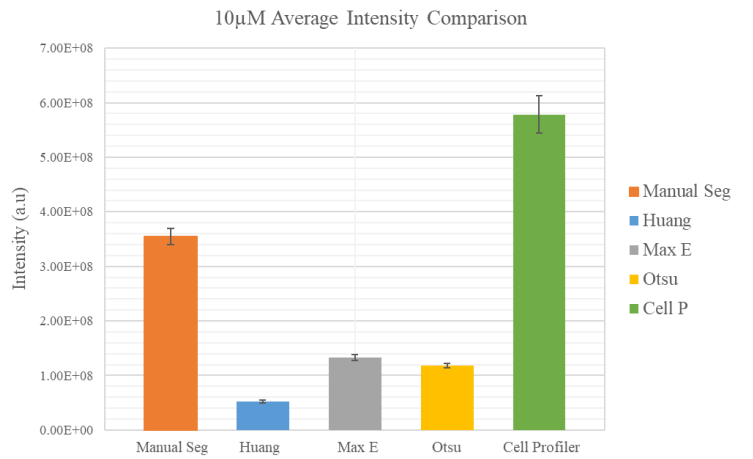


**Figure 3.31** *The average intensity and volume comparison of 10  $\mu$ M Calcein data. The average values here show that using Cell Profiler when compared to the ground truth, the average volume of the data is almost 15 times higher, however, the difference between the average intensity is only about 1.6 times higher. With the automated Fiji Filters, the difference between the average intensity value and the difference between the average volume values are with 20-30% of the ground truth values (Manual Segmentation n=438, Huang n=471, Max Entropy n=202, Otsu n=252, and Cell Profiler n=796)*

The results of CellProfiler measurements on the other hand, shows a larger overlap with the results of the manual segmentation, however, is stretched further along the higher volume end. This could most likely be due to the over segmentation of clumped GUVs within the data set. For instance, using manual segmentation, these GUVs are picked out only if the edges can be properly defined. In the case that the edges are not as defined they are not considered. However, with cell profiler, the algorithm segments the GUVs into smaller areas, leading to the data being stretched out over a larger range on the lower end. An example as illustrated in **figure 3.32** show how the algorithm in Cell Profiler segments the clumped data. When using manual segmentation, the GUV would have been discarded due to its close proximity with clumped objects. The intensity of the GUV would have severely been affected by the halo surrounding the other GUVs. However, using cell profiler, the GUVs are segmented in to three separate areas. One half of two separate GUVs within the clumped clusters near the border of the two tiled images is considered as one. At the larger end of the data, the clusters are segmented a large GUV. This contributes to the phantom larger volume GUVs, as well as high intensity measurements. This further strengthens the choice of selecting manual segmentation as the preferred choice to analyse the remaining data, as it is able to retain as much information as possible with minimal error.

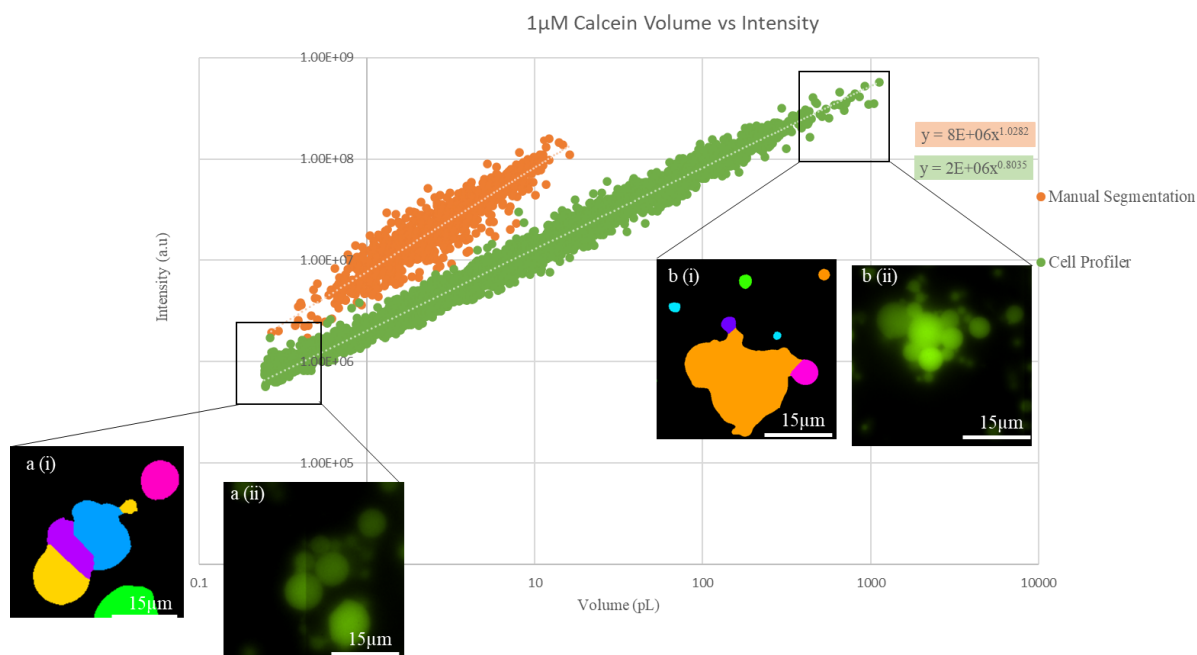


**Figure 3.32:** Graph of volume vs Intensity of 1µM Calcein using comparing CellProfiler and Manual Segmentation. ai) The mask produced by Cell Profiler showing the over segmenting of clumped GUVs adding to phantom small volume vesicles. ii) The corresponding fluorescence section of the segmented area. b(i) The mask produced by Cell Profiler showing the under segmenting of a clumped GUVs in which the cluster of GUVs is considered as one giant vesicles, adding to the phantom large volume vesicles. ii) The corresponding fluorescence image of the imaged section.

A comprehensive analysis of the different thresholding methods demonstrated that manual segmentation is the most optimum approach to analyse a wide-field fluorescence image. The relationship between the GUV volume and total fluorescence intensity was found to be a linear positive correlation as described in **figure 3.33**. As expected, each of the line adopts an upwards gradient, with a ten-fold increase between each of the line. The total fluorescence intensities and volume were normalised and plotted in a histogram to demonstrate a similar gamma type profile for each system. The apparent linear relationship of the plotted logarithmic data suggests that to a degree, as defined by the variation, the concentration of the calcein within the vesicles maybe inferred to be constant. However, as the value of the fluorescence intensity are measured

in arbitrary units, a relative measurement cannot be provided. It is, therefore, not possible to calculate an absolute value for the concentration of the encapsulated calcein within the GUVs. This in extension does not allow the encapsulation efficiency to be determined.

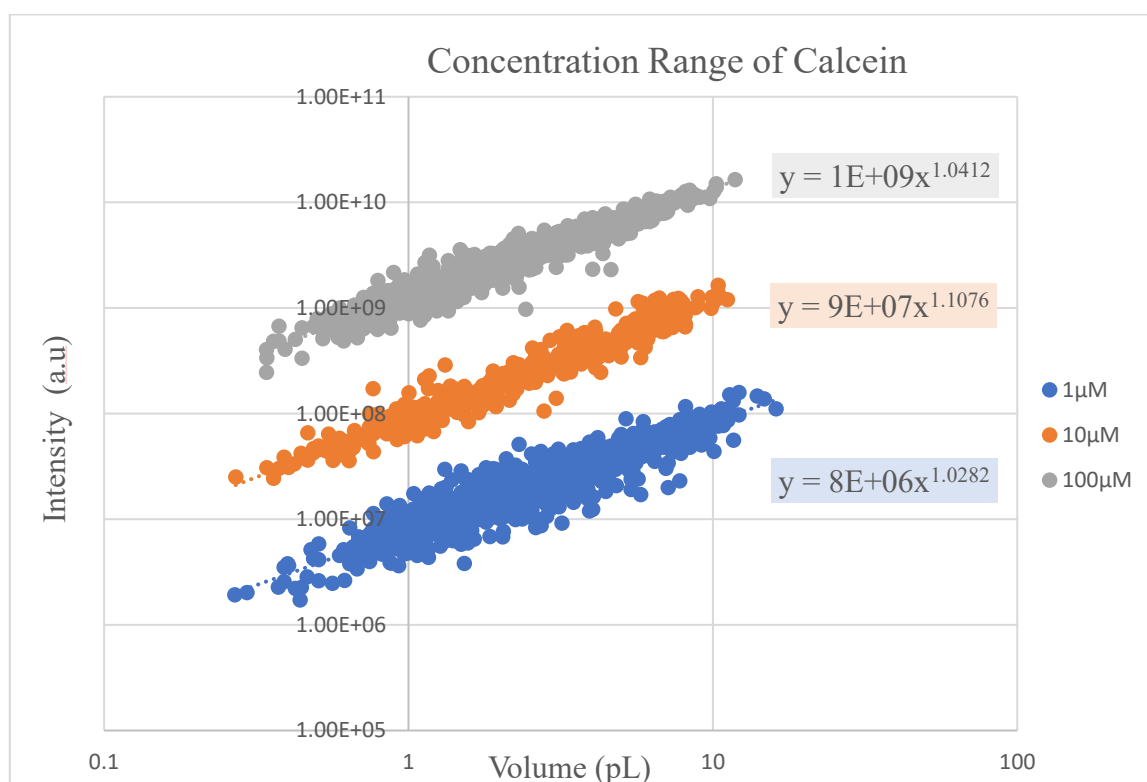


**Figure 3.33:** Assessment of GUVs with logarithmically increasing concentrations of Calcein a) Manual segmentation of individual GUVs to measure the diameter, in which the volume is calculated and total fluorescence. The gradient of each of the lines indicate a positive correlation between the GUV volume and encapsulation efficiency with a constant concentration.

### 3.4.3.2 Streptavidin

The data analysis methods were repeated with GUVs containing a varying concentration of streptavidin between  $10^4$  molecules  $\text{pL}^{-1}$  to  $10^6$  molecules  $\text{pL}^{-1}$ . Streptavidin, a biotin binding protein in this case is tagged with an AlexaFlour-488 fluorescent tag is commonly used in a variety of molecule specific detection as well as in western blotting, flow cytometry, and microscopic imaging.

Using streptavidin as the choice of molecule encapsulated in the internal solution of the vesicle, the data analysis methods were examined to assess the accuracy of these methods. Similarly, to Calcein, we expect the data analysis methods to perform in the same manner. The use of automated Fiji filters once again deviates away from the ground truth. The use of cell profiler to analyse the data also shows the same behaviour in which the data stretches out on the higher end of the volume indicated in **figure 3.35**.

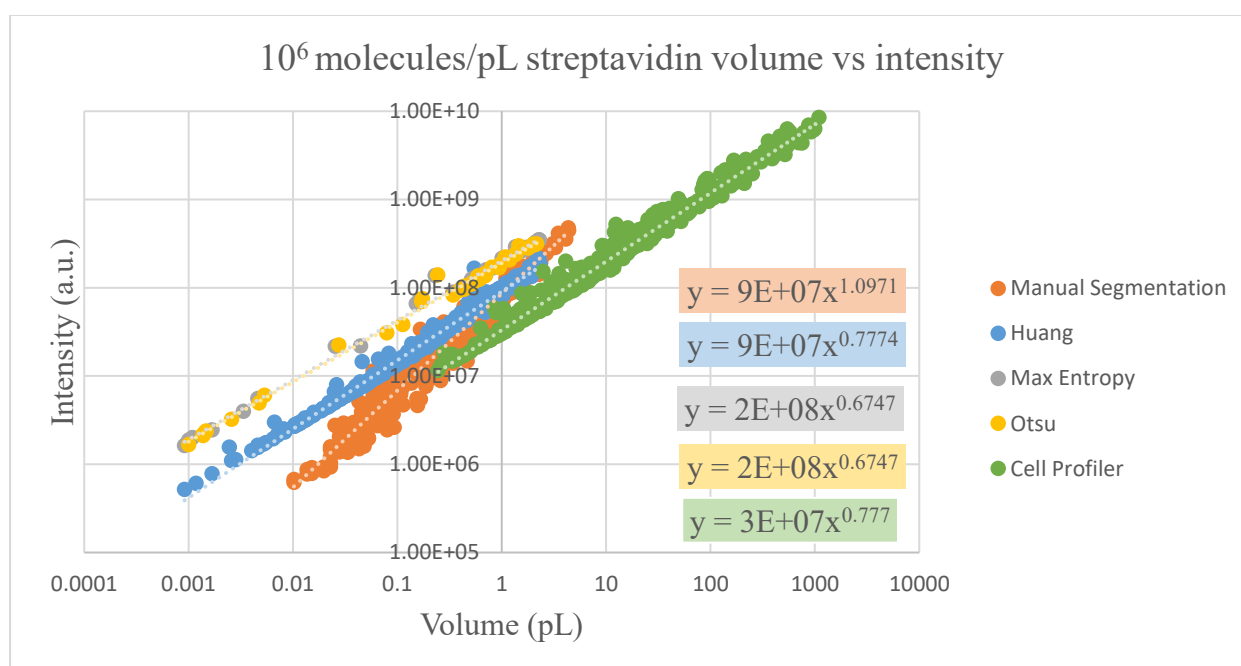


**Figure 3.34:** Assessment of GUVs encapsulated with  $10^6$  molecules  $pL^{-1}$  using the different data analysis methods. The automated Fiji Filters under segment a significant portion of the data leading to the extension of the data points on the lower end of the data. The intensity measurement however is conserved with the Y-intercept within error. Cell Profiler on the other hand over segments the GUVs leading to an extension of the data points on the higher end. The over estimation of the GUV area leads to the overestimation of the GUV intensity of at the higher end.

As expected, the data behaves similarly to the calcein data. Manual segmentation was used to analyse the wide field fluorescence images of the varying concentration of the streptavidin encapsulated GUVs. The graph in **figure 3.34** shows the relationship between the volume calculated as a function of the radius of the vesicles and the fluorescence intensity.

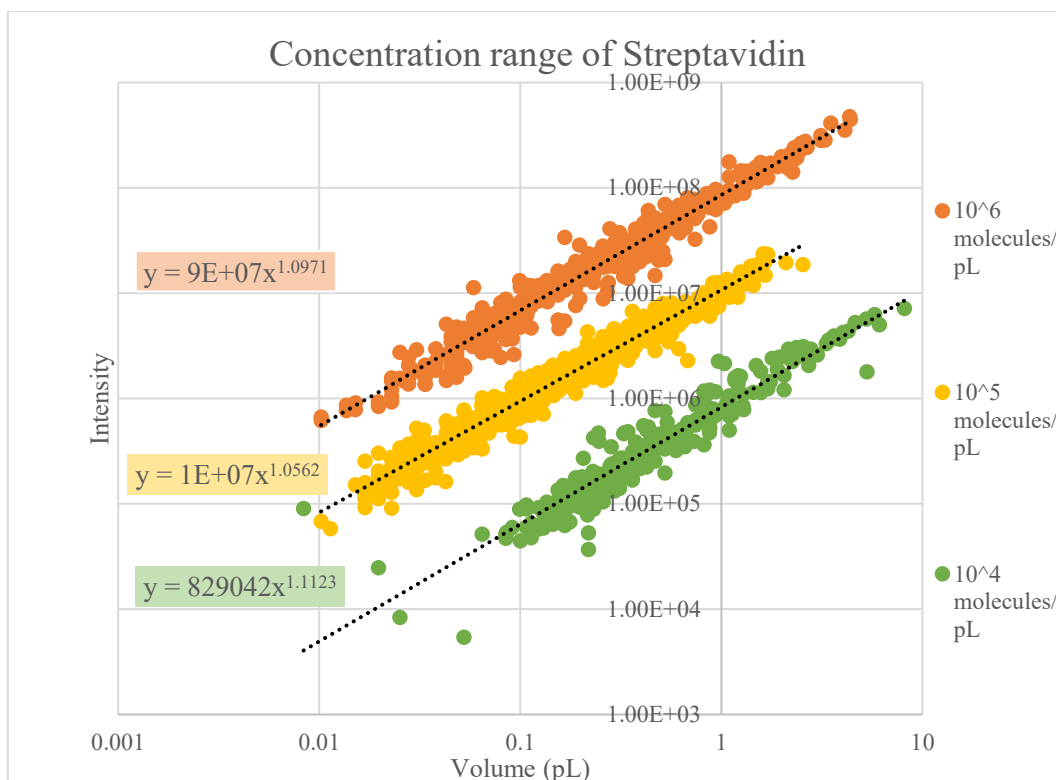


**Figure 3.35:** Concentration range of Streptavidin using 3 varying concentrations. The increase between each line should be of a factor of 10, however, this was not the case. The slight difference between these values shows the sensitivity of the data analysis method.

In theory, the relative difference between each of the concentration should increase by a factor of 10, however, this was not observed here. The difference between the concentrations is of a factor of 12 between  $10^4$  molecules  $\text{pL}^{-1}$  and  $10^5$  molecules  $\text{pL}^{-1}$ , and a factor of 9 between  $10^6$  molecules  $\text{pL}^{-1}$  and  $10^5$  molecules  $\text{pL}^{-1}$ . The deviation away from the actual value could possibly be pinned down to the sensitivity of the data analysis methods. Therefore, in order to test this, the manual segmentation methodology was independently repeated three times on the same data set.

Though manual segmentation has shown to be consistent in showing the distribution of the GUVs, however, it is important to note here that the small changes to the parameters of this method still leads a significant difference. This was tested by repeating the manual segmentation measurements independently on the same dataset. A small yet

significance difference in the resultant gradient of the line of best fit was observed as seen in **Figure 3.36**. Once again, the GUVs with a lower signal to noise ratio is more susceptible to differences within the data analysis method as expected. It is therefore important that the optimised parameters set for manual segmentation is followed.

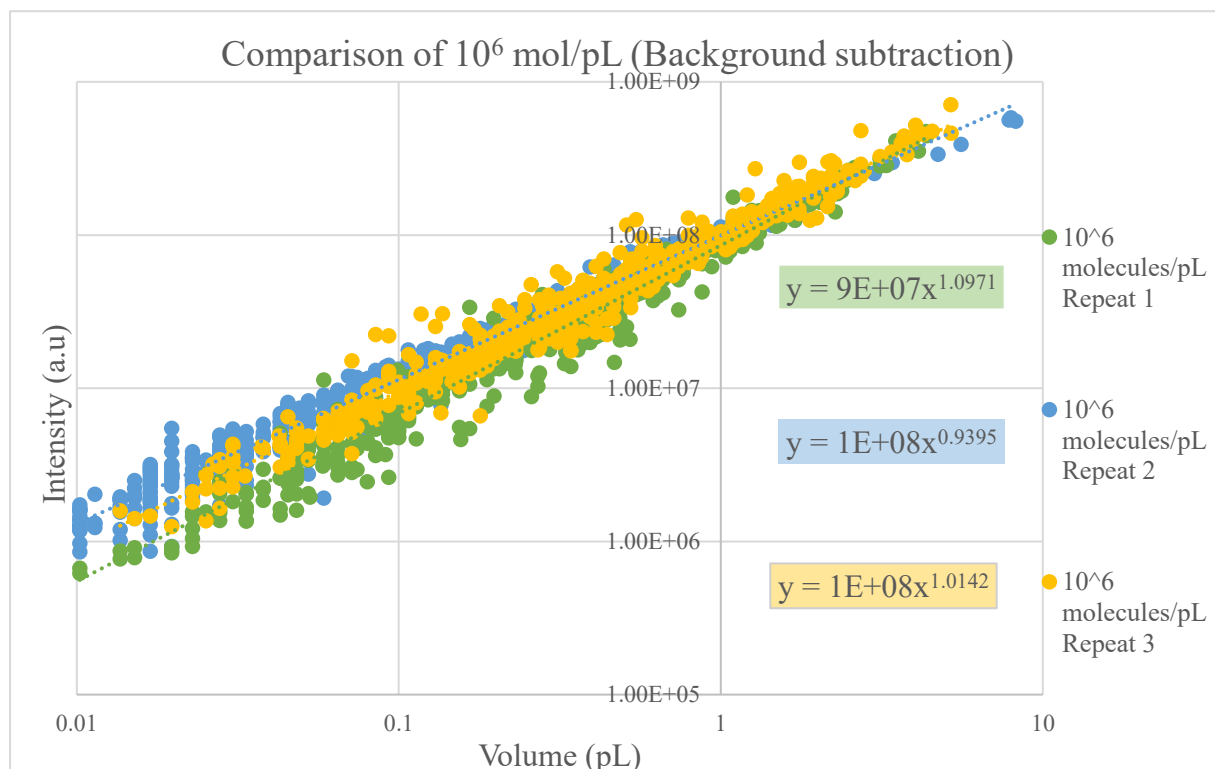


**Figure 3.36:** Assessment of the sensitivity of manual segmentation of  $10^6$  molecules  $\text{pL}^{-1}$ . The graph shows that vesicles of a lower signal to noise ratio is more sensitive to minor adjustments and changes in the parameters of the manual segmentation method as expected.

The variation between each batch of GUVs produced was also assessed by carrying out the similar data analysis method. Using a concentration of  $10^6$  molecules  $\text{pL}^{-1}$ , the results of each of the batch overlap with one another. This shows a minimal variation between each of the batches produced.

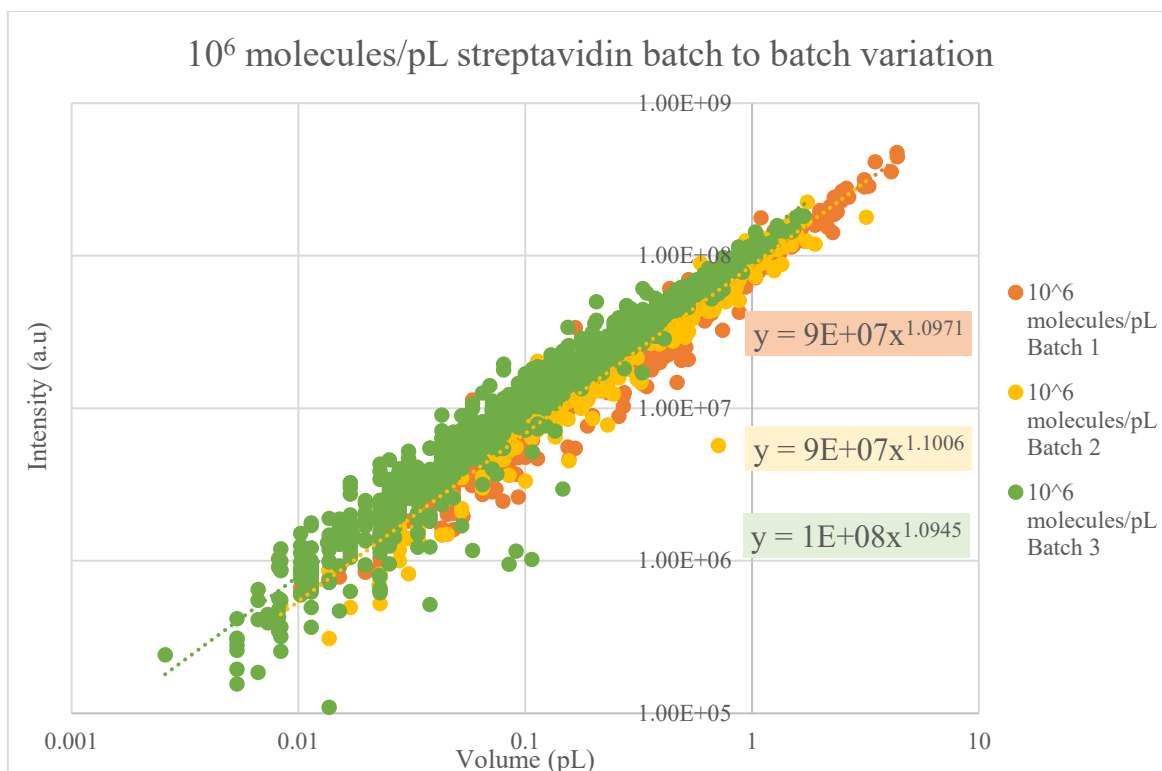


**Figure 3.37:** Assessment of the batch to batch variation of the different populations of GUV with the same starting seed solution.

Both the calcein and streptavidin data closely shows a positive correlation between the volume of the vesicles and the fluorescence intensity. The apparent linearity can be inferred as the constant concentration of the molecules within the data. The variation in the concentration of the vesicles for both calcein and streptavidin at  $10 \mu\text{m}$  and  $10^6$  molecules  $\text{pL}^{-1}$  were plotted as shown in **Figure 3.38**.

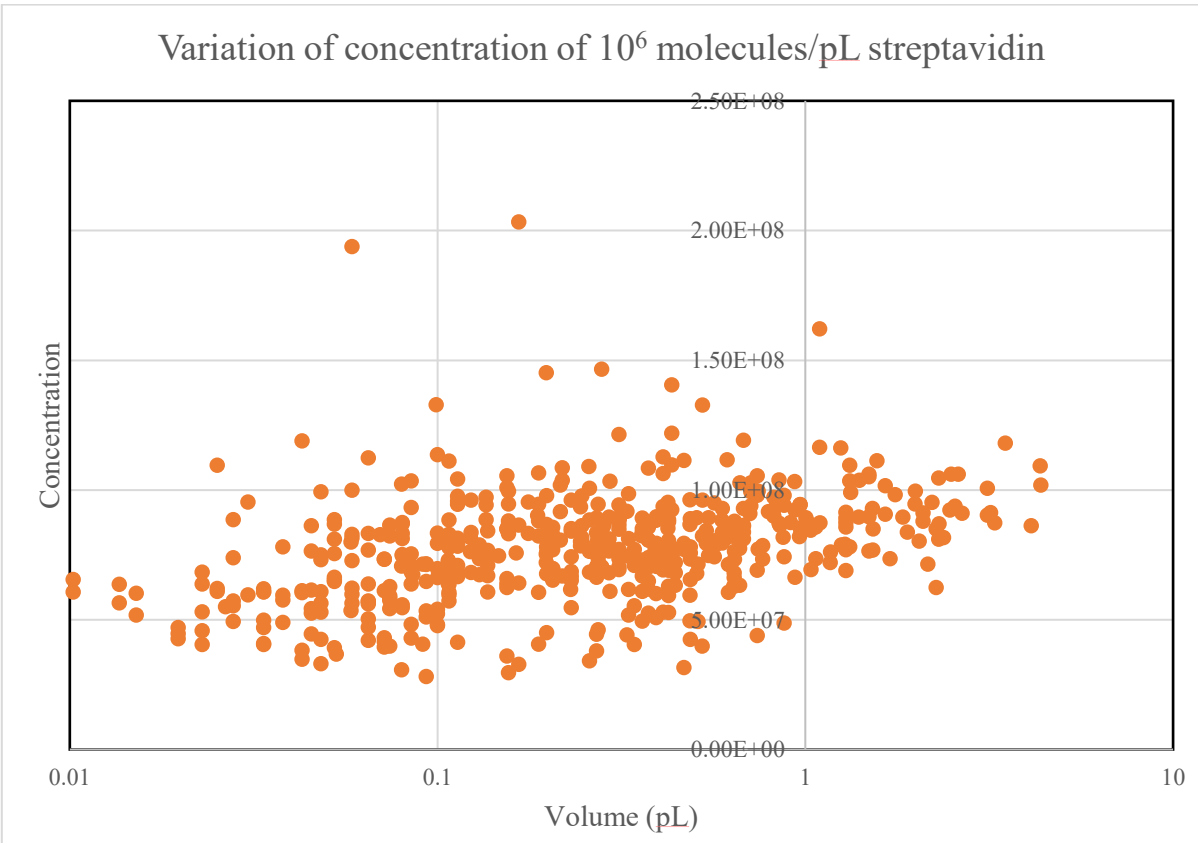
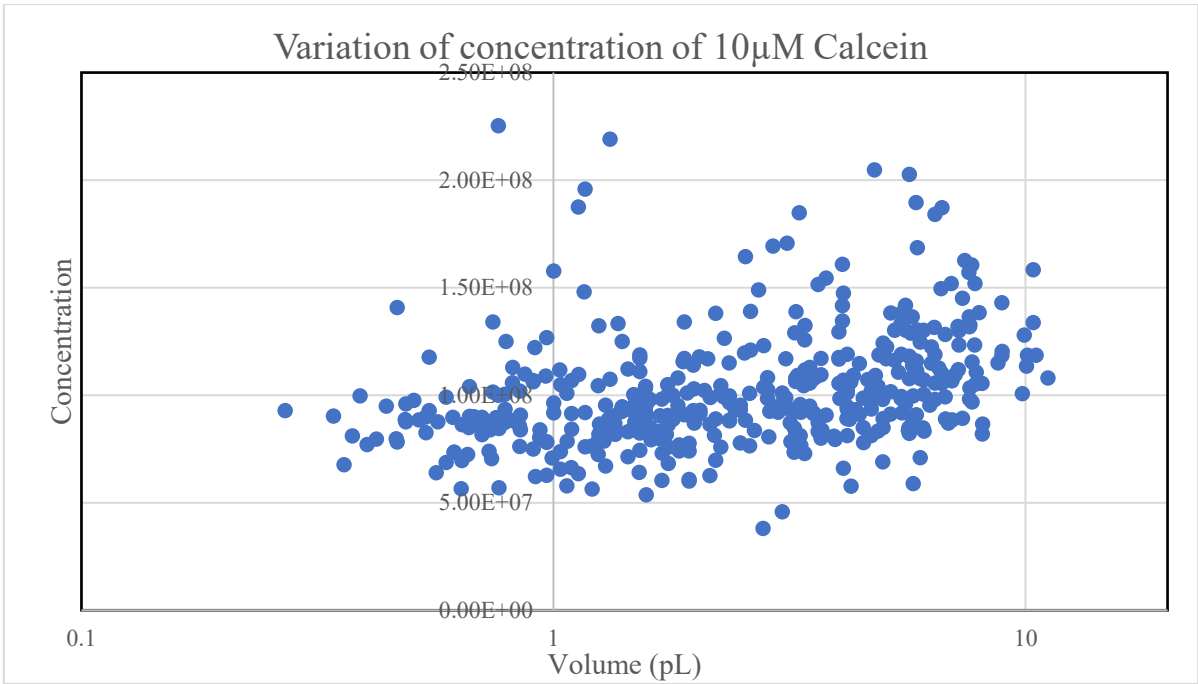


**Figure 3.38:** The variation in the concentration across a range of volume in a) 10 $\mu$ m calcein b)  $10^6$  molecules  $pL^{-1}$

From this graph, a significantly higher variation is observed at the lower volume. However, as the units of the fluorescence intensity is of an arbitrary unit, the absolute value of the number of molecules cannot be calculated and in extension, the encapsulation efficiency which may govern the variation of the concentration across the different volumes. Therefore, in order to be able to obtain absolute number of molecules encapsulated within each vesicle, we move to use a microfluidic based single molecule microarray approach. This is discussed in greater detail in chapter 4.

### 3.5 Chapter Conclusions

The work in this chapter describes the development of the data analysis methodology to understand the distribution of the GUVs.

With respect to the optimisation of the data analysis methods, three different types of data analysis methods were examined. The results show that manual segmentation, a manual method that utilises the ‘measure’ tool to trace the perimeter of the ROIs is most ideal in approximating the area of the GUVs. The use of automated thresholding filters on Fiji led to either overestimation or underestimation of the area. The effect of this was more apparent on vesicles with a low signal to noise ratio. As the signal intensity is closer to the noise floor, the algorithm finds it hard to discriminate between the fluorescence signal and the background. As the data is presented as a function of volume, the error in the area is multiplicative hence, affects the gradient of the distribution more severely. The same case was observed with CellProfiler. Using CellProfiler, the algorithm fails in discriminating clumped vesicles as individual vesicles. This is more apparent with congested data hence causing misrepresentation in the distribution of the sizes, skewed towards the larger volumes. The type of data analysis tool used to look at the distribution of the vesicles over the large image affects the analysis downstream.

From the raw images and histogram of the data, it is clear that the vesicles produced were heterogenous in both size and total fluorescence intensity. The fluorescence intensity per GUV was then plotted against the volume of the GUV as calculated from the radius of each object measured using manual segmentation. The positive linear relationship of the plotted logarithms of the data suggests that the concentration of the

fluorescence molecules within the GUVs can be inferred to be constant. However, the further inspection shows a relatively large variation of the concentration especially with the GUVs on the lower volume. This variation by extension may be due to the difference in the encapsulation efficiency of the emulsion-based phase transfer method used to produce the vesicles. However, as the fluorescence measurements are of an arbitrary unit, the absolute concentration of the encapsulated fluorescence molecule cannot be calculated. The next logical step in order to be able to characterise this is to use an absolutely quantifiable approach to understand the variation in the concentration of the molecules, and by extension the encapsulation efficiency. Therefore, moving forward, a microfluidic based single molecule approach was developed for this purpose.

## 4. Absolute quantification of GUV using microfluidic technology

### 4.1 Chapter Outline

The chapter describes the work carried out to obtain absolute quantification of the number of molecules encapsulated within the GUVs using a microfluidic based single molecule microarray approach.

- **Microfluidic Single Molecule Pulldown Platform**

The method development of a fluorescence based single molecule microarray device that allows the absolute quantification of biomolecules encapsulated with giant unilamellar vesicles.

- **Encapsulation Efficiency of Emulsion Based Phase Transfer**

The single molecule information obtained using the **Pulldown Array Single Molecule High-throughput (PASH) chip** was used to determine the encapsulation efficiency of the vesicles at a single vesicle resolution. In addition to this, further analysis was carried out to understand the batch-to-batch variation and providing a methodology that allows the calibration of measurements to convert epifluorescence measurement into absolute values.

### **4.1.1 Understanding Encapsulation Efficiency**

The growth in the field of bottom-up synthetic biology has paved way for the continuous development of fabricating vesicles that closely mimic the features of a cell. These biological models built from scratch either using synthetic or biological constituents have seen a plethora of functionality. Thus, the encapsulation of various drugs, proteins, DNA and other biomolecules and protein networks have extensively been reported over the recent years. With many of these applications, the predictable loading of the molecule of interest in small numbers with a high encapsulation efficiency (EE) is essential. The encapsulation efficiency can be characterised as to what extent does the molecules present in the seed solution end up being encapsulated within the resultant vesicle.

The work currently done in understanding the encapsulation of molecules in liposome have shown that the concentration in the vesicle does not always match the concentration in the seed solution. Often, these values are reported to be below the concentration with the EE being smaller than one. This can pose a problem for the application of cell mimics especially in the encapsulation of cellular biomolecules that are often available in low concentration and in precious quantities. Critically, in the need to encapsulate a mixture of components, for instance in an in-vitro transcription-translation system (IVTT) expression system, the variation in the EE of individual components would possibly compromise the overall efficiency of the system in question.

The EE have been shown to be sensitive to a variety of factors associated with the vesicles. This includes the physical properties of the membrane surface including

charge, hydrophobicity and rigidity.<sup>144</sup> Besides this, the characteristics of the molecules bound to be encapsulated and the method used to produce these vesicles also play a role in determining the encapsulation efficiency of the vesicle.<sup>145-147</sup> One of the proposed theories relating to a poor EE is mainly thought to be due to the interaction between the protein molecules and the lipid bilayer itself. A study carried out by Colletier et al. indicated that the variation in the EE can be attributed to a number of reasons such as the concentration and composition of the lipid and the composition of the external buffer.<sup>148</sup> The group mainly attributed the reduced encapsulation efficiency down to the interaction between the molecule of interest, in this case a protein with the lipid bilayer. The suggestion of the loss in efficiency is due to this interaction was further strengthened by Hoof et al.<sup>149</sup> Here, using molecular dynamic simulations they successfully showed that the dominant force irrespective of vesicle size is mainly due to the particular interaction between the protein and lipid bilayer. The morphology of the vesicle in regard to its shape, size and lamellarity also influences the encapsulation efficiency of the resultant vesicles.<sup>150,151</sup>

The wide range of factors reflects the sensitivity of the encapsulation to the properties of the solute and the vesicle, further highlighting the importance of establishing a more quantitative method with single vesicle resolution to allow the EE of GUV production to be determined experimentally.

To date, a handful of methodologies have been developed to characterise and measure the encapsulation efficiencies, however these are either not suitable for the detection of proteins or not carried out at a single vesicle level, instead rely on bulk averages. The analysis carried out using bulk analysis may potentially suffer from the inability to

distinguish between the molecules that were unsuccessfully encapsulated from the original seed solution or from the leakage of the vesicles itself. This may lead to the masking of the true value of the encapsulation efficiency. With a growing interest in the use of these vesicles as cell mimics, there has been a growing interest to establish a method that would allow measuring the EE on a single vesicle level.

Colletier et al. investigated the encapsulation of acetylcholinesterase enzyme into liposomes.<sup>148</sup> The use of other a variety of different liposome production methods proved unsuccessful as it denatured the enzyme, however, lipid film hydration technique showed success albeit a poor encapsulation efficiency. Gopfrich et al. introduced a one pot method for the formation of complex single and multicompartiment synthetic cells. This method relied on the formation of charge mediated fusion of SUVs inside surfactant stabilised droplets induced by vigorous vortexing or manual shaking.<sup>152</sup> This method is reported to have a high encapsulation efficiency of the components inside the GUV. This was achieved by successfully encapsulating a variety of molecules such as fluorescent dye, mRNA, and polystyrene beads. Early work in reporting the EE using individual GUVs comes from Sun et al.<sup>153</sup> using single-vesicle photolysis and confocal single-molecule detection to determine the concentration of carboxyfluorescein within the vesicles prepared using rotary evaporation. The vesicles were optically lysed to release the encapsulated molecules and subsequently detected using fluorescence correlation spectroscopy. The data was then fitted to a diffusion model in order to approximate the concentration within the vesicles prior to rupture, thereby allowing the calculated estimation of the encapsulation efficiency. There was a significant degree of variation in the EE for oligo-lamellar and multi-lamellar vesicles with an average value

of  $36.3 \pm 18.9\%$  and  $17.5 \pm 8.9\%$  respectively. Lohse et al. reported the development of a fluorescence-based technique to measure the encapsulation efficiency of small unilamellar vesicles.<sup>154</sup> The vesicles produced using a rehydration technique are loaded with a dye in the membrane and the lumen before being immobilised on a surface. The correlation between the signal intensities were used as a measure to calculate the encapsulation efficiency of single vesicles using size as a function. The reported EE was found to be inversely proportional to the radius of the resultant vesicles. Matosevic et al. also demonstrated the stepwise synthesis of GUVs using a microfluidic device by incorporating flow-focusing and segregated fluid flow.<sup>155</sup> The comparison between the measured fluorescence intensity of the resultant vesicle post-phase transfer and the seed droplets pre-phase transfer allowed for the estimation of the EE of individual vesicles. The estimated EE was at 83% and was shown to be independent of droplet size. Additionally, Keating et al. reported the encapsulated efficiencies of polymers and small molecules within GUVs that were produced by gentle hydration.<sup>156</sup> The EE was determined using the difference between the fluorescence intensity from inside and outside of the vesicle measured using confocal fluorescence microscopy. The reported average values for showed a significant variation from batch to batch ranging from 54% to 188%. They theorised that the increased encapsulation efficiency beyond a 100% could be due to the interaction between the polymer molecules and the lipid bilayer. This resulted in the modified behaviour of the bilayer inducing an artificial increase in the encapsulation of the polymers. Hussain et al. recently developed a range of methods that was able to directly quantify the encapsulation of protein within liposomes.<sup>157</sup> With the use of the Micro BCA protein assay system, the concentration of protein within the

vesicles were measured by the solubilisation of liposomes. The reported encapsulation efficiencies in the presence of neutral lipids range from 34- 38%. The two HPLC techniques used in the experiment to quantify protein was HPLC-evaporative light scattering detector (HPLC-ELSD) and reverse phase HPLC. The use of these measurement techniques removed the need to solubilise the liposome and with a reported EE of  $80 \pm 3\%$ .

The many drawbacks present in carrying out a bulk analysis has led to the need of developing methods that are able to measure the encapsulation efficiency on a single vesicle. It is vital especially for the precise engineering of cell mimics with an end goal of developing such vesicles as an effective tool in studying cell biology or a functional cell-like device. The ability to accurately quantify the encapsulant concentration is desirable for both synthetic cell assembly but also from a biomedical application perspective in particular with drug delivery.

## 4.2 Introduction

### 4.2.1 Single Cell Analysis

The inherent complexity in biological systems come from the many types of cells differing in structure and functionally which make up the system. The recent years in cellular life sciences has seen a significant shift, moving away from bulk cell interrogation towards single cell analysis. Studies using single-cell level resolution allows the unmasking of cellular heterogeneity that exists in an otherwise genetically identical population. Cellular heterogeneity has increasingly been recognised as an important feature of a variety of biological processes including immune response, responses of cells towards drugs, and cell differentiation. One of the factors that has led to the rise of cellular heterogeneity is due to the stochastic nature of gene expression.<sup>158</sup> The increased evidence pointing towards the functional consequences cell-to-cell variation has upon cellular biology has led to more rapid progress in the field.

Conventional cellular analysis pool together responses from a population of cell as an ensemble measurement with the assumption that the most relevant stimulus is one that is averaged over large populations. Data obtained from a large number of cells allow major patterns and features such as high protein abundance or common signalling networks to be deciphered. However, measurements obtained from bulk experiments generally output the average of the mean protein expression for instance, which may produce misleading interpretations. Therefore, it is therefore crucial to look at the cells one-by-one to allow the differences in individual cells to be picked apart. The need to understand the regulatory network functions in normal cells or malfunctions in diseases is an important objective in post genomic research.<sup>159</sup> The inherent complexity of

various regulatory networks has led to the need for a comprehensive molecular profiling to infer the functions of the different biomolecules present.

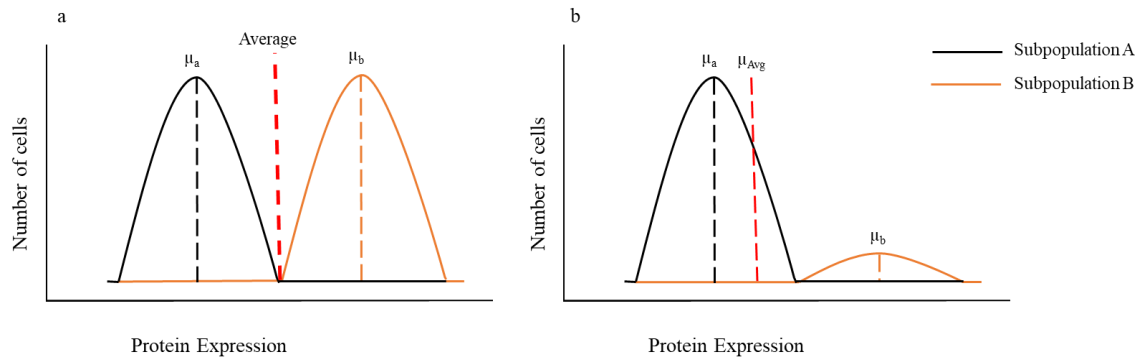


**Figure 4.1:** Averaging results from bulk measurement can lead to misleading results. a) Averaging values from two distinct population distribution often leads to the misrepresentation of the true expression level of both populations. b) Taking an ensemble average measurement has the tendency to mask measurements from rare subpopulations leading to the loss of information about heterogeneity.

The field of single cell analysis can broadly be divided into three main ‘omic’ fields vastly depending on the component of interest. Briefly, single-cell genomics examines the sequence and information present in the DNA of the cell. The genomic techniques mainly rely on the amplification mechanism of DNA to increase its copy numbers, allowing for a signal output to be obtained. Single cell transcriptomics on the other hand examine gene expression by quantifying the amount of RNA transcripts present. The presence of mRNA within cells can be used as an indicator to examine how often certain genes are expressed and was seen to have potential to examine the number of protein copy numbers within a cell.

In the recent years, a number of technologies enabling the multiplexing of single cell DNA and RNA analysis have been developed.<sup>160</sup> Though the efforts in genomic sequencing have advanced our understanding of molecular alterations in human diseases tremendously, these approaches have limitations. Genomic sequences provide

a list of the proteins produced within a cell however does not specify any post translational modifications, or the behaviour of protein interaction. Transcriptomic studies on the other hand, does not provide the entire picture as post-transcriptional regulation can significantly alter the protein copy number present within a cell.<sup>80</sup> In addition, studies have shown the weak correlation between RNA expression and protein abundance.<sup>161,162</sup> Thus, the use of single-cell proteomics technologies will allow the study of protein expression, post-translation modifications and its interactions.

Proteins are biomolecules central to a plethora of biological functions such as transporting molecules, regulation of signal transduction, catalysing biochemical reactions and controlling gene expressions amongst others. Unlike the genome, the proteome is not static. The constant change in the levels of protein expression and the concentration has direct phenotypic consequences. The ability to study a handful of the vast number of proteins found in mammalian cells have allowed scientist to decipher the science of many diseases. Though the study of proteins can offer a significant insight towards cellular function, the lack of an amplification mechanism in protein imposes certain constraints within the available methods for protein detection due to a lack of sensitivity. Furthermore, this adds to the difficulty of directly adopting the high throughput detection methods similar to that of DNA and RNA. Single cell proteomics is a field that associates itself with the levels of proteins present within a cell. The workings of a cell can only be truly understood if the number of active proteins and its interactions are quantified.

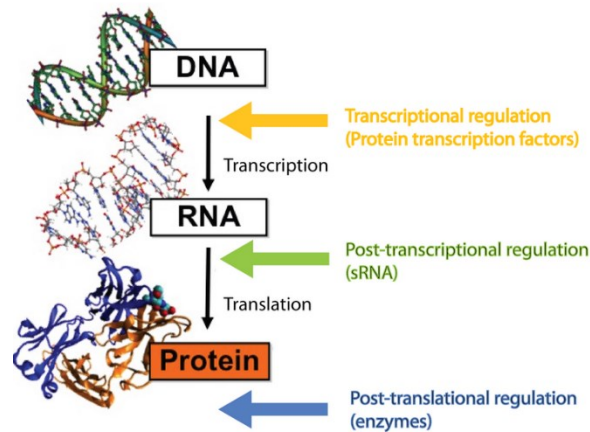


**Figure 4.2:** Schematic illustration of the central dogma within a single cell. Understanding the level of proteins provide a complete picture of cellular function. Figure adapted from reference <sup>163</sup>

Tools for whole-proteome-level analysis at a single level are currently not commercially available however, several technologies have been developed to aid in the multiplexing of protein analysis. An example of a simple tool in single cell proteomics is through the use of fluorescence microscopy and flow cytometry. The coupling of simple molecular recognition elements such as antibodies on a particular surface together with microscopy allows the localisation and imaging of fluorescently tagged antibodies of the target protein. An example of this methodology is immunofluorescence (IF) microscopy. This technique involves the use of a permeabilization agent to perforate the cell, a fixing agent to crosslink and immobilise proteins within the cell and a fluorescent antibody to stain and visualise the protein of interest. It is a technique that could be used as a standalone or in tandem with a variety of cytometric methods such as Fluorescent Activated Cell Sorting. (FACS) Though effective, there are a number of limitations which have prevented this technique to be universally adopted. A major limitation in this technique is the potential spectral overlap of dyes that are used to tag the detection antibodies. The expansion of the detection panel to a larger size could inevitably lead to potential overlap as the dyes used to tag the antibodies may have a

broad absorption or emission spectra. This spectral overlap could lead to accidental excitation of a fluorophore, resulting in false positive measurements. Thus, in order to compensate for this, fluorescence compensation methods were developed as a calibration tool and have made the measurements of 12 fluorescence parameters in flow cytometer possible.<sup>164</sup> However, despite the careful consideration of the choices of dyes, an upper limit for multiplexing still exists within this format.

In an effort to address this spatial resolution issues, one of the proposed methods by Lin et al.<sup>165</sup> is the use of an alkaline solution of hydrogen peroxide to chemically bleach the fluorescent dyes used in antibody staining. The control experiments performed suggested the protein species were not damaged by the bleaching process. However, this method though promising, may leave some of the protein species vulnerable to oxidation by hydrogen peroxide. This would then inhibit the ability to simultaneously detect the protein species and the post-translationally modified analogues.

The use of fluorescence imaging in proteomic studies still lacked the ability of the system to multiplex and have a high detection sensitivity. Therefore, new methods enabling single cell proteomic analysis have been developed. The combination of genetically encoded fluorescent proteins and high-resolution imaging, microarray coupled with microfluidics, flow cytometry or mass cytometry and mass-spectrometry techniques are of the more commonly used approach. Each of these techniques have a unique set of advantages related to the sensitivity, multiplexing and resolution, thus, each of the approaches are applicable to different sets of measurements. A comprehensive review<sup>166</sup> on the different technique can be found elsewhere, however,

the scope of this chapter is focused on the use of microarray system coupled with a high resolution imaging technique and microfluidic technology.

#### **4.2.2 Microarray Platform**

Microarray technology is a powerful tool that allows the parallel analysis of biological markers. Microarrays are defined by a matrix of several individual recognition elements immobilised on a solid support (substrate) using bulk phase mass transfer strategy, in particular by direct spotting of biomolecules on the substrate.<sup>167</sup> It is a highly miniaturised and parallelised solid phase assay systems that uses different capture molecules immobilised at a specific spot within a fixed volume.

The nature and type of recognition elements printed or spotted on to the surface is used to categorise the type of microarrays. The two most recognition elements are that of nucleic acid and proteins which are printed on to a solid substrate. The foundation for microarrays were first laid by Fodor et al.<sup>168</sup> by demonstrating a process to build an array of synthesized peptide by the sequential deposition of amino acid groups on a glass surface. The functionalising of the substrate with a photolabile protecting chemical group which was illuminated through a mask led to the deprotection and the addition of the first chemical building block containing a photolabile protecting group. The use of different masks allowed for an array of 1024 peptides to be synthesised. This technology was repurposed for constructing DNA microarrays. Schena et al.<sup>169</sup> then developed a method that mechanically prints complementary DNA in spots onto glass surface using a quill-type metal pin. Indeed, this technique, a type of contact printing has now become the most widespread technique for the preparation of protein microarrays. The completion of sequencing the human genome shifted the attention

onto proteomes and methods on how to study it. However, similar success of DNA microarray was not immediately replicated by protein microarrays owing to much higher chemical complexity and diversity within proteins themselves.

Protein microarrays can broadly be divided into three main categories. The first being an analytical protein microarray which takes advantage of the highly specific in-built recognition capabilities between antibodies and antigens. The expansion of the conventional immunoassays into antibody array application allowed for a parallel and multiple detection system using small amounts of sample. The good reproducibility and high sensitivity of these arrays made it a valuable tool in studying complex biological samples.<sup>170</sup> The second type of protein microarray was developed by the immobilisation of purified proteins on glass slides. A type of functional protein microarray, it differs from antibody microarrays by spotting proteins encoded by the organism on to the surface. This was mainly useful for the characterisation of protein functions such as protein-protein binding and enzyme substrate relationships to name a few.<sup>171</sup> The third category of protein microarrays is of a more recent development. A reverse-phase array provides an alternative format to analytical microarrays in which the lysate samples are used as the detector molecule on the surface of the substrate. First developed by Pjawaletz et al.<sup>172</sup> to monitor histological changes in prostate cancer patients, this type of microarrays is popularly used to readily assess comparative proteomic changes during the development of a disease.

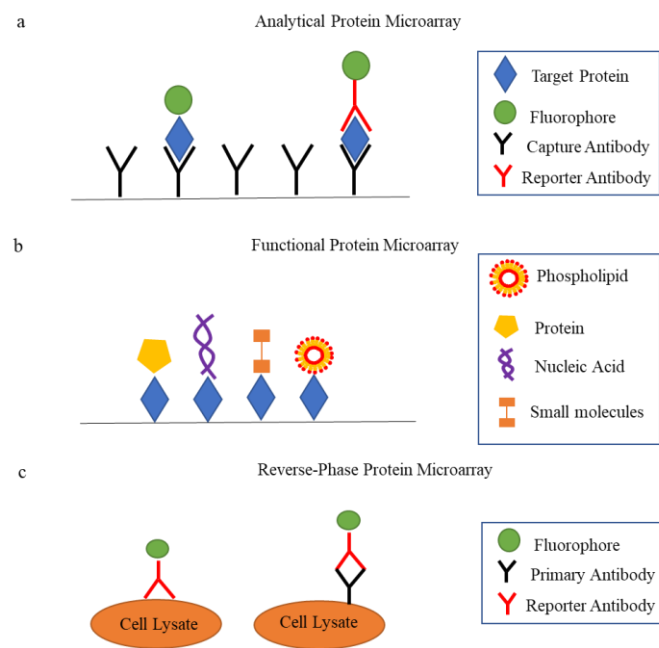


**Figure 4.3:** The three categories of protein microarrays. a) Analytical protein microarray mostly represented by the use of antibodies as detector molecules on the surface of the substrate. The targeted proteins in this class can be detected using direct labelling or a sandwich based assay format. b) Functional protein microarrays involve the immobilisation of protein molecules as detectors and have broad applications in studying protein based interactions. c) Reverse-phase microarray is a contrast of the first two types of microarray where cell lysate samples are immobilised on the surface of the substrate and can be detected using direct labelling. Image modified from the reference <sup>173</sup>

The various aspects of protein microarray including the printing, surface chemistry and capture probes have continuously undergone development over time. The use of protein microarrays has now become relatively common in both research and development industries mainly in the form of antibody arrays which are employed as an analytical and diagnostic tool.

With respect to the antibody protein microarray, the monitoring of proteins over a specified amount of time to measure the amount of bound proteins can be performed using a label free method. Contrary to immunofluorescence, the detection of the protein would occur by lysing the cell to release the molecules in solution. The released proteins would be pulled down by the capture antibody. A detection antibody tagged with a fluorescence dye of choice is used to form a ‘sandwich antibody complex’ detected

using fluorescence microscopy. This microarray approach also avoids the spectral overlap issue as well as avoids the need to carry out cell fixation. The versatility of this technique allows this methodology to be adapted for the use of either live cells or in this case, artificial cells.

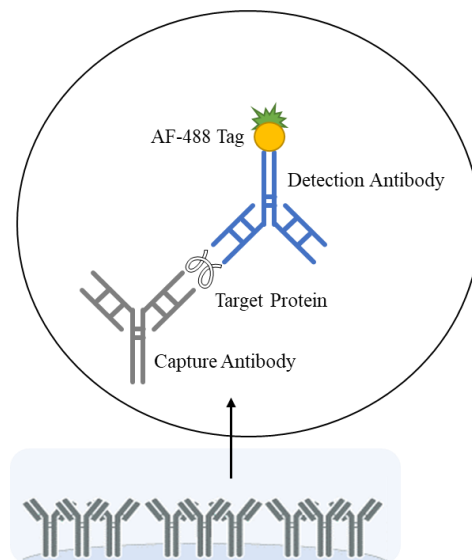


**Figure 4.4:** A schematic illustration showing an antibody sandwich complex that is often found in protein microarrays.

With fluorescence-based strategies as such, improvements to increase the sensitivity of the microarrays have been employed. This can be achieved by discriminating the unbound background protein fluorescence from those bound to the antibody. An increasingly popular and powerful technique to achieve this is by using Total Internal reflection Fluorescence (TIRF) microscopy imaging technique. When light enters a medium of differing refractive index at a given angle, it undergoes refraction in the new medium as well as reflection back into the existing medium. When exceeding a critical angle, the light is totally reflected from the boundary in an event known as total internal reflection (TIR). The use of TIRF microscopy takes advantage of the evanescent field which is generated in the second medium. This particular wave has an identical

frequency to that of the incident wave and decays exponentially away from the boundary. With the evanescent region extending at most beyond a few hundred nanometres away from the surface, only microarray surface bound fluorophores are excited. This dramatically reduces any unwanted background signal from any unbound species, enhancing the ability to detect protein species of low abundance. This technology can be then further extended to include single molecule measurement capabilities. As demonstrated by Tessler et al.<sup>174</sup>, single molecule quantification using TIRF microscopy was performed by counting the binding of single labelled antibodies and proteins immobilised on the surface. The use of single molecule resolution provides a method of absolute quantification of the protein copy number as the exact number of molecules can be measured. This method also removes the need to use an intensity calibrants such as fluorescent beads commonly used in FACS. The improved sensitivity in comparison to typical fluorescence measurement makes this an attractive technique to be used.

#### **4.2.2.1 Lab-on-a Chip Platform**

The analysis of cytosolic proteins requires the need for cellular lysis to take place. However, it is crucial that these releases occur within the confined volume to produce solutions with high enough concentration of the species. Such volume confinement can be made possible by combining the use of microfluidic platforms.

Microfluidics have emerged as a powerful platform in single cell analysis owing to its capability to manipulate small volumes and integrate multiple sample preparation steps into one device. Microfluidic chips of micrometre dimensions match well with the size of typical biological cells, making it a suitable platform involving cell studies and

characterising biochemical and biophysical properties of cells on a single cell level. This allows for the rapid exchange of buffers and reagents thus minimising the gradient of stimulants experienced by the cells. The small volume contained within a microfluidic device also ensures a lower volume of reagents required, hence making this a cost-effective platform in comparison. More specifically, microfluidic systems have the capability to confine individual cells in droplets or microwells. This has allowed the analysis of single cells with minimal sample dilution, shorter reaction times and higher sensitivity. For instance, He et al.<sup>175</sup> demonstrated the use of microfluidic based droplet generation for the selective and controlled encapsulation of a single cell into a picolitre to femtoliter volume aqueous droplet surrounded by an immiscible phase. The precise generation and repeatability of droplet generation has shown that this system may have the potential to become a high throughput platform for cellular proteomics. Addressed as microwells, the droplets pose a way of performing microarray assays by compartmentalising volumes of analyte in individual chambers. Microwells allow for rapid analysis of secreted protein or released metabolites from encapsulated single cells.<sup>176,177</sup> The droplets produced using this methodology can be seen to serve as a ‘container’ for the secreted biomolecules, hence minimising sample dilution whilst increasing assay sensitivity. Huebner et al.<sup>178</sup> for instance developed a quantitative enzyme assay within microdroplets whilst Koester et al.<sup>176</sup> demonstrated the detection of secreted antibodies in individual hybridoma cell. The unique advantages offered by microfluidics and its application has seen a number of biochemical analyses developed.<sup>70</sup>

One of this development has been the introduction of lab-on-a-chip (LOC) devices.<sup>179</sup> These devices combine microfluidic based devices together with analytical protein microarrays. The characteristics of such single cell proteomic assay include its capability in multiplexing, high sensitivity, large dynamic range, and throughput. The multiplexing ability of an assay relates to the number of proteins that can be assayed within a measurement whilst throughput refers to the number of cells that can be analysed in parallel. The majority of this platform measure the proteins in relative units; therefore, calibration curves have to be established to translate the analytical signal to protein concentrations or copy numbers to useful biological insights

The first step towards a practical single cell proteomics was marked in 2011 by Reyhani et al.<sup>58</sup> through the development of the microfluidic antibody capture (MAC) chip. This platform employed the use of printed antibody microarrays together with a microfluidic device to perform EGFP and P53 pulldowns using a BE-GFP cell line. The microfluidic antibody capture (MAC) chip consists of a main channel where the main cell suspension is flown through with side channel leading up to the analysis chambers. The chambers consist an aligned antibody spot printed onto surface of the substrate in advance. Using optical tweezers, the group was successful in selectively isolating cells from the main channel into the individual analysis chambers. Optical trapping provided an advantage in eliminating contact with the printed antibody spot in the chamber, thus resulting in a lower LOD for proteins. The cell now isolated in individual chambers are lysed optically to release its cellular lysate and using single molecule TIRF, the antibody spots of the captured proteins are imaged. The uniqueness of this device at the time lay in its potential to provide absolute quantitative data on cellular protein copy number.

This was achieved by the calibration of the assay against a recombinant protein standard.<sup>58</sup> The limit of detection reported using the preliminary version of the device governed by the background signals were  $10^2$  proteins using a p53 assay and  $0.41 \times 10^5$  proteins using the EGFP assay. Since its inception, the device had been further improved to address the performance of the assay associated with non-specific binding (NSB) through the introduction of surface passivation. The development of this assay is however governed by the availability of antibodies that are compatible with a sandwich assay and a sufficient sensitivity to the target. The platform has been employed to analyse human tissues and clinical samples but also demonstrated promise for its scalability in terms of its capability to study multiple proteins in parallel.<sup>180</sup> To date, users of this technology have achieved the ability to carry out 2-plex measurements.<sup>181</sup> A criticism of the technology however lies in its high throughput capabilities or rather the lack of it. The optical isolation step employs a 'set it-get it' approach in which the user is allowed to choose the specific cell of interest for an experiment and is particularly useful when dealing with samples that are rare. However, as optical trapping is carried out in a series mode, this limits the number of cells that can be processed per experiment between 50-100 cell.

Another major progress towards multiplexing was achieved by Heath et al. in the form of a high throughput single-cell barcoded chip (SCBC).<sup>182</sup> In this approach, single cells are compartmentalised into individual microchambers with each chamber containing an antibody barcode array, patterned as parallel strips. The antibody barcode array allows for the capture of secreted proteins and is detected by a corresponding biotinylated antibody stained with a fluorescence streptavidin used for imaging purposes. The

preparation of the miniaturised barcode array is achieved using DNA-encoded antibody library (DEAL) technology that was developed.<sup>183</sup> The immobilisation of oligonucleotides on polylysine-coated surface as highly dense and uniform barcodes using microfluidic flow channels. The DNA barcodes are then converted to antibody barcodes by the hybridisation of the DNA-antibody conjugates. This technology allows up to 20 antibody strips to be patterned in each microchamber with the potential to quantify 20 varied proteins from a single cell. In their original work, they described this method to have a 10-fold increase in the antibody densities compared to that of a standard protein antibody array. The packing density of the spots as estimated by the authors were  $6 \times 10^{13}$  DNA molecules  $\text{cm}^{-2}$  and showed an increased sensitivity of an order of magnitude when compared to antibody spots in an assay targeted towards IFN- $\gamma$ .<sup>184</sup> This shows the strength of the method developed by the Heath group in its capability to multiplex with minimal compromise on the sensitivity of the assay.

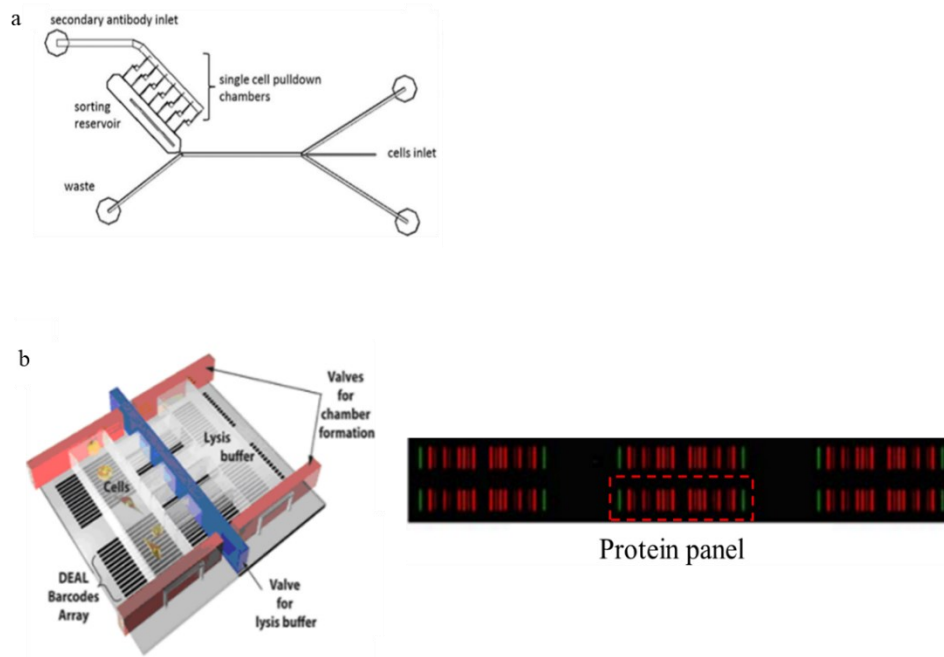


**Figure 4.5:** Microfluidic devices used in single-cell proteomic analysis. a) A schematic of the microfluidic antibody capture (MAC) chip developed by Reyhani et al. Image reproduced from reference <sup>58</sup> b) An illustration of the SCBC platform developed by the Heath group. The fluorescent readout obtained from the device, in which each strip corresponds to an analyte in a panel of 10 proteins. Image adapted from reference <sup>182</sup>

## 4.2.3 Single Cell Protein Pulldown Microarray Experiments

### 4.2.3.1 Concept Workflow

The general concept of the pulldown microarray experiment that was employed throughout this thesis consist of three main elements.

- a. **Single Cell Isolation and trapping:** The isolation of the cell of interest from the bulk solution into microwells or individual analysis chambers
- b. **Cellular Lysis:** The release of the cellular contents from within the cell with no denaturation of the internal cellular components that will affect the assay measurement
- c. **Detection:** The absolute quantitation of the protein of interest.

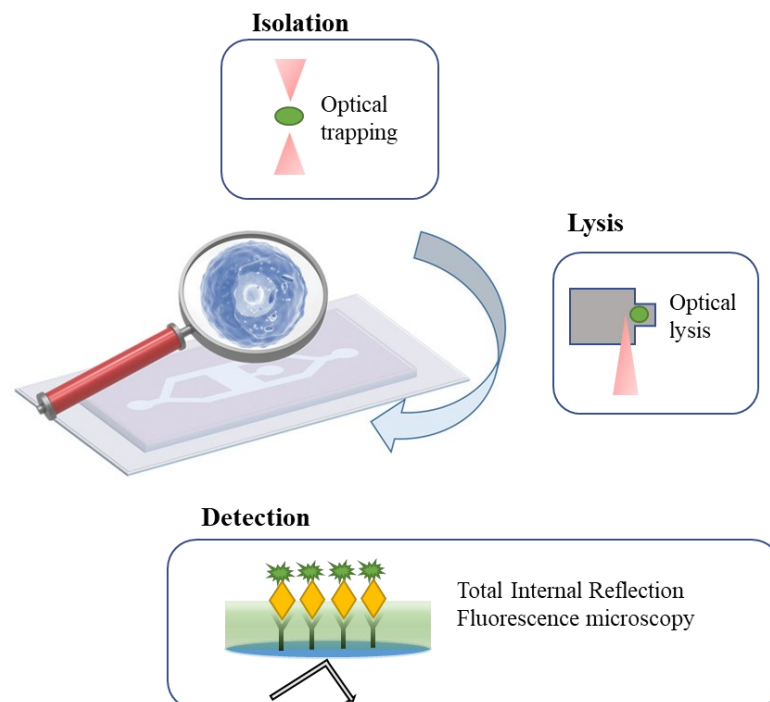


**Figure 4.6:** A schematic depicting the general workflow of the single *GUV* protein pulldown microarray experiment using the *Pulldown Array Single molecule High-throughput (PASH)* chip. Image modified from the following reference <sup>177</sup>

#### 4.2.3.2 Single Cell Isolation and Trapping

Cell cultures can be easily manipulated using a bench top assay or conventional pipettes in volumes typically within the order of microlitres to millilitres. The isolation of individual cells or in this case, GUVs is a precondition for single-cell proteomics analysis. The maintenance of the cellular viability for downstream analysis is key, thus development a mild and efficient isolation approach is key. The ability to manipulate and isolate single cells within predetermined locations and compartments assist in the ability of the platform to perform proteomic measurements, hence making the microfluidic format an ideal candidate for single cell studies. The type of isolation developed using a microfluidic platform can be mainly divided into two main classes; those based on microstructure trapping, such as hydrodynamic, droplet, valve-based and microwell techniques and those based on an external force such as dielectrophoresis and optical and acoustic techniques. The method utilised in this thesis is that of optical trapping. Optical trapping is a powerful laser-based technique that can produce forces within an ideal magnitude to manipulate the cells and subcellular components without denaturing it. It works on the principal a steep spatial light gradient created by using a tightly focused laser beam through an objective lens. The placement of dielectric particles such as cells or vesicles placed within this gradient experience a force in the direction of the greatest intensity, thus drawing the particles towards the focal point of the laser. A scatter force given off by the laser beam also moves the particle along the direction of the beam propagation. This scatter force is a result of the forward momentum transfer between the photon on to the object that is along the beam path. When these two forces

are in equilibrium, the particle is therefore trapped. The position of the cell can be then manipulated by moving the position of the trap within the microfluidic device. The particle should stay trapped in place provided that the drag force on the vesicles does not exceed the trapping force of the laser. The use of optical lasers allows for a stricter cell isolation technique as specific GUVs can be chosen based on criteria such as size. The ability of optical trapping to alter the trajectory of a particle have been well exploited in the microfluidic sorting applications. For instance, Buican et al.<sup>185</sup> developed a system in which cells were propelled by a laser along a default path and sorted into a separate channel by an orthogonal deflection beam upon entering the chamber. Bolognesi et al.<sup>186</sup> also demonstrated the use of an optical tweezer set up to selectively connect vesicles from different sub-populations to generate a network of user-defined architectures. These systems were derived based upon the ability to compartmentalise different chemical species.

The use of optical trapping and manipulation does not require any on-chip modifications and represents a simple system to both fabricate and operate. It does however require the integration of an optical setup on the wider component of the experimental setup. Another downside to this method is that the use of this technique is limited to the field of view of the objective however, despite this, it still remains the most precise method in comparison. Arai et al. demonstrated this by showing the use of optical traps to tie knots in individual actin filaments and strands of DNA.

#### 4.2.3.3 Lysis Method

Following the isolation of the vesicles or cells into individual chambers of the microfluidic device, single cell lysis is critical in extracting the intracellular components. The methodology that is used is chosen with comprehensive consideration of the target molecules, throughput, cell damage as well as the integration with microfluidics. The key criteria in this case would be to ensure the lysing of the cell preserves the integrity of the relevant species at their pre lysis concentrations upon release. Though there are a variety of different lysis options such as electrical, chemical, mechanical, and acoustical, the choice of lysis method used in this thesis was that of optical lysis. This was achieved by focusing a high energy laser pulse into the medium surrounding the vesicle. This produces a cavitation bubble that is capable of rupturing the membrane surrounding the vesicle, therefore releasing the content encapsulated within into the analysis volume. With respect to the use of optical lysis in cellular lysis, Rau et al.<sup>187</sup> used time resolved imaging to determine the primary agent of lysis on a monolayer of cell is the expansion of the cavitation bubble when a pulsed laser is focused at a distance of 10  $\mu\text{m}$  above the monolayer. The maximum radius of the cavitation bubble was found to be greater than the lysed cells. This indicated that the shear stress produced by the displacement of the bubble expansion resulted in the lysing of the cell.

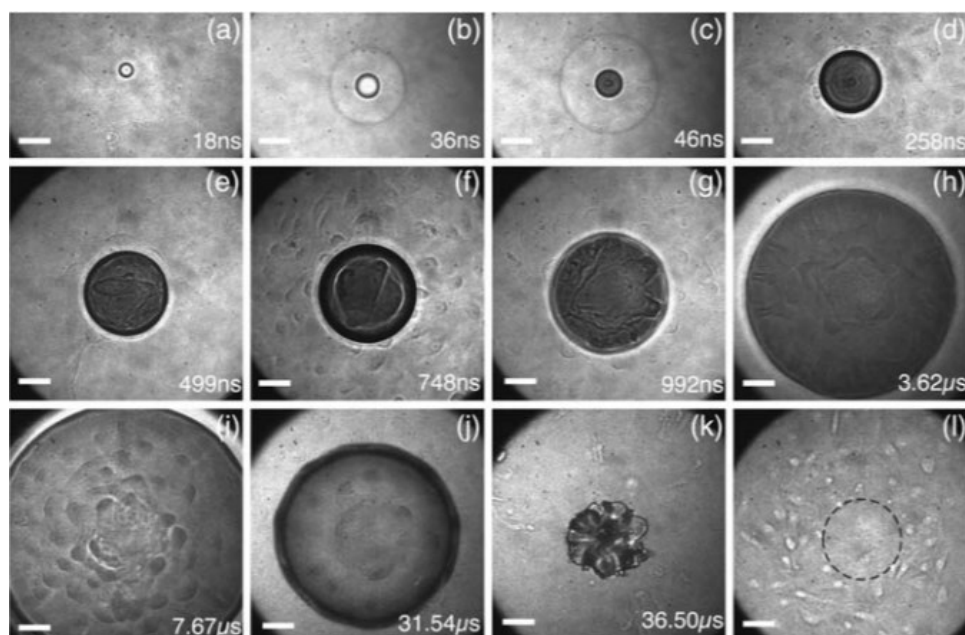


**Figure 4.7:** Time-resolved image series showing the process involved in the lysis of a cell using optical lysis. Plasma formation (a) Shock wave propagation (b-c) Expansion of cavitation bubble (d-i) and the subsequent collapse (i-k). Image is reproduced from reference <sup>187</sup>

The use of optical lysis method is best suited for this work as it offers the highest temporal resolution in comparison to the other methods, and can be used for either single or multiple cells, it is easily compatible with a variety of downstream techniques. Importantly, this method can be easily integrated onto a microfluidic platform with no spatial restrictions on where lysis can occur. In addition to this, the use of optical lysis does not impose any on-chip requirements therefore making fabrication of the microfluidic platform itself simpler.

#### 4.2.3.4 Detection

The measurement of the protein content released from the lysed cell or vesicle is the final step in carrying out single cell proteomics. Usually found in higher quantities than DNA or mRNA, proteins are a difficult target as they cannot be amplified, and their identification is not always straightforward. The protein of interest may be present at

single copy numbers or be highly abundant, therefore the chosen analysis method must have an appropriately wide dynamic range of detection.

In the experiments carried out within this thesis, the protein detection system consisted of a biotinylated BSA that was printed onto the planar surface of the substrate. The system that was developed here exploited the strong binding affinity between streptavidin and biotin as the sole purpose of the assay was to ensure the accurate quantification of the protein content that was encapsulated within the GUV. On the other hand, the detection format of the protein microarray is achieved using a fluorescence-based readout coupled with TIRF microscopy.

### **4.3 Experimental Methods**

#### **4.3.1 Fabrication of Pulldown Array Single-molecule High throughput (PASH) chip**

Based on previous work carried out in the group, a microfluidic platform was prepared for the absolute quantification of molecules encapsulated within the GUVs. The design of the microfluidic chip (**Figure 4.8**) used for the single GUV pulldown experiments consisted of a main channel (1 mm × 36 mm × 35 μm; width × length × height) connected to 100 individual analysis chambers (300 μm × 300 μm × 32.5 μm) with a resultant volume of 2.93 nL for individual analysis chambers. Additionally, the chip consists of 25 chambers on the flow lane. These chambers were used to as a quality control check of the microarrayed antibody spots.

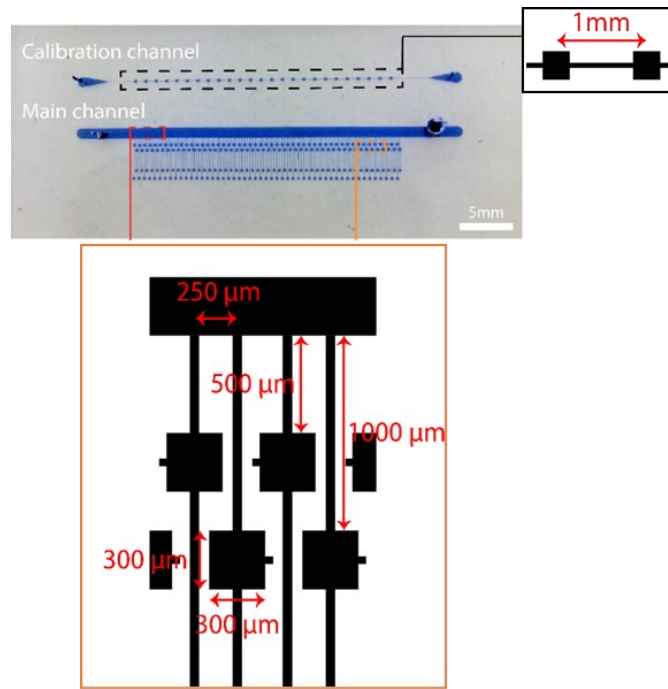


**Figure 4.8:** The schematic of the Pull-down Array Single-molecule High-throughput (PASH) chip. Each of the device consists of a main channel that is connected to 100 individual analysis chambers. The length of the main channel is 36 mm, with a height of  $35\mu\text{m}$ . The volume of each of the chamber is approximately 2.93 nL.

#### 4.3.1.1 Photolithography of Microfluidic Silicon Wafer

The PASH chips are designed and manufactured using well known photolithographic techniques outlined in **Figure 4.9**. All steps of the photolithography process take place in the cleanroom in which the environment is free from any dust particles that could interfere with the masking process.

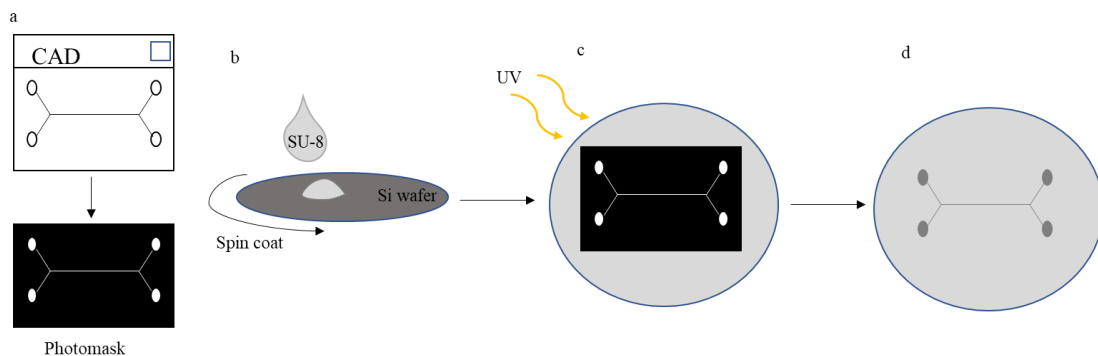


**Figure 4.9:** Major steps involved in the photolithography of producing silicon wafer for the fabrication of microfluidic devices. a) The design of the channels is drawn up in a CAD program which is then used to produce the photomask. b) An epoxy photoresist, SU-8 is spin coated onto a silicon wafer. c) The

*photomask is applied on top of the coated wafer and is exposed to UV rays. d) The exposure to UV rays causes SU-8 to form crosslinks and solidify. This allows the design to be etched onto the surface of the wafer. The design presented here is an example and does not reflect the design of the microfluidic chip design used in this thesis.*

The process begins by designing the general layout of the microstructures and channels of the microfluidic devices using a computer aided design programme (AutoCAD, Autodesk Inc.) Depending on the final requirements of the device, the design was commercially printed either on a photographic film, or a chromium-glass photomask. Generally, film masks are sufficient for designs with features that are no less than 10  $\mu\text{m}$ . For designs containing features that go down to the sub-micron level, a chromium mask is required. The design of the mask is such that the regions containing microfluidic patterns transmit UV light whilst the rest of it is opaque. SU-8 2035 (MicroChem), a negative epoxy photoresist is applied on to a 100mm silicon wafer to form a negative pattern with respect to the geometry of the channel. The SU-8 is applied on to a silicon wafer via spin coating at the appropriate speed as outlined in the data manual of MicroChem. The thickness of the SU-8 layer is dependent on the speed of the spin. The wafer is then pre-baked at 65 °c before being exposed to intense UV rays via the transparent parts of the photomask. Upon exposure, the SU-8 forms crosslink and solidifies. The non-crosslinked parts are then dissolved and washed away using SU-8 developer (Microchem) or propylene glycol monomethyl ether acetate (Sigma Aldrich) hence allowing the design to be etched on to the surface of the wafer. The wafer is washed with Isopropanol and dried under a stream of nitrogen. The wafer is then silanised by coating the surface with 1,1,2,2-perfluorooctyltrichlorosilane (Sigma Aldrich). This provides the wafer a hydrophobic coating which allows the cured PDMS

to be peeled off the surface effectively whilst extending the lifetime of the master over the course of PDMS mould cycle.

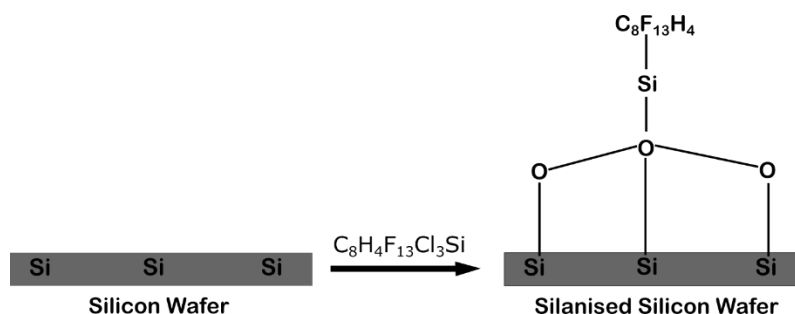


**Figure 4.10:** The figure above describes the chemical reaction scheme of the silanisation process that takes place in the last step of photolithography.

#### 4.3.1.2 Soft Lithography of PDMS Chips

All the microfluidic devices used in the single GUV pulldown experiments composed of Polydimethylsiloxane (PDMS). Slabs of PDMS were also prepared to be used as wells and reservoirs on the assembled microfluidic device. These were all produced using the Sylgard 184 Silicone Elastomer Kit (Dow Corning) consisting of a pre-polymer and curing agent. These two components were mixed together at a 10:1 ratio. The mixture is mixed thoroughly using a pipette tip until it forms a homogenous liquid. This is then poured either on to the silicon wafer mould (Microfluidic device) which was produced using soft lithography method or a clear plastic dish (PDMS sheet). The silicon wafer is then degassed under vacuum for about 10-15 minutes to remove any air bubbles. The PDMS is then left to cure at room temperature on a flat surface for 24-48 hours, or until set solid. It is also possible to cure PDMS quicker at a higher temperature by placing it in an oven, however, the heat causes the expansion of the silicon wafer which made it unsuitable to be used for these set of experiments. Once it is cured, the

chips are then cut from the mould using a scalpel. The inlet/outlet holes are then drilled at the required location before being washed with copious amounts of ethanol to remove any PDMS debris and air dried with nitrogen.

#### **4.3.1.3 Surface Functionalisation**

The surface on which the capture agent is printed on plays an important role to ensure that the signal obtained is not masked by any background noise. The functionalised glass coverslips were prepared in house. To prepare BSA-coated coverslips, glass coverslips (Schott, UK) were placed in a container and rinsed using ultra-pure water three times, followed by 96% ethanol, and ultra-pure water once again. Following this, the glass slides were then ultrasonicated using 1M KOH for 15-20 minutes. Upon completion, the coverslips were then washed and rinsed with 96% ethanol three times, followed by ultra-pure water, and 96% ethanol. The container is then filled with 96% ethanol and ultrasonicated for another 20 minutes. The glass slides were then removed from the container, washed with ethanol and dried with a stream of nitrogen. 100 $\mu$ L of 4% Bovine Serum Albumin (BSA) in PBS (PBSA) is pipetted on to the surface of the coverslips before being sandwiched with another clean coverslips to obtain even coating. The coverslips are then placed in a 60 °c oven for 2 hours. Once dried, the coverslips are washed with ultra-pure water to remove excess PBSA, dried with a stream of nitrogen and placed in coverslip holder and stored at 4 °c before being used.

#### 4.3.1.4 Microarray printing

Advances in genomics and proteomics have led to the development of microarrays generated by the spotting of biomolecules on a solid surface at high spatial density.<sup>188</sup> This allows for the investigation of thousands of targets simultaneously. Early technology of these arrays was DNA-based, however, it has since advanced to protein-based microarrays focused on either function-based microarrays or abundance-based microarrays.<sup>188</sup> The PASH chip uses the basics of a capture microarray where a capture agent is immobilised on a suitable capture surface via contact printing and is housed within a set of microfluidic chambers which provides sensitivity required to measure protein on a single cell level.

Owing to the strong binding affinity between streptavidin and biotin, biotinylated BSA (bBSA) were used as the capture agent in the microarray system. The microarray spots were printed using a contact microarrayer (Omnigrad Micro; DigiLab, UK) and a 946MP2 stealth pin (ArrayIt, USA). Prior to printing, the pin is washed thoroughly by ultrasonication with a surfactant-based cleaning solution (ArrayIt, USA), rinsed with ultra-pure water, and dried with a stream of nitrogen. The environment humidity within the microarray printer was set to 65% to ensure no significant evaporation takes places. The microarray printing buffer consisted of 3x saline sodium citrate buffer, 1.5 M betaine supplemented with 0.01% SDS was optimised by previous work carried out in the group. The printing solution consisted of a 1:1 mix of the printing buffer and bBSA solution, with a final concentration of 0.5 mg ml<sup>-1</sup> in the deposited protein spot. To ensure a homogenous deposition of the capture agent, a pre-print sequence is included. The pin prints three columns of spot lanes (25 spots per lane) before moving on to the

functionalised coverslips. Prior to printing on to the functionalised coverslips, the immersed pin prints 30 spots on the dummy coverslip first. Upon inspection of the preprint slide, it was observed that the diameter of the first few spots are larger than the other spots in the same run. This implementation of this step ensures that the spots printed on the functionalised coverslips will be homogenous irrespective of the number of prints. The microarrayed spots are printed on the functionalised coverslip at position determined by the analysis chambers of the microfluidic chip. The printed coverslips are stored at 4 °c before being used.

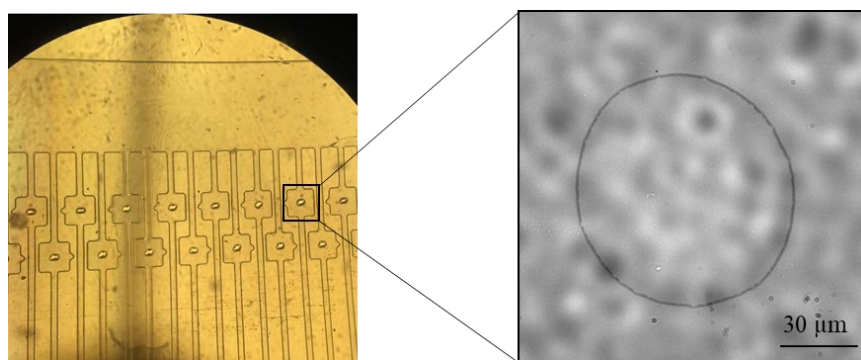


**Figure 4.11:** An exemplar image of a printed and aligned microarrayed spot within the analysis chamber of the PASH chip imaged under bright field with 4X magnification. The inset image shows the arrayed protein spot viewed under a 60× objective.

#### 4.3.1.5 Spot alignment

To assemble the device to be used in experiments, the individual analysis chambers on the microfluidic chip must be aligned to the microarrayed spots. The printed biotinylated spots are aligned to the analysis chamber using a custom built alignment rig (**Figure 4.12**). The rig allows for the translation of the coverslip relative to the PDMS chip in the x, y, z dimension as well as the rotation of the PDMS along the x-y plane. Upon alignment of the spots to the chamber, the PDMS chip is lowered on to the coverslip until contact bonding is occurs. The strength of contact bonding is not

permeant however is strong enough to withstand the flow rates used in the experiments. In some cases where a stronger bond is required, the coverslip and the PDMS chip are bonded to one another using a process called plasma bonding. In this case, this method is not used as it may strip away the functionalised layer present on the coverslip. Two square PDMS pieces are cut, and plasma bonded to each of the inlets. These pieces are used as the solution reservoirs.

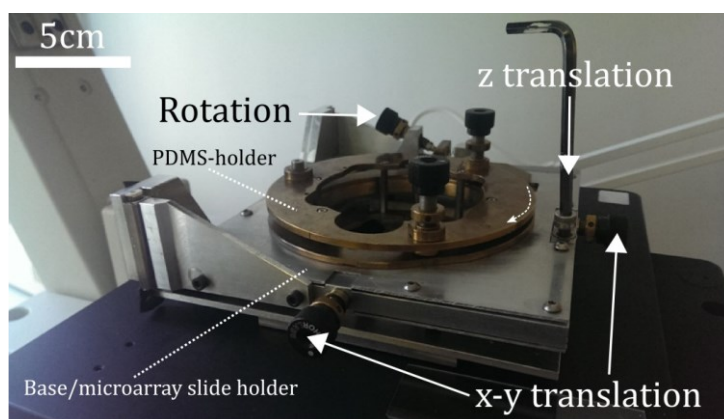


**Figure 4.12:** The custom made alignment jig used to align the microarrayed slide to the analysis chambers of the chip. The translation screws allow for fine adjustments of the PDMS piece relative to the position of the glass slide. Image reproduced from Magness. A PhD thesis 2017, Imperial College London.

### 4.3.2 Inverted Emulsion Phase Transfer for GUV Generation

The protocol for the formation of GUVs have been described in detail in Chapter 2.3.3. Briefly, this method involves the transfer of a lipid stabilised water-in-oil emulsion across a packed oil water interface. The transfer process of the emulsion through this interface is generally driven by the density difference between the internal and external aqueous environment. In this set of experiments, the internal aqueous solution used was 200 mM sucrose with a fluorescently labelled streptavidin ( $0.215 \text{ mg mL}^{-1}$ ) as the encapsulated molecule. The external aqueous environment consisted of 200 mM of glucose dissolved in PBS. The generated GUVs were resuspended in the glucose

solution before being transferred to the reservoirs that are plasma bonded to the assembled microfluidic device. The protocol for the generation of GUV for the use of single molecule/vesicle pulldown experiments is as illustrated in **Figure 2.11** in chapter 2.

### **4.3.3 Device Filling and GUV loading**

The fully assembled PASH chip devices were filled immediately prior to GUV pulldown experiments with solution consisting of 200mM glucose and 4% BSA in Dulbecco's phosphate buffer saline. The filling occurred by placing approximately 500  $\mu\text{L}$  of the solution over the inlet and outlet reservoirs that have been attached to the device. The chip was then placed in a vacuum desiccator for no longer than 10 minutes to degas the device. The device was then placed and secured on the microscope stage and was fitted with a tubing attached to a microfluidic syringe pump system (LabSmith Inc). The GUV pellets are gently broken up and resuspended in 200 mM glucose only prior to the experiment. The now single GUV solution is deposited into the reservoir at the inlet. The vacuum pump then draws the solution of the GUV in at a flowrate of 2.5  $\mu\text{L min}^{-1}$ . The use of high flow rate could potentially introduce air bubbles into the main channel of the device and lead to the delamination of the device, hence making the device unusable. The flow of the device is stopped after 10  $\mu\text{L}$  of solution is pulled through the device. Once in the main channel, individual GUVs are identified using fluorescence microscopy and isolated into analysis chambers by optical trap.

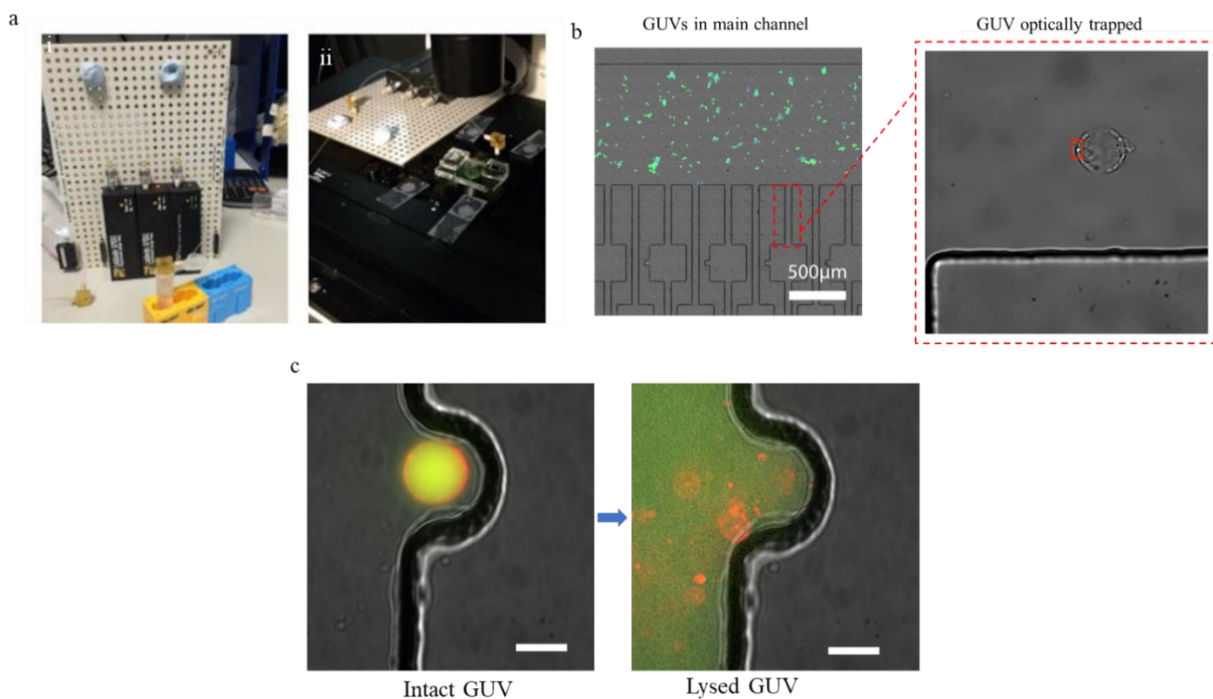


**Figure 4.13:** a) i) The microfluidic pump syringe system setup used to introduce the GUVs into the assembled PASH chip ii) The complete set-up of the pump attached to the outlet on the chip. The pump is mounted on the microscope stage as above. b) The loading of the GUVs into the main channel followed by the use of optical tweezers to individually isolate the vesicles into the chambers. The red square is used as a reference point at which the laser is focused at. c) An example of the process of optically lysing the GUV to release the contents into the chamber. The labelled lipid material is compromised and the intraGUVular material is dispersed within the analysis chamber, free to be assayed.

#### 4.3.4 Data collection and Analysis

Throughout the course of the experiment several sets of images were acquired to be used for data analysis. The PASH chip readout is performed using a single-molecule total internal reflection fluorescence (TIRF) microscopy whilst fluorescence microscopy is used to obtain images of the isolated GUVs.

- a) **Spot Background Image:** Prior to the filling of the device with the glucose solution, individual bright field images of the microarrayed spots were acquired using the 60 $\times$  objective lens. This was performed to ensure the quality of the printed spot.

**b) Background Image:**

Two background images were acquired using 60× TIRF measurement.

**i) Spot Background**

The spot background was acquired after the chip was filled with the background solution. This was to ensure that the spots were not affected by any impurities that may be present within the solution.

**ii) Pre-Lysis Spot Background**

These images were obtained prior to the optical lysis of the individually isolated GUVs. The single molecule (SM) count used to determine the diffusion background. The SM count here in this data set is a result of the possible diffusion of the streptavidin solution from ruptured GUVs in the main channel down the analysis chamber.

**c) Fluorescence GUV Image:** 60× FITC image of the GUVs that were isolated are acquired. The images were used to measure the area of the vesicles and subsequently the volume of the GUVs. A fluorescence image sweep was also carried out across the device upon lysis as a confirmation to ensure the GUVs have been fully lysed.

**d) Post Lysis TIRF Image**

The raw data obtained from the experiment consists of a sequence of single molecule fluorescence images of the analyte complex on the printed antibody spot. The images obtained were;

## 1. Time Series:

The sequence of images taken over a period of two hours showing the increase in the fluorescence due to the accumulation of the analyte on the spot. The sequence of images were used as a guide to confirm that the assay has reached equilibrium

## 2. Single Time point:

A single image acquired at a specific time point as the assay has reached equilibrium after 30 minutes. This image is subsequently used as part of the data analysis to obtain SM counts of the encapsulated streptavidin molecule.

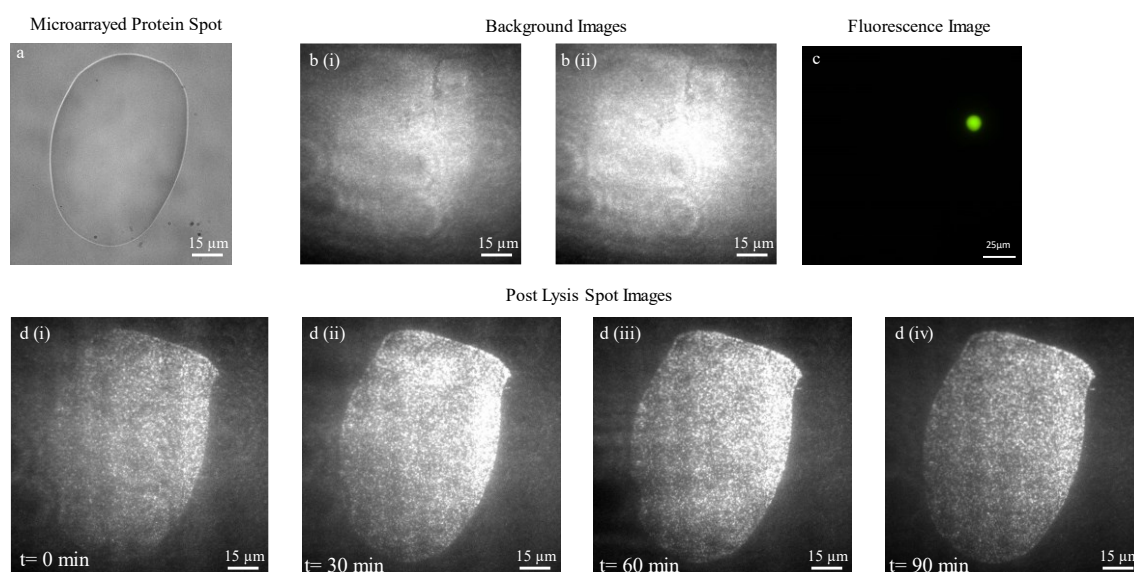


**Figure 4.14:** The different type of images acquired over the duration of a single GUV pulldown experiment. a) An image of the printed antibody spot on the surface of the substrate acquired prior to the filling of the chip. b) The background images readout i) Spot background image obtained after the chip has been filled with the blocking solution of 200mM glucose and 4% BSA. ii) Spot background image obtained after the optical trapping of the GUVs and prior to optical lysis. The resultant SM count in from this set of images are used to determine the contribution of diffusion background. c) An example of a  $60\times$  FITC fluorescence image of individually isolated GUVs in the chambers of the chip. These images are used to obtain the size information and the fluorescence information of the GUV. d(i-iv) The TIRF readout of a time course single molecule data viewed using under 488 nm illumination.

Data analysis of the images are performed using a series of custom developed single molecule counting algorithm in ImageJ that was written by my doctoral supervisor Dr. Ali Salehi-Reyhani. This is discussed in detail in section 2.5. Briefly, a 2D Gaussian peak fitting is performed by implementing a GDSC plugin originally developed by Alex Herbert for ImageJ/Fiji.<sup>90</sup> The total number of single molecules are defined by the peaks present in the image which converge to a 2D gaussian profile. This is determined by the least square fitting of the data. This is usually the case for non-congested images, where there is minimal overlap between the individual peaks. However, in images where there is a significant degree of single molecule overlap, the single molecule count is estimated by dividing the total intensity of the thresholded image by the average single molecule intensity.

#### 4.3.5 Calibration Curve

Standard solutions of protein with known concentrations are flowed through separate PASH chip devices and allowed to reach binding equilibrium with the binding spots that had been aligned to each of the chamber. The protein solution is diluted with 200 mM glucose with 4% pBSA alongside AF488 using **equation 4.1**.

$$V_1 C_1 = V_2 C_2 \quad \text{Eq. 4.1}$$

Where V is the volume of the solution and C is the concentration of the solution.

The concentration series is performed to determine the single molecule count at equilibrium for known concentrations of the AF-488 Streptavidin protein from 10 to 10<sup>9</sup> molecules per chamber. The SM count obtained from each individual data set is plotted against the known concentration to build a calibration curve. The curve is then fitted using a 5-parameter logistic fit. The fitted function enables the single molecule

counts obtained from lysed single GUV to be converted exact concentration values of streptavidin per vesicle.

## 4.4 Results and Discussions

### 4.4.1 Pulldown Array Single Molecule High-throughput (PASH) chip Development

The following section is a discussion on the method development of the PASH chip used to obtain the absolute quantification of the encapsulated streptavidin molecule within individual GUVs. Several parameters were taken into consideration in relation to the platform and will be discussed in detail in the following sections.

#### 4.4.1.1 Lipid Concentration

The multiple steps involved in the inverted emulsion method can lead to unseen errors within the production of GUVs leading to a low yield. An extensive study optimising various parameters of the inverted emulsion-based method to maximise the yield of GUVs was recently carried out by Dimova et al.<sup>57</sup> One of the parameters that was tested out to help improve the yield of GUV production was the lipid concentration.

Using a range of lipid concentration of 2 mg mL<sup>-1</sup>, 1mg mL<sup>-1</sup>, 0.5mg mL<sup>-1</sup> and 0.13 mg mL<sup>-1</sup>, the effect of the lipid concentration upon the formation of the vesicles were investigated. **Figure 4.15** shows the GUV yield produced using the varying concentration of lipid in the mineral oil solution. The use of a reduced concentration within the solution shows an overall reduced quantity of GUVs within a population.

The concentration of the lipid within the solution was varied using the volume of the mineral oil added to the lipid film. This variation of the lipid concentration has a direct influence upon the formation of both the interface as well as the water-in-oil emulsion. At lower lipid concentrations, the unavailability of lipids to cover the interfacial area of the vesicle may result in the release of the internal solution into the background solution.

Additionally, with low concentrations of the lipid, the interface may not be sufficiently replenished, thus causing poorly formed unilamellar vesicles. Therefore, it is important that the interfacial lipid monolayer is sufficiently assembled prior to the addition of the emulsion.

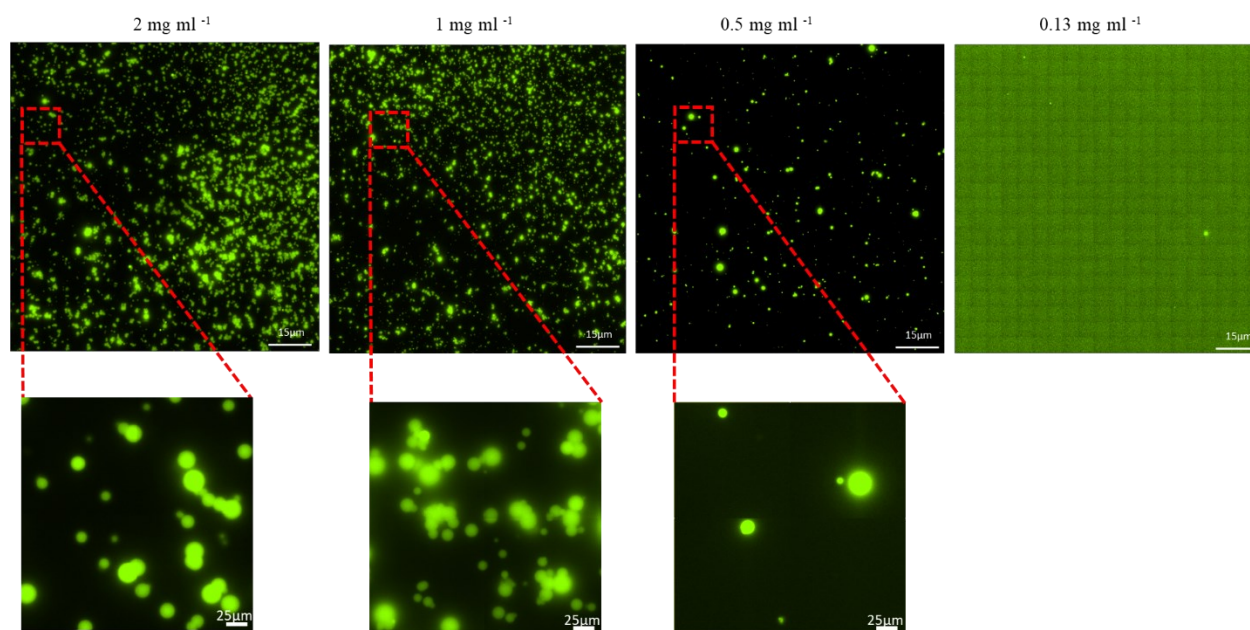


**Figure 4.15:** GUVs encapsulated with streptavidin Alexa Fluor 488 (green) were resuspended in collection buffer systems containing 200mM glucose in PBS. The concentration of lipid used within the lipid oil solution varied between 2 to 0.13 mg ml<sup>-1</sup>. The GUVs were incubated at room temperature for 30 minutes prior to imaging. The images here indicate the reduced yield of the GUVs as the concentration of lipid in mineral oil is reduced.

Moving forward, 2 mg mL<sup>-1</sup> was used as the final lipid concentration for the formation of the vesicles.

On the other extreme, it is also possible to oversaturate the solution with lipid. This was tested out by dissolving the lipid film in mineral oil to obtain a final concentration of 10mg mL<sup>-1</sup>. This led to the crashing out of the lipid into the solution as shown in the **figure 4.16**. The oil-lipid solution could not be used to produce GUV. The crashing out of lipid is due to the possible aggregation of lipid molecules within the given area. Due

to the high concentration of lipid molecules, the probability of the lipid molecules coalescing with one another is significantly higher.

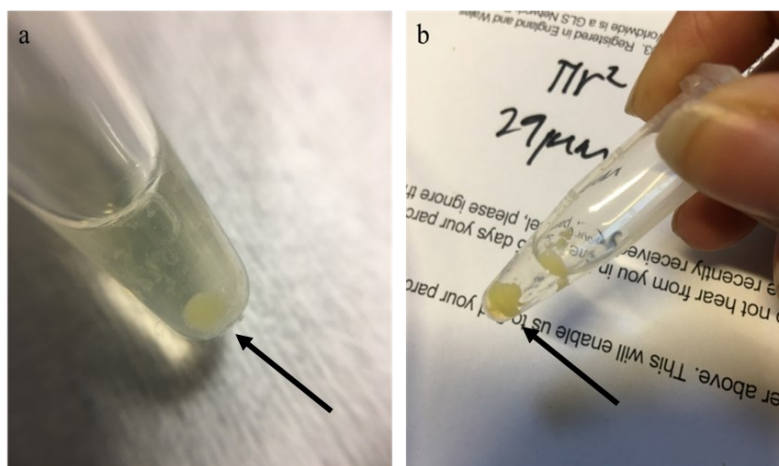


**Figure 4.16:** The lipid in oil mixture from using different concentration of the lipid. a) The pellet at the bottom of the Eppendorf shows the successful generation of GUVs using  $2\text{mg mL}^{-1}$  lipid. b) The lipid in oil solution was unable to be used as to form GUVs as it crashed out due to the oversaturation of the lipid molecules in the oil.

#### 4.4.1.2 Optical Trapping Time Frame

The GUVs were drawn into the main channel using a microfluidic pump at a flow rate of  $0.25\ \mu\text{L min}^{-1}$ . Upon introducing the GUVs within the main channel, the GUVs are allowed to settle into the main channel prior to optical trapping. Optical tweezers are then used to individually isolate the vesicles into the respective analysis chamber. Due to the close similarity in the refractive index between the external buffer and the internal solution of the GUV, observing the vesicles using bright field is difficult, thus fluorescence microscopy is used to assist in locating GUVs within the main channel. The large size distribution of the vesicles due to phase transfer technique contributes to the increased time taken to isolate the GUVs. It was observed that the larger sized GUV tends to coalesce with one another or with smaller vesicle when in close proximity. The functionalisation of the surface as discussed in section 3.3.1.2 circumvented the issue

of the vesicles adhering to the glass surface of the device. The increased power of the trapping laser from 400 mW to 700 mW also aided in the process of isolating GUVs.

Despite these precautions, the coalescence of the vesicle still proved to be a major challenge in the single GUV pulldown. In addition, prolonged periods of around 3-4 hours of optical trapping was shown to have a significant impact in the SM count of the spot prior to optical lysis.

During optical trapping, the chambers that were not filled with GUVs acted as control chambers. The average single molecule count of the background is  $526 \pm 191$  molecules per spot. The comparison between the control analysis chambers from the top row and the bottom row show an increase in one order of magnitude. In a test sample of 92 empty chambers, the average SM count in the bottom row analysis chamber is  $1.33 \times 10^4$  molecules per spot whilst the SM count of the top row is  $2.47 \times 10^5$  molecules. The difference in the single molecule counts from the background value shows the possible increased interaction between the streptavidin AF-488 molecule with the biotinylated BSA despite the absence of a vesicle. In theory, as these chambers are control chambers, the SM count should remain relatively at the same value as the background SM count. A possible explanation for the increase of the SM count in both the top and bottom row could possibly be due to the diffusion of the unencapsulated streptavidin solution from the main channel into the analysis chamber. The rupturing of vesicles inside the main channel releases the streptavidin molecules into the main channel. Over time, the molecules most likely diffuse into down the channel and subsequently into both the control and filled analysis chamber. It is also observed that the chamber on the top row is more severely affected by the diffusion affect compared to the chambers on the

bottom row. This is due to the difference in the length of the channels connecting the main channel and analysis chamber. Due to the longer channel length of the chambers in the bottom row, the time taken for the molecules to diffuse down the channel is also longer.

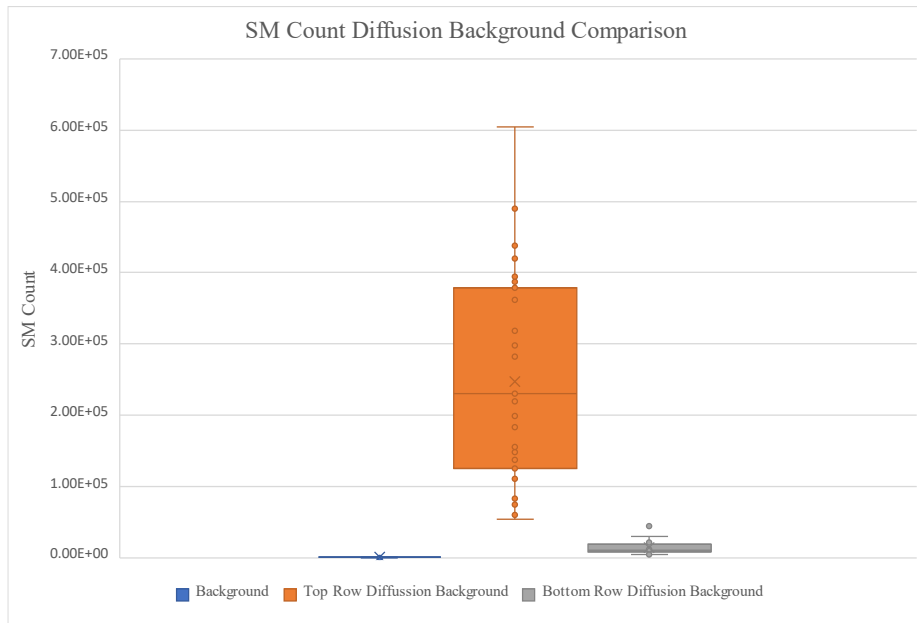


**Figure 4.17:** The comparison of the diffusion background single molecule counts between the control analysis chambers in the device. Chambers that are not filled with a *GUV* are used as the control. The background SM count of the experiment is  $526 \pm 191$  molecules. The bottom row of the device exhibits a significantly smaller change in SM count from the background in comparison to the chambers on the top row.

As discussed previously, the mixing in microfluidics is mainly dominated by diffusion.

The diffusion time is given by

$$t = \frac{x^2}{2D} \quad \text{Eq. 4.2}$$

Where  $t$  is the elapsed time since diffusion began,  $x$  is the mean distance travelled by the solute along the axis and  $D$  is the diffusion coefficient.

The diffusion coefficient can be defined using the Stokes-Einstein equation (**Equation 4.3**).

$$D = \frac{K_b T}{6\pi\eta r} \quad \text{Eq. 4.3}$$

Where  $K_b$  is Boltzmann's constant,  $T$  is the temperature in Kelvin,  $\eta$  is the viscosity of the solution and  $a$  is the radius of the diffusing particle.

Streptavidin is a 52 kDa protein consisting of four binding sites. In water at 295 K, streptavidin molecule has been reported to have a diffusion coefficient of  $6.2 \times 10^{-7} \text{ cm}^2 \text{ s}^{-1}$ .<sup>189</sup> Thus, using this value, the time taken for a streptavidin molecule to diffuse down the channel of the top row with a shorter distance of 500  $\mu\text{m}$  is 33 minutes whilst it would take 2 hours for the streptavidin molecule to diffuse down the channel connected to the bottom row with a distance of 1000  $\mu\text{m}$ . However, we expect the diffusion times to be slightly longer due to the higher molecular weight of the conjugated streptavidin. Taking this into account, the optical trapping time frame was set between one to two hours to reduce the diffusion effect of streptavidin down the channel. Moving forward, only chambers on the bottom row were taken in consideration for the pulldown experiment. In the chambers that were filled with GUVs, the increase in the SM count can be attributed to two factors. One being the diffusion of the streptavidin and the released content from within the GUV. Therefore, during data analysis, a diffusion background parameter is introduced to ensure the final SM count used in the encapsulation efficiency calculation is purely due to the encapsulated material within the GUV.

#### 4.4.2 Streptavidin AF488 and Biotinylated BSA Assay

The primary objective of using this platform is to ultimately understand the encapsulation efficiency of using GUVs as a biomimetic model. From the fluorescence work, we have shown that the production of the GUV using EPT has a wide distribution and to show a positive correlation between the volume and fluorescence with a constant concentration throughout. However, as the value of the fluorescence is of an arbitrary unit, the use of a quantitative method is required in order to obtain an exact concentration value. Thus, to solve and understand this problem, the platform was designed using a validated sandwich assay comprising of Streptavidin AF-488 molecule and Biotinylated BSA.

The interaction between biotin and streptavidin is highly specific and is one of the strongest known non-covalent interactions with a reported dissociation constant,  $K_d$  of  $4 \times 10^{-14}$  M.<sup>190</sup> The rationale behind the use of this particular assay system is on the basis that the ability to chemically attach a biologically active compound with biotin molecule through its valeric acid side chain does not significantly impact the biological and physiochemical properties of the molecule.<sup>191</sup> Streptavidin on the other hand is a tetrameric binding protein. The ability of the biotin molecule to be readily attached to a variety of molecules including large macromolecules such as BSA with minimal impact on its characteristics makes this an attractive platform. The conjugation of BSA on to biotin is relatively common.<sup>192</sup> BSA has often been used as a scaffold to immobilise peptides and small molecules on to the surface of the glass slide to form microarrays.

The inertness of the molecule also makes this is a suitable candidate and is often used as a blocking agent to prevent non-specific probe surface binding.

The presence of four binding sides on streptavidin available for biotin adds another dimension to the already multifaceted system. The addition of a reporter molecule attached to the streptavidin enables the system to be used for multiple purposes. In this case, the streptavidin molecule is conjugated with an Alexa Fluor488 FITC probe. The exceptionally high affinity and stability of the complex ensures a desired conjunction between the biotinylated binder and streptavidin-based probe. The use of the streptavidin-biotinylated BSA complex also amplifies the response signal hence dramatically improving the detection sensitivity. The versatility of the system with minimal tweaks has enabled the use of this system to be used in a variety of affinity capture and immobilisation applications.<sup>193,194</sup> In the future, this assay can be modified and utilised for the detection of other protein molecules using encapsulated within the vesicle.

#### 4.4.3 Calibration Curve of Streptavidin AF488 and Biotinylated BSA Assay

Traditional sandwich assays are frequently used as a tool to detect and quantify specific analytes within biological samples. These samples can easily range from cell culture supernatant, serum, plasma. In the set of experiments run in this thesis, the sandwich assay comprised of a biotinylated BSA as the capture agent with a fluorescently tagged streptavidin as the molecule of interest.

In order to determine the absolute concentration of the streptavidin encapsulated within the vesicle, a standard or calibration curve is produced using a concentration series of the protein. This is carried out using a range of the streptavidin molecules spanning across 9 orders of magnitude from  $10^0$  to  $10^9$  molecules per chamber ( $V_{\text{chamber}} = 2.93$  nL) in separate PASH chip devices each filled directly with the respective solution. The calibration curve was carried out this way in order to ensure the assay environment closely mimics the environment during a single pulldown experiment. The use of the flow channel in order to carry out the calibration curve may require additional parameters to be considered possibly due to the different geometries.

The loss out of the channel can potentially contribute to the loss of the analyte of interest, which is an undesirable process in antibody capture methods. Here, in **figure 4.18**, the background measurements in this system caused by NSB on the surface will be constant whilst the saturation limit defined by the number of antibodies will be constant. The loss of analytes or the affinity defined by the dissociation constant,  $K_d$  between the bound and unbound molecules will not affect these limits. In the limit whereby the rate of loss of the analyte by far exceeds the capture rate defined by the antibody affinity, then little to no signal will be observed. However, in the case where

the rate of capture exceeds the rate of loss, the analytes will be captured. We can optimise the rate of capture by using high affinity capture agents. We can also minimise loss by the design of the microfluidic channels. Ideally, the analysis volume will be closed; however, the loss in the open format of the microfluidic may be minimised by the ratio of the width of the chamber to the width of the channels, the size of the antibody spot within the chamber and the height of the analysis chamber. In our case, the rate of capture is maximised due to the high affinity of streptavidin to biotin. Additionally, the geometry of the chamber, also promotes the interaction however this is limited to the size of the GUV. This aspect of a microarray assay is further explored and discussed in the following reference.<sup>180</sup>

Upon the lysis of the vesicle within the chamber, the diffusion of the molecule is isotropic within the confines of the chamber and the channels. The loss of these molecules is significant; however, the low limit of detection still enables the encapsulation to be assessed. The lower limit of detection does however, affect the minimum concentration that can be measured within a vesicle. The use of the calibration curve allows for the loss out of the chamber and the dissociation constant to be factored out, however, it does not factor out the loss of the molecules due to the encapsulation efficiency of the system.

The calibration curve, **Figure 4.18** of the AF-488 streptavidin in the PASH chip device exhibits a linear region within the range of  $10^5$  molecules per chamber and  $10^7$  molecules per chamber. At  $10^8$  molecules per chamber, the saturation of the spot was observed. This is concurrent with the plateauing of the graph as the concentration is increased by 10-fold. The number of streptavidin molecules captured in the saturating

limit is  $1.91 \times 10^7$  molecules bound to a spot. For a  $100 \mu\text{m}$  diameter microarray spot, we expect density of the biotin molecules to be on the order of or exceed  $2.43 \times 10^3 \mu\text{m}^{-2}$ . For a  $100 \mu\text{m}$  diameter microarray spot, we expect density of the biotin molecules to be on the order of or exceed  $2.43 \times 10^3 \mu\text{m}^{-2}$ .

The limit of detection of the system was determined to be at  $10^3$  molecules  $\text{nL}^{-1}$ . At the lower end of the calibration curve, the signal to noise ratio is lower, therefore most of the single molecule signals are masked by the noise. The addition of the blocking agent onto the surface showed a reduction in the non-specific binding (NSB) of the free streptavidin molecule onto the surface of the coverslip. This was important as an increased non-specific binding could significantly skew the intensity level of the background images. The inflation of the background intensity may then potentially lead to a pronounced undercounting of the true number of single molecules in the image alongside an overestimation of the mean single molecule intensity used to calculate the SM count in congested images.

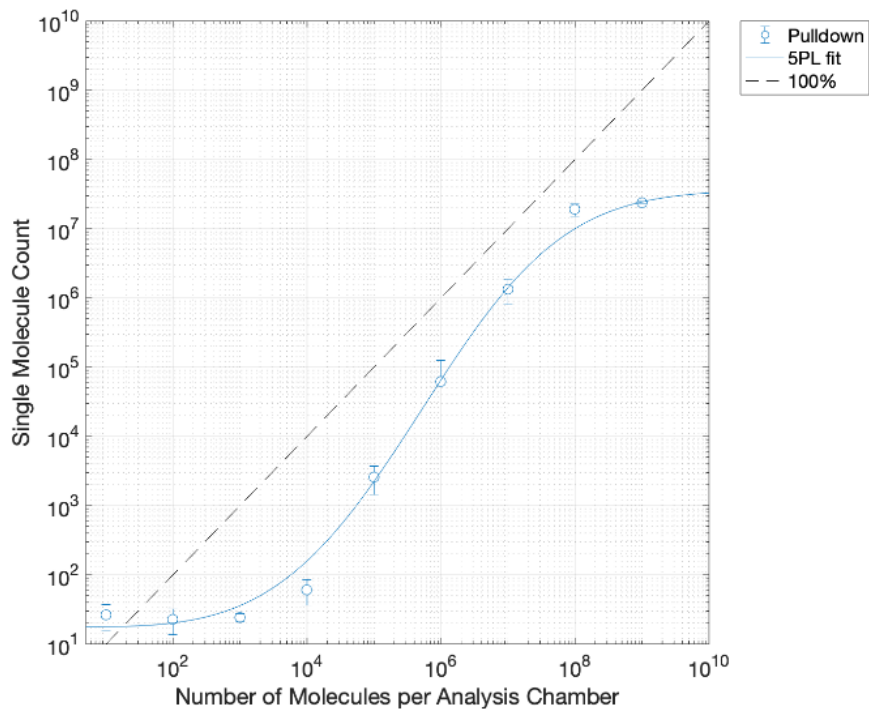


**Figure 4.18:** Calibration curve produced for the AF488 Streptavidin determined for the PASH chip using the analysis chambers (2.93nL). The level of non-specific binding using a BSA functionalised coverslip is  $25 \pm 1.85$  molecules. The dynamic range of the system lie between  $10^5 - 10^7$  at the linear part of the calibration curve. The conversion of single molecule count to the number of streptavidin molecules per vesicles is done by solving the number of streptavidin molecules present per chamber ( $x$ ) based on the detected TIRF signal ( $y$ ). ( $n=25$ )

The curve fit model chosen to carry out the analysis of the calibration plays a vital role in ensuring the accuracy and reliability of the result. Standard immunoassay curves typically produce an S-shaped sigmoidal curve. Logistic regression allows for the curve fitting to be carried out beyond the linear range of the curve and is known as the logistic range. A 5-parameter logistic fit is usually used to fit an asymmetrical curve, similar to the one obtained in these experiments. The use this model offers an extra flexibility as it takes into account the asymmetrical parameter that reduces the lack-of-fit error that would otherwise be present. The 5-PL model fit in this thesis is defined using the equation:

$$N_{SM} = N_{SM\ sat} + \frac{N_{SM\ bkd} - N_{SM\ sat}}{\left(1 + \left(\frac{\log_{10} N_{prot}}{m}\right)^c\right)^A} \quad \text{Eq. 4.4}$$

Where  $N_{SM}$  is the number of single molecules counted,  $N_{SM\ bkd}$  is the number of single molecules counted in the background,  $N_{SM\ sat}$  is the number of single molecules counted at the saturation limit of the antibody spot,  $m$  is the slope parameter of the response,  $c$  is the inflection point parameter, and  $A$  is the control of the asymmetry of the response towards the background and saturation asymptotes.

The calibration curve is produced using a regression fitting algorithm which is intended to minimise the error in the central region of the calibration curve. In our experiments, the seed protein solution used was  $2.037 \times 10^7$  molecules  $\text{pL}^{-1}$ . The resultant SM counts obtained experimentally span between  $10^3$  to  $10^6$ , the approach of using a weighted function at the linear region was used as most of the SM counts from the single GUV pulldowns fall within this region. The calibration curve is then subsequently used to solve for the number of proteins per chamber based upon the  $N_{SM}$  obtained experimentally. The equation above is rearranged for  $N_{prot}$  and is as shown in **Equation 4.5**.

$$\log_{10} N_{prot} = m \left[ \left( \frac{N_{SM\ bkd} - N_{SM\ sat}}{N_{SM} - N_{SM\ sat}} \right)^{\frac{1}{A} \frac{1}{c}} - 1 \right] \quad \text{Eq. 4.5}$$

#### 4.4.4 Encapsulation efficiency

The variation of in the encapsulation efficiency by producing vesicles using emulsion-based phase transfer is apparent upon carrying out a wide field fluorescence scan. With fluorescence microscopy, the brightness of the object can be correlated to the number

of molecules within a particular object. We would generally expect a difference in the fluorescence intensity in GUVs of varying sizes as the intensity is a measure of the total number of molecules within the GUV. Thus, the total measured intensity would be different however, we would not expect a difference in the concentration of the molecules that have been encapsulated. However, a distinct observation that was made is the difference in visible brightness of the GUVs that were relatively of the same size. For instance, GUVs centred around a cluster of other GUVs appear significantly brighter than its surrounding counterpart. In other cases, ‘ghost vesicles’ were observed as seen in **Figure 14.9(b)**. The ‘ghost vesicle’ could potentially be a GUV with zero concentration of streptavidin. This observation is an indication of the presence of a variation in the encapsulation of the molecules. However, it is also highly probable that these phenomena are a result of the leakage of the encapsulated material into the solution.

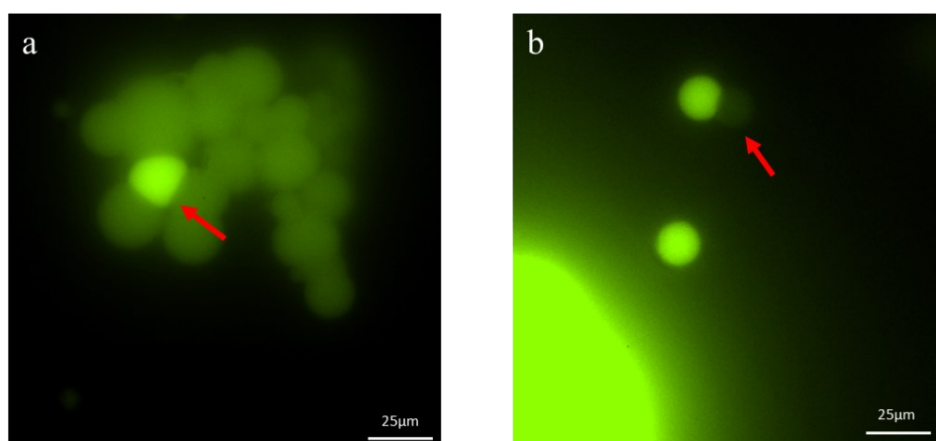


**Figure 4.19:** Exemplar images of GUVs due to the difference in the efficiency of encapsulating molecules within the GUVs produced using emulsion based phase transfer a) An example of a vesicle that is extremely concentrated in a cluster surrounded by other vesicles with a lower concentration. The vesicles surrounding this bright vesicle are all approximately the same size. b) The presence of

*'ghost vesicles' where the vesicle coalesces to an adjacent vesicle that is significantly brighter than itself. This ghost vesicle is often only visible due to the attached vesicle.*

A common phenomenon observed during the formation of GUVs is the fusing of the vesicles. The high number of vesicles produced using emulsion-based phase transfer could lead to the fusion between two or more GUVs. This is mainly observed due to the electrostatic interactions that exist between the fusing membrane.<sup>195</sup> The coalescence of the vesicles leads to the formation of DIB like structures, possibly inducing the destabilisation of the membrane bilayer. This could potentially lead to the formation of transient pores at the point where the bilayer coalesces, leading to the movement of the encapsulated material between the two vesicles. However, the size of the pores formed may not be sufficient enough to facilitate the movement of a large dye molecule such as streptavidin AF-4488 through. Even in the case that the pores are large enough to facilitate the movement of such a large dye molecule, the intensity between these two structures should show minimal difference as the diffusion would have equilibrated over time. In addition to this, the use of a time resolved microscopy further indicates no evidence of any dye leakage from the vesicles. This further strengthens the argument for the need to understand what this efficiency is in order to be able to take it into account especially if these vesicles are being developed to study different biological processes or as drug delivery vessels.

The encapsulation efficiency of GUVs using Emulsion based phase transfer method is calculated as a ratio of the calibrated number of measured streptavidin molecules against the expected number of streptavidin molecules.

$$\text{Encapsulation Efficiency} = \frac{N_{\text{strep encapsulated}}}{N_{\text{strep expected}}} \quad \text{Eq. 4.6}$$

Where  $N_{\text{strep}_{\text{encapsulated}}}$  is the absolute number of encapsulated streptavidin molecules, and  $N_{\text{strep}_{\text{expected}}}$  is the calculated value of the number of streptavidin molecules per GUV.

The expected number of molecules were calculated using the original concentration of the seed solution and the volume of the corresponding GUV. The concentration of the seed solution used in the experiments were  $2.03 \times 10^7$  molecules  $\text{pL}^{-1}$ . The fluorescence intensity measurement of the GUVs obtained prior to optical lysis is used to obtain the radius of the GUV, and subsequently the volume of the GUV.

The SM count obtained from the image after lysis does not correspond to the number of streptavidin molecules encapsulated within the GUV. The increase of the SM count post optical lysis could be due to the diffusion effect described earlier alongside the increased interaction between the biotinylated BSA and the released streptavidin molecule. Therefore, when calculating the final SM count, two different background measurements are considered. The first being the spot background, where the signal of the SM counts are a result of the non-specific binding of molecules present in the device prior to the flow of the GUV solution into the device. The second background, the diffusion background is calculated as the average single molecule counts measured from the increase in the SM counts of the control chambers.

$$Final\ SM_{count} = Total\ SM_{count} - [SM_{diffusion\ bck} - SM_{spot\ bck}] \quad \text{Eq. 4.7}$$

The number of molecules counted per spot using the single molecule detection algorithm is dependent on but not necessarily numerically equal to the number of molecules originally encapsulated within the GUVs. The final  $SM_{count}$  is calibrated

using **equation 4.7** to obtain an absolute value of the number of streptavidin molecules.

Upon obtaining the calibrated value, the encapsulation efficiency is then calculated.

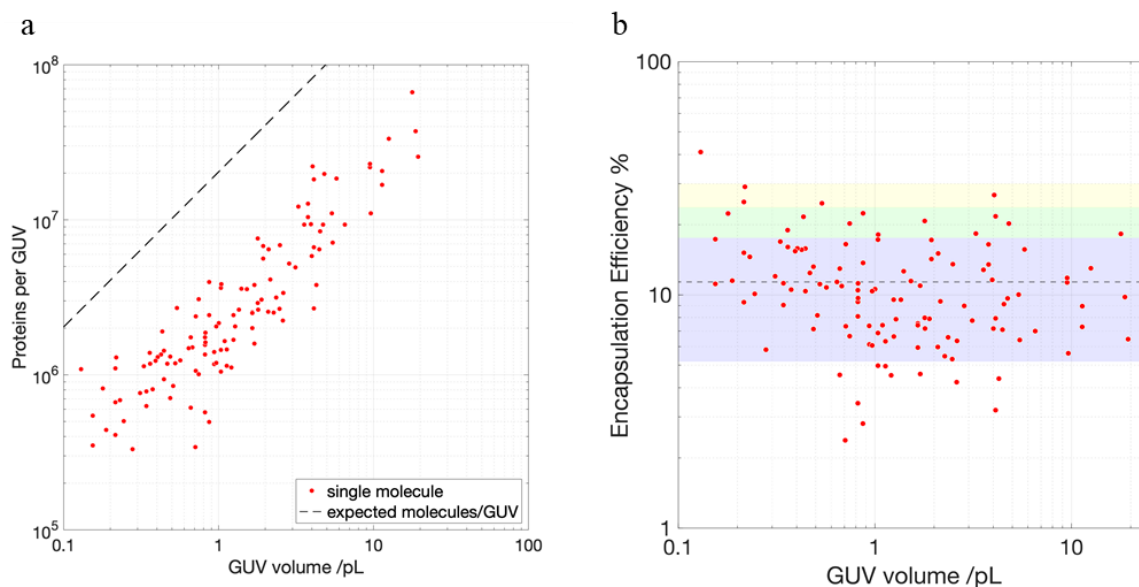


**Figure 4.20:** a) The plot of the volume of GUV against the number of protein molecules in GUV b) The encapsulation efficiency of the vesicles produced using emulsion based phase transfer spans between two orders of magnitude varying from 2.4- 41 %. The orthogonal variation as a function to the volume is significantly apparent. The mean of the encapsulation efficiency was calculated at 11.4% represented by the dashed line. The coloured regions on the graph indicate the confidence level. The purple region represents a 68% confidence interval ( $\pm 1$  standard deviation away from mean). The green region and yellow region represent a 95% (2 standard deviation away from mean) and 99% (3 standard deviation away from mean) confidence interval respectively.

The encapsulation efficiency calculated spanned across two orders of magnitude varying between 2.4 to 41%. **(Figure 4.20)** The weak correlation between the volume and the EE may suggest that the surface area to volume ratio of the vesicles may possibly play a role in understanding the loss mechanism of the streptavidin solution. Knowledge on the distribution of the encapsulation efficiency would allow us to further understand the mechanisms of the formation of GUV. This certainly poses a problem especially in the use of these vesicles as models to study a variety of biological processes containing different biomolecules. The poor EE could potentially compromise the activity of the biosystem in question.

However, one could argue that the poor EE could be compensated for by the increasing the concentration of the encapsulant material. Though this may be sufficient in shifting the modal value of the number of molecules within the GUV populations, it still does not address the variance of the population. The presence of the orthogonal variation is most likely due to the technique used to study the absolute quantification or in the method used to generate these vesicles. The variance could be improved by the optimisation of the phase transfer technique by manipulating a variety of the different variables within the phase transfer technique. In order to fully address the presence of the orthogonal variation, the mechanisms that govern the loss of the proteins need to be further investigated.

The reason for the low encapsulation efficiency of the resultant vesicles is still poorly understood. Several ideas that have been theorised were tested in order to fully understand where and how the streptavidin becomes lost during phase transfer. The EE is calculated based as a ratio of the starting concentration of the seed solution to the calibrated number of molecules captured by the assay system. An initial theory to explain this difference was in the possibility of the ineffectiveness of using optical lysis as a method to liberate the encapsulated material from within the vesicles. The use of optical lysis is dependent on ensuring the single pulsed laser is positioned close enough to the membrane of the vesicle. This allows for the complete rupture of the membrane as a result of the expansion of the cavitation bubble formed. The ineffectiveness of liberating the proteins into the chamber volume may lead to an artificial decrease in the number of proteins captured by the immobilised capture agent. The ineffective lysis of

the GUV could lead to the formation of smaller sized vesicles with some of the protein molecules still encapsulated within it.

Therefore, in order to test if the poor encapsulation efficiency is a result of the laser-based lysis being ineffective, single GUV experiments were performed using RIPA lysis buffer to lyse the vesicles. The lysis buffer (RIPA 10X) is flown through the main channel of the device. The lysis buffer takes approximately 5-10 minutes to completely lyse the GUVs. This was monitored using the gradual decrease of the fluorescence signal of the GUVs within the chambers. The detergent-based buffer solubilises the bilayer by inserting itself into the bilayer and saturating the bilayer. Eventually, micelles are formed as more detergent interacts and saturates the bilayer. During this process, the encapsulated materials are released into the chamber and allows to interact with the capture agent. Once lysis has occurred, the channels are flushed with 4% PBSA. This is to remove the excess RIPA buffer that may possibly compromise the binding assay. The PASH chip is then left for two hours to allow the binding to reach equilibrium, after which TIRF images of each of the chambers are acquired. The single molecule count corresponding to each of the microarrayed spot is calculated to determine the amount of cellular protein expressed in each of the cell. The result (**Figure 4.21**) showed no substantive increase in the measured SM count. The close correlation between the two sets of data provides evidence that the lysis method is not the issue here. This agrees with previous publications that investigated the effectiveness of optical lysis.

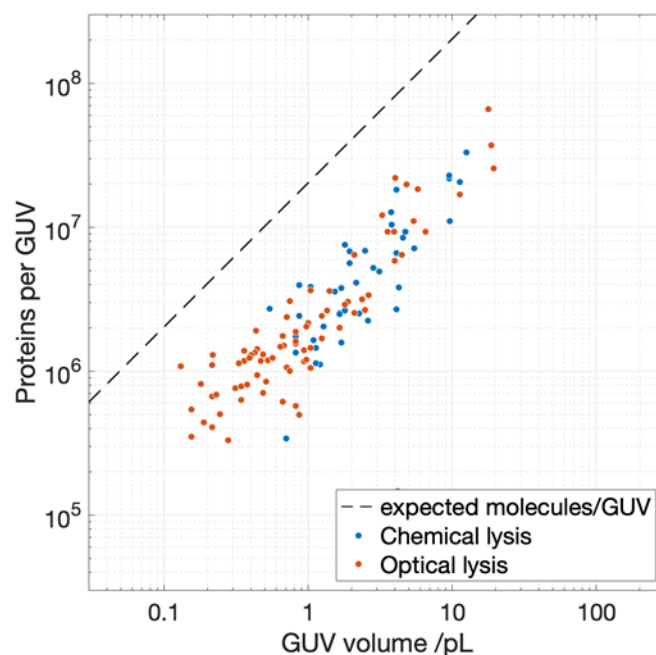


**Figure 4.21:** The calibrated SM count of the single vesicle pulldown experiments obtained using chemical and optical lysis. ( $n=125$ ) The close correlation between the two data sets indicate that the method of lysis is not a contributing factor to the low EE values.

The loss of the protein molecule could also be a result of the rupture or the coalescence of the water-in-oil emulsion. The formation of emulsions occurs spontaneously when two immiscible phases are brought together due to the low interfacial energy. The addition of the lipid molecules that act as a surfactant further stabilises the formation emulsion and reduce the coalescence of the droplets. The size distribution of the emulsion is more tightly controlled however, this tightness is lost as the droplets move pass the interface to form the vesicle. The distribution becomes more widely spread out. It is highly probably that during this stage, the droplets lose its stability and start to coalesce with one another or rupture to form smaller droplets hence spreading out the distribution. This could also explain the poor encapsulation efficiency. Moving forward, efforts has been focused on developing on-chip method to produce the droplets prior to

passing it through an interface to form the vesicles. This will be further discussed in the following chapter.

The results here indicate that during the use of GUVs as simplified cell models, the encapsulation efficiency should be accounted for especially in analysing and interpreting dynamic models. The rate of the encapsulation could be compensated for however by manipulating the starting concentration of the different biomolecules that are to be encapsulated. However, another problem that could likely arise would be the random variation of the EE that exist between one batch of GUVs to another.

The batch to batch variation of the data sets were studied and presented in **figure 4.22**. The box-whisker plot shows the distribution of the encapsulation efficiency across the batches of the GUVs that were formed. The batch to batch variation was minimal with the distribution of the encapsulation efficiency of the GUV to be remarkably similar with a median of 10%. This increased the confidence that the variation of the EE between the batches of the vesicle produced would not remain a problem as they are fairly reproducible. The minimal batch to batch variation between the production of the vesicles ultimately become useful as it allows the user to direct how much is exactly put into the vesicle for the intended application.

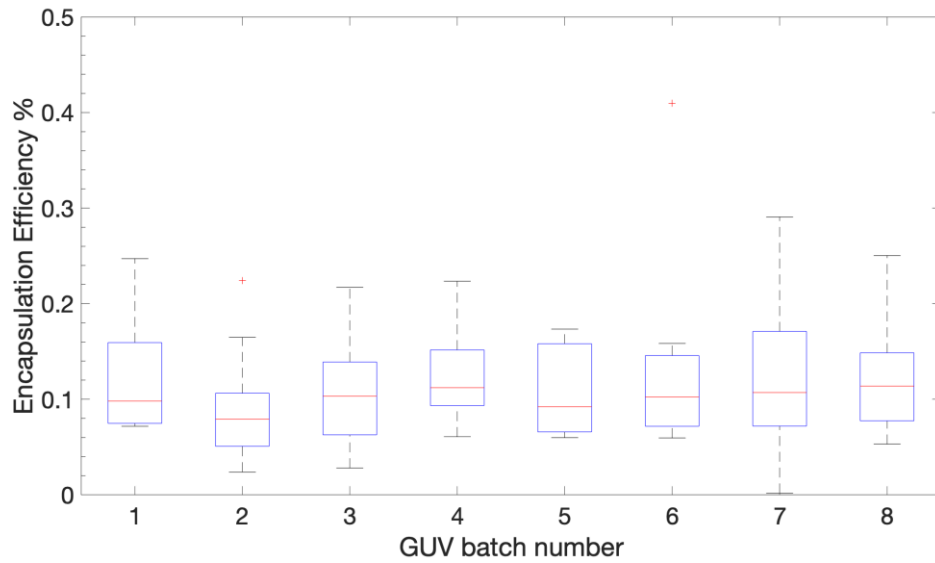


**Figure 4.22 :** The box plot showing the distribution of the encapsulation efficiency as a function of the different batches of the vesicles produced. The horizontal line at the bottom indicates the lowest value of the EE for each of the batch. The red line in the centre of the box is the median EE. The lower edge and upper edge of the boxes represent the lower and upper quartile respectively. The top horizontal line indicates the 98<sup>th</sup> percentile of the populations. Batch 2 and batch 4 have an outlier each on the upper side of data. (Total n=125, Batch 1:8 Batch 2:19 Batch 3:29 Batch 4:14 Batch 5:14 Batch 6:14 Batch 7:20 Batch 8:7)

#### 4.4.5 Application of GUVs

The consistency of the encapsulation efficiency across the different samples opens the door for the structures to be used as a calibration standard. In order to achieve this, the single molecule and fluorescence microscopy data was compared with one another. The GUVs produced using the emulsion-based phase transfer that was analysed using both fluorescence microscopy and single cell pulldown technique were calibrated and compared with one another. With respect to the fluorescence-based data, the resultant log plot of the volume against fluorescence intensity can be presented by the following equation;

$$I_{total} = \mu_{microscopy} \times V^{k_{microscopy}} \quad Eq. 4.8$$

Where  $I_{total}$  is the total fluorescence intensity,  $\mu_{microscopy}$  is the y-intercept,  $V$  is the volume of the GUV and  $k_{microscopy}$  is the gradient of the resultant slope.

Whilst, for the single molecule data, the calibrated number of protein molecules can be plotted with respect to the volume of the GUVs. The resultant log plot can be represented by the following equation;

$$N_{protein} = \mu_{SM} \times V^{k_{SM}} \quad Eq.4.9$$

Where  $N_{prot}$  is the number of protein molecules per GUV,  $\mu_{SM}$  is the y-intercept,  $V$  is the volume of the GUV and  $k_{SM}$  is the gradient of the resultant slope.

The measurement carried out using both of the microscopy technique used here result in a similar distribution shape. Given that both methods have sufficient limit of detection and resolution, the shape of the distribution can be measured to a sufficient degree to allow for comparison. As similar objects have been measured, the shape of

the distribution of the absolute protein number per vesicle as determined by TIRF microscopy corresponds to the fluorescence intensity as measured using fluorescence microscopy.<sup>196</sup>

This leads to the conclusion that there is an equivalence between the single vesicle pulldown measurement and the fluorescence microscopy results.

With the k values on both of the graphs equating to 1 and the volume of the GUVs being equal, the equations above can then be rearranged to obtain the calibration factor that will allow for the direct conversion of the fluorescence data to obtain absolute values.

$$\frac{N_{\text{Protein}}}{I_{\text{total}}} = \frac{\mu_{SM}}{\mu_{\text{microscopy}}}$$

$$N_{\text{prot}} = \frac{\mu_{SM}}{\mu_{\text{microscopy}}} \times I_{\text{total}} \quad \text{Eq.4.10}$$

In which  $\frac{\mu_{SM}}{\mu_{\text{microscopy}}}$  is the scaling factor,  $N_{\text{protein}}$  is the number of protein molecules and  $I_{\text{total}}$  is the total fluorescence intensity.

The ability to calibrate the data obtained from fluorescence microscopy to absolute values is desirable as the information obtained from microscopy are expressed in arbitrary fluorescence units, often times meaningless beyond the relative assessment of the protein encapsulation. The microscopy data was then calibrated using this calibration factor was plotted on to the same data set and the single molecule pulldown data. The mathematical manipulation of the data would obviously lead to the data corresponding to one another however, the variance of each of the method is comparable to one another.

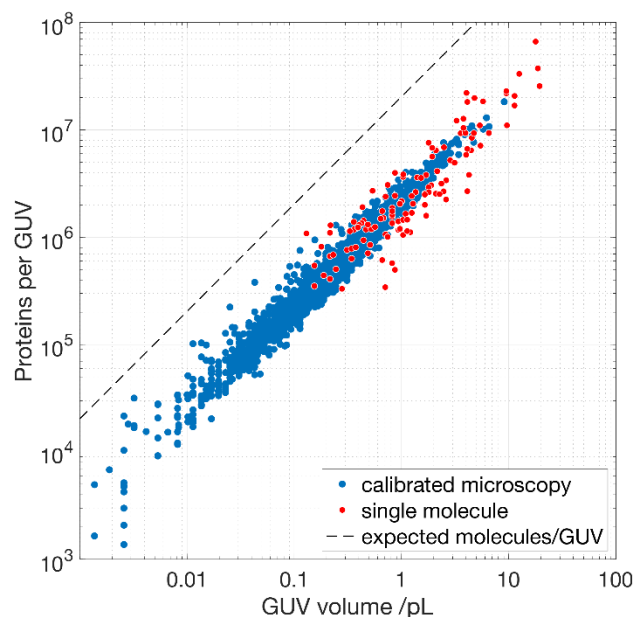


**Figure 4.23:** The plot of the measured number of molecules per GUV against volume of both the single molecule pulldown data (red) and the calibrated microscopy data (blue). The microscopy data is calibrated by a factor obtained from the ratio of the two constants of the respective distributions. (Calibrated microscopy  $n=1780$  single molecule  $n= 125$ )

In order to further test this, a concentration series studies were performed. 4 varying concentrations of streptavidin molecules starting at  $1 \times 10^4$ ,  $1 \times 10^5$ ,  $1 \times 10^6$  and  $2 \times 10^7$  molecules  $\text{pL}^{-1}$  were used as the seed solution. By taking into consideration both the encapsulation efficiency and the calibration factor, a graph of the number of molecules against the volume was plotted (**Figure 4.24a**).

The graph here also can be used as a calibration chart for the future production of GUV. The graph could be used as a guide to produce vesicles that have specific end concentrations. For instance, if we were interested in producing GUVs with an end concentration of  $10^3$  molecules per GUV, the user can then use a starting solution of  $1 \times 10^5$  molecules  $\text{pL}^{-1}$ . The resultant vesicles can then be screened to the corresponding size in order to obtain the desired final concentration. Alternatively, the concentration

of the seed solution can be altered for the desired end concentration with respect to the volume of the GUV.

The distribution of each of the concentration was also plotted in order show the comparison between the nominal concentration and the measured concentration. **(Figure 4.24b)**. The calculated values obtained were in close agreement to the nominal concentration. The tightness of the distribution of the vesicles with the varying concentration allows further strengthens the ability to use these vesicles as calibration standards. This would allow us to move away from the need to use single molecule pulldown techniques which would generally require specialised equipment and training. The high cost of such equipment is often seen as a barrier to entry within this field. However, with these standards in place, the imaging tool required would be the use of a fluorescence microscopy, one that is already commonly used and readily available. The vesicles here obviously have been calibrated to the imaging system and the molecules that have been specifically used in this experiments. As a follow on, it would be interesting to reproduce the vesicles at these concentrations and run it through an array of various imaging tools such as a mass spectrometer, FACS system, and different microscopes to investigate the variability of the data set. This would allow us to further comprehend the ability to use these vesicles as a calibration system in the future.

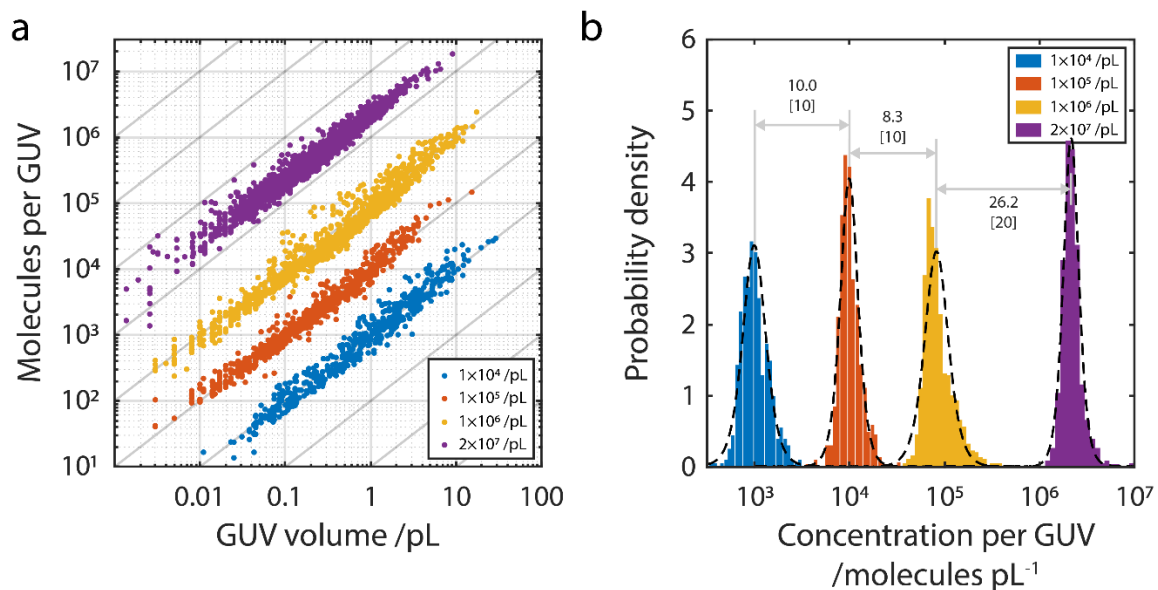


**Figure 4.24:** a) The plot of the calibrated molecules per GUV against the volume of the concentration series b) The distribution of the concentration series as a function of the concentration per GUV. The histogram shows the close agreement between the nominal and measured concentration series, further increasing confidence in the methodology that was developed.

More interestingly, the results here show that the use of phase transfer has the capability to produce simplified models of gene expression capable in testing the changes in copy number of biomolecules down to the resolution of two-fold.

These allows for the generation of varying populations of GUVs that has half the concentration of another. However, there is a greater degree of confidence in the population of GUVs with a ten-fold difference in the copy number as the degree of overlap between the two populations that are produced will be lower. These vesicles could be used as a simplified system to study the changes in the concentration of the starting material for particular gene expression system. The assumption that would be made here however would be that the results obtained here would be directly applicable to different biomolecules. Though this may not be the case, we can assume that for a molecule of a similar size and chemical properties to streptavidin, this particular method could be applicable.

In certain cases of genetic mutations, the reduction of the copy number may not necessarily lead to the change in the phenotype, and in some this might not be the case. For example, haploinsufficiency is a genetic condition in which the total copy number of the gene product produced falls below a threshold that is not sufficient for the cells to function normally. The use of these simplified model allows for the study and understand such genetic expression pathways to be carried out in isolation.<sup>197</sup>

The results here (**Figure 4.24b**) therefore show that in the instance that the copy number of the starting material is altered by a 10-fold change, the certainty of producing two distinct populations that have means of a 10-fold difference can be done to a higher degree of precision. However, if the copy numbers were altered to have a 2-fold change, there would be a significantly high degree of overlap between the distribution of the population due to the variance in the data. This indicates that a significant proportion of the GUV could potentially have the same amount of concentration within the vesicle. For such distributions, the GUVs at the edges can be distinguished, however, that may not be true for the vesicles near the mean of the distribution. A high proportion of the GUV at the overlap may exhibit similar biological behaviour, inferring that the doubling of the copy number of the gene in question does not lead to a phenotypical change, leading to distorted interpretations. However, if the same was repeated for with a change in the copy number of a gene at a ten-fold change, the populations would be more distinct with minimal overlap between the populations of the vesicles produced. This therefore allows for conclusions to be made with a higher degree of confidence.

One of the backbones of synthetic biology is the push to take on a more engineering-based approach in the development of artificial cell or biological mimics. This approach

towards the design of the simplified biological models require the understanding of the precise encapsulation of the copy numbers of different molecular constituents encapsulated. In order to be fully confident that concentration of the encapsulant is being precisely controlled, the behaviour of the important constituents of the molecular machinery is being studied. It is critical to the overall production of the bioproduct of the network that is being investigated. The encapsulation of these molecules can be done however, the efficiency of these different molecule has yet to be fully studied and understood. Therefore, the question of how the concentration of the copy number of the starting material can be controlled to remove the variability that may exist from the different components still remains. Additionally, to be confident that the concentration of the encapsulant is being controlled, we need to understand the behaviour of the important constituent of the molecular machinery that is being studied. In most cases, the GUV imaged is often based upon the fluorescence of the gene product, i.e. a fluorescent protein for instance. Often this requires a genetic addition that produces a tagged gene product. Though the question of how we could control the concentration of the starting material to remove any variability that may exist as a result of this still remains.

The understanding of the encapsulation efficiency explored in the scope of this thesis provides us with an insight of this. The EE to a certain extent allows for some degree of control over the concentration of the starting material. However, this issue becomes more crucial in biological networks that are sensitive to small changes in the concentration.

One of the potential applications of these model systems are in its use in the field of bio-therapeutics. It can be used as a vehicle to transport drug precursor, antibodies or even vaccines to target areas within the body. In the cases of such applications, there is a need to design systems that can achieve a higher degree of control over the concentration of the end product or systems that are more robust to the change in the concentration of the starting material. A methodology that could be used to achieve this would be using a chemist-based approach, where the reactions are optimised by altering the 'reaction conditions', including the exact concentration of the starting material.

Alternatively, in order to remove the variability that may arise from the different reaction conditions, a feedback loop system can be introduced within into the system. For instance, the design rules of the system can be such that the building blocks be introduced to the system in excess, together with a genetic control of a feedback loop such that when the gene product reaches a certain concentration, the gene expression is shutdown through a negative feedback loop. This could potentially allow for the concentration of the end product to be precisely monitored; however, such a system would be dependent upon the strength of the negative feedback loops. Alternatively, methods to improve and more precisely encapsulate the starting materials could be explored as well. This could include the use of a more microfluidic based approach to encapsulate the starting material of known concentrations within the vesicles. However, both these approaches may not seem as trivial and comes with its own sets of drawbacks.

## 4.5 Chapter conclusion

The work in this chapter described the development of a single molecule microarray method to measure the protein content of a vesicle based artificial cell. The method involved the use of a microfluidic device coupled with single molecule imaging capabilities that allowed for the encapsulation efficiency of GUVs to be determined. The GUVs encapsulating streptavidin molecules were produced using emulsion-based phase transfer, a facile technique that generates vesicles in high yield. This technique was demonstrated using a model protein system, however, can be adaptable to label-free proteins using an antibody sandwich assay or any class of biomolecules for which a suitable capture agent exists.

The absolute quantification of the encapsulation efficiency assists in providing a higher degree of control over the concentration of the encapsulant material. The encapsulation efficiency was calculated as a ratio of the calibrated number of molecules obtained experimentally to the expected number of molecules with respect to the volume of the individual vesicles. This was calculated to be between 2.4-41%. The results show a weak correlation between the encapsulation efficiency and the volume. The orthogonal variation of the encapsulation efficiency that exist within the same range of volume poses a problem in regard to the application as biological models. The loss mechanisms contribution to the non-ideal encapsulation efficiencies are still poorly understood however, would be crucial in order to optimise the production of such vesicles for its use as well-defined cell mimics. There was minimal variation in the encapsulation efficiency between different batches of samples. It shows that the data obtained is fairly reproducible and is for users to be confident in the use of this technique.

The work done in this chapter has allowed for the development of a calibration system. It shows that the single molecule technique can be used to calibrate the epifluorescence measurements to achieve absolute measurements. This was done by using the equivalence of the distribution of the data fitted using a logistics fit. Beyond this, the work also provided a potential calibration chart for future production of GUVs.

The tight distribution of the concentration series measurements shows the use of phase transfer to produce GUVs to study changes of copy numbers of biological networks and pathways in isolation at a 10-fold change. This can be carried out at a ten-fold change with a high degree of reliability. This is because the populations of the GUVs produced show distinct distributions with almost minimal overlap. The limitation of producing GUVs and measuring the distribution of the population using the methods we have developed here is at a 2-fold change. This is due to a significant overlap of the populations which would make it hard to distinguish between the population.

Emulsion based phase transfer remains a facile and easy method for the production of GUVs. The insight gained by understanding the limitations of the methods to study biomolecules of low copy numbers, strengthens the efficacy of this methodology. However, methods to help improve the variance of the encapsulation efficiency present within a population should be further explored to help develop the production of GUVs for its application as biological models.

## **5. Conclusions and Future Work**

The key objective behind this thesis was to develop a single molecule microarray platform capable of quantitatively assessing the encapsulated internal molecular constituent of vesicles. Previously reported methods to do so have failed to provide an absolutely quantitative assessment of the encapsulation efficiency as most methods mainly rely on semi quantitative measurements of the vesicles. In line with this, the ability to measure the exact concentration of the encapsulated biomaterial allows for the encapsulation efficiency the GUVs to be calculated at a single vesicle level. Encapsulation efficiency is an important parameter that should be considered when assessing the synthesis of GUVs for applications where the absolute amount of substrate within these vesicles are required. Additionally, a detailed data analysis methodology was developed and investigated for the analysis of wide field fluorescence microscopy data. A summary of the key findings in each chapter is given as follows.

### **5.1 Summary of Key Findings**

Chapter 3 described the use of a semi quantitative method of wide field fluorescence microscopy to characterise the distribution of the GUVs within populations. Using this method, we were able to obtain the relative concentration of the encapsulated protein within individual GUVs. The data presented showed a positive log linear relationship between the volume of the vesicle and the measured fluorescence intensity. However, due to the nature of the measurement that is of arbitrary units, the absolute concentration within the GUVs could not be determined hence leading to the development of microfluidic-based microarray platform. Additionally, wide field fluorescence microscopy was employed as an imaging tool to understand the distribution of the

GUVs. The use of the manual segmentation, a manual method used to trace the perimeter of the ROI was shown to be most ideal in approximating the area of the GUV. The use of the automated methods, Fiji thresholding filters and Cell Profiler was found to have a higher tendency to either overestimate or underestimate area, hence leading to a multiplicative error in the volume estimation. This effect is more apparent on the vesicles with a lower signal to noise ratio. This was an important tool to be optimised as the methodology of data analysis affected the interpretation of the data.

Chapter 4 detailed the development of a single molecule microarray method used to measure the protein content of vesicle based artificial cells. The use of this lab-on-a-chip approach allowed for the absolute concentration of the protein within each vesicle to be determined, and subsequently the encapsulation efficiency of encapsulating streptavidin using emulsion-based phase transfer. The method allowed for the variation of the EE across populations to be determined at  $11.4 \pm 6.2\%$ . By using a concentration series of the seed solution, the limitation of phase transfer was also investigated. The results obtained showed that the vesicles produced can be used to investigate biological networks with the precision of up to two-fold changes in the copy number of the starting material. However, the orthogonal variation that still exist within the population of the GUVs need to be controlled to improve the precision of these techniques especially for the use of the models in biotherapeutics applications. Thus, it is still key to understand the loss mechanisms associated with the non-ideal encapsulation efficiencies.

## 5.2 Future Work

### 5.2.1 On-chip Droplet Formation

The formation of the vesicles has mainly been carried out using a facile method of emulsion-based phase transfer technique. The reported mean encapsulation efficiency has shown to be significantly poor. Additionally, the work carried out has shown the existence of an orthogonal variation within the population of the GUV that may affect its use as artificial reaction vessels. Therefore, in a bid to improve this, a microfluidic-based droplet generator was used.

The generation of the droplet emulsion using microfluidics-based devices have been long carried out. The use of a microfluidic platform allows for better control over the formation of the droplets and bilayer formation. The platform here used would require a two-step process production process. The first step involves the use generation of the droplets using the microfluidic device, followed by a similar protocol of the inverse emulsion phase transfer protocol. For example, Tan et al. <sup>198</sup> showed a microfluidic vesicle formation method that was used to control the encapsulation with the capability of encapsulating various biological materials ranging from cancerous cells to micron sized beads. The stability of the vesicles produced using this methodology was over 3 weeks. The high degree of stability of the vesicles is an important additional parameter to be considered as it provides a greater degree of flexibility in its downstream application as artificial cell constructs or a drug delivery microreactors.

The droplet generation chip (The Dolomite Centre Ltd, United Kingdom.) is a glass microfluidic device that is designed for the generation of droplets that consisting of up to 3 different reagents. The standard surface of the device is of a hydrophobic coating

that allows for the generation of aqueous droplets in an oil carrier phase. The device consists of 4 different inlet channels and 2 outlet channels with a flow junction. The serpentine channel designed within the device also allows for the stabilisation of the droplet prior to the collection of the droplets at the outlet channel. The geometries of the device are given in the **figure 5.1**.

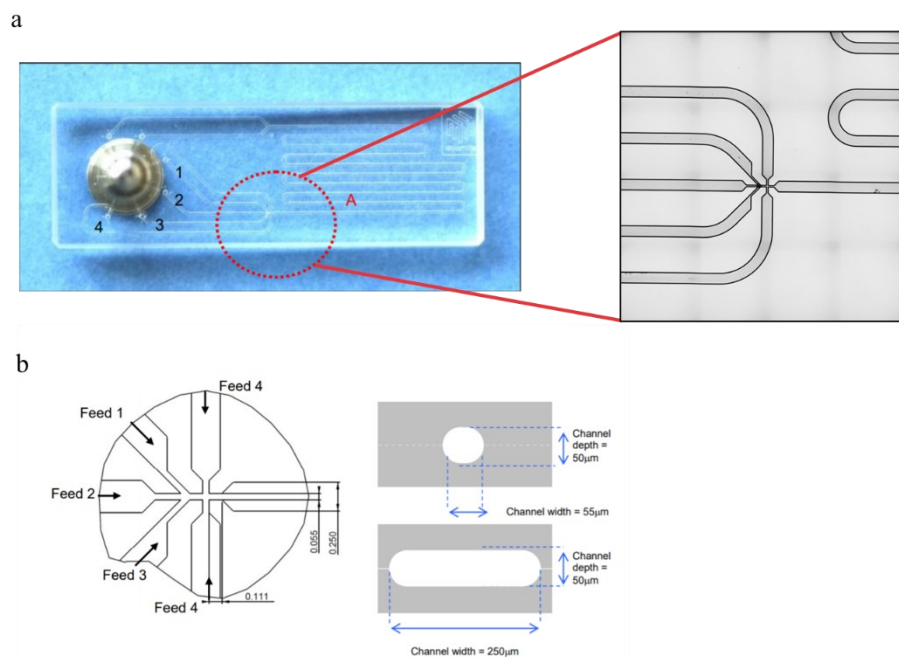


**Figure 5.1:** The figure above shows the design of the droplet generation chip. a) The device consists of a header with 4 inlets for the reagents, 2 outlets, a flow focusing junction (inset) and the serpentine channel. b) The geometries and the size of the channels of the device. Reproduced from reference <sup>199</sup>

The droplets would consist of an internal aqueous solution made up of sucrose and protein. The external solution would consist of the lipid in oil mixture. The droplets that are formed on-chip would be collected off-chip in prior to passing it through an interface to produce unilamellar vesicles. The W/O droplets and the resultant vesicles would be imaged in order to obtain the distribution of the sizes. As part of the experimental design, the addition of a surfactant may be vital to help improve the stability of the droplets. The presence of surfactants such as SPAN-80 may possibly improve the

consistency of the droplet formation, therefore preventing the coalescence of the droplet after formation. The use of a microfluidic device allows for the fine tuning of the size of the droplets by manipulating the flow rates of the two different phases.

The distribution analysis on the initial W/O emulsion and the resultant giant vesicles, was performed by Hamada et al.<sup>200</sup> and showed that the size of the emulsion directly affects the resultant sizes. In theory, controlling the distribution of the emulsion droplets could possibly narrow the distribution of the resultant vesicles. The tuneability of the volume range and the concentration of the molecules within the droplets can help narrow the distribution of the GUV population. It would be interesting to investigate if this would have an effect on the orthogonal variation of the concentration that currently exists.

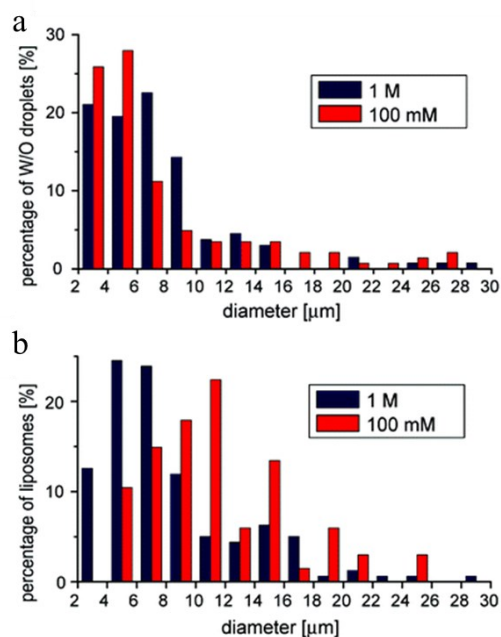


**Figure 5.2:** Comparison of size distribution of initial emulsion and resultant vesicle. a) W/O droplets produced before the transfer ( $N = 133$  (1 M), 143 (100 mM)) b) Vesicle resulting from the transfer of the droplets. ( $N = 159$  (1 M), 67 (100 mM)) Two varying concentration of the glucose solution was used in this experiment by Hamada et al. to show the dependence of the system on sugar molecules in the aqueous buffer solution. The histogram here is reproduced from the reference<sup>200</sup>

Initial preliminary work using the device showed the formation of droplets consisting of an internal sucrose solution as the aqueous phase with POPC lipid dissolved in mineral oil as the oil phase. Additionally, 1% (v/v) SPAN-80 was added to further stabilise the droplets. The resultant droplets were collected in an Eppendorf tube with additional mineral oil. The droplets were then imaged using 20× wide field microscopy and analysed. The image analysis was carried out by manually segmenting the individual droplets to obtain the size and subsequently volume information of the droplets.

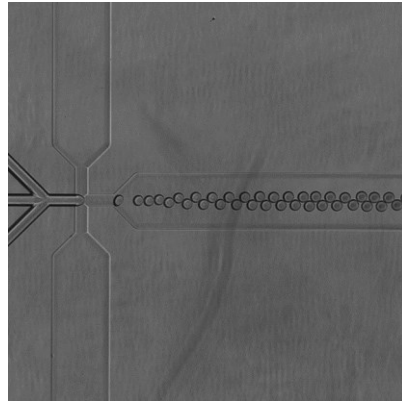


**Figure 5.3:** *The image of the droplets obtained using the droplet generation chip. The droplets were imaged using wide field microscopy. This methodology shows a narrow distribution of the droplet. These data were acquired together with another doctoral student, Zibo Wang.*

The distribution of the droplets produced showed a narrow range of the volumes. However, no early conclusions could be drawn as these were not used to produce the vesicles. Moving forward, this work needs to be further developed to allow for the distributions to be further understood. By recognizing the factors that give rise to the variation, we may be one step closer to having a better understanding of the loss mechanisms of the protein.

### **5.2.2 Automation of Data Analysis**

The most accurate data analysis method employed for the wide field fluorescence microscopy was by manually segmenting the individual vesicles. Though this methodology has shown to be most effective in producing distributions closest to the ground truth, it is particularly time consuming. The use of simple image analysis algorithms was insufficient to distinguish between objects that were in close proximity or significantly overlapped. Therefore, employing an automated method that comprehensively recognises the individual vesicles within large data sets in an

unsupervised manner is crucial. Additionally, it would be able to distinguish between clumped objects to avoid the resulting distribution becoming skewed away from the ground truth, especially for vesicles with a lower signal to noise ratio. The ability to do so would ensure the data analysis process to be both more efficient and of a higher throughput.

### **5.3 Concluding Statements**

This thesis has outlined the progress made in further understanding and developing a quantitative method to study the encapsulation efficiency of vesicles using inverted emulsion phase transfer. The work here shows the development of a single molecule microarray method that can be used to achieve absolute quantification of the protein content, thus measuring the encapsulation efficiency of GUVs using a model protein. This technique however can be extended to study systems comprising of label free proteins or any other classes of biomolecules for which a suitable capture agent is available. The production of artificial cells and the ability to control them on a molecular level is an immense and unprecedented challenge to which it has the potential to transform the future of therapeutics. Furthermore, the work here help in achieving an understanding in the limitation posed by the use of inverted emulsion phase transfer in the formation of cell mimics. The ability to use this method to study systems with a 2-fold increase in their concentrations will help pave way to the understanding of various different types of cellular systems. However, methods to help improve the variance of the encapsulation efficiency present within a population is still important and can serve as a stepping stone to the optimisation and design of these model membrane systems especially in the study of systems biology. One aspect that is crucial is to truly have an

understanding of the loss mechanisms that govern the non-ideal encapsulation efficiencies as this will be crucial in optimising the production of well-defined cell-mimics.

# References

---

- 1 European Commission, *Synthetic Biology - Applying Engineering to Biology - Report of a NEST High-Level Expert Group*, 2005.
- 2 A. S. Khalil and J. J. Collins, *Nat. Rev. Genet.*, 2010, 11, 367–379.
- 3 Y. Flores Bueso and M. Tangney, *Trends Biotechnol.*, 2017, 35, 373–378.
- 4 K. E. French, *Nat. Sustain.*, 2019, 2, 250–252.
- 5 D. E. Cameron, C. J. Bashor and J. J. Collins, *Nat. Rev. Microbiol.*, 2014, 12, 381–390.
- 6 J. C. Lachance, S. Rodrigue and B. O. Palsson, *Elife*, , DOI:10.7554/eLife.45379.
- 7 E. Andrianantoandro, S. Basu, D. K. Karig and R. Weiss, *Mol. Syst. Biol.*, 2006, 2, 2006.0028.
- 8 C. Xu, S. Hu and X. Chen, *Mater. Today*, 2016, 19, 516–532.
- 9 D. G. Gibson, J. I. Glass, C. Lartigue, V. N. Noskov, R. Y. Chuang, M. A. Algire, G. A. Benders, M. G. Montague, L. Ma, M. M. Moodie, C. Merryman, S. Vashee, R. Krishnakumar, N. Assad-Garcia, C. Andrews-Pfannkoch, E. A. Denisova, L. Young, Z. N. Qi, T. H. Segall-Shapiro, C. H. Calvey, P. P. Parmar, C. A. Hutchison, H. O. Smith and J. C. Venter, *Science (80-. )*, 2010, **329**, 52–56.
- 10 M. A. J. Roberts, R. M. Cranenburgh, M. P. Stevens and P. C. F. Oyston, *Microbiol. (United Kingdom)*, 2013, **159**, 1219–1220.
- 11 C. A. Hutchison, R. Y. Chuang, V. N. Noskov, N. Assad-Garcia, T. J. Deerinck, M. H. Ellisman, J. Gill, K. Kannan, B. J. Karas, L. Ma, J. F. Pelletier, Z. Q. Qi, R. A. Richter, E. A. Strychalski, L. Sun, Y. Suzuki, B. Tsvetanova, K. S. Wise, H. O. Smith, J. I. Glass, C. Merryman, D. G. Gibson and J. C. Venter, *Science (80-. )*, 2016, **351**, aad6253–aad6253.
- 12 Synthetic Biology: Life, Remixed | Max-Planck-Gesellschaft, [https://www.mpg.de/8219292/synthetic\\_biology](https://www.mpg.de/8219292/synthetic_biology), (accessed 10 March 2020).

- 13 H. Huang and D. Densmore, *Lab Chip*, 2014, 14, 3459–3474.
- 14 S. J. Moore, J. T. MacDonald and P. S. Freemont, *Biochem. Soc. Trans.*, 2017, 45, 785–791.
- 15 T. M. S. Chang, *Artif. Cells, Blood Substitutes, Biotechnol.*, 2007, 35, 545–554.
- 16 Y. Elani, *Biochem. Soc. Trans.*, 2016, **44**, 723–730.
- 17 A. Pohorille and D. Deamer, *Trends Biotechnol.*, 2002, 20, 123–128.
- 18 T. M. Swi Chang, *Nat. Rev. Drug Discov.*, 2005, 4, 221–235.
- 19 T. Osaki and S. Takeuchi, *Anal. Chem.*, 2017, 89, 216–231.
- 20 Y. Zhang, W. C. Ruder and P. R. LeDuc, *Trends Biotechnol.*, 2008, **26**, 14–20.
- 21 P. Schwille, J. Spatz, K. Landfester, E. Bodenschatz, S. Herminghaus, V. Sourjik, T. J. Erb, P. Bastiaens, R. Lipowsky, A. Hyman, P. Dabrock, J.-C. C. Baret, T. Vidakovic-Koch, P. Bieling, R. Dimova, H. Mutschler, T. Robinson, T.-Y. Y. D. Tang, S. Wegner, K. Sundmacher and D. Tang, *Angew. Chemie - Int. Ed.*, 2018, **57**, 13382–13392.
- 22 A. Salehi-Reyhani, O. Ces and Y. Elani, *Exp. Biol. Med.*, 2017, **242**, 1309–1317.
- 23 A. X. Lu, H. Oh, J. L. Terrell, W. E. Bentley and S. R. Raghavan, *Chem. Sci.*, 2017, **8**, 6893–6903.
- 24 E. Sokolova, E. Spruijt, M. M. K. Hansen, E. Dubuc, J. Groen, V. Chokkalingam, A. Piruska, H. A. Heus and W. T. S. Huck, *Proc. Natl. Acad. Sci. U. S. A.*, 2013, **110**, 11692–11697.
- 25 J. P. Douliez, A. Perro and L. Béven, *ChemBioChem*, 2019, 20, 2546–2552.
- 26 Y. Ai, R. Xie, J. Xiong and Q. Liang, *Small*, 2020, 16, 1903940.
- 27 N. Yaakov, K. Ananth Mani, R. Felfbaum, M. Lahat, N. Da Costa, E. Belausov, D. Ment and G. Mechrez, *ACS Omega*, 2018, **3**, 14294–14301.
- 28 N. Yeh Martín, L. Valer and S. S. Mansy, *Emerg. Top. Life Sci.*, 2019, **3**, 597–607.
- 29 V. Nele, M. N. Holme, U. Kauscher, M. R. Thomas, J. J. Douch and M. M. Stevens,

- Langmuir*, 2019, **35**, 6064–6074.
- 30 Y. Elani, S. Purushothaman, P. J. Booth, J. M. Seddon, N. J. Brooks, R. V. Law and O. Ces, *Chem. Commun.*, 2015, **51**, 6976–6979.
- 31 M. Pinot, F. Chesnel, J. Z. Kubiak, I. Arnal, F. J. Nedelec and Z. Gueroui, *Curr. Biol.*, 2009, **19**, 954–960.
- 32 P. J. Booth, M. L. Riley, S. L. Flitsch, R. H. Templer, A. Farooq, A. R. Curran, N. Chadborn and P. Wright, *Biochemistry*, 1997, **36**, 197–203.
- 33 Y. H. M. Chan and S. G. Boxer, *Curr. Opin. Chem. Biol.*, 2007, **11**, 581–587.
- 34 A. D. Bangham and R. W. Horne, *J. Mol. Biol.*, 1964, **8**, 660–668.
- 35 P. Stano, P. Carrara, Y. Kuruma, T. Pereira De Souza and P. L. Luisi, *J. Mater. Chem.*, 2011, **21**, 18887–18902.
- 36 J. Knobloch, D. K. Suhendro, J. L. Zieleniecki, J. G. Shapter and I. Köper, *Saudi J. Biol. Sci.*, 2015, **22**, 714–718.
- 37 H. Zhao and P. Lappalainen, *Mol. Biol. Cell*, 2012, **23**, 2823–2830.
- 38 T. O. B. Olusanya, R. R. H. Ahmad, D. M. Ibegbu, J. R. Smith and A. A. Elkordy, *Molecules*, 2018, **23**, 907.
- 39 A. D. Bangham, M. M. Standish and J. C. Watkins, *J. Mol. Biol.*, 1965, **13**, 238–252.
- 40 G. Bozzuto and A. Molinari, *Int. J. Nanomedicine*, 2015, **10**, 975–999.
- 41 T. Oberholzer, K. H. Nierhaus and P. L. Luisi, *Biochem. Biophys. Res. Commun.*, 1999, **261**, 238–241.
- 42 Y. Elani, R. V. Law and O. Ces, *Phys. Chem. Chem. Phys.*, 2015, **17**, 15534–15537.
- 43 S. Fujii, T. Matsuura and T. Yomo, *Biophys.*, 2015, **11**, 67–72.
- 44 M. Tsugane and H. Suzuki, *Sci. Rep.*, 2018, **8**, 9214.

- 45 Y. Elani, T. Trantidou, D. Wylie, L. Dekker, K. Polizzi, R. V. Law and O. Ces, *Sci. Rep.*, , DOI:10.1038/s41598-018-22263-3.
- 46 P. M. Gardner, K. Winzer and B. G. Davis, *Nat. Chem.*, 2009, **1**, 377–383.
- 47 C. Kurokawa, K. Fujiwara, M. Morita, I. Kawamata, Y. Kawagishi, A. Sakai, Y. Murayama, S. I. M. Nomura, S. Murata, M. Takinoue and M. Yanagisawa, *Proc. Natl. Acad. Sci.*, 2017, **114**, 7228–7233.
- 48 S. Berhanu, T. Ueda and Y. Kuruma, *Nat. Commun.*, 2019, **10**, 1–10.
- 49 J. W. Hindley, D. G. Zheleva, Y. Elani, K. Charalambous, L. M. C. Barter, P. J. Booth, C. L. Bevan, R. V Law and O. Ces, *Proc. Natl. Acad. Sci. U. S. A.*, 2019, **116**, 16711–16716.
- 50 G. Villar, A. D. Graham and H. Bayley, *Science (80-. )*, 2013, **340**, 48–52.
- 51 M. J. Booth, V. R. Schild, A. D. Graham, S. N. Olof and H. Bayley, *Sci. Adv.*, 2016, **2**, e1600056.
- 52 J. P. Reeves and R. M. Dowben, *J. Cell. Physiol.*, 1969, **73**, 49–60.
- 53 M. I. Angelova and D. S. Dimitrov, *Faraday Discuss. Chem. Soc.*, 1986, **81**, 303–311.
- 54 K. S. Horger, D. J. Estes, R. Capone and M. Mayer, *J. Am. Chem. Soc.*, 2009, **131**, 1810–1819.
- 55 S. Pautot, B. J. Frisken and D. A. Weitz, *Langmuir*, 2003, **19**, 2870–2879.
- 56 P. Supramaniam, O. Ces and A. Salehi-Reyhani, *Micromachines*, , DOI:10.3390/mi10050299.
- 57 A. Moga, N. Yandrapalli, R. Dimova and T. Robinson, *ChemBioChem*, 2019, **20**, 2674–2682.
- 58 A. Salehi-Reyhani, J. Kaplinsky, E. Burgin, M. Novakova, A. J. Demello, R. H. Templer, P. Parker, M. A. A. Neil, O. Ces, P. French, K. R. Willison and D. Klug, *Lab Chip*, 2011, **11**, 1256–1261.
- 59 Z. Li, J. Zhao, X. Wu, C. Zhu, Y. Liu, A. Wang, G. Deng and L. Zhu, *Biotechnol. Biotechnol. Equip.*, 2019, **33**, 223–230.

- 60 A. Marsano, C. Conficconi, M. Lemme, P. Occhetta, E. Gaudiello, E. Votta, G. Cerino, A. Redaelli and M. Rasponi, *Lab Chip*, 2016, **16**, 599–610.
- 61 M. L. Coluccio, G. Perozziello, N. Malara, E. Parrotta, P. Zhang, F. Gentile, T. Limongi, P. M. Raj, G. Cuda, P. Candeloro and E. Di Fabrizio, *Microelectron. Eng.*, 2019, **208**, 14–28.
- 62 N. Convery and N. Gadegaard, *Micro Nano Eng.*, 2019, **2**, 76–91.
- 63 A. B. Theberge, F. Courtois, Y. Schaerli, M. Fischlechner, C. Abell, F. Hollfelder and W. T. S. Huck, *Angew. Chemie - Int. Ed.*, 2010, **49**, 5846–5868.
- 64 K. Song, G. Li, X. Zu, Z. Du, L. Liu and Z. Hu, *Micromachines*, 2020, **11**, 297.
- 65 Y. Chen, P. Li, P. H. Huang, Y. Xie, J. D. Mai, L. Wang, N. T. Nguyen and T. J. Huang, *Lab Chip*, 2014, **14**, 626–645.
- 66 W. Weaver, H. Kittur, M. Dhar and D. Di Carlo, *Lab Chip*, 2014, **14**, 1962–1965.
- 67 K. Churski, P. Korczyk and P. Garstecki, *Lab Chip*, 2010, **10**, 816–818.
- 68 D. T. Chiu, A. J. DeMello, D. Di Carlo, P. S. Doyle, C. Hansen, R. M. Maceiczky and R. C. R. Wootton, *Chem*, 2017, **2**, 201–223.
- 69 J. H. Huang, J. Kim, Y. Ding, A. Jayaraman and V. M. Ugaz, *PLoS One*, 2013, **8**, 73188.
- 70 T. M. Squires and S. R. Quake, *Rev. Mod. Phys.*, 2005, **77**, 977–1026.
- 71 X. Jiang, Q. Xu, S. K. W. Dertinger, A. D. Stroock, T. M. Fu and G. M. Whitesides, *Anal. Chem.*, 2005, **77**, 2338–2347.
- 72 V. V. Abhyankar, M. A. Lokuta, A. Huttenlocher and D. J. Beebe, *Lab Chip*, 2006, **6**, 389–393.
- 73 D. B. Weibel and G. M. Whitesides, *Curr. Opin. Chem. Biol.*, 2006, **10**, 584–591.
- 74 A. Hatch, A. E. Kamholz, K. R. Hawkins, M. S. Munson, E. A. Schilling, B. H. Weigl and P. Yager, *Nat. Biotechnol.*, 2001, **19**, 461–465.

- 75 C. N. Baroud, F. Okkels, L. Ménétrier and P. Tabeling, *Phys. Rev. E - Stat. Physics, Plasmas, Fluids, Relat. Interdiscip. Top.*, 2003, **67**, 4.
- 76 R. Powers and J. C. Copeland, *Encyclopedia of Biophysics*, 2013.
- 77 J. D. Tice, H. Song, A. D. Lyon and R. F. Ismagilov, *Langmuir*, 2003, **19**, 9127–9133.
- 78 M. Joanicot and A. Ajdari, *Science (80-. )*, 2005, 309, 887–888.
- 79 X. Casadevall I Solvas and A. Demello, *Chem. Commun.*, 2011, **47**, 1936–1942.
- 80 E. Lakatos, A. Salehi-Reyhani, M. Barclay, M. P. H. Stumpf and D. R. Klug, *PLoS One*, , DOI:10.1371/journal.pone.0177336.
- 81 A. Ashkin, *VoLUMK 24*, 1970.
- 82 A. Ashkin, J. M. Dziedzic and T. Yamane, *Nature*, 1987, **330**, 769–771.
- 83 R. B. Brown and J. Audet, *J. R. Soc. Interface*, 2008, 5.
- 84 S. Chatzimichail, P. Supramaniam, O. Ces and A. Salehi-Reyhani, *J. Vis. Exp.*, , DOI:10.3791/56110.
- 85 Capsid Constructors, <https://capsidconstructors.github.io/lab-book/imaging/tirf.html>, (accessed 21 May 2021).
- 86 Fluorescence Microscopy - Basic Concepts in Fluorescence | Olympus Life Science, <https://www.olympus-lifescience.com/en/microscope-resource/primer/techniques/fluorescence/filters/>, (accessed 17 August 2020).
- 87 L. Smith, M. Kohli and A. M. Smith, *J. Am. Chem. Soc.*, 2018, **140**, 13904–13912.
- 88 A. Salehi-Reyhani, *Sci. Rep.*, 2017, **7**, 17957.
- 89 J. Schindelin, I. Arganda-Carreras, E. Frise, V. Kaynig, M. Longair, T. Pietzsch, S. Preibisch, C. Rueden, S. Saalfeld, B. Schmid, J. Y. Tinevez, D. J. White, V. Hartenstein, K. Eliceiri, P. Tomancak and A. Cardona, *Nat. Methods*, 2012, 9, 676–682.

- 90 T. J. Etheridge, R. L. Boulineau, A. Herbert, A. T. Watson, Y. Daigaku, J. Tucker, S. George, P. Jönsson, M. Palayret, D. Lando, E. Laue, M. A. Osborne, D. Klenerman, S. F. Lee and A. M. Carr, *Nucleic Acids Res.*, , DOI:10.1093/nar/gku726.
- 91 D. Sage, H. Kirshner, T. Pengo, N. Stuurman, J. Min, S. Manley and M. Unser, *Nat. Methods*, 2015, **12**, 717–724.
- 92 A. E. Knight, *Pure Appl. Chem.*, 2014, **86**, 1303–1320.
- 93 I. L. Jørgensen, G. C. Kemmer and T. G. Pomorski, *Eur. Biophys. J.*, 2017, **46**, 103–119.
- 94 M. Dezi, A. Di Cicco, P. Bassereau and D. Lévy, *Proc. Natl. Acad. Sci. U. S. A.*, , DOI:10.1073/pnas.1303857110.
- 95 P. Girard, J. Pécréaux, G. Lenoir, P. Falson, J. L. Rigaud and P. Bassereau, *Biophys. J.*, 2004, **87**, 419–429.
- 96 J. M. Hanson, D. L. Gettel, S. R. Tabaei, J. Jackman, M. C. Kim, D. Y. Sasaki, J. T. Groves, B. Liedberg, N. J. Cho and A. N. Parikh, *Biophys. J.*, 2016, **110**, 176–187.
- 97 S. Sachdev, A. Muralidharan, D. K. Choudhary, D. L. Perrier, L. Rems, M. T. Kreutzer and P. E. Boukany, *Soft Matter*, 2019, **15**, 9187–9194.
- 98 A. KÜchler, M. Yoshimoto, S. Luginbühl, F. Mavelli and P. Walde, *Nat. Nanotechnol.*, 2016, **11**, 409–420.
- 99 L. Hosta-Rigau, M. J. York-Duran, Y. Zhang, K. N. Goldie and B. Städler, *ACS Appl. Mater. Interfaces*, 2014, **6**, 12771–12779.
- 100 C. P. O’Neil, T. Suzuki, D. Demurtas, A. Finka and J. A. Hubbell, *Langmuir*, 2009, **25**, 9025–9029.
- 101 K. K. Nishimura, T. Matsuura, K. K. Nishimura, T. Sunami, H. Suzuki and T. Yomo, *Langmuir*, 2012, **28**, 8426–8432.
- 102 H. Soga, S. Fujii, T. Yomo, Y. Kato, H. Watanabe and T. Matsuura, *ACS Synth. Biol.*, 2014, **3**,

- 372–379.
- 103 Y. Bashirzadeh and A. P. Liu, *Soft Matter*, 2019, **15**, 8425–8436.
- 104 Y. Kuruma, P. Stano, T. Ueda and P. L. Luisi, *Biochim. Biophys. Acta - Biomembr.*, 2009, **1788**, 567–574.
- 105 J. Steinkühler, R. L. Knorr, Z. Zhao, T. Bhatia, S. M. Bartelt, S. Wegner, R. Dimova and R. Lipowsky, *Nat. Commun.*, 2020, **11**, 1–11.
- 106 R. Fielding and D. Lasic, *Expert Opin. Ther. Pat.*, 1999, **9**, 1679–1688.
- 107 T. M. Allen and P. R. Cullis, *Adv. Drug Deliv. Rev.*, 2013, **65**, 36–48.
- 108 J. O. Eloy, M. Claro de Souza, R. Petrilli, J. P. A. Barcellos, R. J. Lee and J. M. Marchetti, *Colloids Surfaces B Biointerfaces*, 2014, **123**, 345–363.
- 109 K. Tsumoto, H. Matsuo, M. Tomita and T. Yoshimura, *Colloids Surfaces B Biointerfaces*, 2009, **68**, 98–105.
- 110 K. I. Akashi, H. Miyata, H. Itoh and K. Kinoshita, *Biophys. J.*, 1996, **71**, 3242–3250.
- 111 J. Larsen, N. S. Hatzakis and D. Stamou, *J. Am. Chem. Soc.*, 2011, **133**, 10685–10687.
- 112 M. Buchanan, J. Arrault and M. E. Cates, *Langmuir*, 1998, **14**, 7371–7377.
- 113 R. B. Lira, R. Dimova and K. A. Riske, *Biophys. J.*, 2014, **107**, 1609–1619.
- 114 A. Weinberger, F. C. Tsai, G. H. Koenderink, T. F. Schmidt, R. Itri, W. Meier, T. Schmatko, A. Schröder and C. Marques, *Biophys. J.*, 2013, **105**, 154–164.
- 115 N. López Mora, J. S. Hansen, Y. Gao, A. A. Ronald, R. Kiełtyka, N. Malmstadt and A. Kros, *Chem. Commun.*, 2014, **50**, 1953–1955.
- 116 T. J. Politano, V. E. Froude, B. Jing and Y. Zhu, *Colloids Surfaces B Biointerfaces*, 2010, **79**, 75–82.
- 117 T. Shimanouchi, H. Umakoshi and R. Kuboi, *Langmuir*, 2009, **25**, 4835–4840.

- 118 E. M. Schmid, D. L. Richmond and D. A. Fletcher, *Methods Cell Biol.*, 2015, **128**, 319–338.
- 119 A. Witkowska, L. Jablonski and R. Jahn, *Sci. Rep.*, , DOI:10.1038/s41598-018-27456-4.
- 120 Y. Zhou, C. K. Berry, P. A. Storer and R. M. Raphael, *Biomaterials*, 2007, **28**, 1298–1306.
- 121 R. Wick, M. I. Angelova, P. Walde and P. L. Luisi, *Chem. Biol.*, 1996, **3**, 105–111.
- 122 K. Karamdad, R. V. Law, J. M. Seddon, N. J. Brooks and O. Ces, *Lab Chip*, 2015, **15**, 557–562.
- 123 A. Yamada, T. Yamanaka, T. Hamada, M. Hase, K. Yoshikawa and D. Baigl, *Langmuir*, 2006, **22**, 9824–9828.
- 124 H. Bouvrais, T. Pott, L. A. Bagatolli, J. H. Ipsen and P. Méléard, *Biochim. Biophys. Acta - Biomembr.*, 2010, **1798**, 1333–1337.
- 125 A. Salis, M. Boström, L. Medda, F. Cugia, B. Barse, D. F. Parsons, B. W. Ninham and M. Monduzzi, *Langmuir*, 2011, **27**, 11597–11604.
- 126 H. Pan, Y. Xia, M. Qin, Y. Cao and W. Wang, *Phys. Biol.*, , DOI:10.1088/1478-3975/12/4/045006.
- 127 F. Ruggeri, F. Zhang, T. Lind, E. D. Bruce, B. L. T. Lau and M. Cárdenas, *Soft Matter*, 2013, **9**, 4219–4226.
- 128 C. Kataoka-Hamai, Y. Kaizuka and T. Taguchi, *Langmuir*, 2016, **32**, 1250–1258.
- 129 W. Xu, B. Nathwani, C. Lin, J. Wang, E. Karatekin, F. Pincet, W. Shih and J. E. Rothman, *J. Am. Chem. Soc.*, 2016, **138**, 4439–4447.
- 130 H. Y. Liu, W. L. Chen, C. K. Ober and S. Daniel, *Langmuir*, 2018, **34**, 1061–1072.
- 131 C. Hamai, P. S. Cremer and S. M. Musser, *Biophys. J.*, 2007, **92**, 1988–1999.
- 132 Y. L. Jeyachandran, E. Mielczarski, B. Rai and J. A. Mielczarski, *Langmuir*, 2009, **25**, 11614–11620.

- 133 V. Militello, C. Casarino, A. Emanuele, A. Giostra, F. Pullara and M. Leone, *Biophys. Chem.*, 2004, **107**, 175–187.
- 134 H. Larsericsdotter, S. Oscarsson and J. Buijs, *J. Colloid Interface Sci.*, 2005, **289**, 26–35.
- 135 B. Yang and C. E. Wyman, *Biotechnol. Bioeng.*, 2006, **94**, 611–617.
- 136 K. Reimhult, K. Petersson and A. Krozer, *Langmuir*, 2008, **24**, 8695–8700.
- 137 E. Ploetz, B. Visser, W. Slingenbergh, K. Evers, D. Martinez-Martinez, Y. T. Pei, B. L. Feringa, J. T. M. De Hosson, T. Cordes and W. F. Van Dorp, *J. Mater. Chem. B*, 2014, **2**, 2606–2615.
- 138 B. Sweryda-Krawiec, H. Devaraj, G. Jacob and J. J. Hickman, *Langmuir*, 2004, **20**, 2054–2056.
- 139 T. R. Jones, I. H. Kang, D. B. Wheeler, R. A. Lindquist, A. Papallo, D. M. Sabatini, P. Golland and A. E. Carpenter, *BMC Bioinformatics*, 2008, **9**, 482.
- 140 J. C. Stachowiak, D. L. Richmond, T. H. Li, A. P. Liu, S. H. Parekh and D. A. Fletcher, *Proc. Natl. Acad. Sci.*, 2008, **105**, 4697–4702.
- 141 L. K. Huang and M. J. J. Wang, *Pattern Recognit.*, 1995, **28**, 41–51.
- 142 N. Otsu, *IEEE Trans Syst Man Cybern*, 1979, **SMC-9**, 62–66.
- 143 J. N. Kapur, P. K. Sahoo and A. K. C. Wong, *Comput. Vision, Graph. Image Process.*, 1985, **29**, 273–285.
- 144 S. B. Kulkarni, G. V. Betageri and M. Singh, *J. Microencapsul.*, 1995, **12**, 229–246.
- 145 P. Walde and S. Ichikawa, *Biomol. Eng.*, 2001, **18**, 143–177.
- 146 S. G. M. Ong, L. C. Ming, K. S. Lee and K. H. Yuen, *Pharmaceutics*, , DOI:10.3390/pharmaceutics8030025.
- 147 A. Gonzalez Gomez, S. Syed, K. Marshall and Z. Hosseinidoust, *ACS Omega*, 2019, **4**, 10866–

- 10876.
- 148 J.-P. P. Colletier, B. Chaize, M. Winterhalter and D. Fournier, *BMC Biotechnol.*, 2002, **2**, 9.
- 149 B. Van Hoof, A. J. Markvoort, R. A. Van Santen and P. A. J. Hilbers, *J. Phys. Chem. B*, 2014, **118**, 3346–3354.
- 150 M. Guimarães Sá Correia, M. L. Briuglia, F. Niosi and D. A. Lamprou, *Int. J. Pharm.*, 2017, **516**, 91–99.
- 151 G. V. Betageri and D. L. Parsons, *Int. J. Pharm.*, 1992, **81**, 235–241.
- 152 K. Göpfrich, B. Haller, O. Staufer, Y. Dreher, U. Mersdorf, I. Platzman and J. P. Spatz, *ACS Synth. Biol.*, 2019, acssynbio.9b00034.
- 153 B. Sun and D. T. Chiu, *Anal. Chem.*, 2005, **77**, 2770–2776.
- 154 B. Lohse, P. Y. Bolinger and D. Stamou, *J. Am. Chem. Soc.*, 2008, **130**, 14372–14373.
- 155 S. Matosevic and B. M. Paegel, *J. Am. Chem. Soc.*, 2011, **133**, 2798–2800.
- 156 L. M. Dominak and C. D. Keating, *Langmuir*, 2007, **23**, 7148–7154.
- 157 M. T. Hussain, N. Forbes and Y. Perrie, *Pharmaceutics*, 2019, **11**, 39.
- 158 Y. Li, Y. Shan, R. V Desai, K. H. Cox, L. S. Weinberger and J. S. Takahashi, *Proc. Natl. Acad. Sci. U. S. A.*, 2020, **117**, 10350–10356.
- 159 F. S. Collins, E. D. Green, A. E. Guttmacher and M. S. Guyer, *Nature*, 2003, **422**, 835–847.
- 160 Y. Hu, Q. An, K. Sheu, B. Trejo, S. Fan and Y. Guo, *Front. Cell Dev. Biol.*, 2018, **6**, 28.
- 161 C. Vogel and E. M. Marcotte, *Nat. Rev. Genet.*, 2012, **13**, 227–232.
- 162 Y. Liu, A. Beyer and R. Aebersold, *Cell*, 2016, **165**, 535–550.
- 163 Team:DTU-Denmark/Background sRNA - 2011.igem.org, [http://2011.igem.org/Team:DTU-Denmark/Background\\_sRNA](http://2011.igem.org/Team:DTU-Denmark/Background_sRNA), (accessed 6 July 2020).

- 164 G. Szalóki and K. Goda, *Cytom. Part A*, 2015, 87, 982–985.
- 165 J. R. Lin, M. Fallahi-Sichani and P. K. Sorger, *Nat. Commun.*, 2015, 6, 1–7.
- 166 M. Labib and S. O. Kelley, *Nat. Rev. Chem.*, 2020, 4, 143–158.
- 167 H. Sun, G. Y. J. Chen and S. Q. Yao, *Chem. Biol.*, 2013, 20, 685–699.
- 168 S. P. A. Fodor, J. L. Read, M. C. Pirrung, L. Stryer, A. T. Lu and D. Solas, *Science (80-. )*, 1991, 251, 767–773.
- 169 M. Schena, D. Shalon, R. W. Davis and P. O. Brown, *Science (80-. )*, 1995, 270, 467–470.
- 170 E. Kopf and D. Zharhary, *Int. J. Biochem. Cell Biol.*, 2007, 39, 1305–1317.
- 171 S. M. Zhou, L. Cheng, S. J. Guo, H. Zhu and S. C. Tao, *Front. Biol. (Beijing)*, 2012, 7, 336–349.
- 172 C. P. Pjaweletz, L. Charboneau, V. E. Bichsel, N. L. Simone, T. Chen, J. W. Gillespie, M. R. Emmert-Buck, M. J. Roth, E. F. Petricoin and L. A. Liotta, *Oncogene*, 2001, 20, 1981–1989.
- 173 F. X. X. R. Sutandy, J. Qian, C. S. Chen and H. Zhu, *Curr. Protoc. Protein Sci.*, 2013, 72, 27.1.1-27.1.16.
- 174 L. A. Tessler and R. D. Mitra, *Proteomics*, 2011, 11, 4731–4735.
- 175 M. He, J. S. Edgar, G. D. M. Jeffries, R. M. Lorenz, J. P. Shelby and D. T. Chiu, *Anal. Chem.*, 2005, 77, 1539–1544.
- 176 S. Köster, F. E. Angilè, H. Duan, J. J. Agresti, A. Wintner, C. Schmitz, A. C. Rowat, C. A. Merten, D. Pisignano, A. D. Griffiths and D. A. Weitz, *Lab Chip*, 2008, 8, 1110–1115.
- 177 X. Xu, J. Wang, L. Wu, J. Guo, Y. Song, T. Tian, W. Wang, Z. Zhu and C. Yang, *Small*, 2020, 16, 1903905.
- 178 A. Huebner, L. F. Olguin, D. Bratton, G. Whyte, W. T. S. Huck, A. J. De Mello, J. B. Edel, C. Abell and F. Hollfelder, *Anal. Chem.*, 2008, 80, 3890–3896.

- 179 B. Fan, X. Li, D. Chen, H. Peng, J. Wang and J. Chen, *Sensors (Switzerland)*, 2016, **16**, 232.
- 180 A. Salehi-Reyhani, S. Sharma, E. Burgin, M. Barclay, A. Cass, M. A. A. Neil, O. Ces, K. R. Willison and D. R. Klug, *Lab Chip*, 2013, **13**, 2066–2074.
- 181 A. J. Magness, J. A. Squires, B. Griffiths, K. Khan, A. Swain, K. R. Willison, D. Cunningham, M. Gerlinger and D. R. Klug, *Converg. Sci. Phys. Oncol.*, 2017, **3**, 024003.
- 182 Q. Shi, L. Qin, W. Wei, F. Geng, R. Fan, Y. S. Shin, D. Guo, L. Hood, P. S. Mischel and J. R. Heath, *Proc. Natl. Acad. Sci. U. S. A.*, 2012, **109**, 419–424.
- 183 Y. S. Shin, H. Ahmad, Q. Shi, H. Kim, T. A. Pascal, R. Fan, W. A. Goddard and J. R. Heath, *ChemPhysChem*, 2010, **11**, 3063–3069.
- 184 C. Ma, R. Fan, H. Ahmad, Q. Shi, B. Comin-Anduix, T. Chodon, R. C. Koya, C. C. Liu, G. A. Kwong, C. G. Radu, A. Ribas and J. R. Heath, *Nat. Med.*, 2011, **17**, 738–743.
- 185 T. N. Buican, M. J. Smyth, H. A. Crissman, G. C. Salzman, C. C. Stewart and J. C. Martin, *Appl. Opt.*, 1987, **26**, 5311.
- 186 G. Bolognesi, M. S. Friddin, A. Salehi-Reyhani, N. E. Barlow, N. J. Brooks, O. Ces and Y. Elani, *Nat. Commun.*, 2018, **9**, 1–11.
- 187 K. R. Rau, P. A. Quinto-Su, A. N. Hellman and V. Venugopalan, *Biophys. J.*, 2006, **91**, 317–329.
- 188 J. LaBaer and N. Ramachandran, *Curr. Opin. Chem. Biol.*, 2005, **9**, 14–19.
- 189 A. E. Kamholz, E. A. Schilling and P. Yager, *Biophys. J.*, 2001, **80**, 1967–1972.
- 190 E. A. Bayer and M. Wilchek, in *Journal of Chromatography*, 1990, vol. 510, pp. 3–11.
- 191 M. Wilchek and E. A. Bayer, *Methods Enzymol.*, 1990, **184**, 5–13.
- 192 J. C. Gildersleeve, O. Oyelaran, J. T. Simpson and B. Allred, *Bioconjug. Chem.*, 2008, **19**, 1485–1490.

- 193 O. H. Laitinen, H. R. Nordlund, V. P. Hytönen and M. S. Kulomaa, *Trends Biotechnol.*, 2007, 25, 269–277.
- 194 C. M. Dundas, D. Demonte and S. Park, *Appl. Microbiol. Biotechnol.*, 2013, **97**, 9343–9353.
- 195 S. Trier, J. R. Henriksen and T. L. Andresen, *Soft Matter*, 2011, **7**, 9027–9034.
- 196 S. Chatzimichail, P. Supramaniam and A. Salehi-Reyhani, *Anal. Chem.*, 2021, **93**, 6656–6664.
- 197 A. M. Deutschbauer, D. F. Jaramillo, M. Proctor, J. Kumm, M. E. Hillenmeyer, R. W. Davis, C. Nislow and G. Giaever, *Genetics*, 2005, **169**, 1915–1925.
- 198 Y. C. Tan, K. Hettiarachchi, M. Siu, Y. R. Pan and A. P. Lee, *J. Am. Chem. Soc.*, 2006, **128**, 5656–5658.
- 199 Droplet Generation Chip with Header,  
[https://www.johnmorrisgroup.com/Content/Attachments/23570/droplet\\_generation\\_chip\\_with\\_header\\_product\\_datasheet.pdf](https://www.johnmorrisgroup.com/Content/Attachments/23570/droplet_generation_chip_with_header_product_datasheet.pdf), (accessed 16 August 2020).
- 200 T. Hamada, Y. Miura, Y. Komatsu, Y. Kishimoto, M. Vestergaard and M. Takagi, *J. Phys. Chem. B*, 2008, **112**, 14678–14681.